

## Abstract

Treatments of a surface ion trap:  
A study of electric-field noise at a contaminated metal surface

by

Maya Gloria Berlin-Udi

Doctor of Philosophy in Applied Science and Technology

University of California, Berkeley

Professor Hartmut Häffner, Chair

All surfaces generate electric-field noise, yet the physical origins of this noise are not well understood. This has been an active area of research in the ion-trapping community for the past two decades, as ions are highly sensitive to electric-field fluctuations. With our work, we aim to illuminate the microscopic processes that drive charge dynamics on metal surfaces, so as to enable the engineering of low-noise quantum devices.

We use a single trapped  $^{40}\text{Ca}^+$  as a detector to study noise generated by the surface of the ion trap. We study this noise by observing how it responds to changes in the properties of the trap surface. The surface properties are altered using treatments including prolonged heating, argon ion milling, and electron bombardment. Characterization tools are used to monitor the effects of these treatments. Our measurements are consistent with noise produced by an ensemble of thermally activated fluctuators, so our data is discussed in this context.

In this dissertation, we present results from a complicated series of surface-treatment experiments, the majority of which took place on a single Al/Cu substrate. The results of these experiments indicate that argon ion milling can lower noise both by removing contaminants and by altering the morphology of the trap surface. The effects of morphology are isolated from the effects of contaminant removal through heat treatments, which alter the structure of the surface without changing its composition. Through electron bombardment experiments, we begin an exploration of the relationship between hydrocarbon adsorbate structure and electric-field noise. In addition, we compare the noise characteristics of a set of similarly-fabricated traps, and determine that atmosphere exposure has a major impact on noise from Al/Cu substrates.

These experiments establish links between the electric-field-noise characteristics and the microscopic properties of a contaminated metal trap surface. The insights developed in this work can inform the next generation of ion trap engineering, storage, and treatment.

# Contents

<b>1</b>	<b>Introduction</b>	<b>1</b>
<b>2</b>	<b>Electric-field noise in ion traps</b>	<b>3</b>
2.1	Surface electric-field noise . . . . .	3
2.2	Trapped ions . . . . .	4
2.3	Quantum information processing . . . . .	4
2.4	Current progress . . . . .	5
<b>3</b>	<b>Micro-fabricated surface trap</b>	<b>7</b>
3.1	RF quadrupole traps . . . . .	7
3.2	Chip design . . . . .	9
3.3	Fabrication process . . . . .	11
3.4	Properties of the trap surface . . . . .	13
<b>4</b>	<b>Noise measurement methods</b>	<b>15</b>
4.1	Optical control of calcium ions . . . . .	15
4.2	Ion heating rate measurements . . . . .	17
4.3	Calculation of electric-field noise . . . . .	20
4.4	Frequency scaling of ion heating rates . . . . .	21
4.5	Experimental setup . . . . .	22
<b>5</b>	<b>Surface treatment &amp; characterization techniques</b>	<b>26</b>
5.1	Trap substrate heating . . . . .	27
5.2	Auger spectroscopy & electron bombardment . . . . .	31
5.3	Argon ion milling . . . . .	37
5.4	Ion-trapping side effects . . . . .	37
<b>6</b>	<b>Thermally activated fluctuators</b>	<b>39</b>
6.1	Mathematical framework . . . . .	39
6.2	Fit to ion-heating-rate data . . . . .	41
6.3	The physical embodiment of TAFs . . . . .	46
6.4	Summary . . . . .	48
<b>7</b>	<b>Timeline of data and surface treatments</b>	<b>49</b>

<b>8 Heating rates in different aluminum-copper traps</b>	<b>66</b>
8.1 Background on four aluminum/copper ion traps . . . . .	66
8.2 Linking fabrication process variations & heating-rate magnitudes . . . . .	68
8.3 Material removal & changes in surface composition . . . . .	71
8.4 Material removal & ion heating rate reductions . . . . .	73
8.5 Summary . . . . .	74
<b>9 Thermal transformation of electric-field noise</b>	<b>76</b>
9.1 Thermal transformation versus thermal activation . . . . .	76
9.2 Saturation of the thermal transformation effect . . . . .	77
9.3 Insights from argon ion milling . . . . .	79
9.4 Intermittent transformations . . . . .	80
9.5 Investigation of contaminant deposition . . . . .	85
9.6 Investigation of chemical changes . . . . .	86
9.7 Investigation of atomic restructuring . . . . .	89
9.7.1 Recrystallization temperatures . . . . .	89
9.7.2 Morphological changes: annealing . . . . .	90
9.7.3 Morphological changes: milling . . . . .	92
9.7.4 TAF distributions and surface binding energies . . . . .	95
9.7.5 Correlation lengths of noise sources . . . . .	98
9.7.6 Ex-situ surface treatment and characterization experiments . . . . .	99
9.8 Summary . . . . .	100
<b>10 Electron bombardment experiments</b>	<b>102</b>
10.1 Overview of experimental results . . . . .	102
10.1.1 Treatment parameters . . . . .	103
10.1.2 Substrate properties . . . . .	104
10.1.3 Heating rate measurements . . . . .	107
10.2 Materials interacting with energetic electrons . . . . .	109
10.2.1 Conductors . . . . .	109
10.2.2 Insulators . . . . .	109
10.2.3 Organic contaminants . . . . .	110
10.2.4 Electron beam induced deposition . . . . .	111
10.3 The underlying physics of five electron treatments . . . . .	111
10.3.1 Electron 1 . . . . .	112
10.3.2 Electron 2 . . . . .	113
10.3.3 Electron 3 . . . . .	116
10.3.4 Electron 4 . . . . .	117
10.3.5 Electron 5 . . . . .	118
10.4 Summary and plans for future work . . . . .	120
<b>11 High-temperature shoot off</b>	<b>122</b>
<b>12 Summary and outlook</b>	<b>127</b>



# Chapter 1

## Introduction

For the past two decades, the physical origins of surface electric-field noise have been an active area of research in the ion-trapping community. This is because ions are highly sensitive to electric-field fluctuations, and these fluctuations are generated by all ion trap surfaces. A trapped atomic ion can operate as an ultra-sensitive narrow-band electric-field-noise detector. Because of these detection capabilities, a trapped ion is a powerful tool in the study of microscopic surface charge dynamics. An understanding of these dynamics would enable the engineering of ultra-low-noise ion trap chips, which would enhance the ability of trapped ions to serve as vehicles for quantum information processing and tests of fundamental physics.

We aim to illuminate the physics of these dynamic processes by observing how the electric-field noise from a metal surface changes in response to surface treatments. The data-taking stage of this project began in 2017, when we took the first systematic measurements of electric-field noise in an ion trap substantially above room temperature. After completing these initial measurements, we planned an experiment that involved a series of small-dose surface sputter treatments, interspersed with Auger spectroscopy and noise measurements at multiple temperatures and frequencies.

What was expected to be a simple, month-long experiment became a highly-involved project that continued over a period of almost two years. First, we observed that the electron beam from the Auger spectrometer had a significant impact on surface noise, and must be considered as a surface treatment in its own right. When we began the sputter treatments, the noise in this trap responded differently to sputtering than similarly-fabricated traps had in the past. Our first round of noise measurements in a hot trap were stable and repeatable, but after a few rounds of sputtering, the heat began to induce persistence changes in the surface noise magnitude.

Piecing together our complicated array of measurement results, and the vast literature on surface treatments performed in different contexts, we have been able to uncover many new insights about the noise in our trap. This project was highly exploratory, and leaves many questions unanswered, but can provide a strong jumping-off point for future experiments in ion trap surface science.

This dissertation is organized as follows. In Chapter 2, we provide an overview of previous experimental and theoretical studies of ion-trap surface noise. In Chapter 3, we present the details of our ion trap. Details include the principles of its operation as an electronic device,

the fabrication process through which it was made, and the physical properties of the metal film that coats its surface. In Chapter 4, we introduce standard optical control methods for calcium ions, and explain how we use these methods to measure the power-spectral-density of the electric-field noise at the ion. In Chapter 5 we introduce our other surface characterization and treatment tools, including Auger spectroscopy, trap heating, and argon ion milling.

In Chapter 6, we introduce the thermally-activated-fluctuator model, and do a meta-analysis of all of our data in the context of this model. In Chapter 7, we show a timeline of all of the noise measurements, Auger spectra and surface treatments that took place during this experiment. This timeline establishes a naming convention so that datasets can be referred to consistently throughout the remaining chapters of this dissertation. In Chapter 8, we compare the noise measured in our trap to noise in other similarly fabricated ion traps, both treated and untreated. In Chapter 9, we discuss how surface roughness affects electric-field noise, and we present data from milling, heating and select electron-bombardment experiments. In Chapter 10 we focus exclusively on electron-bombardment experiments, and explore how these experiments can inform our understanding of how carbon compounds generate electric-field noise. Finally, in Chapter 11, we discuss the phenomenon in which the noise magnitude shoots up around 600 K, and speculate about possible underlying causes.

# Chapter 2

## Electric-field noise in ion traps

### 2.1 Surface electric-field noise

Surface electric-field noise is the fluctuation of an electric field due to charge movement at the surface of a material. Noise from metal surfaces is of particular interest to the ion trapping community, as these surfaces play a key role in trapped-ion quantum information processing. While it is generally understood that dynamic processes such as defect hopping and contaminant diffusion take place at metal surfaces, it is not known which microscopic processes specifically dominate charge dynamics.

Measurements of electric-field noise in ion traps have varied widely between different research groups and different traps [1], including variations in noise magnitudes, frequency and distance dependencies, and treatment responses. This is an indication that no single process is responsible for all surface noise. Most likely, in any given system there are multiple competing mechanisms at play. To understand electric-field noise from metal surfaces in general, we must first disentangle these mechanisms through in-depth studies of individual surfaces.

In order to investigate the underlying microscopic processes that take place in our specific physical system, an Al/Cu surface ion trap, we combine electric-field noise measurements with surface treatments. Electric-field noise is characterized by its power spectral density, which can be measured with great precision using a trapped ion as a detector. As the physical properties of the surface change in response to treatments, the power spectral density of the electric-field noise changes as well. By alternating between different types of surface treatments, while tracking the state of the surface and its electric-field noise, we can begin to pin down properties of the underlying noise sources.

The advancement of our understanding of surface charge dynamics would open new avenues for ion trap engineering. It could also benefit other technologies which suffer from surface noise of various kinds, both inside and outside of the field of quantum information processing. Charge states are tied to crystal lattice configurations, chemical bond structures, and likely other phenomena of interest to scientists and engineers in a diverse range of disciplines. As a result, the development of trapped ions as a tool to investigate surface charge dynamics could have far reaching applications.

## 2.2 Trapped ions

A trapped ion is a single charged particle, levitated in vacuum by an electromagnetic field. For the purpose of measuring electric-field noise, the ideal ion has a simple energy structure with transitions that are accessible with existing laser technologies. Lasers can then be used to initialize, control, and read out the electronic state of the ion. We will describe the control scheme that we use for our  $^{40}\text{Ca}^+$  ions in Section 4.1.

In order to measure the power spectral density of the electric-field noise, the ion is held in a harmonic potential. In our system, we use a RF quadrupole trapping configuration, the details of which will be discussed in Section 3.1. The harmonic potential has evenly spaced vibrational energy levels with a transition energy of  $\hbar\omega$ . Electric-field noise at frequency  $\omega$  drives transitions between these vibrational energy levels, thus causing the ion to heat up.

When the ion heats up, the control lasers become Doppler shifted with respect to the electronic transitions in the ion. This changes the speed at which a laser pulse can alter the electronic state. As a result, after a laser pulse, the electronic state of the ion depends on its motional state. Having already developed the tools to initialize and read out electronic states, it is now possible to deduce the vibrational energy of the trapped ion. To measure the power spectral density of the electric-field noise, one measures how quickly the vibrational energy of an ion changes in the presence of an electric field. Section 4.2 will describe these measurements and calculations in more detail.

## 2.3 Quantum information processing

Trapped ions have proven to be a promising architecture for quantum information processing [2]. Every ion of the same species is exactly identical, and electronic states of select species can be reduced to simple two-level systems. Levitated ions are well isolated, and can safely store qubit information for over ten minutes without error correction [3]. Ion qubits can be initialized and read out optically. In addition, high-fidelity single-qubit gates and multi-qubit entangling gates can be performed using simple laser pulse sequences.

Quantum computers are designed to take advantage of the computational power of entangled superpositions. These superpositions can contain massive amounts of information. Through carefully engineered constructive and destructive interference, some superpositions can be distilled down to reveal simple solutions to complex problems. Some interesting problems that are intractable in classical computing are thought to be solvable with a quantum computer.

Long-term quantum-computing goals include breaking classical encryption schemes and simulating chemical reactions, but these milestones require quantum computers far more powerful than those in existence today. The first useful application of a quantum information processor will likely be a quantum emulation. Even simple quantum systems are difficult to simulate classically, but could be emulated and studied with a small-scale quantum processor. In order to build such a processor, many engineering challenges must be overcome, including the mitigation of surface electric-field noise.

Electric-field noise lowers the fidelity of both single- and multi-qubit gates. Gates depend on laser pulses with precise frequencies and stable amplitudes [4]. Uncontrolled ion vibrations

can introduce frequency instability via Doppler shifts, and amplitude instability via the movement of the ion away from the center of focused laser beams. Multi-ion gates are particularly sensitive to electric-field noise, as these gates require ultra-stable motional states. Coulomb interactions between ions in a chain cause the ions to share motional modes. In a multi-ion gate operation, the motional modes of the chain are used as a bus to entangle together the electronic states of different ions [Molmer1999]. If electric-field noise drives a change in the motional state of the chain during a multi-qubit operation, the operation will fail.

The fidelity of a two-qubit entangling gate performed in a standard 3D ion trap is not typically limited by surface electric-field noise [5]. However, the engineering required to scale up this system into a useful quantum processor amplifies electric-field-noise-induced motional heating. A useful ion-based processor must contain many ions, yet the heating rate of the center-of-mass vibrational mode of a chain scales linearly with its ion number. The processor must be capable of quickly shuttling ions between different chains, but shuttling requires the ions to be close to the surface of the electrodes. The closer an ion gets to the noisy metal surface, the higher the noise at the ion becomes. In addition to enabling shuttling, moving the ion close to the electrode makes it possible to raise the ion trap frequency without raising the electrode voltage, thus lowering the time required for entangling gates. Furthermore, traps with small ion-electrode distances can be microfabricated, enabling complex electrode configurations that would not otherwise have been possible to build.

## 2.4 Current progress

Many ion-trapping projects could benefit greatly from the successful mitigation of surface electric-field noise. For this reason, over the past two decades, a significant effort has been put towards studying electric-field noise in ion traps. In early literature on this subject, these efforts were referred to as the study of *anomalous heating*, as it was not known where the noise was coming from.

Electric-field-noise power spectral densities ranging from  $10^{-16}$  to  $10^{-6}$  V $^2$ /m $^2$ Hz have been measured by trapped ions. Over the course of many different experiments, noise has been studied at frequencies between 0.1 and 20 MHz, at ion-surface distances between 30 and 3500  $\mu$ m, and at temperatures between 4 and 600 K [1, 6].

Power spectral density measurements taken in many different ion traps show that surface noise scales as  $1/f^\alpha$ , where  $f$  is the noise measurement frequency. Measurements of  $\alpha$  cluster around 1 and 1.5 [1]. Noise has been found to scale as  $1/d^\beta$ , where  $d$  is the ion-electrode distance.  $\beta$  has been measured to be 2.4 and 4 in different systems [7, 8]. Measurement of electric-field noise as a function of temperature have revealed a variety of different scaling behaviors, but in most cases noise decreases as the substrate temperature is lowered, and increases as the substrate temperature is raised, indicating that the dominant noise sources are heat activated [9, 10, 6]. A study comparing traps with different species of untreated metal films found only small differences between noise levels in different electrode materials [11].

Several different types of surface treatments have been done in ion traps in conjunction with electric-field-noise measurements. Laser ablation reduced electric-field noise by about

50% in one ion trap [12]. Ion milling reduced noise by up to two orders of magnitude [13, 14, 15, 16], and oxygen plasma reduced noise by a factor of four [17]. In all cases, these treatments removed contamination from the surface of the trap. These results indicate that surface contaminants play a key role in generating electric-field noise in ion traps.

However, the relationship between contamination and electric-field noise is not straightforward. Daniilidis et. al. found that a trap recontaminated after milling maintained a low noise magnitude [13]. Sedlacek et. al. observed that for some materials, ion milling actually increased noise at cryogenic temperatures, and Sedlacek et. al. found that noise first rose and then fell in response to a series of small-dose ion milling treatments [16].

The data gathered through measurements of electric-field noise in ion traps can be used to inform models of the underlying noise processes. In surface noise experiments, a serious effort is made to remove electromagnetic pickup and technical noise from trapping electronics, so these mechanisms can be set aside. Metals are known to produce black-body radiation and Johnson-Nyquist noise. These sources have been carefully considered and ruled out, as their magnitudes are far too low to explain the observed noise [1].

Some promising physical models include fluctuating adsorbate dipoles [18], adsorbate diffusion on surfaces [19], noise from a surface dielectric layer [20], and noise from thermally activated fluctuators [6]. No single model has been able to fully explain the experimental data described above, but all are able to describe an interesting subsection of the observed noise behaviors and characteristics. Additional discussion of noise models can be found in the surface noise review by M. Brownnutt et. al. [1].

In summary, electric-field-noise measurements taken in ion traps reveal a jumbled and confusing landscape of information. In this dissertation, we combine electron bombardment, heat treatment and argon ion milling in a single trap to further investigate the complexities of electric-field noise generated by contaminants. Our exploratory surface treatment work provides a clear and consistent overview of noise in one trap, which can pave the way for more concrete studies of surface noise.

# Chapter 3

## Micro-fabricated surface trap

The ultimate goal of our work is to understand the microscopic processes that generate electric-field noise on metal surfaces. To this end, we perform a variety of surface treatments on a single ion trap substrate, and use trapped ions to measure changes in the surface electric-field noise. In these experiments, the metal film on the surface of the ion trap is the subject of our scientific inquiry, and it is also a critical component of an actively-operating electronic device. In this chapter we will explain how this device (the quadrupole ion trap) works, present the design of our trap, describe our microfabrication processes, and show results from surface characterization measurements.

### 3.1 RF quadrupole traps

The RF quadrupole ion trap, also known as the Paul trap, is a well-established tool in experimental atomic physics. It is designed to trap charged particles at the null point of an electric field. The field is generated by a set of electrodes carrying DC and RF voltages.

To create a stable trapping point, the electric field at that point must be zero, and the field must exert a restoring force if the trapped particle (the ion) is displaced in any direction. A positive ion will encounter a restoring force along a given axis if the second derivative of the electric potential with respect to position is negative along that axis. If the second derivative is positive, then a slight displacement will cause the ion to be ejected away from the null point instead of restored back. It is impossible to create a stable 3D trapping point with static electric fields, as electric potentials must obey the Laplace equation. The Laplace equation states:

$$\Delta^2 V = \frac{\partial^2 V}{\partial x_1^2} + \frac{\partial^2 V}{\partial x_2^2} + \frac{\partial^2 V}{\partial x_3^2} = 0, \quad (3.1)$$

where  $V$  is the electric potential and  $x_1$ ,  $x_2$  and  $x_3$  are orthogonal spatial dimensions. It follows that if there is a restoring force along any axis, then a different axis must have an ejecting force so that the second derivatives of the potentials sum to zero.

Remarkably, it is possible to create a stable, 3D restoring force using oscillating electric fields. Electrodes in Paul traps are designed to produce a saddle potential. A two-dimensional saddle potential is shown in Figure 3.1a. In this image, red and blue coloring

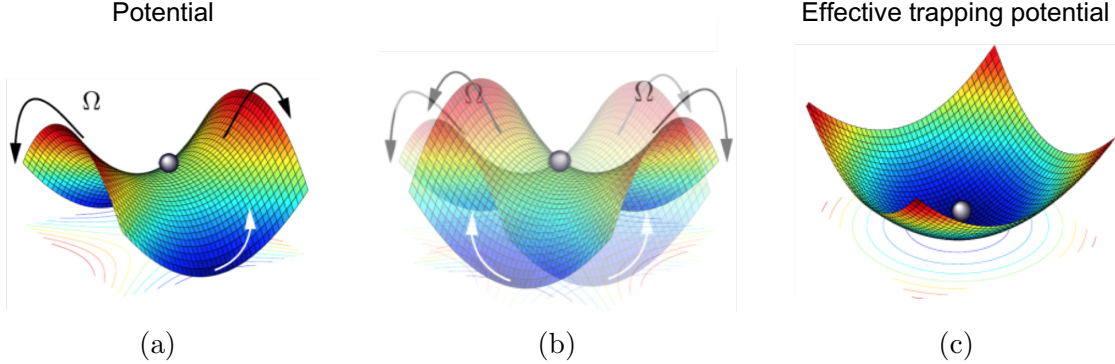


Figure 3.1: Illustration of RF trapping mechanism, adapted from [21]. (a) 2D saddle potential, where red and blue coloring correspond to areas with high and low potential respectively. (b) Saddle oscillating between two configurations. (c) Effective trapping potential, achieved when trapping parameters meet conditions for stability.

correspond to areas with high and low potential respectively. A saddle potential provides a restoring force along one axis, and an ejecting force along the other, thus obeying the Laplace equation.

In Figure 3.1b, the saddle oscillates at frequency  $\Omega$ , while keeping constant the potential at the position of the ion. This can be implemented in an ion trap by applying an oscillating voltage to some of the electrodes. The motion of an ion in an oscillating saddle potential can be derived from the Mathieu equation.

If the electrode geometry, voltages, and RF drive frequency  $\Omega$  are optimized to the mass and charge of the ion, the oscillating saddle generates an effective trapping potential, as illustrated in Figure 3.1c. For a discussion of the Mathieu equation in the context of ion trapping, including how to determine stable trapping parameters for a given ion, see reference [22].

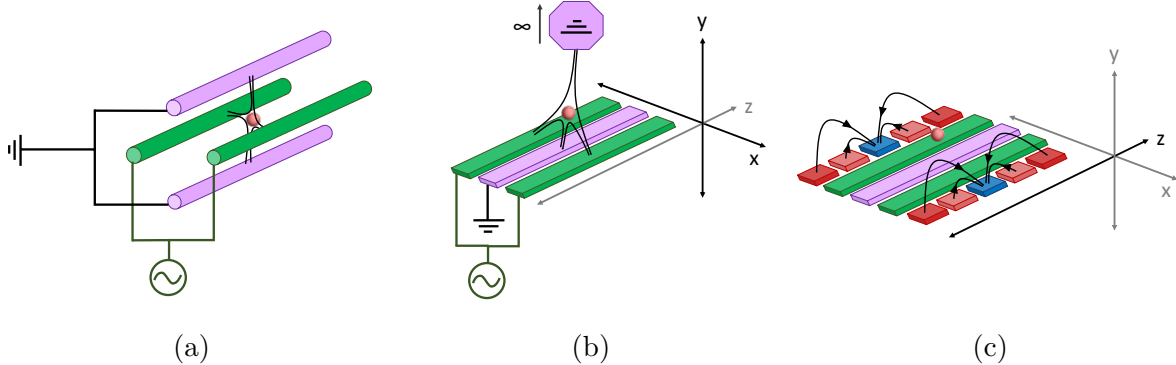


Figure 3.2: a) Cartoon of a simple 3D RF quadrupole Paul trap. (b) Microfabricated surface trap with RF-generated radial confinement. (c) Microfabricated surface trap with DC-generated axial confinement.

A cartoon of a simple 3D RF quadrupole Paul trap is shown in Figure 3.2a. This trap has four poles, two of which are grounded, and two of which oscillate between positive and

negative voltages at a frequency of  $\Omega$ . An ion is trapped between the poles. Typically, a 3D Paul trap also has DC end-cap electrodes to provide confinement along the z-axis.

The first RF Paul trap was built in 1954 [23] by Wolfgang Paul. In 2005, Chiaverini et. al. developed the microfabricated surface trap [24]. This trap was designed to be a modular component of a large-scale trapped-ion quantum information processor. As illustrated in Figure 3.2b, the surface trap is a 3D trap in which the poles have been rearranged. In a surface trap, two oscillating and one grounded electrode are fabricated on a flat plane. The grounded vacuum chamber serves as the fourth electrode, and the ion is trapped above the microfabricated center electrode. Typically the distance between the ion and the nearest electrode surface is smaller in a surface trap than in a 3D trap.

The electrodes illustrated in Figure 3.2b provide confinement along the x- and y-axes, commonly referred to as the radial directions. In a surface trap, additional planar DC electrodes generate confinement along the z-axis, which is commonly referred to as the axial direction. Axial confinement electrodes are illustrated in Figure 3.2b. For more information on the techniques we use to engineer the RF and DC confinement in surface traps, refer to Littich masters thesis [21].

## 3.2 Chip design

Having outlined the basic operating principles of surface RF quadrupole traps, we will now present the specific details of our trap design. Figure 3.3 shows a top view of the ion trap chip, with DC and RF electrodes highlighted. In this design, the RF electrodes are connected together. The RF electrodes are driven at frequency  $\Omega = 2\pi \times 36$  MHz, with a peak-to-peak amplitude of about 100 V.

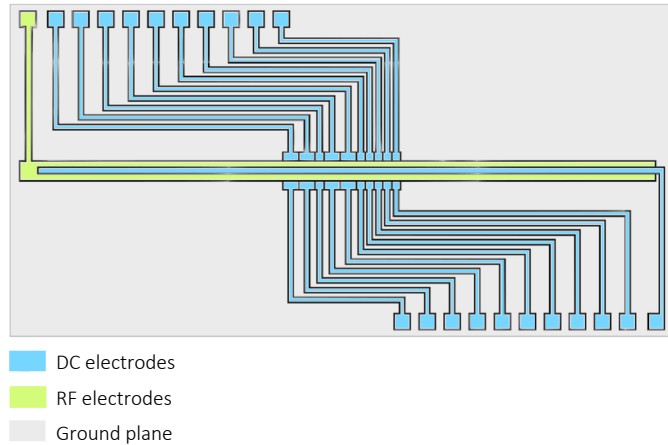


Figure 3.3: Electrode design of TRAP C.

As shown in Figure 3.4, the electrodes are designed so that ions can be trapped within a central trapping region. Electrical connections between the trap electrodes and the control electronics are made via wirebonds at the outer edges of the chip.

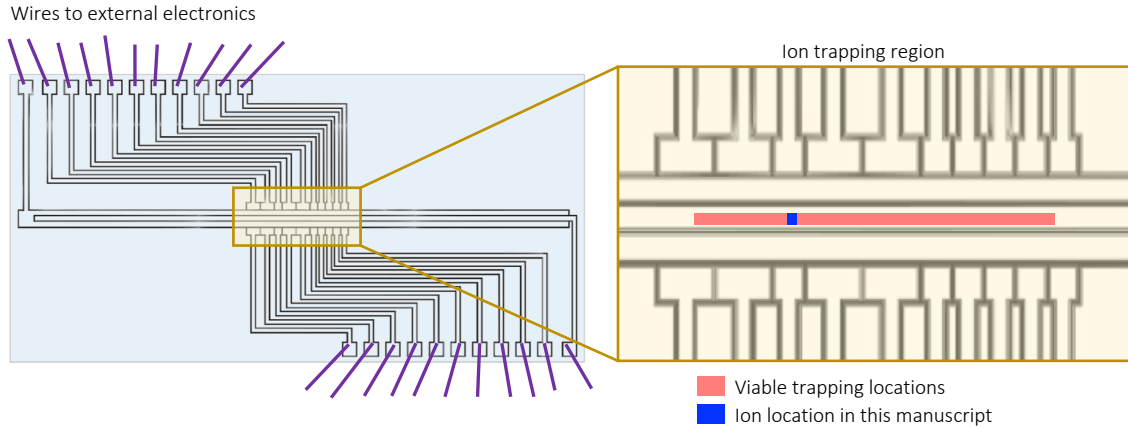


Figure 3.4: TRAP C electrode wiring and ion trapping position.

This chip contains 21 independent DC electrodes. The availability of a large number of electrodes is useful for surface treatment experiments, as treatments can sometimes cause electrodes to short. If DC electrodes short, then the voltages on the remaining DC electrodes can be adjusted to compensate. In addition, with this electrode design ions can be trapped at many different locations along the trap axis, as illustrated in Figure 3.4. The majority of measurements presented in this dissertation were taken at a single trapping location, but an earlier publication compared measurements from three separate locations in this trap ??.

The position of the ion along the trap axis is set by dynamically-adjustable voltages on the DC electrodes. In contrast, the height of the ion is fixed by the geometry of the RF electrodes, and cannot be altered. In this trap, the two RF electrodes have widths of 65 and 80  $\mu\text{m}$ , and are separated by a distance of 105  $\mu\text{m}$ . With this geometry, the ion height is fixed at 72  $\mu\text{m}$ . Further details on trap potential control and simulation can be found in the Littich masters thesis [21].

After designing a chip and running simulations to confirm that it can produce a stable trapping potential for a calcium ion, the electrode pattern is etched into a fused silica chip. Trenches with 100  $\mu\text{m}$  depth and 20  $\mu\text{m}$  width surround all electrodes, as illustrated in Figure 3.5.

The surface is coated with 1.09  $\mu\text{m}$  of metal, which is deposited via e-beam evaporation at a vertical angle of 45°. The angled evaporation coats the top surface of the electrodes with metal, which is necessary to conduct electricity to the trapping location, while preventing metal from coating the entirety of the trenches. To prevent metal from being deposited at the base of the trenches, all trench lines are oriented parallel to the trap edges, and evaporation takes place at a horizontal angle of 45°.

Evaporation is done from two orthogonal directions, as shown in Figure 3.5. With these two evaporation steps, we are able to coat the top 20  $\mu\text{m}$  of each sidewall with metal. This coating acts as shield between the ion and the electrically-noisy dielectric substrate. In each evaporation step we include a titanium sticking layer, a thick layer of aluminum to act as the primary medium for electrical conduction, and a layer of copper to slow oxidation of the surface between and after evaporation steps.

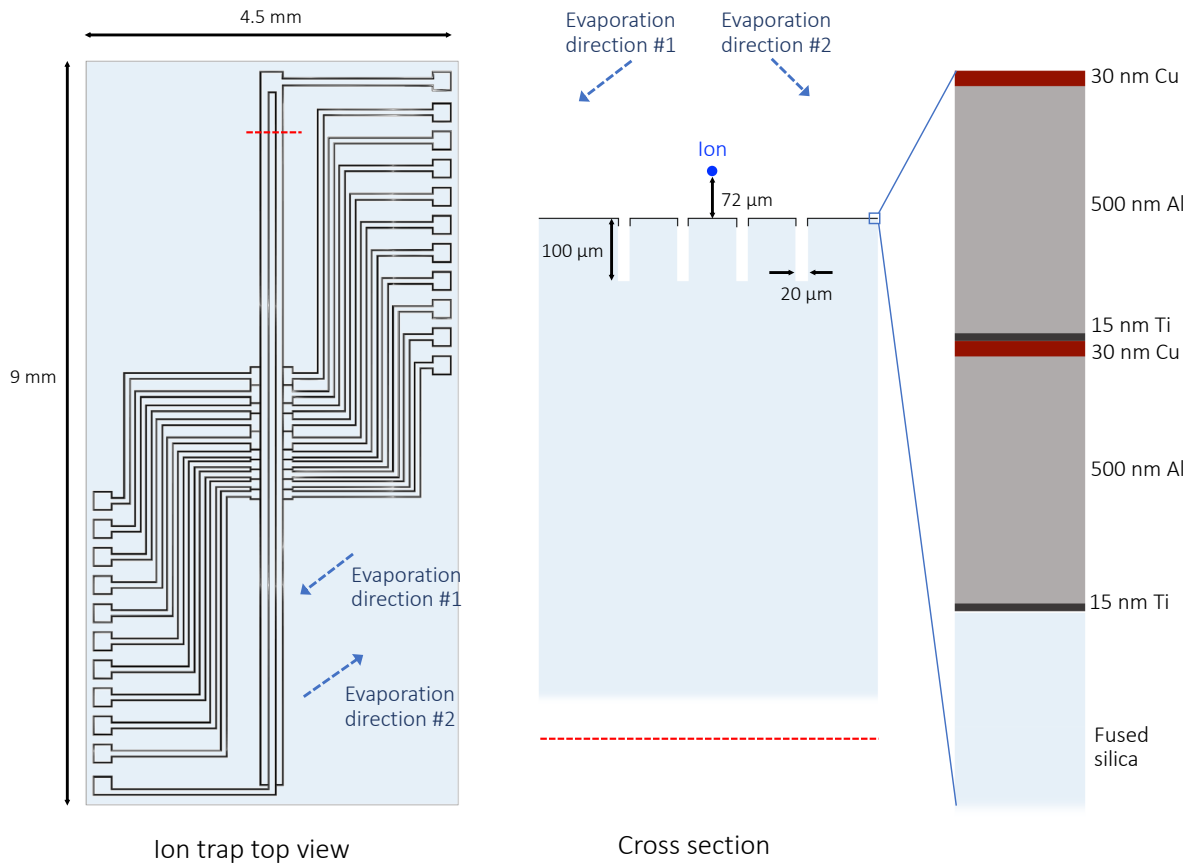
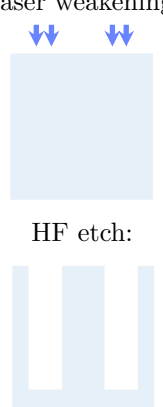
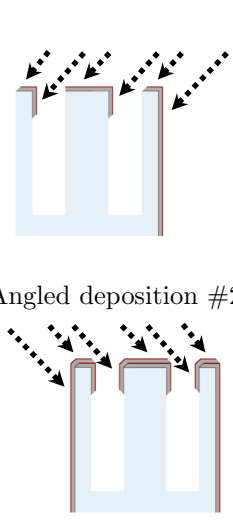
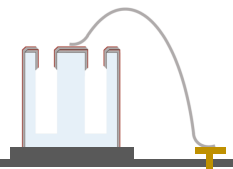
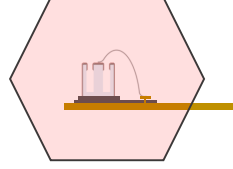


Figure 3.5: On the left is the top view of TRAP C, with arrows to illustrate the horizontal orientations of the two evaporation steps. In the center is a cross section of a portion of the trap illustrating the geometry of the trenches. This cross section also includes arrows to illustrate the vertical orientations of the two evaporation steps. On the right is a further zoomed-in cross section of the evaporated metal film after all evaporation has been completed.

### 3.3 Fabrication process

The following table (Table 3.1) contains the details of our ion trap microfabrication process, including trench etching and metal deposition. Information about the packaging and handling of the trap after fabrication is also included, as these steps affect the properties of the metal film. In Chapter 8 we will discuss how variations in handling correspond to variations in surface electric-field noise.

Table 3.1: Ion trap chip fabrication process

<b>Step 1:</b> Etch trenches into fused-silica chip		Pattern trenches onto fused silica chip using laser ablation.  Remove material from trenches using hydrofluoric acid.  Pattern designed at Häffner lab (Figure 3.5)  Performed by Translume, Ann Arbor, MI [25].
<b>Step 2:</b> Deposit metal onto surface		Remove organic contaminants in 20-minute Piranha bath before deposition. Rinse in DI water, blow dry with nitrogen. Use microscope to check for dust. Repeat until trap is dust-free.  Electron-beam evaporation at two angles to coat the side-walls of the trenches and shield the ion from the noisy fused-silica dielectric.  Pressure in chamber during evaporation = $5 \times 10^{-7}$ Torr.  At first angle, deposit: 15 nm Ti (deposition rate = .5 Å/s) 500 nm Al (deposition rate = 5 Å/s) 30 nm Cu (deposition rate = 1 Å/s)  Expose trap to atmosphere for 5 minutes to manually rotate the trap by 180°.  Repeat deposition at second angle.  Performed by Häffner lab at Berkeley Marvell Nanolab, Class100 clean room.
<b>Step 3:</b> Package and store trap		Mount chip to carrier and use wire-bonds to connect each electrode to the control electronics.  Store trap in Class100 clean room at Marvell Nanolab until ion-trapping vacuum chamber is prepared.
<b>Step 4:</b> Install and bake		Install trap in vacuum chamber at Häffner lab.  Bake vacuum chamber at 160° C, $1 \times 10^{-8}$ Torr, to achieve post-bake chamber pressure below $9 \times 10^{-11}$ Torr.

An image of an ion trap mounted and wire-bonded to a chip carrier is shown in Figure 3.6. This image was taken before the trap was baked.

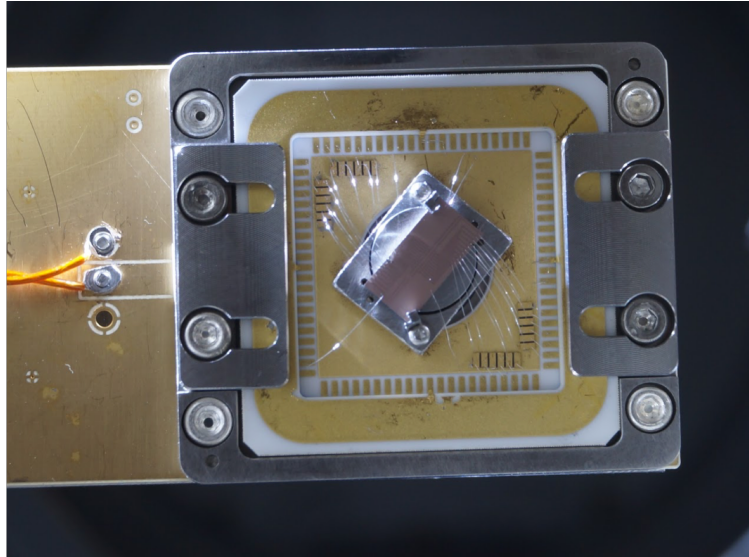


Figure 3.6: Photograph of an ion trap mounted and wire-bonded to a chip carrier.

### 3.4 Properties of the trap surface

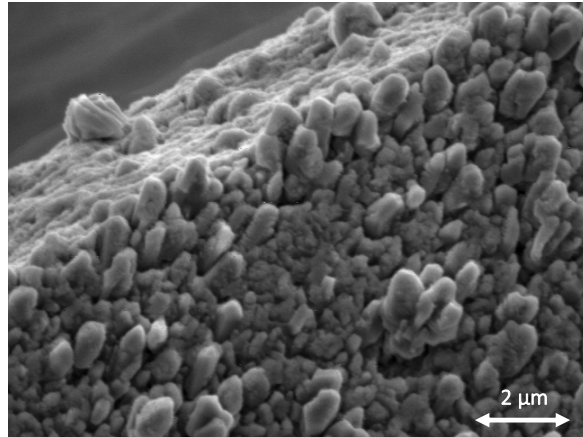


Figure 3.7: SEM of an ion trap surface at edge of a trench. This trap was fabricated as described in Table 3.1, and baked for 9 weeks at a temperature of 160 C under 5e-8 Torr vacuum before this image was taken.

The metal film on the surface of the trap is highly irregular, with features on the order of 1  $\mu\text{m}$  in size. These features are visible in the SEM image presented in Figure 3.7. The trap

in this image was fabricated with the process presented in Table 3.1 and baked for 9 weeks at a temperature of 160° C. These features form during the evaporation process. Angled evaporation is known to enhance shadowing effects and grow bumpy surfaces [26].

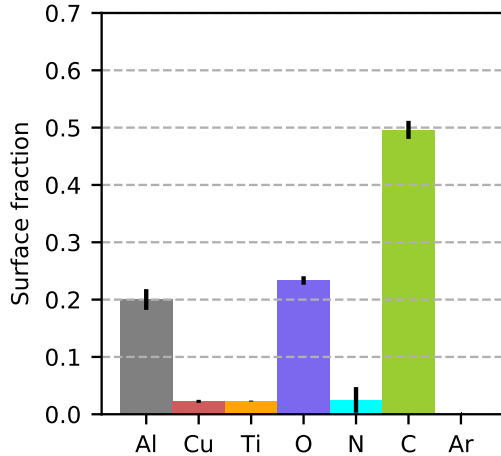


Figure 3.8: Relative surface fractions of metals and contaminants measured using in-situ Auger spectroscopy before milling of TRAP C.

Although the final layer of metal was composed of 30 nm of copper, by the time we began performing surface treatment experiments, the surface composition had changed considerably. Many weeks of baking and local heating of the trap caused the metals to mix, bringing a considerable amount of aluminum to the surface. In addition, a large amount of oxygen and carbon were deposited onto the surface during extended periods of both atmosphere exposure and vacuum-chamber baking.

The complexity of the surface composition and topology of our ion trap substrate make its microscopic dynamics impossible to model from first principles. In addition, in a system with this complexity there can be many different noise processes taking place simultaneously. However, it has been shown that traps fabricated with these methods can have very low noise magnitudes compared to many other surface ion traps, as will be discussed in Chapter 8. For this reason, the traps produced by these methods merit investigation.

# Chapter 4

## Noise measurement methods

Measuring electric-field noise requires precise control over the electronic and vibrational energies of a trapped ion. In this chapter, we will first describe our optical control and read-out methods. Then, we will present the method that we use to measure the motional heating rate of the ion, and describe how this measurement can be used to determine the power spectral density of the electric-field noise that drives motional heating. Next, we explain how the spectrum of the electric-field noise can be measured. Finally, we will give an overview of the experimental setup that makes all of these measurements possible.

### 4.1 Optical control of calcium ions

A background on standard optical control methods for trapped  $^{40}\text{Ca}^+$  ions can be found in the Roos thesis [27]. Here we will review only the basics of the methods required in our experiments.

To determine the motional state of an ion, we cycle through a specific laser-mediated control sequence while varying its timing parameters. The sequence has four major components: Doppler cooling, electronic initialization via optical pumping, coherent operation on a quadrupole transition, and electronic-state read out. The illustration of the electronic energy levels and transitions that are relevant to each step can be found in Figure 4.1.

At the beginning of each measurement, we use Doppler cooling to reduce the vibrational energy of the ion. This is accomplished using a 397 nm laser, which is red-shifted with respect to the transition between the electronic ground state and the short-lived (7 ns)  $4\text{P}_{1/2}$  excited state, as illustrated in Figure 4.1a. The incoming photons are only resonant with the  $4\text{S}_{1/2} \rightarrow 4\text{P}_{1/2}$  transition when the ion is approaching the laser. When the ion is hot, each absorption event has a high probability of providing a momentum kick that counteracts the ion's motion and reduces its vibrational energy. The absorption of a 397 nm photon is rapidly followed by a decay of the electronic state. If the ion decays to the  $4\text{S}_{1/2}$  ground state, it can continue the cooling process by absorbing another red-shifted photon. If instead it decays to the meta-stable  $3\text{D}_{3/2}$  state, as will happen 6.5% of the time, a 866 nm laser pumps the ion back to  $4\text{P}_{1/2}$ . This process is driven until cooling has plateaued.

After Doppler cooling, the ion may be in either of the two Zeeman sublevels of the  $4\text{S}_{1/2}$  ground state. Before we can commence with a controlled operation, the ion must be

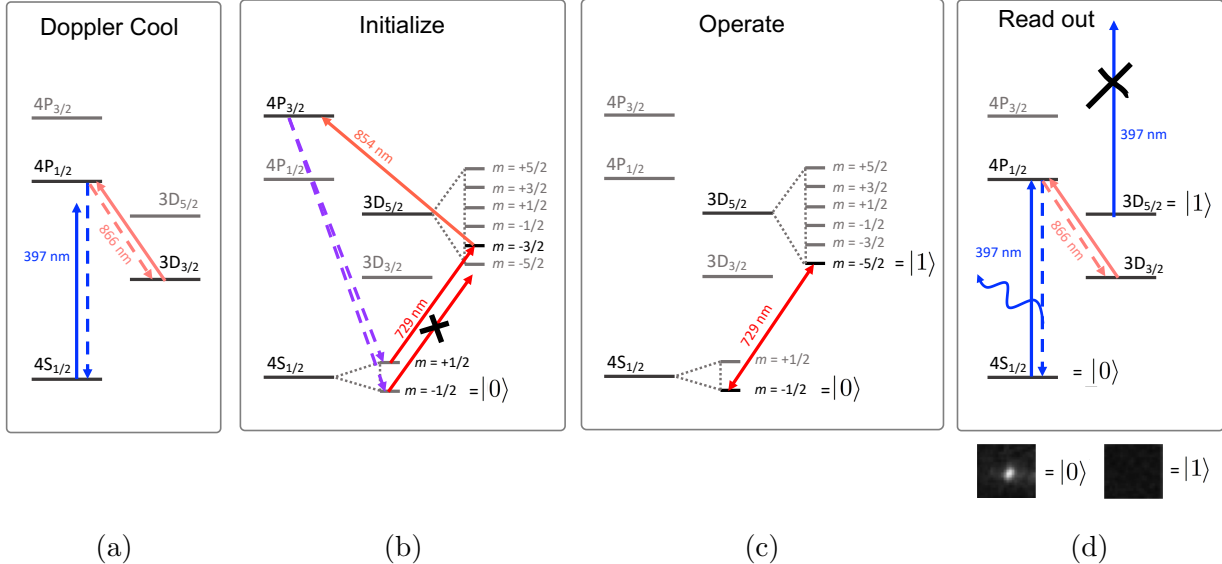


Figure 4.1: The hydrogenic level structure of  $^{40}\text{Ca}^+$  in the context of our laser-mediated ion control scheme. Dotted lines correspond to spontaneous emission, and solid lines correspond to laser-driven transitions. (a) Doppler cooling with a red-shifted cycling laser and a re-pump laser. (b) Initialization via optical pumping, with a laser tuned to selectively pump the ion out of the  $m = +1/2$  Zeeman sublevel of the ground state, and into the  $m = -1/2$  ground state sublevel. (c) Quadrupole operation on the  $\text{S}_{1/2} \leftrightarrow \text{D}_{5/2}$  qubit transition. (d) Optical read-out of qubit state via detection of emitted photons.

initialized to a specific sublevel. This initialization is performed via a process called optical pumping. A 2 G magnetic field removes the degeneracy of the Zeeman sublevels of the  $4\text{S}_{1/2}$  and  $3\text{D}_{5/2}$  states, splitting them by about 2 MHz, ensuring that these levels can be addressed individually.

With a 729 nm, 200 Hz line-width laser tuned to the  $4\text{S}_{1/2}(m = +1/2) \leftrightarrow 3\text{D}_{5/2}(m = -5/2)$  transition, the ion is pumped selectively out of the  $m = +1/2$  sublevel of the ground state. It is subsequently driven to the  $4\text{P}_{3/2}$  level with a 854 nm laser, at which point it decays back down to the ground state, as illustrated in Figure 4.1b. If it decays instead to the  $3\text{D}_{5/2}$  or  $3\text{D}_{3/2}$  levels, it will be re-pumped to  $4\text{P}_{3/2}$  by 854 and 866 nm lasers respectively (not pictured). If it decays to the  $m = +1/2$  ground state, the optical pumping cycle will repeat. Finally, if it decays to the  $m = -1/2$  ground state, the ion will no longer be able to absorb light from the 729 nm laser, and the pumping cycle will cease. If this process is carried out for a suitable amount of time, we can guarantee with almost perfect certainty that the ion will be pumped into the  $m = -1/2$  ground state.

Now that the ion has been cooled and initialized, we can perform an operation on the  $4\text{S}_{1/2}(m = -1/2) \leftrightarrow 3\text{D}_{-5/2}(m = -5/2)$  transition. This can be thought of as a qubit operation, where  $|0\rangle = 4\text{S}_{1/2}(m = -1/2)$  and  $|1\rangle = 3\text{D}_{-5/2}(m = -5/2)$ , as illustrated in Figure 4.1c. This is a dipole-forbidden, quadrupole-allowed ( $(\Delta m = 0, \pm 1, \pm 2)$ ) transition, and has a lifetime of about 1.2 s. The laser-driven transition rate depends on the parameters of the laser, and on the vibrational energy of the ion. This interaction will be discussed further in

Section 4.2. At the end of the quadrupole operation, the ion will be in a superposition of states  $|0\rangle$  and  $|1\rangle$ .

In the read-out step of the control sequence, we use 866 and 397 nm lasers to read out the state of the ion as it is projected into either state  $|0\rangle$  or state  $|1\rangle$ . If the ion is in state  $|0\rangle$ , it will cycle rapidly between the ground state and a short-lived excited state as described in the context of Doppler cooling and illustrated in Figure 4.1d. Each time the ion decays from this excited state, it emits a photon. In contrast, if the ion is in state  $|1\rangle$ , it will not cycle or emit light in the presence of a 397 nm driving laser. To determine the electronic state of the ion, we can either take an optical image of the ion, or collect its light with a photomultiplier tube (PMT). As shown in Figure 4.1d, the ion will appear as a bright spot on the camera if it is in state  $|0\rangle$ , and it will appear dark if it is in state  $|1\rangle$ . After the state has been read out, the ion is pumped into the  $4P_{3/2}$  state with the 854 nm laser, at which point it decays down and is continuously Doppler cooled until the next experiment begins.

As experiments are carried out, the laser positions, frequencies, powers and pulse timings are frequently tuned to optimize the speed and precision of each step in the control sequence. The read-out excitation threshold and photon collection optics are also adjusted as needed.

## 4.2 Ion heating rate measurements

The vibrational energy state of the ion can be coupled to the electronic state via a simple qubit operation. Since we have all of the necessary tools to manipulate and read out the electronic state, we can take advantage of these same methods to measure the vibrational energy.

The ion is held in a 3D harmonic potential using the electronic trapping methods described in Chapter 3. In a quantum harmonic potential, states are evenly spaced, with a transition energy of  $\hbar\omega$ . The motional state of the ion can be characterized by its vibrational occupation numbers  $n_x$ ,  $n_y$  and  $n_z$ , where  $x$ ,  $y$  and  $z$  correspond to the axes of ion's motional modes. The magnitudes of the secular trap frequencies  $\omega_x$ ,  $\omega_y$  and  $\omega_z$  depend on the strength of the confinement along each axis.

As illustrated in Figure 4.2, we align the qubit operation laser so that it is nearly parallel with the  $z$ -axis. This ensures that our measurements of vibrational energy are dominated by the axial mode of motion. We are able to selectively probe a single mode of motion because our electric-field-noise detection method essentially measures the Doppler shift of the laser due to the motion of the ion. Oscillations perpendicular to the  $k$ -vector of the laser will not induce a Doppler shift. In all future discussion of vibrational occupation numbers and secular trap frequencies, we will use the variables  $n$  and  $\omega$  and it can be assumed that these correspond to  $n_z$  and  $\omega_z$ .

A laser tuned to the qubit transition can drive the ion back and forth between the two qubit states in a process called Rabi flopping. With a few reasonable assumptions, we can describe the interaction between the trapped-ion qubit and the 729 nm laser with the following Hamiltonian:

$$H_I = \frac{1}{2}\hbar\Omega_n(\sigma^+ + \sigma^-) \quad (4.1)$$

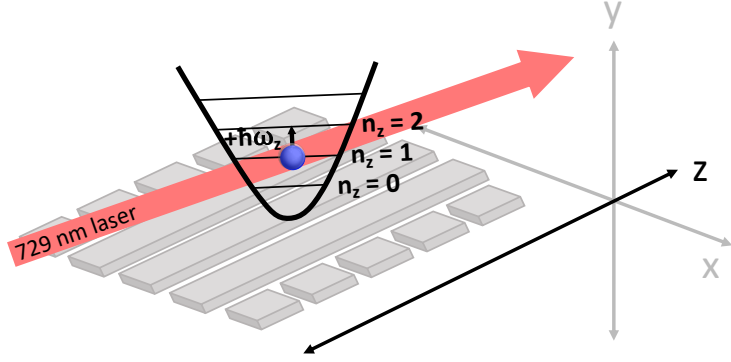


Figure 4.2: DC-electrode-generated axial confinement of the ion produces a harmonic trapping potential with evenly spaced energy levels. Alignment of the 729 nm laser at a small angle ( $11.5^\circ$ ) to the  $z$ -axis ensures that measurements of the motional occupation number will be dominated by the axial mode of motion.

where  $\sigma^+$  and  $\sigma^-$  are the qubit raising and lowering operators, and  $\Omega_n$  is the Rabi flop oscillation frequency. This Hamiltonian applies to a two-level system, an exactly-resonant driving laser, and a motional heating rate far slower than the timescale of the Rabi excitation. For a more thorough quantum-mechanical treatment of ion Rabi flopping, refer to [28]. For justifications for our simplifying assumptions, refer to the Noel thesis [29].

The Rabi frequency  $\Omega_n$  depends on the vibrational occupation number  $n$ , to first order, according to the equation:

$$\Omega_n = \Omega_0(1 - \eta^2 n) + \text{h.o.} \quad (4.2)$$

where  $\Omega_0$  is the bare Rabi frequency, and  $\eta$  is the Lamb-Dicke parameter.  $\Omega_0$  is proportional to the power of the driving laser.  $\eta$  depends on the secular trap frequency and the angle between the driving laser and the vibrational mode of motion. It characterizes the strength of the coupling between the electronic and vibrational energy states of the ion. We have made the assumption that the laser light has projection onto predominantly only one motional mode.

An ion under the Hamiltonian from Equation 4.1 will evolve in time according to the equation:

$$P_D(t) = \sin^2(\Omega_n t) \quad (4.3)$$

where  $P_D$  is the probability that the ion will be found in the  $D_{5/2}$  state after a qubit operation pulse of length  $t$ . Rabi flops simulated from ions with the same bare Rabi frequency but different motional occupation numbers are plotted in Figure 4.3a. The excitation time on the  $x$ -axis corresponds to the pulse length of the qubit operation performed with the 729 nm laser.

Since the frequency of the Rabi flop is tied to the motional state of the ion, we can measure the vibrational occupation number by mapping out a Rabi flop. However, this measurement

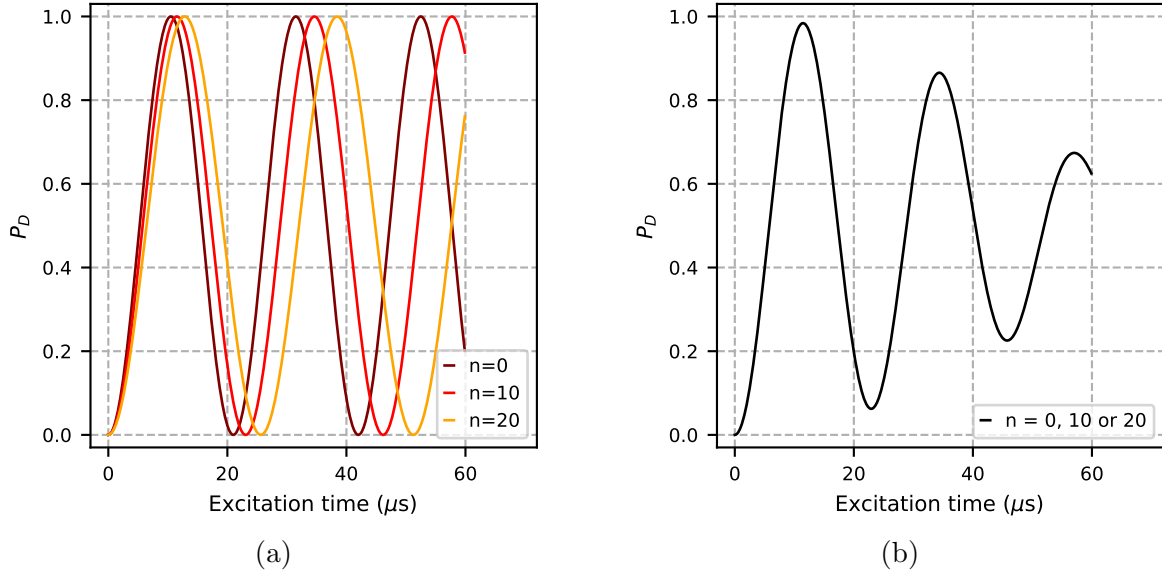


Figure 4.3: Simulated Rabi flops, where  $P_D$  is the excitation probability. (a) Ions with higher vibrational energies flop more slowly, as illustrated by Rabi flops from ions in three different Fock states. (b) If the ion is in an equal superposition of the three simulated Fock states, the Rabi flop will decay as a function of excitation time.

is complicated by the fact that to map out a Rabi flop, the sequence of cooling, initialization, operation and state-readout must be repeated many times. Each time the ion is cooled, it can end up in one of many different motional states. As a result, the measured Rabi flop will be a convolution of many sine waves with different frequencies. This is illustrated in Figure 4.3b, where we have plotted a simulated measurement in which the ion had an equal probability of being in states  $n=0$ ,  $n=10$ , and  $n=20$ . As shown, the Rabi flop decays as the three sine waves dephase.

It is reasonable to assume that an ensemble of Doppler cooled ions will have a thermal distribution of vibrational energies. A set of measurements from a single ion is equivalent to a single measurement of an ensemble of ions, so we can assume that the occupation probability  $P_n$  for any vibrational state  $n$  will be approximately equal to:

$$P_n = \frac{\bar{n}^n}{(\bar{n} + 1)^{n+1}} \quad (4.4)$$

where  $\bar{n}$  is the average motional occupation number. We combine Equations 4.3 and 4.4 to make a fitting function appropriate for our Rabi flop measurements:

$$P_D(t) = \sum_{n=0}^{\infty} P_n \sin^2(\Omega_n t). \quad (4.5)$$

We use this function to fit for  $\bar{n}$  and  $\Omega_0$ .

Examples of three Rabi flop measurements taken in our system along with fits to Equation 4.5 are plotted in Figure 4.4. Each point in this plot corresponds to 100 measurements in which the ion was cooled, initialized, operated on and read out. We plot in what fraction

of these measurements the ion was projected into the excited  $D_{5/2}$  state during state read out. Then, we change the excitation time (the qubit operation pulse length) and repeat this process to map out the Rabi flop. When Rabi flop data is fitted in practice, measured datapoints are weighted to account for projection noise, and an additional fit parameter is included to account for initialization errors.

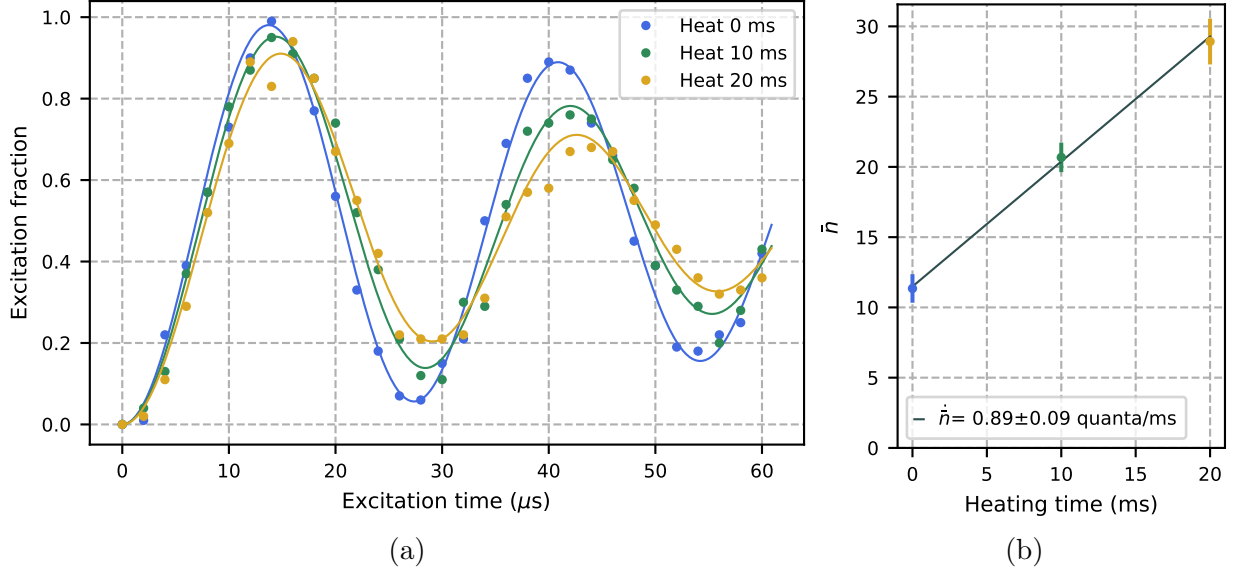


Figure 4.4: (a) Excitation fraction measurements (points) and Rabi flop fits (lines), taken with a secular trap frequency  $\omega = 2\pi \times 1.3$  MHz. (b) Average occupation numbers extracted from Rabi flop fits (points) and a linear fit (line) to determine the ion heating rate.

Figure 4.4b contains the  $\bar{n}$  values associated with the fits from Figure 4.4a. The heating time, on the  $x$ -axis, corresponds to a waiting time added between the initialization and operation steps of each measurement. Since the ion is not cooled during this waiting time, it is free to heat up in response to electric fields fluctuating at the secular trap frequencies. The longer the ion is allowed to heat, the higher  $\bar{n}$  will become. The ion heating rate is equal to the slope of a linear fit of  $\bar{n}$  with respect to the heating time.

### 4.3 Calculation of electric-field noise

The electric-field-noise power spectral density  $S_E(\omega)$  is directly proportional to the ion heating rate according to [1]:

$$S_E(\omega) = \frac{4m\hbar\omega}{q^2} \dot{\bar{n}}(\omega), \quad (4.6)$$

where  $m$  and  $q$  are the mass and the charge of the ion,  $\hbar$  is the reduced Planck constant, and  $\omega$  is the secular trap frequency.  $S_E(\omega)$  is a measure of the amplitude of the electric-field-noise at frequency  $\omega$ . The power spectral density depends on the autocorrelation function of the fluctuating electric field according to:

$$S_E(\omega) = 2 \int_{-\infty}^{\infty} d\tau \langle \delta E_t(\tau) \delta E_t(0) \rangle e^{-i\omega\tau}. \quad (4.7)$$

The majority of the data in this dissertation will be presented in the form of ion heating rates. These heating rates are presented to a measurement frequency of  $2\pi \times 1$  MHz unless otherwise specified. A heating rate of 1 quanta/ms measured by  $^{40}\text{Ca}^+$  with a trap frequency of  $2\pi \times 1$  MHz corresponds to a power spectral density of  $6.85 \times 10^{-12} \text{ V}^2/(\text{m}^2 \text{ Hz})$ .

## 4.4 Frequency scaling of ion heating rates

For the purpose of characterizing the noise in our system, it is interesting to measure how the spectral noise density changes as a function of frequency. We accomplish this by measuring ion-heating-rate amplitudes at a range of different frequencies. We will refer to this as a frequency-scaling measurement.

Our heating rates, as described in Section 4.2, are sensitive only to noise at the axial trap frequency. In the axial direction, harmonic confinement is generated by DC electrodes, which can be tuned to set the measurement frequency anywhere between 0.4 and 2.4 MHz. We do simulations to predict the DC voltages that are needed to set the trap frequency to a specific value. After the DC voltages have been set, the trap frequency can be measured and adjusted with a precision of about 1 kHz.

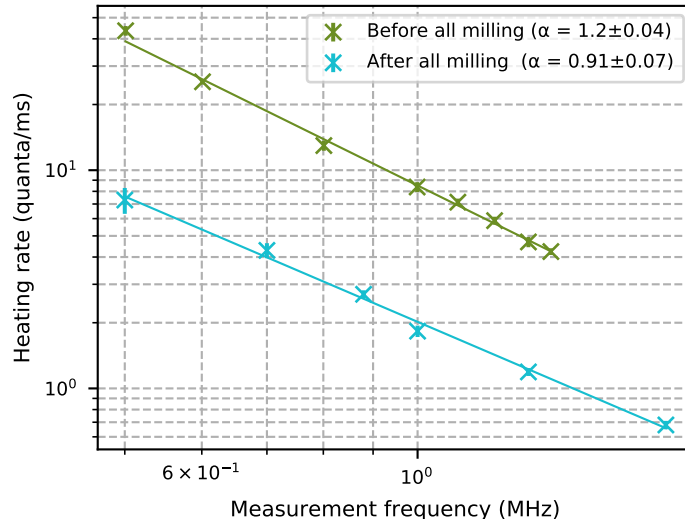


Figure 4.5: Frequency scaling measurements of ion heating rates taken in TRAP C while the substrate was at room-temperature. Measurements were taken before and after a series of surface treatments including argon ion milling reduced the magnitude of ion heating rates at all measured frequencies.

Two frequency-scaling measurements are plotted in Figure 4.5. One was measured before TRAP C was milled, and other was measured when the noise was at its lowest point after extensive milling. In both cases, the heating rate scaled as:

$$\Gamma = \dot{n} \propto 1/f^{1+\alpha} \quad (4.8)$$

where  $\Gamma$  is the ion heating rate and  $\alpha$  is the so-called frequency scaling exponent of the noise. The corresponding noise power spectral density scales as  $1/f^\alpha$ . Noise that has this frequency dependence, and a value of  $\alpha$  close to 1, is referred to in academic literature as  $1/f$  noise, flicker noise, or pink noise.  $1/f$  noise is found in many physical systems, and in Chapter 6 we will discuss how previous measurements and models of  $1/f$  noise can inform our study of noise in ion traps.

In addition to establishing a link between our work and other studies of  $1/f$  noise, the data presented in Figure 4.5 helps us to confirm that our heating rate measurements are not dominated by technical noise. We put great care into filtering electrodes, shielding the trap from electromagnetic pickup, and choosing electronic grounding configurations so that measurements in our system are surface-noise limited. Technical noise often has sharp frequency resonances. Our noise measurements at different frequencies form a smooth line, and show no indication of resonances. In addition, the amplitude of technical noise can vary by orders of magnitude over daily or hourly time periods. In our measurements, the heating rates are very stable over time. This gives us confidence that technical noise is not a problem in our system.

Both of the frequency scaling measurements plotted in Figure 4.5 were taken while the trap substrate was at room temperature. We also have taken many measurements of  $\alpha$  while the substrate temperature was elevated. In early measurements of TRAP C, we confirmed that the noise generated by the heated substrate had a frequency scaling consistent with Equation 4.8. This work is published in reference ??.

## 4.5 Experimental setup

Accomplishing the feat of trapping an ion and measuring its heating rate requires a large number of tools. Pictured in Figure 4.6 is the vacuum chamber that houses TRAP C, and many of the instruments required in the ion trapping process.

### Vacuum

All ion-trapping experiments are performed in ultra-high vacuum (UHV) chambers. If a gas molecule collides and chemically reacts with a trapped ion, the ion can be ejected from the trap, so ideally all background gasses should be removed.

To achieve low pressures in our experiment, our trap is installed in a vacuum chamber and then the whole chamber is baked at 160° C for two or more weeks. During the baking process, a pressure of  $10^{-8}$  Torr is maintained by two turbo pumps. After baking is complete, a titanium sublimation pump is run to further reduce the pressure.

During general operation of the ion trap, the chamber is continuously pumped by an ion pump, which is able to achieve pressures below  $10^{-10}$  Torr. At these low pressures, the average ion lifetime is approximately 6 hours. The pressure in the chamber is measured using a residual gas analyzer (RGA).

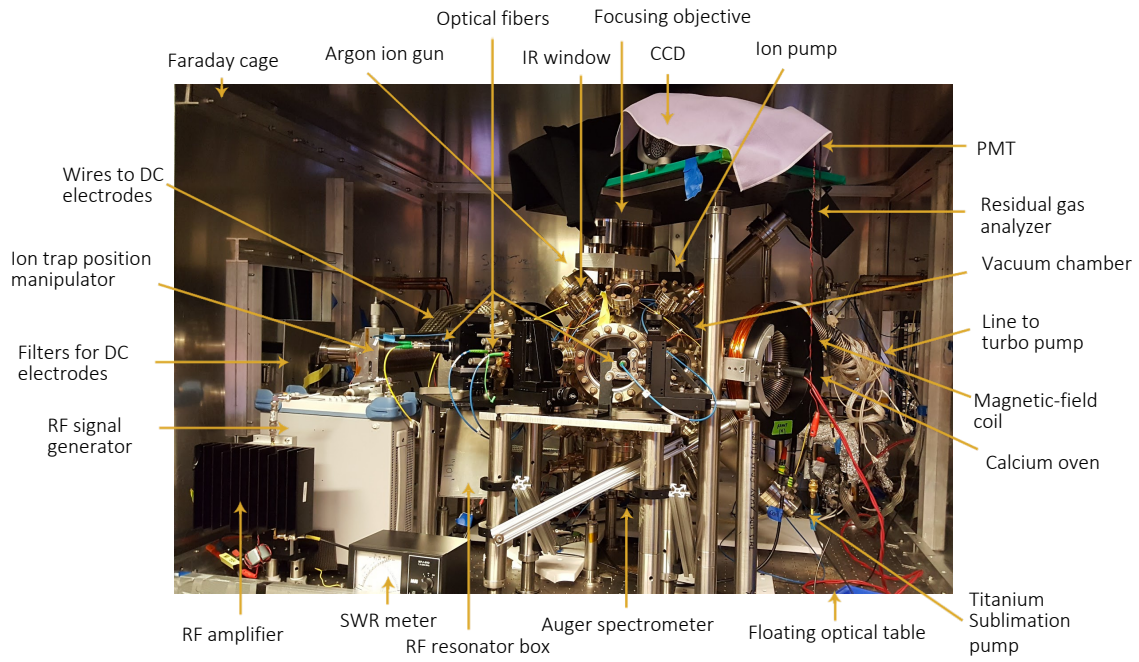


Figure 4.6: Photograph of our ion trapping chamber and other various tools.

## Ion trapping electronics

In Chapter 3, we described how RF and DC voltages applied to ion trap electrodes can create a stable trapping potential for a  $^{40}\text{Ca}^+$  ion.

In our setup, DC voltages are set via a computer interface. The computer communicates to an FPGA (field programmable gate array) which sends a signal to a series of DACs (digital to analog converters) which output the voltages. These voltages are then amplified to the desired values, which can be between -40 and +40 V. Between the amplifier and the trap electrodes there are five stages of RC filters, plus a set of capacitors soldered directly to the chip carrier. These filters remove excess electric-field noise that could interfere with measurements of surface noise.

In an additional effort to minimize electronic noise, the entire vacuum chamber is surrounded by a 1.25 mm thick aluminum Faraday cage. Wires and power cables are low-pass filtered as they enter the cage.

Inside the Faraday cage, a Rohde & Schwarz signal generator outputs the RF signal required for radial confinement of the ion. This signal is amplified, passed through a standing wave ratio (SWR) meter and inductively coupled to the in-vacuum RF electrode circuit via a helical resonator. The frequency of the output signal is tuned to maximize the ratio between the forward and reflected RF power, as measured on the SWR meter.

In addition to the trapping electronics, two coils of wire are present on opposite ends of the vacuum chamber. By passing a current through these coils, we generate a 2 G magnetic field to control and separate the Zeeman sublevels of trapped ion.

For further details and diagrams of our trapping electronics, filtering, and vacuum system,

refer to Chapter 4 of the Noel thesis [29].

## Calcium ion generation

Once the RF and DC trapping voltages are in place, we use a two-photo photoionization process to generate ions from a beam of neutral atoms as it passes through the trapping location.

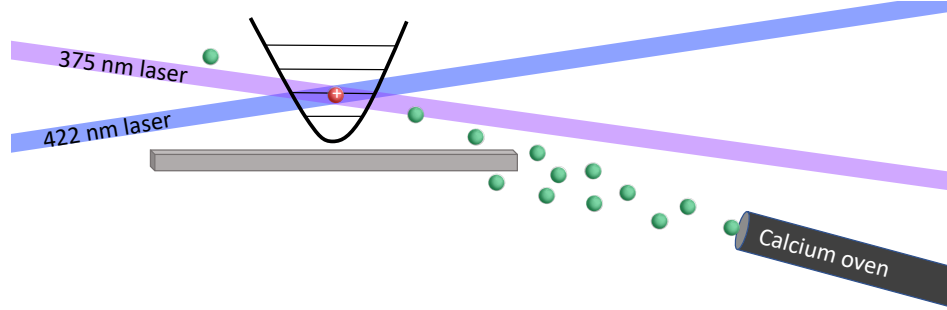


Figure 4.7: Diagram of calcium ion generation. A beam of neutral calcium atoms (green) passes through the electronic trapping point, while intersecting with lasers that excite and ionize the calcium. Trapped, ionized calcium is shown in red.

The neutral atom beam is produced by a home-built calcium oven. The oven consists of a thin tube with calcium granules placed at its base. When the tube is resistively heated, it produces a beam of calcium atoms. The tube is placed below the trap as shown in Figure 4.7, so that calcium atoms can reach the trapping location but will not be deposited onto the surface of the trap.

The two lasers for the two-photon photoionization process are aligned to intersect at the ion trapping location above the surface of the trap. A portion of the calcium ions will be excited by the 422 nm laser, and subsequently ionized by the 375 nm laser. Doppler cooling lasers are also present (though not picture) to cool down the ions so that they can be trapped.

## Lasers

As presented earlier in this chapter, the electronic state of the ion can be manipulated and read out using four lasers with wavelengths of 397, 729, 854 and 866 nm. Calcium is ionized using two additional lasers with wavelengths of 375 and 422 nm. The injection-locked 729 laser is described in Section 4.1 of the Gorman theses [30]. The setups of the other five lasers are described in Chapter 3 of the Pruttivarasin thesis [31].

The two photoionization lasers are manually unblocked when a new ion needs to be trapped, and manually re-blocked once trapping has been successful. However, during the process of taking heating-rate measurements, the cooling and state-control lasers must be turned on and off with sub-microsecond precision. In addition, their frequencies must be dynamically tuned to selectively drive different transitions in the ion. For these reasons, the measurement lasers must be controlled digitally.

At the beginning of each experiment, the parameters of its pulse sequence are programmed into a computer. This computer communicates with an FPGA, which transmits precisely-timed electrical signals to four acousto-optic modulators (AOMs). Each of the AOMs controls the frequency, amplitude and phase of one of the four measurement lasers.

After each laser beam is passed twice through an AOM (called a double-pass configuration), it is coupled into an optical fiber. The laser output from each fiber is aligned to the trapped ion. To reduce vibrations, the whole setup is mounted to a floating optical table. The table and some of the optical fibers are visible in Figure 4.6.

## Imaging

A trapped calcium ion emits 397 nm light as it cycles between the  $4S_{1/2}$  and  $4P_{1/2}$  energy states. We use this light to identify when an ion has been trapped, and to determine its electronic state after a qubit operation. The emitted light is focused through an objective aligned above the trap, then passed through a filter to remove stray light of other wavelengths, and finally directed into either a PMT or a CCD camera. Both the PMT and camera are used to detect ions when they are initially trapped, but only the PMT is used for state readout.

## Control system

All ion measurement experiments are run via the LabRAD digital control software, as described in Appendix A of the Ramm thesis [32]. We use this software to control the voltages on the DC electrodes, run laser pulse sequences, record the ion fluorescence, and process the collected data.

## Surface treatment and characterization tools

In addition to all of the equipment used for ion trapping and heating-rate measurements, some of our surface treatment and characterization tools are also pictured in Figure 4.6. These tools include an Auger spectrometer positioned below the vacuum chamber, an ion gun at the back of the chamber, and an IR window through which we can detect light for substrate temperature measurements. Also pictured is the ion trap position manipulator, which allows us to rotate and shift the trap so that it can be aligned to each of these treatment and characterization tools. These tools will be discussed in the following chapter.

# Chapter 5

## Surface treatment & characterization techniques

The experiments presented in this dissertation incorporate a range of different in-situ surface treatment and characterization techniques. An illustration of how these tools are arranged around the ion trap is shown in Figure 5.1.

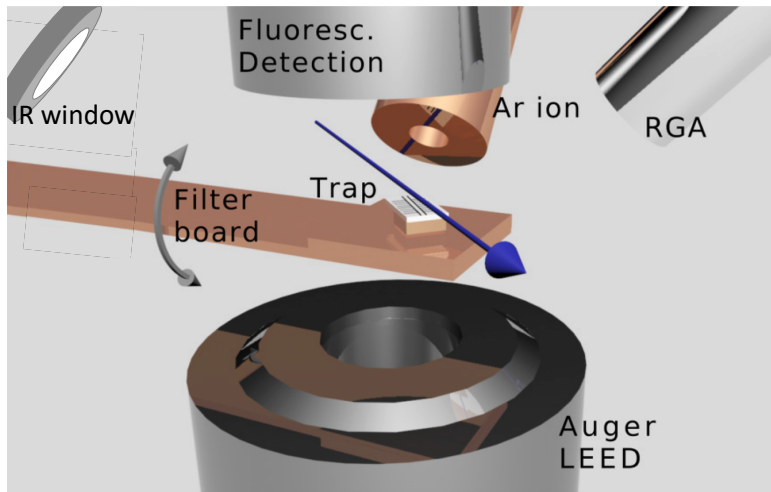


Figure 5.1: Arrangement of in-situ surface treatment and characterization tools. Adapted from [13]

Earlier, in Figure 3.6, we showed how the ion trap is clamped and wire-bonded to a chip carrier. This chip carrier is screwed onto a filter board, which is attached to a manipulator arm. With this manipulator arm, the trap can be rotated by  $\pm 180^\circ$  and moved along the x, y and z axes without breaking vacuum. The trap must be shifted and rotated each time we switch between taking ion-heating-rate measurements, doing argon ion milling, or using the Auger spectrometer.

During ion-heating-rate measurements, the trap is faced upward and aligned to the center of the fluorescence detection optics. Lasers for ion trapping and state manipulation enter the chamber parallel to the trap surface through a series of windows. The trap is rotated downward for Auger spectroscopy, and diagonally backward for argon ion milling.

In this chapter we will describe the tools we use to treat and characterize the trap surface in-situ. For a summary of all surface treatments and measurement results, refer to Chapter 7.

## 5.1 Trap substrate heating

The trap sits directly on top of a resistive button heater that was manufactured by HeatWave Labs (101136 0.320" 1200oC UHV Button Heater). With this heater, the temperature of the trap can be raised to over 620 K. The plateau temperature of the heater is dependent on its thermal load.

The heater and trap are clamped together and thermally isolated from the gold-plated top of the ceramic chip carrier using a stainless-steel holder. This holder was built by machinists in the UC Berkeley Physics Machine Shop. The heater stem and wire pass through a hole in the center of the chip carrier, where the stem is secured by a small screw and the wire is connected to an external power source. An exploded image of this setup is shown in Figure 5.2.

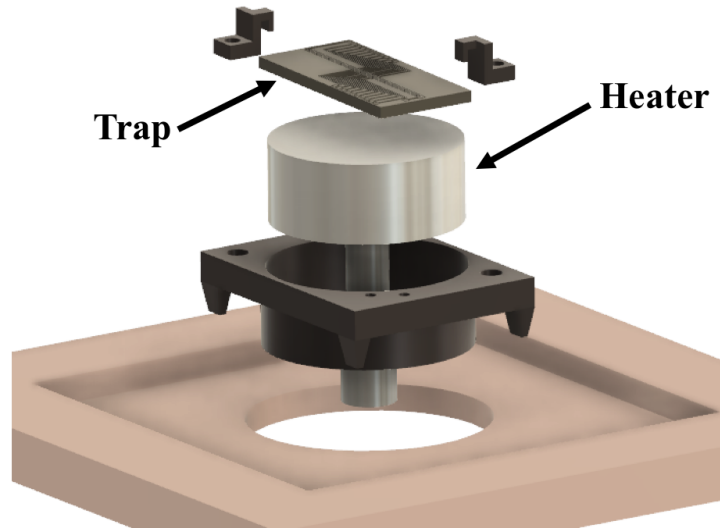


Figure 5.2: Exploded image of the trap, button heater, steel holder, and chip carrier.

### Substrate temperature measurement

We use a Seek Thermal, model CompactXR, camera to determine the temperature of the heated trap. An IR-transmitting ZnSe window is installed in the chamber so that the trap temperature can be taken while the trap is oriented for ion-heating-rate measurements, as shown in Figure 5.1.

A thermal image of the trap, heater and holder, as shown in Figure 5.3, will display a range of different temperatures. The temperature read out directly from an object will be a convolution of its true temperature and the emissivity of its surface. Surfaces with

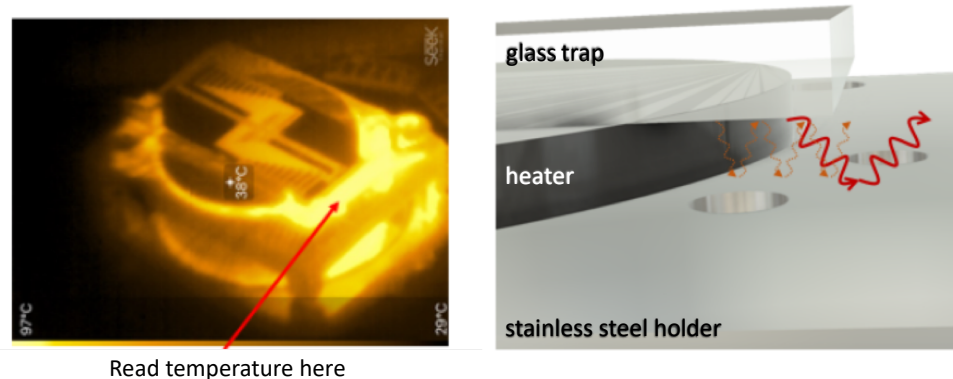


Figure 5.3: Left: thermal image of heated ion trap and holder. Right: cartoon illustrating the path of photons emitted from the glass bottom of the ion trap.

emissivities close to 1, such as glass, are read out most accurately. Surfaces with lower emissivities, such as the metal-coated surface of an ion trap, appear in the thermal camera to be colder than they actually are.

Although the top of the fused-silica trap is coated with metal, the bottom is smooth and glassy, and thus has an emissivity close to 1. The corners of the trap hang off the top of the heater, which is raised slightly above the base of its holder. This leaves just enough space for blackbody radiation emitted from the bottom of the fused silica chip to reflect off of the stainless steel holder and then out through the ZnSe window. With this reflected light, we can accurately determine the temperature of the trap. The cavity created between the glass and the holder, as illustrated on the right in Figure 5.3, further enhances the accuracy of this measurement.

Before the reflected blackbody radiation reaches the infrared camera, it passes through a window and a series of lenses that attenuate its intensity. We use a second ZnSe window, identical to the one installed on the vacuum chamber, to calibrate the thermal camera and lenses before they are mounted in place for in-situ measurements. In this calibration process, we cycle a hot plate through a wide range of heat settings. We measure the hot-plate temperature directly using a thermal imaging gun, while also measuring the temperature read out by the thermal camera through the ZnSe window. With these measurements, we generate a mapping between the true temperature and the read-out temperature. All substrate temperatures reported in this dissertation have been scaled using these mappings.

### Temperature scaling of ion heating rates

A measurement of how surface electric-field noise responds to heat can provide valuable information about the microscopic noise sources. In our experiments, we determine the temperature scaling of the surface noise by measuring ion heating rates between room temperature and 605 K. At around 600 K, the trapped ion can be held in the trap for an average of five minutes before ejection. The lifetime rapidly deteriorates at temperatures above 600 K. Ions cannot be trapped at all when the substrate temperature is above 605 K.

In Figure 5.4a is a plot of a measurement in which we raised the temperature of the

trap from room temperature to 580 K, while stopping periodically to measure heating rates at 0.88 and 1.3 MHz. We did measurements similar to this before and after every surface treatment described in this dissertation. By measuring temperature scalings simultaneously at multiple frequencies, we are able to determine how the frequency scaling exponent  $\alpha$  scales with temperature. This is valuable information in the context of the TAF model, which we will discuss in Chapter 6. In later chapters, when we explore how the magnitude of the heating rates change in response to surface treatments, it is much simpler to present single-frequency temperature scalings.

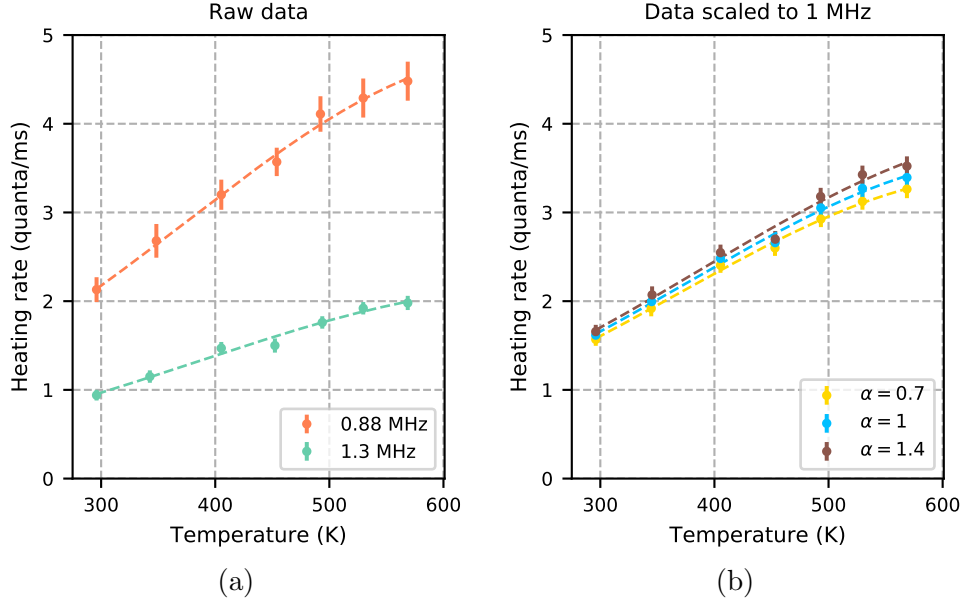


Figure 5.4: Heating rate temperature scaling measurements, with Gaussian fit lines to guide the eye. (a) Temperature scaling of heating rates, measured with two different trap frequencies. (b) Temperature scalings re-scaled to a measurement frequency of 1 MHz using three different values of  $\alpha$ . For each value of  $\alpha$ , the measurements are scaled to 1 MHz and then averaged together in 20 K bins. Even using the highest and lowest measured values of  $\alpha$ , the re-scaled temperature scalings differ by at most one standard deviation from  $\alpha=1$ .

Unless otherwise specified, all temperature scalings presented in this dissertation are scaled to 1 MHz assuming the heating rates scale as  $1/f^\alpha + 1$  where  $\alpha = 1$ . After data has been scaled, measurements taken at similar temperatures are averaged together according to:

$$\bar{\Gamma} = \frac{\sum_{i=1}^n \Gamma_i \times \sigma_i^{-2}}{\sum_{i=1}^n \sigma_i^{-2}}, \quad (5.1)$$

where  $\Gamma_i$  is the measured heating rate and  $\sigma_i$  is its standard error. The standard error of the average heating rate  $\bar{\Gamma}$  is equal to:

$$\sigma_{\bar{\Gamma}} = \frac{1}{\sqrt{\sum_{i=1}^n \sigma_i^{-2}}}. \quad (5.2)$$

The measurement temperatures are averaged together according to Equation 5.1 using the standard error of the corresponding heating rate measurements. The averaged temperature is not assigned an error.

Values of  $\alpha$  measured throughout our experiments typically lie between 0.9 and 1.1, but in rare cases are as high as 1.4 and as low as 0.7. Figure 5.4b shows the data from Figure 5.4a scaled to 1 MHz assuming three different values of  $\alpha$ . Since we typically measure heating rates at frequencies both above and below 1 MHz, the chosen value of  $\alpha$  has very little impact on the magnitude of the re-scaled temperature scaling.

In all temperature-scaling plots, the temperature on the x-axis refers to the temperature of the substrate. The heating rate on the y-axis refers to the rate of the rise of the motional state of the ion in response to electric-field noise, as introduced in Chapter 4. To avoid confusion, we will often refer to the heating rate as the *ion heating rate*. If the word *ion* is ever omitted, it is for the sake of brevity, and is never in reference to a different type of heating.

### Heat as a surface treatment

In a typical heating experiment, we measure the temperature scaling as the temperature is raised, and again when it is lowered. In some experiments, such as the one plotted in Figure 5.5a, the initial and final temperature scalings match. In other experiments, the noise is transformed by the heat treatment, and we observe that the initial and final temperature scalings are different. An example of this type of experiment is shown in Figure 5.5b.

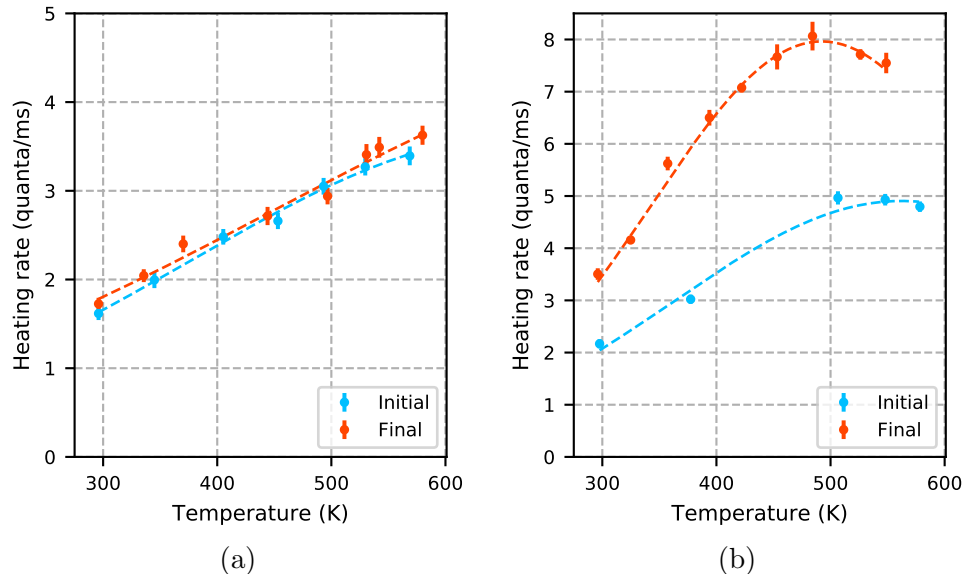


Figure 5.5: Examples of heating experiments in which (a) the initial and final temperature scalings match, and (b) the heat transforms the substrate, thus changing the temperature scaling.

A chronological summary of all of the heating experiments we have done can be found in Chapter 7.

## 5.2 Auger spectroscopy & electron bombardment

### Tools

The surface composition of the trap is measured in-situ using an Auger spectrometer (OCI Vacuum Microengineering model BDL800IR). The system includes an electron-beam power supply (model LPS-075/300), a lock-in amplifier (model SR830), and retarding field analyzer a gold-coated-tungsten wire-mesh grid. The electron beam has an energy of 2 keV and is generated by a thermally emitting tungsten-rhenium filament. The tool has a 20 mm sample-to-optics working distance, and when the electron beam reaches the trap it has a diameter of 1 mm, as illustrated in Figure 5.6.

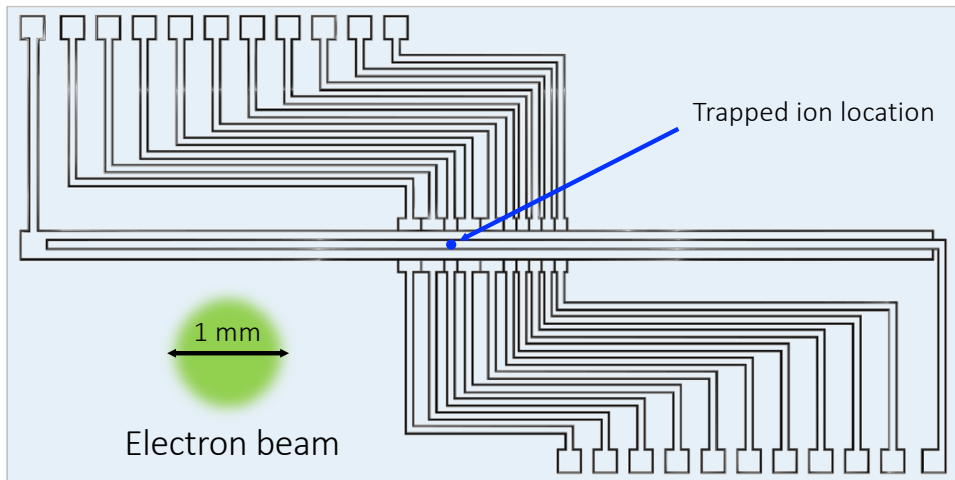


Figure 5.6: The spot size of the Auger electron beam shown in the context of the ion trap substrate.

### Auger spectrum data processing

The lock-in amplifier outputs the derivative ( $dN/dE$ ) of the Auger-electron emission intensity ( $N$ ) as a function of energy ( $E$ ). This is the signal that we analyze and plot. The energies, shapes and relative amplitudes of the peaks in an Auger spectrum can be used to gain information about the atomic and chemical composition of the surface of the substrate. This measurement is sensitive to the top 3 to 10 monolayers of material [33].

After taking an Auger spectrum, the first thing that we do is identify the elements on the surface by comparing measured peaks to known reference spectra. In our measurements, we have found signals from aluminum, copper, titanium, nitrogen, oxygen, carbon and, after ion milling, argon. Next, we use a three-step process to remove the background from the data. Removing the background improves the accuracy of peak amplitude measurements, and makes it easier to plot spectra with different backgrounds side-by-side.

The background-subtraction steps are shown in Figure 5.7 using one of our measured spectra as an example. In Step 1, we remove the peaks from all identified elements by replacing the signal from each element with a straight line. The line resulting from this

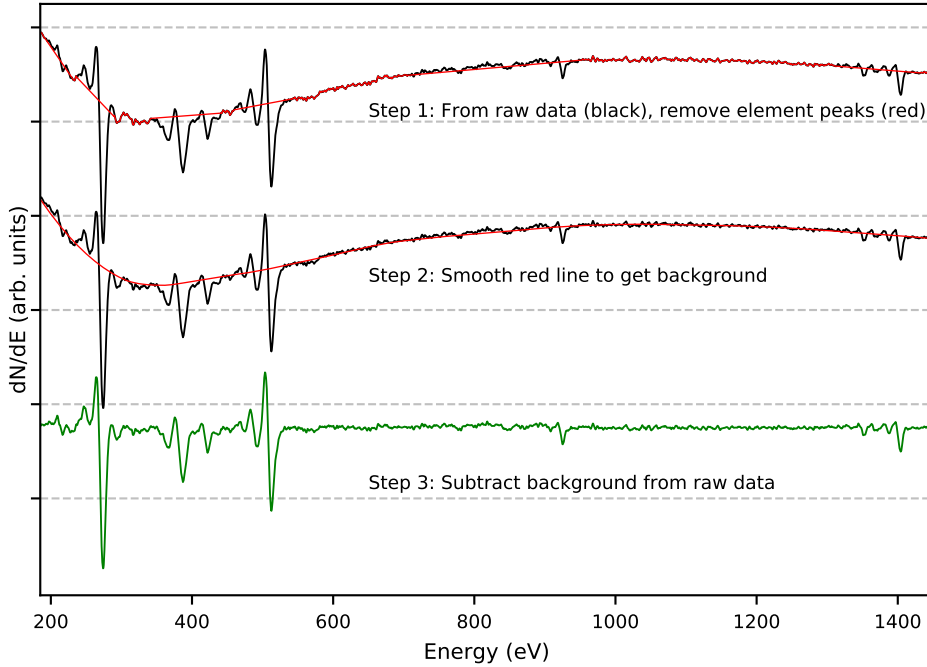


Figure 5.7: Illustrate of our background correction method using a typical measured Auger spectrum as an example.

removal is shown in red in Step 1 of Figure 5.7, along with the raw data which is plotted in black. Next, we use a Savitzky–Golay filter to smooth the red line. The smoothed line is shown in red in Step 2. Finally, we subtract the background (the red line in Step 2) from the raw data. The final background-subtracted result, for this example, is plotted in green.

The relative amplitudes of the differential Auger peaks are used to determine the atomic composition of the trap surface. In Figure 5.8, we have plotted a background-corrected spectrum and highlighted the strongest (high energy) peak from each element. To determine the fraction of each element, we measure the peak-to-peak amplitude of all of the strongest peaks. This amplitude is equal to the difference in voltage between the lowest and highest points in each highlighted region. Each amplitude is scaled by the Auger sensitivity of its corresponding Auger energy. These sensitivities were provided by the manufacturer of the spectrometer, and are listed in Table 5.1.

The surface fraction of a given element is proportional to the peak-to-peak amplitude of its strongest peak, divided by the corresponding Auger sensitivity. This procedure works well for all elements except for nitrogen, which will be discussed separately. After all amplitudes have been measured and scaled, the set is normalized so that all fractions add up to 1. The surface composition corresponding to the Auger spectrum in Figure 5.8a is shown in Figure 5.8b.

The surface fractions plotted in figure 5.8b include an error bar that corresponds to the peak-to-peak measurement uncertainty. Each Auger scan has some high-frequency, low-magnitude noise. A zoomed-in plot of a portion of a scan containing no Auger peaks is

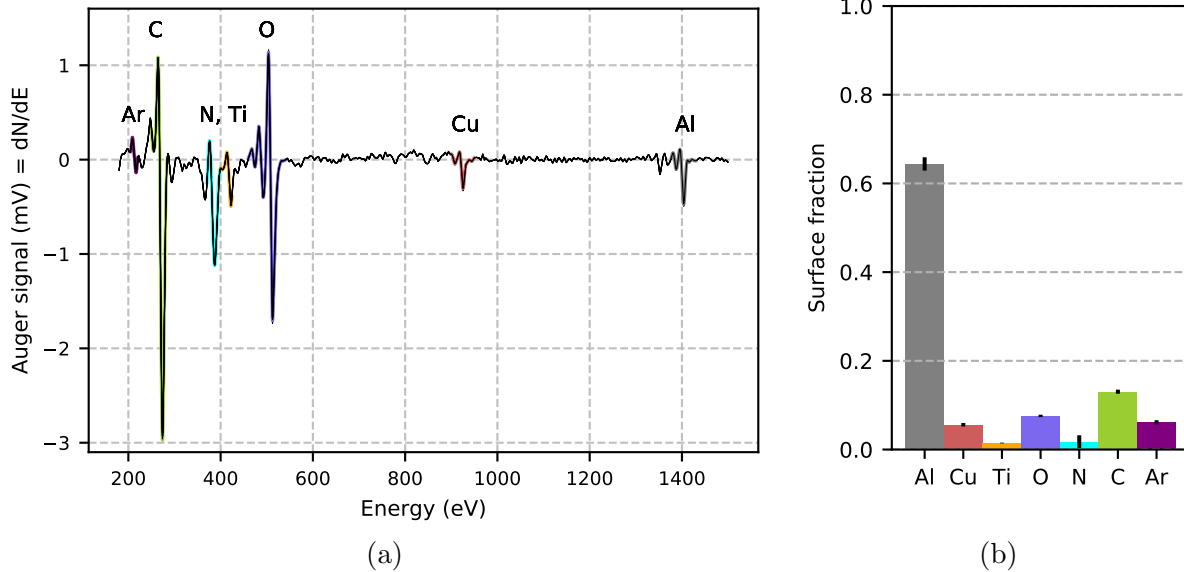


Figure 5.8: This data corresponds to [Electron 4](#) in Chapter 7. (a)Auger spectrum with the strongest peak of each element highlighted. (b) The atomic surface composition extracted from (a).

Table 5.1: Auger sensitivity

Element	Peak energy (eV)	Auger sensitivity
Aluminum	1396	.0076
Aluminum oxide	1396	.0076
Argon	215	.0522
Calcium	294	.5543
Carbon	272	.2426
Copper	920	.0639
Nitrogen	379	.0921
Oxygen	503	.3023
Titanium	418	.3297

shown in Figure 5.9. The standard deviation of this data is 0.2 mV, so it gives rise to a peak-to-peak error of 0.3 mV.

The errors reported in Figure 5.8b are equal to the 0.3 mV error scaled by the Auger sensitivities from Table 5.1 and multiplied by the normalization factor. The reported error is a lower bound. It does not account for imperfections in background correction, uncertainty in the scaling factors, or the fact that electrons with different energies can travel different distances through the substrate. In addition, this error does not account for electron-beam-induced changes in the surface composition. The Auger measurement process deposits carbon and can cause low-energy elements such as oxygen and nitrogen to desorb from the surface. Since elements are measured one-by-one, the calculated surface fractions will not exactly represent the state of the substrate either before or after the spectrum was taken.

We will now address how we determine the surface fraction of nitrogen. The measurement

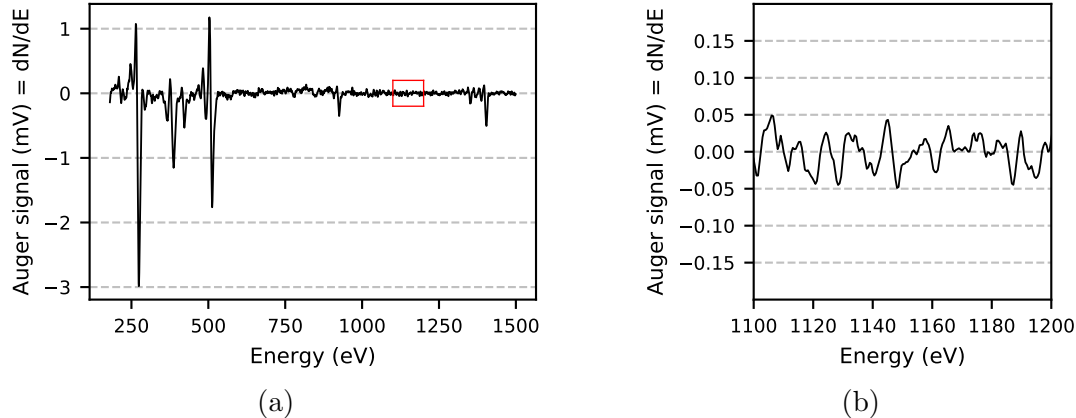


Figure 5.9: (a) Background-corrected Auger scan. (b) Zoom in on area of scan with no Auger peaks, illustrating high-frequency noise with a standard deviation of 0.2 mV.

of nitrogen is complicated by the fact that the only nitrogen peak in our measurement regime overlaps with one of the titanium peaks. As shown in Figures 5.10a and 5.10b, both elements have peaks at 380 eV. To determine the surface fraction of nitrogen we must subtract out the titanium.

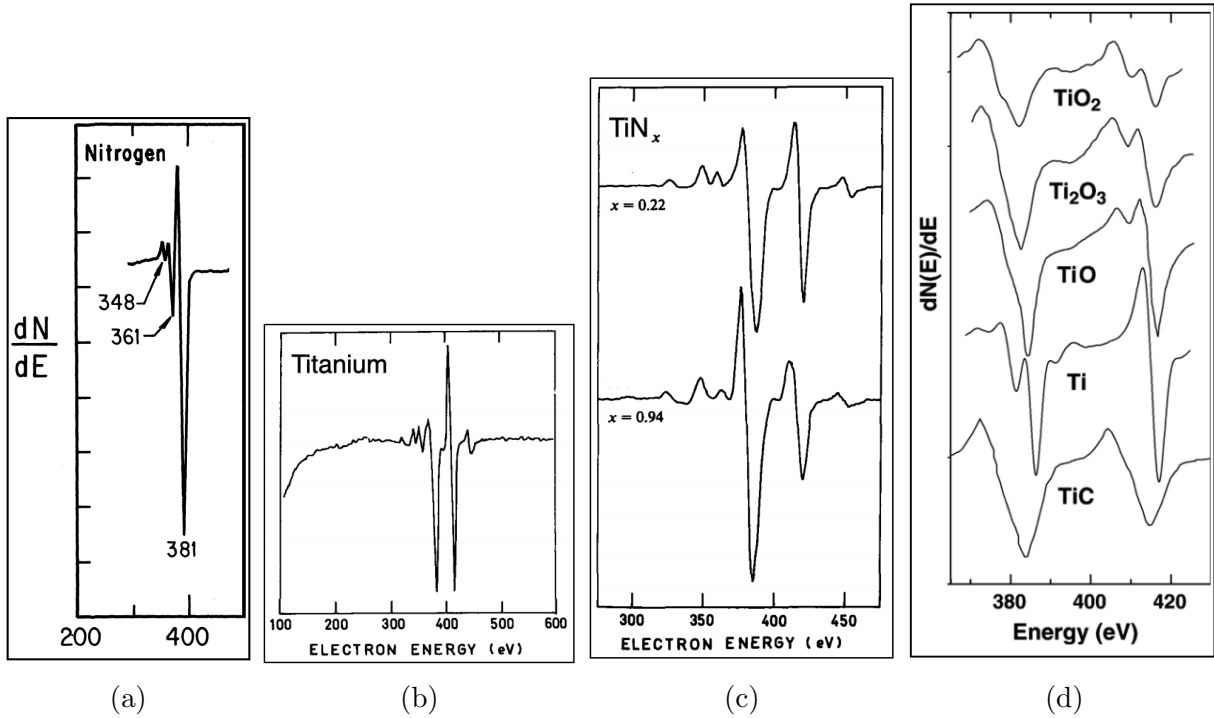


Figure 5.10: Reference Auger spectra: (a) Nitrogen adapted from [34], (b) Titanium adapted from [35], (c) Titanium nitride adapted from [35], (d) Titanium carbide and oxide adapted from [36].

If the relative heights of the 380 eV and 420 eV peaks were determined solely by the relative amplitudes of nitrogen and titanium, then the subtraction process would be simple.

Figure 5.10c shows how the relative heights of these peaks change as the titanium/nitrogen ratio changes. However, in our system there are many other elements present including oxygen and carbon. Oxygen and carbon auger peaks do not overlap with nitrogen or titanium, but when oxygen and carbon bond with titanium they alter the relative amplitudes of the titanium peaks, as shown in Figure 5.10d.

To estimate the surface fraction of nitrogen, we first measure the peak-to-peak amplitudes of both the 380 and 420 eV peaks. We set the nitrogen amplitude to the amplitude of the 380 eV peak minus the amplitude of the 420 eV peak, as this provides a good estimate for the nitrogen fraction in titanium nitride. If the 420 eV peak is small as compared to the 380 eV peak, then we can state with confidence that the 380 eV signal is nitrogen, and analyze it as such. If, however, the two peaks are similar in size, we do not know whether the relative heights of the titanium peaks have been altered by bonds with nitrogen, carbon, oxygen, or a combination of the three. To account for this uncertainty, we set the error of the nitrogen amplitude to the amplitude of the 420 eV titanium peak. This is equivalent to the statement that the error in the nitrogen peak is proportional to the amount of titanium present.

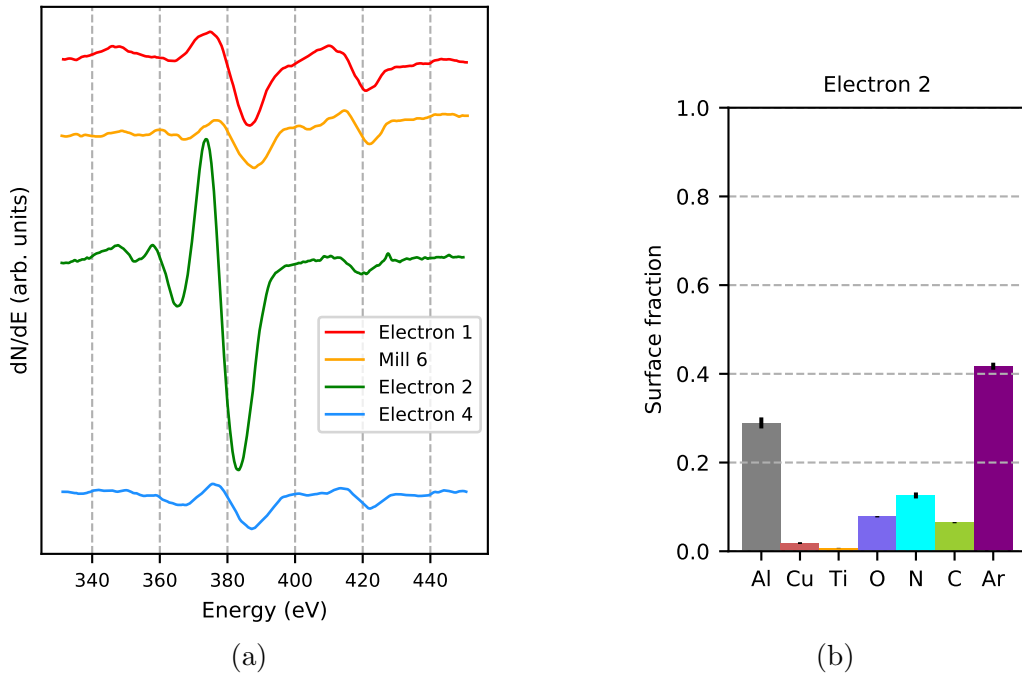


Figure 5.11: (a) Spectra of nitrogen and titanium measured throughout our surface treatment experiments. For the full context of these measurements, refer to [Electron 1](#), [Auger Mill 6](#), [Electron 2](#), and [Electron 4](#) in Chapter 7. (b) Relative surface fractions from Electron 2 shows a large nitrogen fraction with low uncertainty.

Four representative titanium spectra measured throughout our surface treatment experiments are shown in Figure ???. The line labelled *Electron 1* was taken before all argon ion milling, but after extensive heating. The other three spectra were taken after increasing amounts of argon ion milling and heat treatments. The four spectra are measured chronologically, top to bottom. When the line-shapes from *Electron 1*, *Mill 6* and *Electron 4* are

compared to the reference spectra from Figure 5.10, we see that the shapes look consistent with titanium nitride, but the features are not clear enough to make a definitive judgement. In contrast, in the spectrum from Electron 2 the 380 eV peak is far stronger than the 420 eV peak, indicating that a large amount of nitrogen is present. The fractional composition corresponding to treatment Electron 2 is shown in Figure 5.11b.

In this dissertation, we sometimes plot Auger spectra that have been directly smoothed by a Savitzky–Golay filter. Examples of smoothed carbon and aluminum spectra are plotted in Figure 5.12. Smoothing is never done before fractional analysis, as it systematically reduces the amplitudes of the peaks.

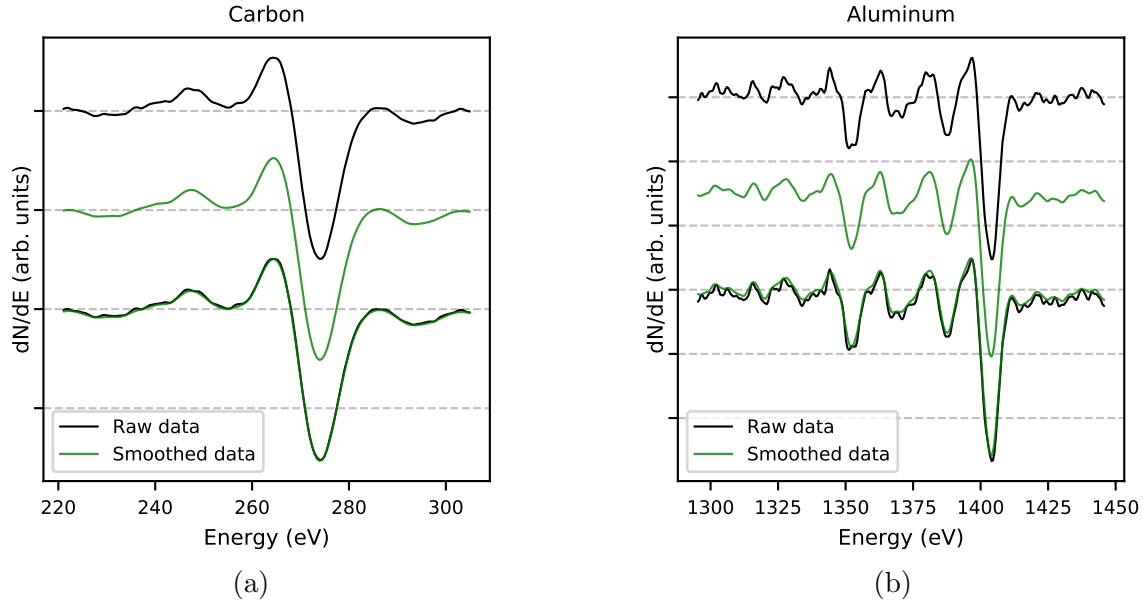


Figure 5.12: Examples of Auger spectra smoothed with a Savitzky–Golay. (a) Smoothed carbon spectrum. (b) Smoothed aluminum spectrum.

The Auger spectra also contains information about the chemical state of the surface. In our discussion of titanium, we compared its line-shape to reference spectra and found that it is difficult to make a clear statement on its chemical state. However, the line-shapes of carbon and aluminum can be interpreted much more clearly. We will present reference spectra for these elements in later chapters as their chemical states become relevant.

### Electron bombardment as a surface treatment

The electron beam from the Auger spectrometer can alter the chemical composition and physical structure of the trap surface. Figure 5.6 showed the size of the electron beam in relation to the trap electrodes. When the Auger spectrometer is performing as a surface treatment tool, the electron beam is centered on the ion trapping location. When our goal is to measure the surface composition without affecting the electric-field noise at the ion, we align the electron beam so that it hits the ground plane near the outer edges of the trap.

To determine the location of the electron beam, we direct the beam towards the trap, and measure the current passing from the electron beam through each of the 21 DC electrodes.

We track these currents while adjusting the position of the trap until the beam is aligned to the desired location. To determine the total energy deposited during an electron bombardment treatment, we first measure the current passing through the electrodes nearest to the ion trapping site. We estimate the surface area of the overlap between the electron beam and each electrode, and from this we can calculate the current density. The total energy deposited during an electron treatment can be calculated directly from the electron beam energy (2 keV), the current density, and the treatment time.

When the filament for the electron beam is turned on, the pressure in the chamber rises from  $10^{-10}$  Torr to  $10^{-8}$  Torr. We use a residual gas analyzer (ExTorr RGA model XT100M) to gain chemical information about the gasses in the chamber before and after the filament is turned on.

### 5.3 Argon ion milling

Ion-milling surface treatments are performed using an in-situ argon ion sputter gun. Before the treatment begins, the ion trap is shifted and rotated so that the beam will hit the trap at the desired angle and location. From measurements of individual electrodes, we estimate that the diameter of the ion beam is larger than the size of the ion trap chip. Next, the electron source in the ion gun is turned on, and the entire vacuum chamber is filled with argon gas. When argon diffuses into the gun, it is bombarded with electrons and becomes ionized. Ionized argon ions are accelerated toward the surface of the trap. We have performed milling treatments with ion energies of 200, 400 and 500 eV.

To prevent electrodes from shorting, the RF electrode is biased -2 V with respect to ground during ion milling, and the DC electrodes are biased +2 V with respect to ground. If a bridge of metal begins to form between differently-biased electrodes during the sputter process, a current will flow through the bridge and quickly burn it off. The efficacy of this technique has not been verified.

While the milling process is underway, we continuously measure the amplitude of the current that passes through the DC electrodes as a consequence of argon-ion bombardment. We know the surface area of the combined DC electrodes, so we can calculate the current density of the argon treatment. With the argon ion energy, current density and treatment time the total deposited energy can be calculated.

The SRIM (the stopping range of ions in matter) simulation software [37] is used to estimate how much material is removed by each ion milling treatment. These estimates depend on the energy, mass and angle of the ion beam. They also depend on the atomic composition of the substrate, as different elements can have widely varying sputter rates. Our milling experiments were interspersed with Auger spectroscopy. We extrapolated between these surface composition measurements to find the appropriate surface compositions to input into the SRIM simulations.

### 5.4 Ion-trapping side effects

We deliberately alter the surface of an ion trap chip using heat treatments, electron bombardment, and argon ion milling. We have observed changes in ion heating rates in response

to these treatments. There are also several ways in which the trap can be altered as a side effect of its operation as an ion trapping device. In our lab, teams have observed heating rate increases after RF current spikes, UV laser exposure, and calcium ion deposition. In addition, our titanium sublimation pump may deposit titanium onto the surface of the trap.

We take measures to avoid these side effects, and we have not found them to have any effect on ion heating rates in our system. The neutral calcium beam, as previously discussed, is angled upward to avoid depositing calcium onto the trap surface. The titanium sublimation pump is similarly angled. All lasers are angled parallel to the trap surface to prevent UV-induced surface reactions. The RF power is continuously monitored, and we have never observed any spiking behaviors.

# Chapter 6

## Thermally activated fluctuators

The surface of a typical ion trap is far too complicated to simulate fully from first principles. Trap surfaces have multiple length-scales of surface roughness, a variety of atomic species in different chemical configurations, and complicated crystal grain structures. In the absence of first-principle simulations, the thermally activated fluctuator (TAF) model is a powerful tool, as it provides an accessible way to investigate how a physical system generates electric-field noise.

The TAF model was developed by P. Dutta, P. Dimon, and P. M. Horn to describe 1/f noise processes in metals [38]. In 2018, our team found evidence that this model is relevant to studies of electric-field noise in ion traps. A detailed overview of the TAF model in the context of ion trapping can be found in reference [6]. This reference presents early data from the trap referred to as TRAP C in this dissertation, analyzed through the lens of the TAF model. It also includes a discussion of why we ruled out, for this trap, other noise models that have been previously proposed to describe ion-trap surface noise.

In this chapter, we will present the mathematical framework of the TAF model. Then, we will demonstrate that the data taken in TRAP C throughout a series of surface treatment experiments can be described by ensembles of TAFs with different distributions of energy barriers. Finally, we explore physical processes that are known to take place in metals, have dynamics that are consistent with the TAF model, and can generate electric-field noise.

### 6.1 Mathematical framework

A single two-level fluctuator can populate one of two possible states at any given time. To change between these states, the fluctuator must pass over a static energy barrier with magnitude  $E_a$ . In the thermally-activated regime, jumps between states are thermally driven. We assume, for simplicity, that the two states are at the same energy level. These concepts are illustrated in Figure 6.1a.

A single fluctuator produces random telegraph noise with a Lorenzian spectrum centered at zero. As shown in Figure 6.1b, the magnitude and corner frequency of the noise spectrum are temperature dependent. If the noise of a fluctuator is measured at a single frequency as its temperature is varied, the measured noise amplitude will peak at the temperature at which the corner frequency  $\Gamma$  is equal to the measurement frequency  $\omega$ . For this reason,  $\Gamma$  is

called the characteristic frequency of the fluctuator. If the measurement temperature is raised such that  $\Gamma$  is higher than the measurement frequency  $\omega$ , then the fluctuator jumps quickly between states, and produces noise predominantly at high frequencies. In the opposite case, when the temperature is lowered and  $\Gamma$  becomes lower than  $\omega$ , the fluctuator produces noise predominantly at low frequencies.

The characteristic frequency  $\Gamma$  depends on the substrate temperature  $T$  and energy barrier  $E_a$  according to the equation:

$$\Gamma = \frac{1}{\tau_0} e^{-E_a/k_B T}, \quad (6.1)$$

where  $\tau_0$  is a temperature-independent attempt time that depends on the physical embodiment of the fluctuator. We assume that  $E_a \gg k_B T$ , where  $k_B$  is the Boltzmann constant.

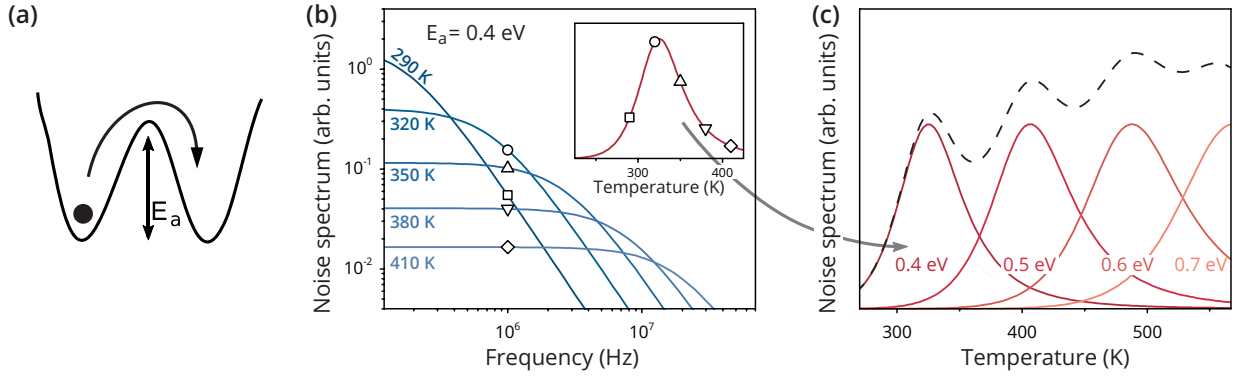


Figure 6.1: Illustration of TAF spectral properties. (a) Cartoon picture of a TAF showing a charge hopping between two potential wells separated by an energy barrier  $E_a$ . (b) Noise spectra for a single TAF with  $E_a = 0.4$  eV at different temperatures. Inset: Temperature dependence of noise at a frequency of  $2\pi \times 1$  MHz. Corresponding data points are displayed in the same shape. (c) Noise spectrum as a function of temperature for four TAFs (continuous curves) at  $2\pi \times 1$  MHz. The dashed line shows the sum. (This figure and caption are reproduced from reference [6], and assume  $\tau_0 = 10^{-13}$  s.)

In a macroscopic physical system, such as a metal film, TAF noise is produced by an ensemble of fluctuators with a distribution of energy barriers. Noise from a sample distribution of fluctuators is plotted as a function of temperature in Figure 6.1c. If the distribution of TAF energies  $D(E_a)$  is continuous and slowly varying, we can make the approximation [38]:

$$S(\omega, T) \propto \frac{k_B T}{\omega} D(\bar{E}), \quad (6.2)$$

where  $S$  is the noise amplitude at measurement frequency  $\omega$  and temperature  $T$ , and  $\bar{E}$  is the activation energy when  $\Gamma = \omega$  for a given temperature.

This approximation can be used to extract a fluctuator distribution from measurements of noise at a range of different temperatures or frequencies. We use this capability to draw a link between ion-heating-rate measurements and the behaviors of underlying noise processes. It is, however, important to recognize that a TAF distribution extracted from an ion-heating-rate

temperature scaling may have smoother features than the true physical TAF distribution. This is due to the fact that even a TAF with an infinitely-precise activation energy produces smoothly-varying noise distributions in frequency in temperature space, as illustrated in Figure 6.1c.

## 6.2 Fit to ion-heating-rate data

The TAF model does not predict a functional form for how noise from a generic distribution of fluctuators should scale with temperature (though it does exclude sharp features). Instead, it establishes that there is a very specific relationship between the temperature scaling and frequency scaling of TAF noise.

TAF noise from a slowly-varying distribution of fluctuators scales inversely with frequency according to the equation:

$$S(\omega) \propto \omega^\alpha \quad (6.3)$$

where  $\alpha$  is the frequency scaling exponent, and the measurement frequency  $\omega$  is equal to the secular frequency of the ion. In Chapter 4, we presented experimental evidence that noise in TRAP C follows this scaling behavior.

The TAF model predicts that  $\alpha$  will depend on the slope of the temperature scaling according to the following equation [38]:

$$\alpha(\omega, T) = 1 - \frac{1}{\ln \omega \tau_0} \left( \frac{\partial \ln S}{\partial \ln T} - 1 \right). \quad (6.4)$$

To test this prediction in our system, we measure electric-field noise as a function of temperature at two frequencies. The temperature-scaling slope is analyzed in the context of the TAF model to make a prediction of how  $\alpha$  scales with temperature, and then this prediction is compared to the directly-measured values of  $\alpha$ .

Before these predictions are made, each temperature scaling is binned in 10 K increments, and certain measurements are excluded that are known to be outside of the TAF model. Specifically, we exclude all data taken above 545 K. At high temperatures, the heating rates abruptly increases in magnitude. This high-temperature shoot off is not consistent with TAF noise, and will be discussed in detail in Chapter ???. An example of a data set including the high temperature shoot-off is plotted in Figure 6.2a, where excluded datapoints are marked with black x's.

Excluding all data taken above 545 K also removes measurements that were taken while the TAF distribution was undergoing a time-sensitive heat-induced transformation. Although noise during an active transformation may still be dominated by TAFs, temperature scaling slopes and frequency scaling exponents lose physical significance when each measurement samples a different underlying TAF distribution. An example of a data set in which a thermal-induced transformation took place is plotted in Figure 6.2b. Thermal transformations will be discussed further in Chapter 9.

After high-temperature data has been excluded, and data taken at similar temperatures have been averaged together, we fit a Gaussian to each temperature scaling to obtain noise distributions with smoothly-varying slopes. The choice to use a Gaussian fit is not a

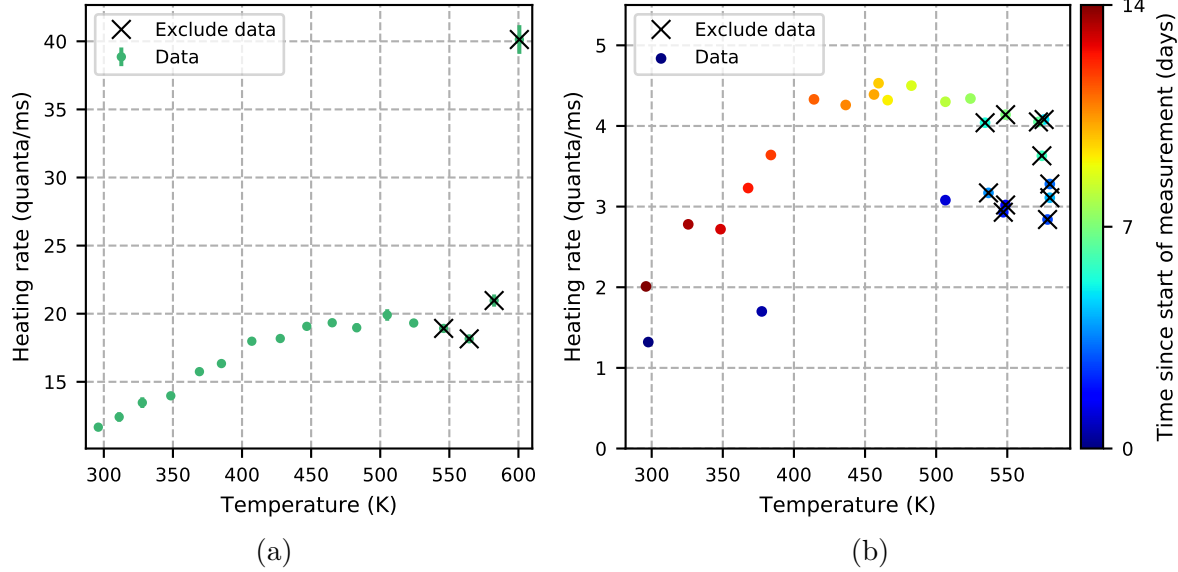


Figure 6.2: (a) Heating rates following treatment ELECTRON 1 scaled to 1 MHz, with data from the high-temperature shoot off excluded. (b) Heating rates measured at 1.3 MHz following treatment MILL 7, with data taken during an active thermal transformation excluded.

statement about the underlying physics. It is simply versatile enough to fit the temperature scalings that we measure.

Before the smoothed heating-rate temperature scaling can be used to make a prediction of how  $\alpha$  scales with temperature, a value must be chosen for attempt time  $\tau_0$ . In the context of defect dynamics in solid state systems, attempt times between  $10^{-12}$  and  $10^{-14}$  s have been used, as this is on the order of the inverse phonon frequency [39, 40, 41]. Attempt times on the same order have been used in the context of adatom diffusion on metal surfaces [42]. In contrast, Weckesser et. al. measured an attempt time of  $10^{-10}$  s in a study of hydrocarbon diffusion on metals [43]. Figure 6.3 illustrates the impact that the choice of  $\tau_0$  has on the analysis of a temperature scaling measurement.

Figure 6.3a contains a plot of a heating-rate temperature scaling measured at a frequency of 0.88 MHz, along with a Gaussian fit. This data was taken immediately after surface treatment MILL 7 & HEAT. The slope of the Gaussian fit from Figure 6.3a is inserted into Equation 6.4 to predict how frequency scaling exponent  $\alpha$  will scale with temperature. Predictions made with two different choices of  $\tau_0$  are plotted in Figure 6.3b.

We measure  $\alpha$  as a function of temperature by measuring heating rates at two or more frequencies between 0.5 and 2.0 MHz from room temperature to 575 K. The  $\alpha$  values measured after treatment MILL 7 & HEAT are plotting in black in Figure 6.3b. To determine the accuracy of the TAF prediction, we do a normalized  $\chi^2$  analysis of this data, assuming that there is zero error in the TAF prediction lines. The normalized  $\chi^2$  values are calculated as follows:

$$\chi_N^2 = \frac{1}{n} \times \sum_{i=1}^n \left( \frac{\alpha_i - p_i}{\sigma_i} \right)^2 \quad (6.5)$$

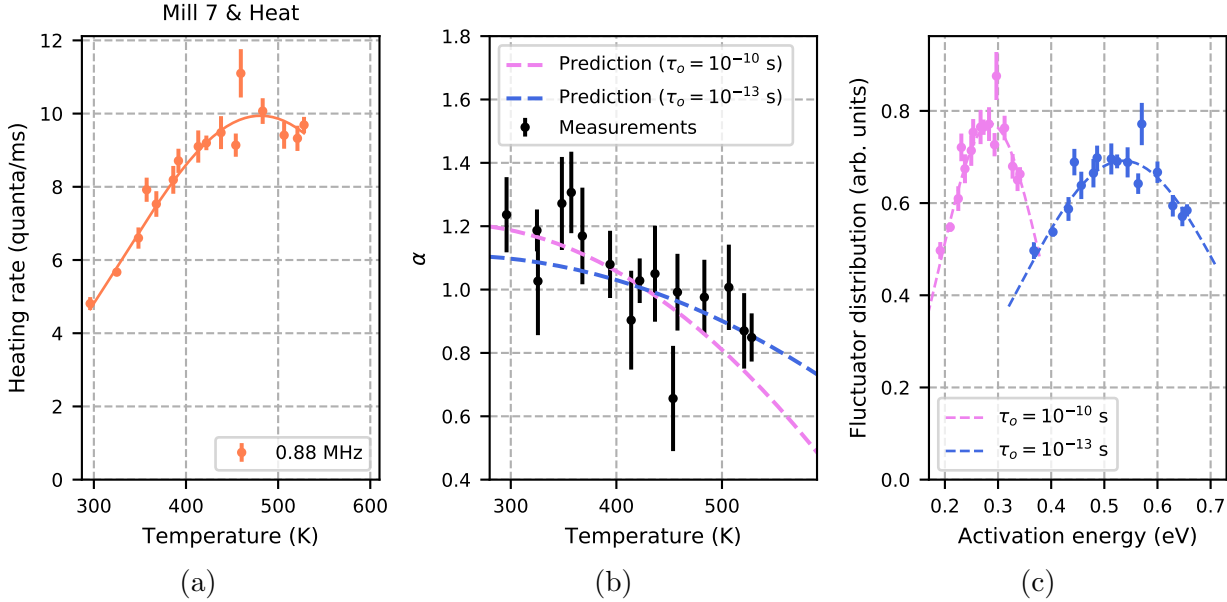


Figure 6.3: (a) Temperature scaling measured at 0.88 MHz with a Gaussian fit. (b) Measurements of the frequency scaling exponent as a function of temperature and predictions from the TAF model (Equation 6.4) using the slope of temperature scaling and two possible attempt time values. Using  $\tau_0$  values of  $10^{-10}$  and  $10^{-13}$ , the normalized  $\chi^2$  values are 0.97 and 0.94 respectively. (c) TAF distributions calculated from the temperature scaling using two possible attempt times.

where  $\alpha_i$  are direct measurements of the frequency scaling exponent at different temperatures,  $\sigma_i$  is the standard error of  $\alpha_i$ , and  $N$  is the total number of  $\alpha$  measurements.  $p_i$  is the prediction of  $\alpha_i$  extracted from the temperature scaling using the TAF model. For the data and predictions plotted in Figure 6.3b using  $\tau_0$  values of  $10^{-10}$  and  $10^{-13}$ , the  $\chi^2_N$  values are 0.97 and 0.94 respectively. From these numbers, we conclude that this data-set is consistent with the TAF model in both cases.

In Figure 6.3c are plotted two possible TAF distributions calculated directly from the temperature scaling in Figure 6.3a using two different attempt times. There are stark differences in the amplitudes and peak energies of these distributions. This illustrates that we must take great care in interpreting our extracted TAF distributions as we cannot measure  $\tau_0$  directly and must use values measured in other systems.

Figure 6.4a shows temperature scalings measured at two different frequencies after surface treatment MILL 1. As expected in a TAF system, the  $\alpha$  predictions plotted in Figure 6.4b are the same for both temperature scalings, and match the measurements with  $\chi^2_N = 1.41$ . The TAF distributions, as plotted in Figure 6.4c, are slightly offset in energy, and they match in regions where the energies overlap. Demonstrating that measurements at different frequencies probe the same underlying ensemble of TAFs is equivalent to demonstrating that the measured  $\alpha$  values match the predicted values.

The analysis presented in Figure 6.4c is reproduced in Figure 6.5c for a second data-set. In both figures, the reported  $\chi^2_N$  is calculated using the 1.3 MHz data. For the data presented in Figure 6.4a, the slope of the temperature scaling is constant, and the TAF

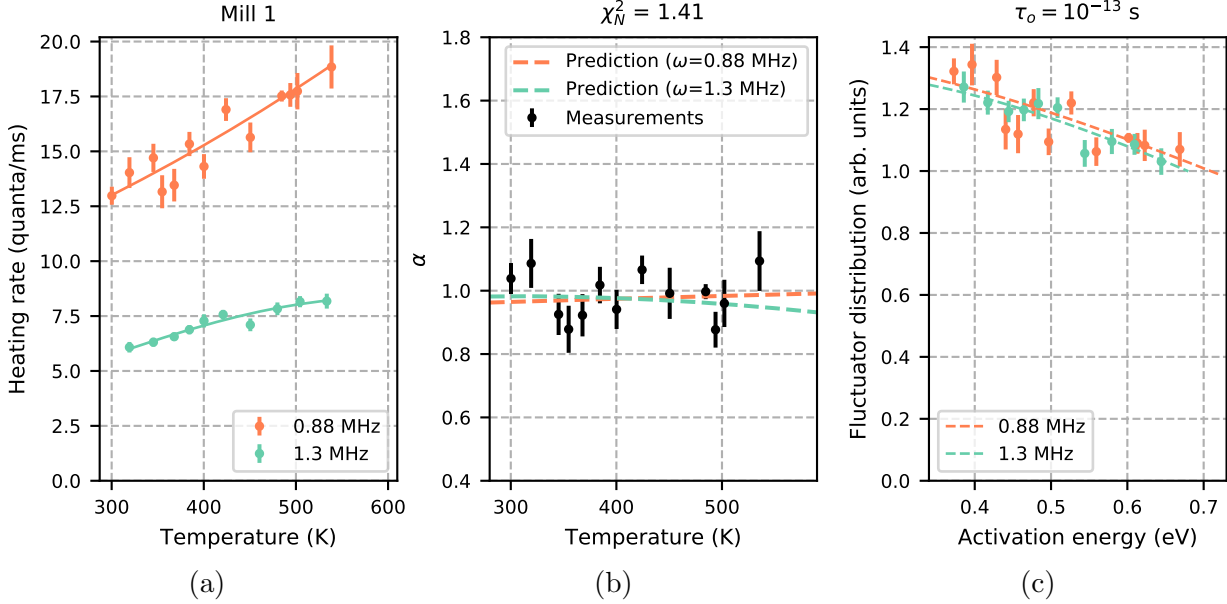


Figure 6.4: (a) Temperature scalings measured at two frequencies after treatment MILL 1, with Gaussian fit lines. (b) Measurements of the frequency scaling exponent and predictions from the TAF model (Equation 6.4) from each of the two temperature scalings. (c) A single TAF distribution measured at two frequencies.

model predicts that  $\alpha$  will be constant as a function of temperature. The measured values of  $\alpha$  are consistent with this prediction. For the data presented in Figure 6.5a, the slope of the temperature scaling steadily decreases with temperature, so the TAF model predicts that  $\alpha$  will decrease with temperature as well. Again the measured values of  $\alpha$  are consistent with the prediction.

The success of the TAF model in predicting two significantly different trends in  $\alpha$  is a strong indication that the TAF model is relevant to our system. During the series of experiments performed on TRAP C, there were twenty instances in which we did a surface treatment and then measured the temperature scaling of ion heating rates at two or more frequencies. To further investigate the relevance of the TAF to the data in our system, we do a quantitative assessment of how well the TAF model fits to the twenty-data-set collection.

For each dataset, we determine at which frequency the greatest number of measurements were taken. We then fit a Gaussian to those measurements to make a prediction of the temperature-dependence of  $\alpha$ . Finally, we calculate  $\chi^2_N$  for each data-set to quantify how well the measured values of  $\alpha$  match the prediction. This analysis was performed twice: once with an attempt time  $\tau = 10^{-13}$  s, and once with  $\tau = 10^{-10}$  s. Histograms including all  $\chi^2_N$  values are shown in Figure 6.6.

The majority of the  $\chi^2_N$  values plotted in Figure 6.6a are below 3.5. These values are low enough to conclude that these data-sets are ~~not~~ inconsistent with the TAF model, considering that we have not accounted for all sources of uncertainty.

For example, we assumed, for the purpose of these calculations, that the  $\alpha$  predictions have zero uncertainty. This cannot be the case, as we have not measured the derivatives of the heating-rate temperature scalings with perfect accuracy. In addition, we have chosen specific

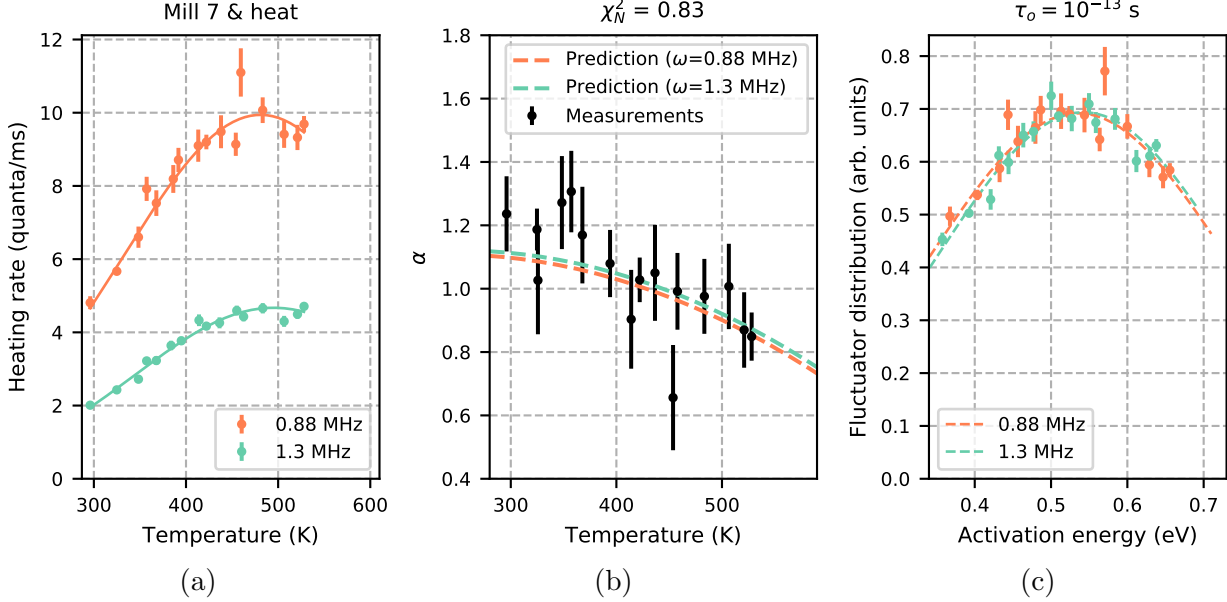


Figure 6.5: (a) Temperature scalings measured at two frequencies after the thermal transformation following MILL 7, with Gaussian fit lines. (b) Measurements of the frequency scaling exponent and predictions from the TAF model (Equation 6.4) from each of the two temperature scalings. (c) A single TAF distribution measured at two frequencies.

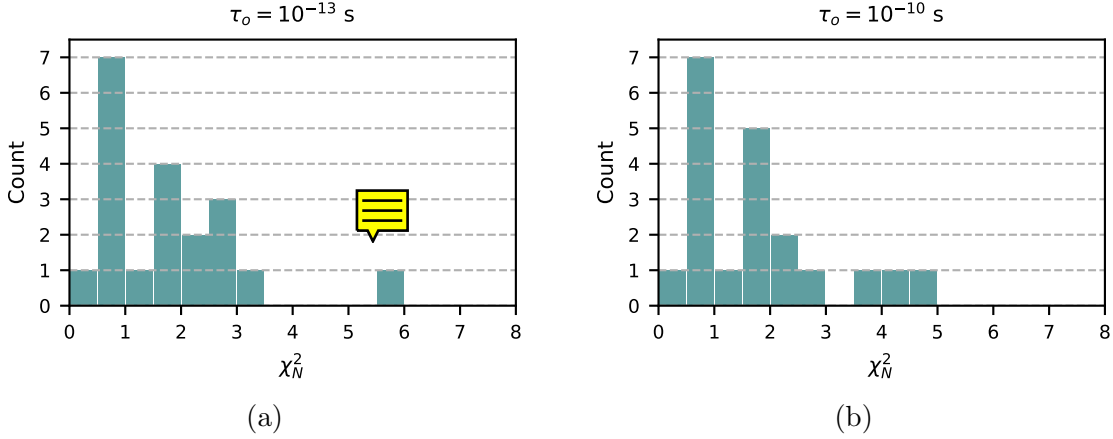


Figure 6.6: (a) Histogram of normalized  $\chi^2$  values calculated with attempt time  $\tau_0 = 10^{-13} \text{ s}$ . (b) Histogram of normalized  $\chi^2$  values calculated with attempt time  $\tau_0 = 10^{-10} \text{ s}$ .

values of  $\tau_0$ , and assumed that  $\tau_0$  is constant for all of the TAFs in a given distribution. This is not a good assumption in our system, as we likely have simultaneous noise contributions from multiple types of fluctuators. Measurements of  $\alpha$  are further complicated by the possibility that thermally-driven TAF transformations took place without our knowledge.

Perhaps the most significant sources of unaccounted-for noise in our system are intermittent fluctuations in laser frequency and power. An concerted effort is made to stabilize and monitor the measurement lasers, but laser fluctuations occasionally cause heating rate outliers. This raises the  $\chi_N^2$  value, but does not change the overall trend in  $\alpha$  as a function

of temperature.

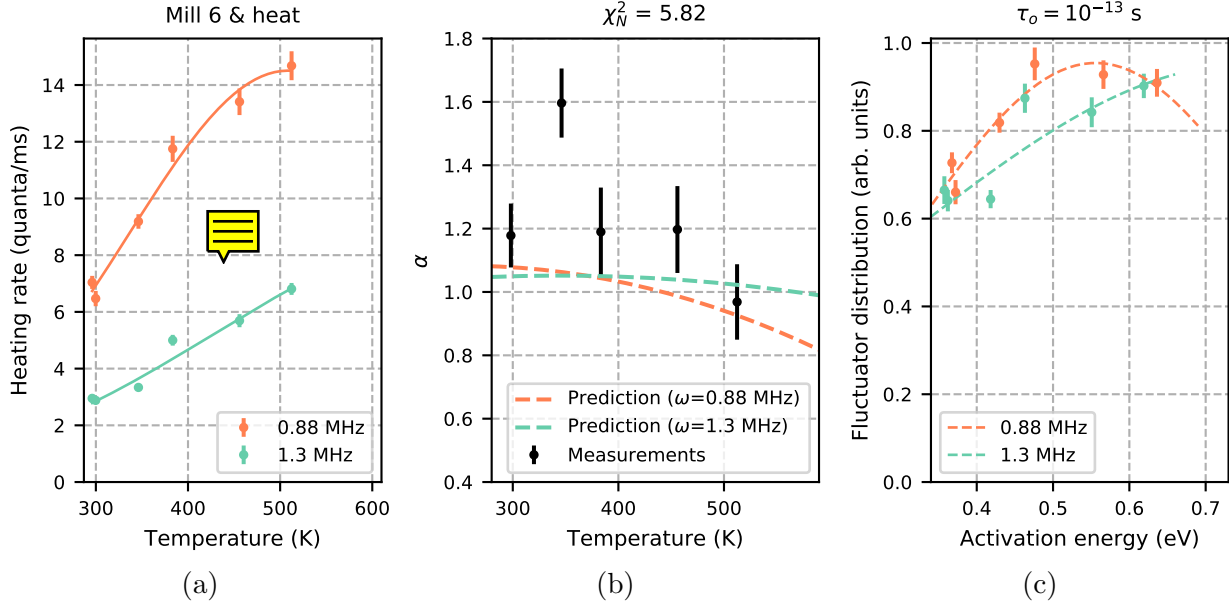


Figure 6.7: (a) Temperature scalings measured at two frequencies after the thermal transformation following MILL 6, with Gaussian fit lines. (b) Measurements of the frequency scaling exponent and predictions from the TAF model (Equation 6.4) from each of the two temperature scalings.  $\chi_N^2$  is calculated using the 1.3 MHz data. (c) A single TAF distribution measured at two frequencies.

The dataset with the highest  $\chi_N^2$  value is plotted in Figure 6.7. This data-set was taken after an unsaturated thermal transformation, and includes only five measurements of  $\alpha$ . A single outlier measurement is responsible for the high value of  $\chi_N^2$ . Most likely this outlier is a result of measurement error, laser instabilities, or another intermittent source of error. Since the trend of the other measurements of  $\alpha$  is consistent with TAF, this single outlier should not be used to rule out TAF as a surface noise model relevant to this data-set.

For information on how each individual data-set fits with the TAF model, refer to Chapter 7. Chapter 7 includes plots of all of the temperature scalings measured during TRAP C surface treatment experiments, scaled to a measurement frequency of 1 MHz assuming  $\alpha = 1$ . Also plotted are the corresponding TAF distributions, extracted from unscaled heating-rate measurements, assuming an attempt time of  $10^{-13} \text{ s}$ . In twenty of these data sets, temperature scalings were measured at two or more frequencies. The degree of overlap of TAF distributions extracted from temperature scalings measured at different frequencies gives a qualitative indication of how well each data set fits to the TAF model.

## 6.3 The physical embodiment of TAFs

After having demonstrated that the noise in TRAP C is consistent with TAFs, we consider the physical embodiment of the fluctuators. Earlier we made approximations assuming that each fluctuator hops between exactly two states with equal energies, but these are not necessary

requirements for physical TAFs. The TAF model requires only that the fluctuators are repeatedly thermally driven across energy barriers between stable states. For TAF electric-field noise specifically, these states must have distinct charge distributions.

With attempt times between  $10^{-10}$  and  $10^{-13}$  s, measurement frequencies between 0.7 and 2.0 MHz, and measurement temperatures between 300 and 600 K, we are sensitive to noise from TAFs between 0.2 and 0.7 eV. These energies and attempt times are consistent with atomic energy barriers associated with metal surfaces. There are several ways in which atomic and molecular fluctuators could produce electric-field noise. We will consider two possible categories of atomic fluctuators: migrating adsorbates, and near-surface defect motion.

In the category of migrating adsorbates, the physical fluctuators are adsorbates, and the TAF energies correspond to the surface migration barriers. Our previously discussed attempt times and energy barriers are realistic for hydrocarbon and adatom adsorbates diffusing on metal and oxide substrates [42, 44, 45, 43]. Molecular and atomic adsorbates bound to metal substrates have induced dipole moments, and these dipole moments depend both on the chemical structure of the adsorbate-metal bond and on the atomic-scale surface roughness of the substrate [46]. When an adsorbate hops between binding sites with different local curvatures, its interaction energy can fluctuate by an order of magnitude, leading to large fluctuations in its induced dipole moment [47]. These dipole fluctuations generate electric-field noise.

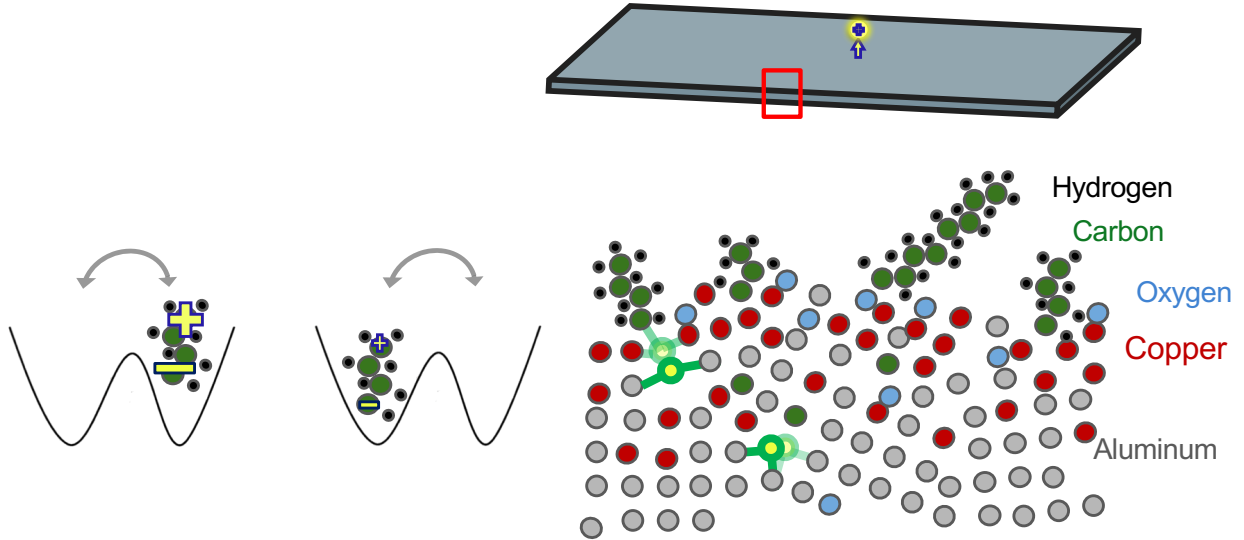


Figure 6.8: Left: cartoon of hydrocarbon dipole moment fluctuating in magnitude. Right: cartoon of trap cross section, illustrating metal defect fluctuations at and below the metal surface.

In the category of near-surface defect motion, the physical fluctuators are metal defects and impurities, and the TAF energies correspond to the defect diffusion energies. An attempt time of  $10^{-13}$  s and energy barriers between 0.4 and 1 eV are realistic for aluminum defect motion [40, 41, 39]. There is no charge associated with a point defect in an aluminum lattice, so a defect in isolation will not generate electric-field noise. A defect near the surface of a contaminated metal may activate dipole fluctuations in adsorbates, as the local curvature

of the surface can fluctuate with the presence and absence of the vacancy. This process is illustrated in Figure 6.8,

Electric-field noise may also be produced by the motion of impurities in the bulk of the metal film. Impurities deep in the bulk will be shielded by the metal, but in a highly-contaminated surface layer the shielding will be suppressed. Unlike metal vacancy defects, impurities can have a charge associated with them. For example, an oxygen impurity atom will pull electrons from the metal bulk to fill its outer shell, and in doing so it will become doubly charged. The motion of oxygen impurities, and other highly electronegative atoms such as nitrogen, can produce electric-field noise.

We can approximate the density of fluctuating dipoles required to produce the electric-field noise levels in our trap. The power spectral density of electric-field noise from averaged dipoles fluctuating parallel to the surface is given by [1]:

$$S_E = \frac{3\pi}{4\sigma_d} \frac{1}{(4\pi\epsilon_0 d^2)^2} S_\mu, \quad (6.6)$$

where  $\sigma_d$  is the dipole density by area, and  $d$  is the distance between the trapped ion and the surface of the metal. For fluctuators with a distribution of energy barriers  $D(E_b)$ ,

$$S_\mu = \mu^2 \frac{\pi k_B T}{4\omega} D(E_b = -k_B T \log(\omega\tau_0)). \quad (6.7)$$

where  $\mu$  corresponds to the difference between the dipole moments of the two fluctuator states. Dipole moments of adsorbed hydrocarbons, carbon atoms, and oxygen atoms on aluminum are approximately 1, 0.5, and 5 D respectively. As previously mentioned, these values can fluctuate by an order of magnitude if the adsorbate moves between binding sites with different local curvatures. If we assume that  $D(E_b)$  is a Gaussian and that the dipole moment fluctuation  $\mu = 5$  D, then  $\sigma_d \approx 7 - 10 \times 10^{18} \text{ m}^{-2}$ , or approximately 7-10 TAF dipoles per square nanometer. For comparison, a flat aluminum surface has about 12 surface atoms per square nanometer. Considering the high contamination levels measured in TRAP C before milling, and the likelihood that there are both surface adsorbate and sub-surface noise sources, these numbers are very reasonable.

## 6.4 Summary

In this section, we introduced the mathematical framework of the TAF model and demonstrated that the temperature- and frequency-scaling data taken in TRAP C are consistent with this framework. We also discussed physical processes that may produce TAF electric-field noise in metal films such as ours, including fluctuating adsorbates and near-surface defects. The TAF model will be drawn upon throughout this dissertation to aid in the interpretation of how TRAP C responded to surface treatments.

# Chapter 7

## Timeline of data and surface treatments

This chapter includes all of the data taken and surface treatments performed on the ion trap that is the focus of this dissertation - TRAP C. This timeline establishes a naming and numbering system for all surface treatments. When these treatments and data-sets are presented and discussed in other chapters, they are referred to using these names. The purpose of this system is to clarify the context in which each measurement was taken, without complicating future chapters with bulky and repetitive explanations of the trap history.

Table 7.1: Electron bombardment surface treatments

Treatment	Energy deposited (kJ/cm <sup>2</sup> )	Treatment time (hr)	Carbon state
Electron 1	2	0.1	Graphite
Electron 2	76	3.0	Carbide
Electron 3	176	3.2	Carbide
Electron 4	281	3.2	Carbide
Electron 5	2130	23.0	Carbide

Beam energy of all treatments = 2 keV

Current density = 3 mA/cm<sup>2</sup> to 12 mA/cm<sup>2</sup>

In most cases, longer electron treatments deposit more carbon.

Table 7.2: Argon ion milling surface treatments

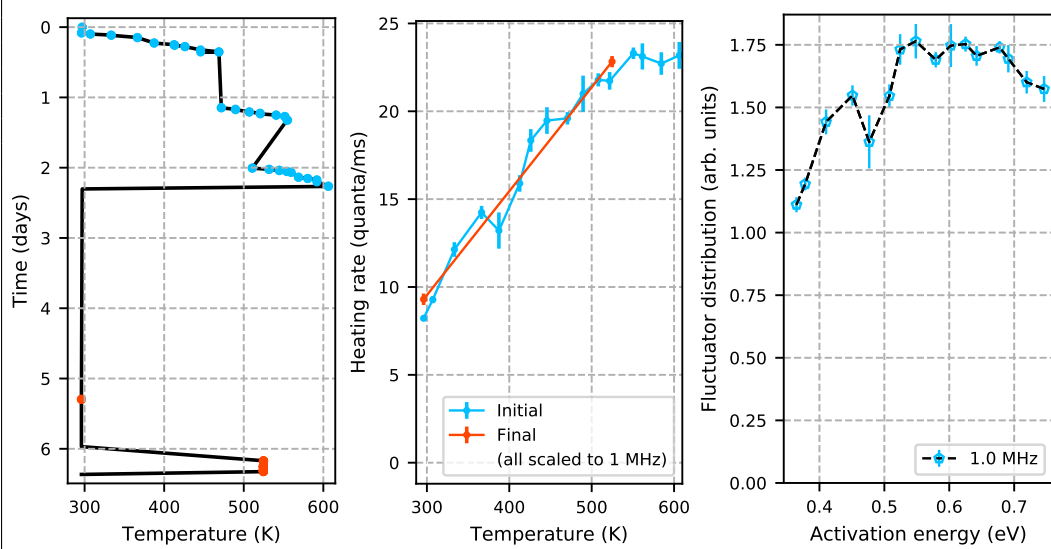
Treatment	Energy deposited (J/cm <sup>2</sup> )	Cumulative energy (J/cm <sup>2</sup> )	Material removed (nm)	Beam Angle	Beam Energy (eV)
Mill 1	0.1	0.1	0.13	normal	200
Mill 2	0.1	0.2	0.13	normal	200
Mill 3	0.5	0.7	0.6	normal	200
Mill 4	1.2	1.9	1.5	normal	200
Mill 5	2.9	4.8	3.9	normal	400
Mill 6	7.5	12.3	11.4	normal	400
Mill 7	8.8	21.1	16.4	normal	200
Mill 8	0.2	21.3	0.6	normal	200
Mill 9	0.6	21.9	1.3	normal	200
Mill 10	4.9	26.8	12.2	normal	200
Mill 11	9.7	36.5	18.9	45°	400
Mill 12	5.2	41.7	9.8	45°	500

Current density = 5 to 10  $\mu\text{A}/\text{cm}^2$

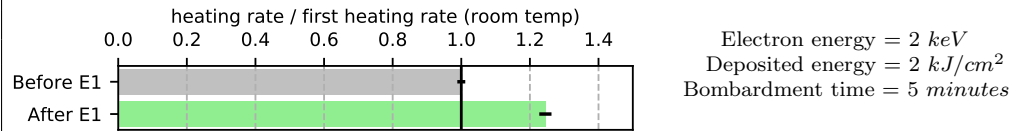
Argon pressure =  $1 \times 10^{-5}$  to  $5 \times 10^{-5}$  Torr

Table 7.3: Timeline of surface treatments and data

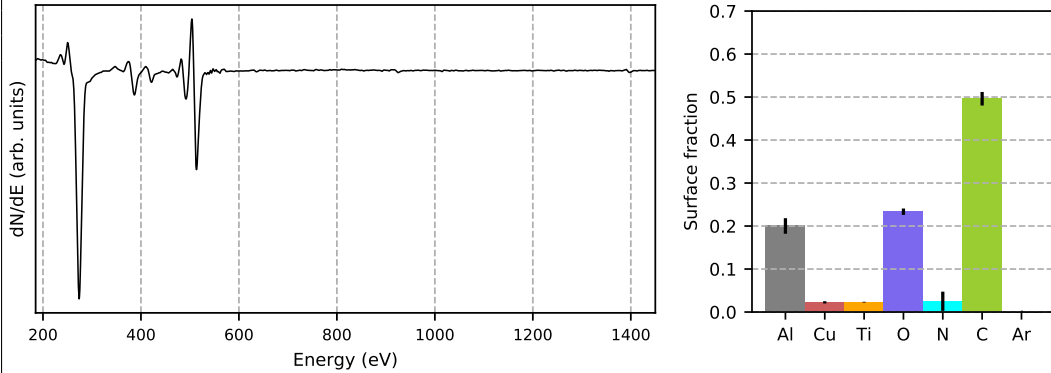
First  
heating rates  
&  
**Heat  
Treatment**

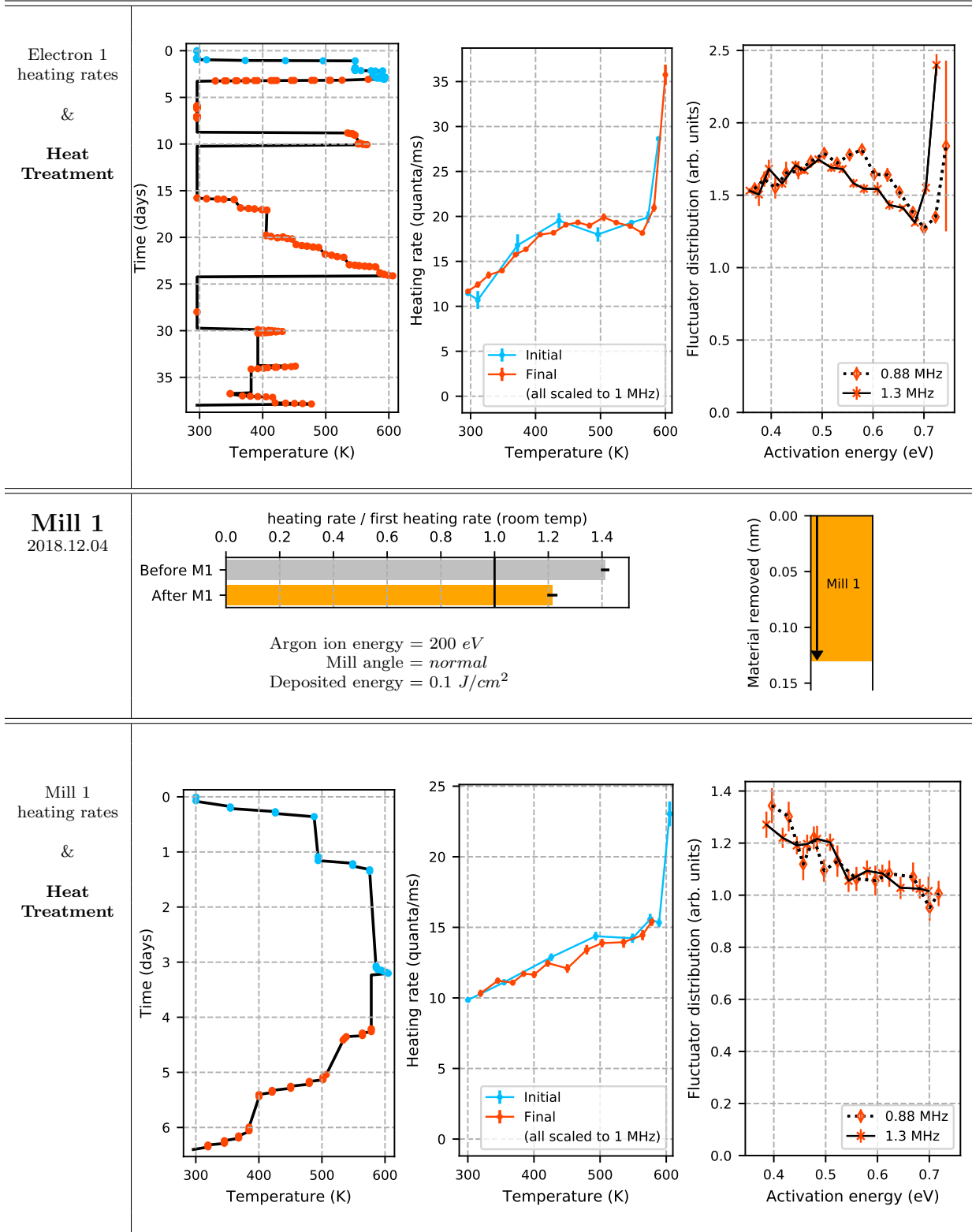


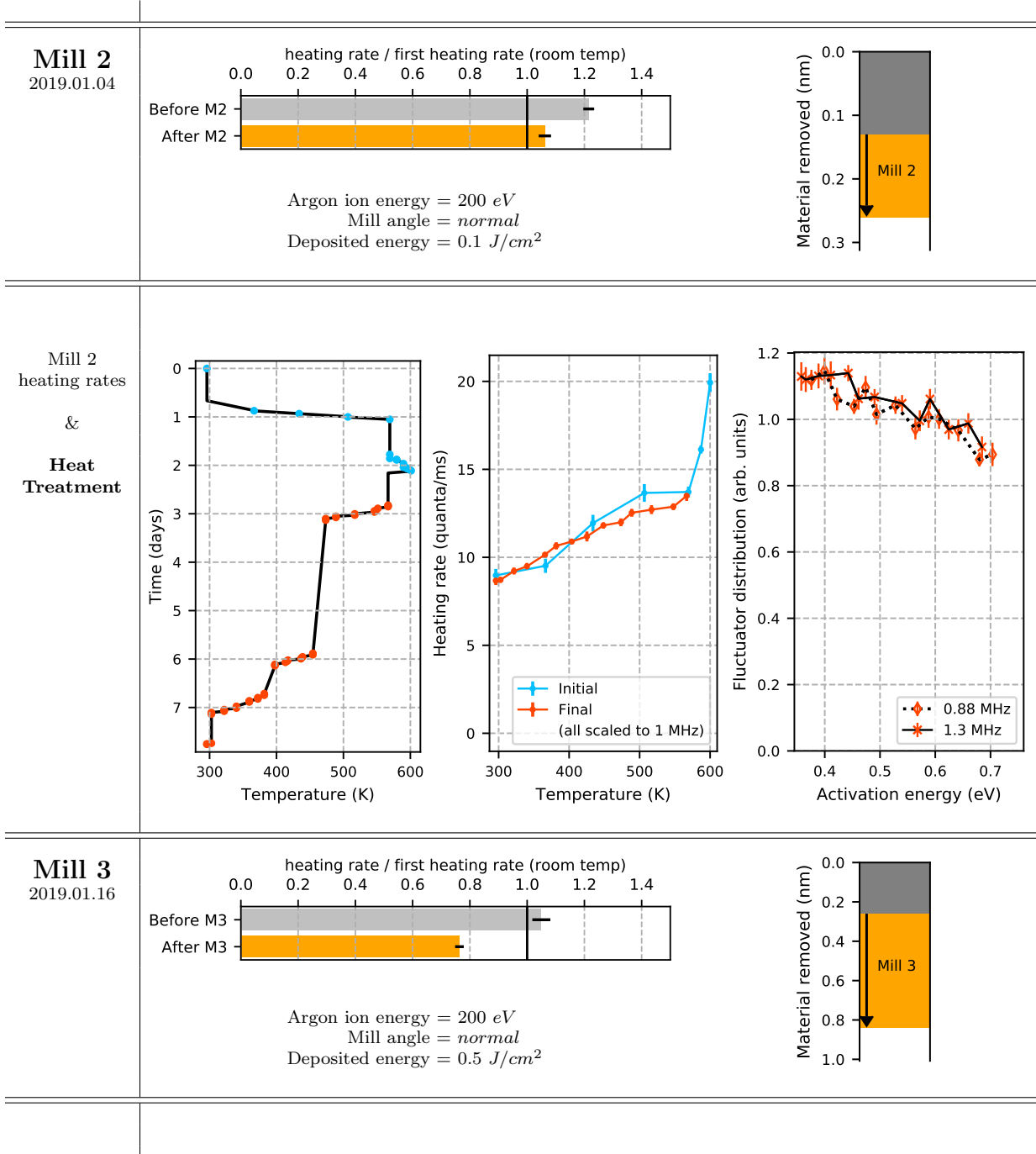
**Electron 1**  
2018.06.22

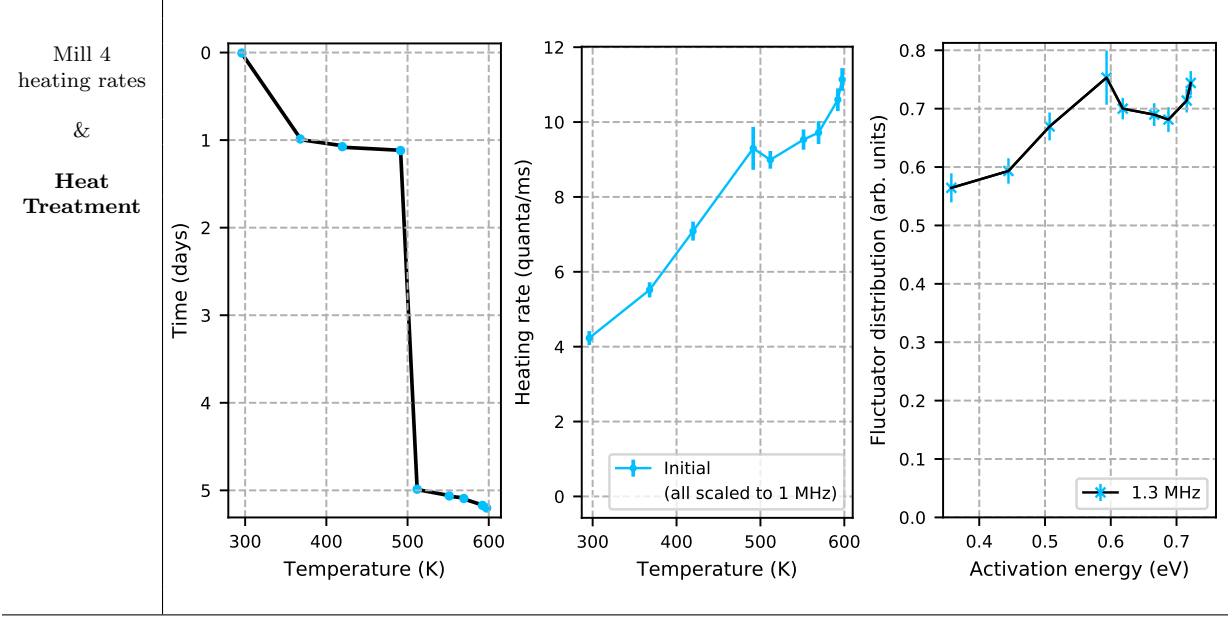
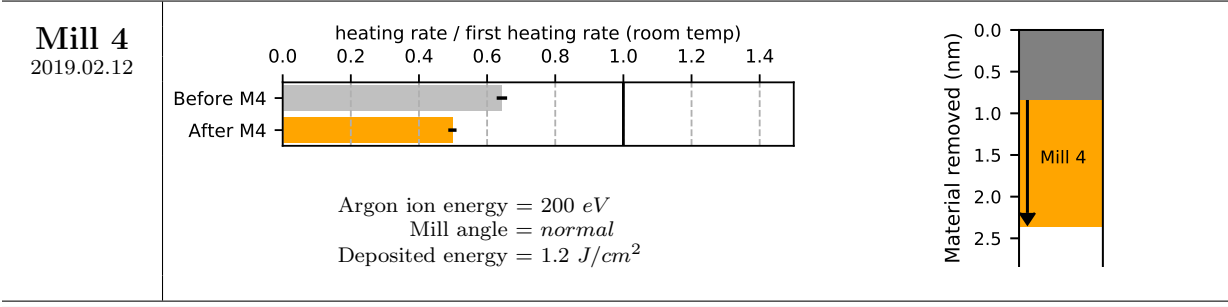
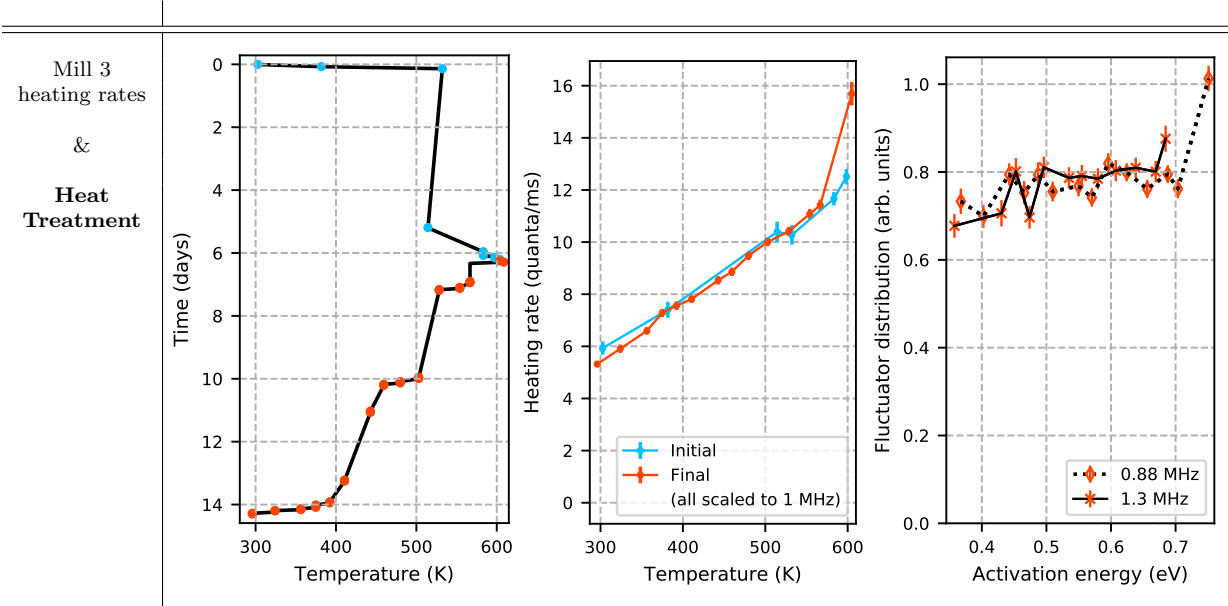


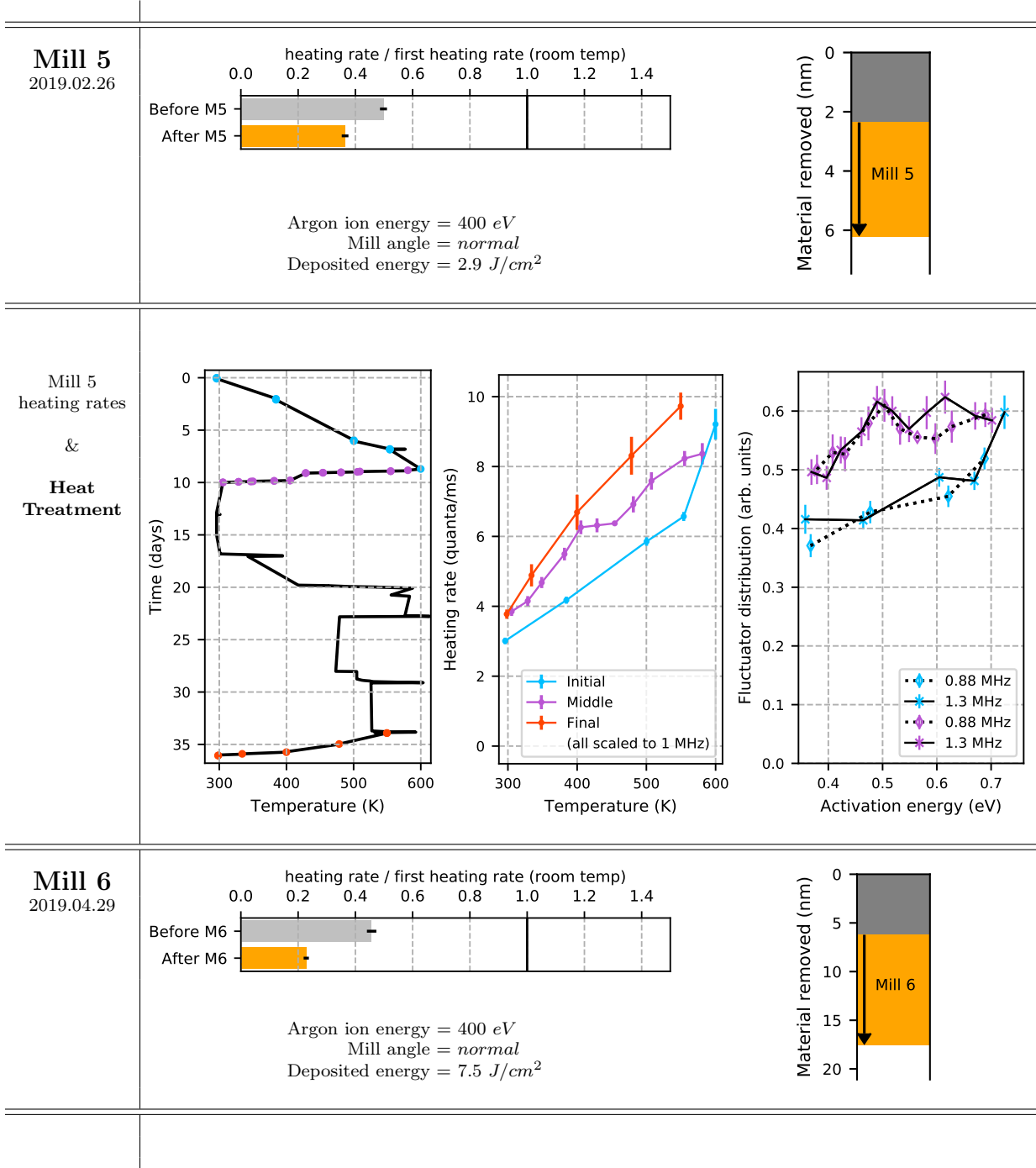
Electron 1  
Auger spectrum

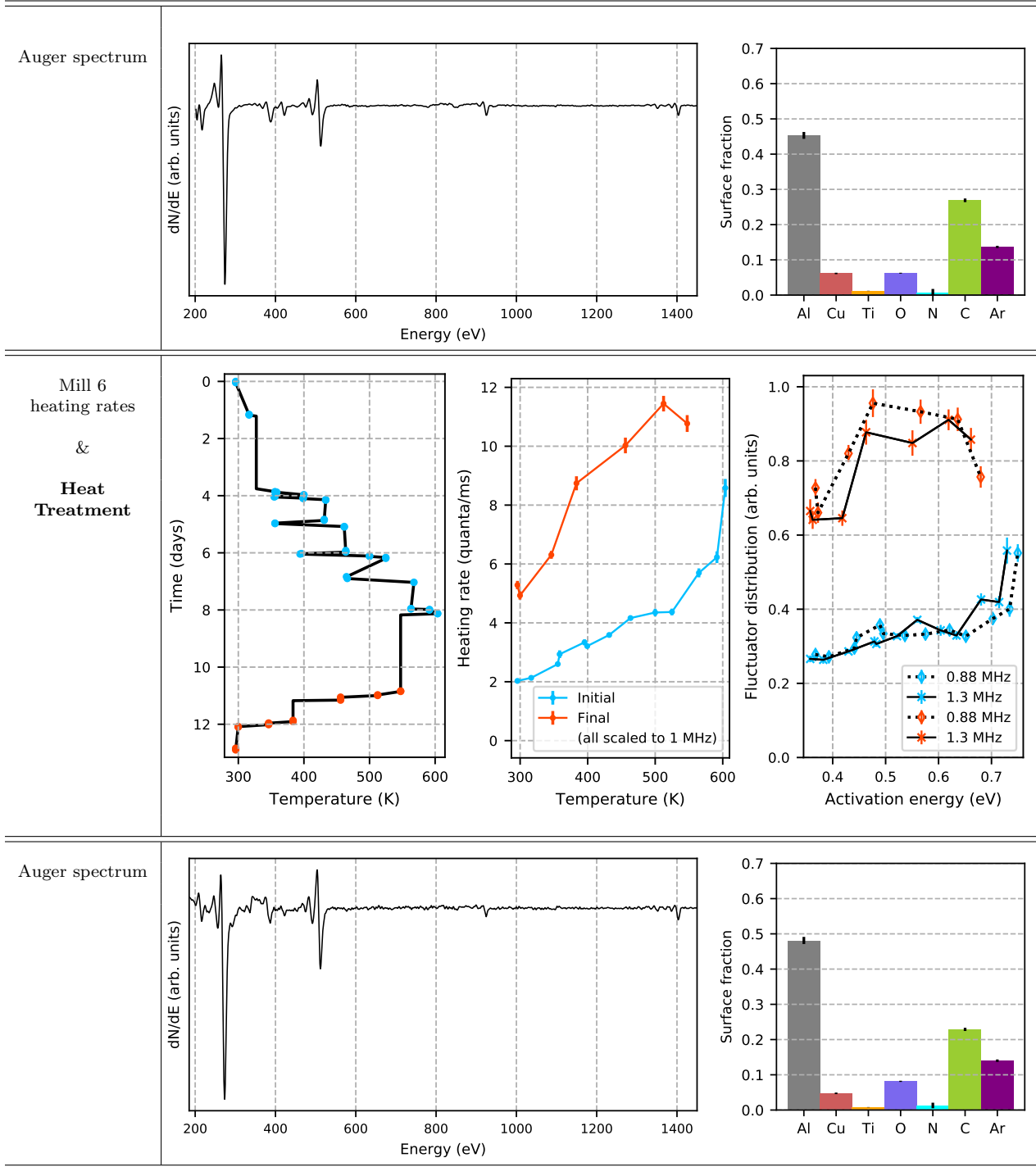


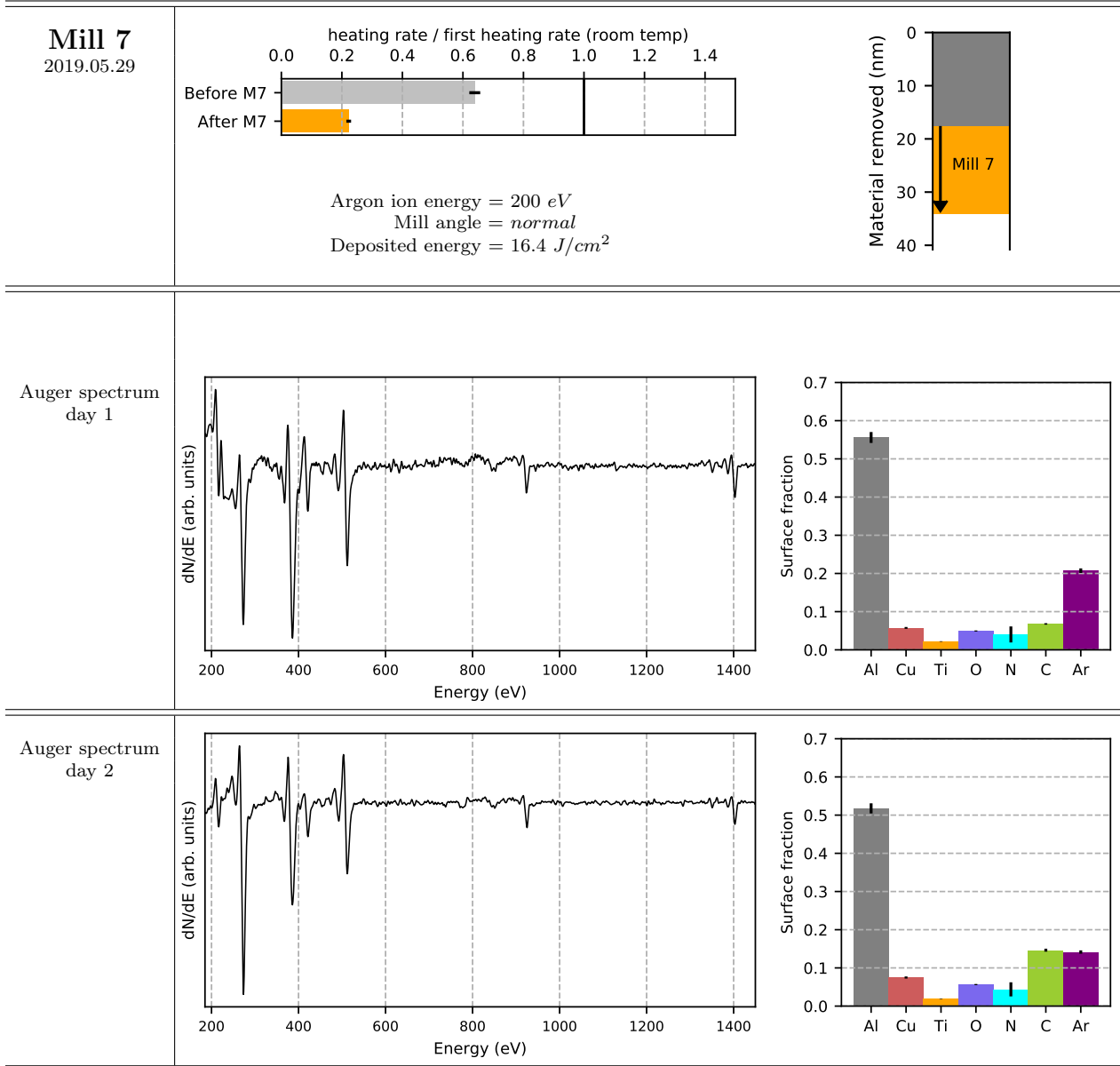


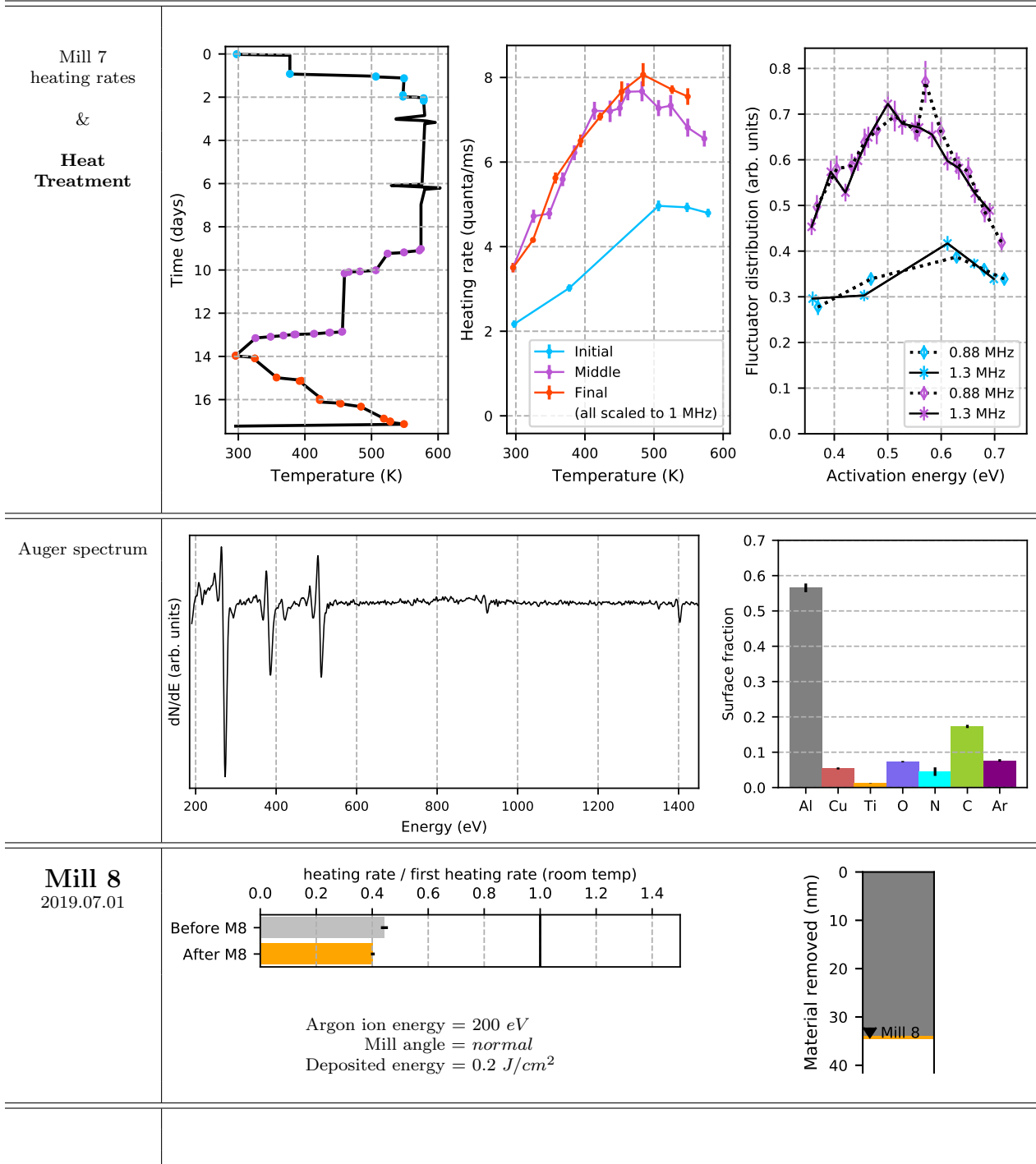


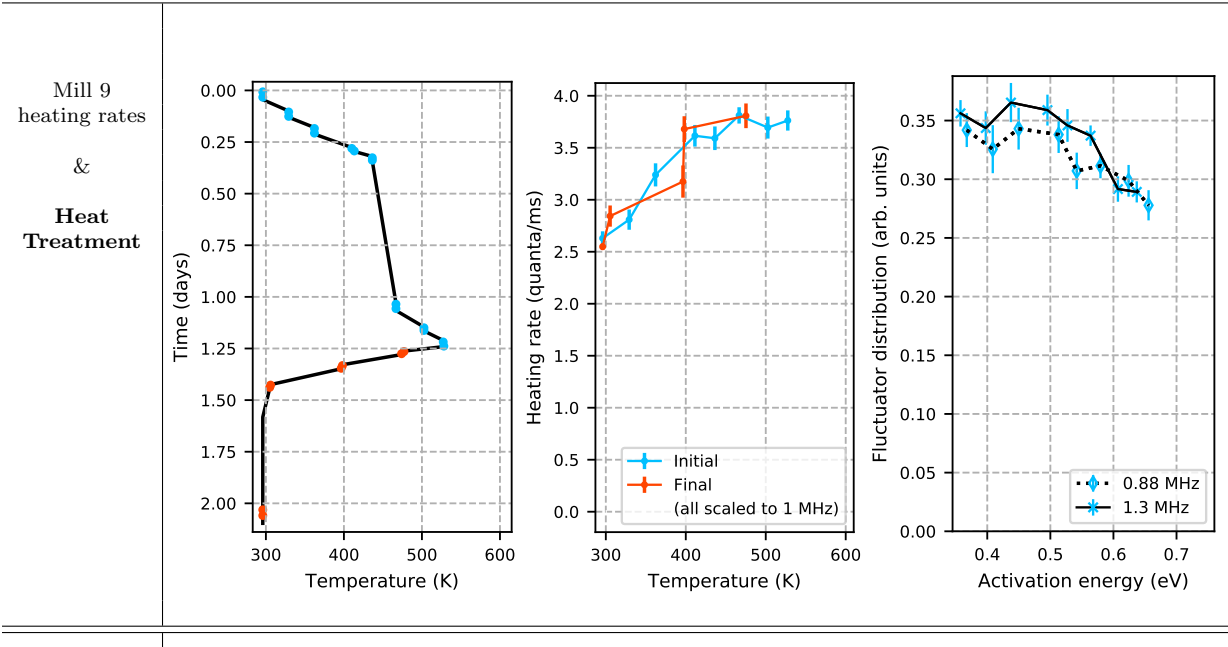
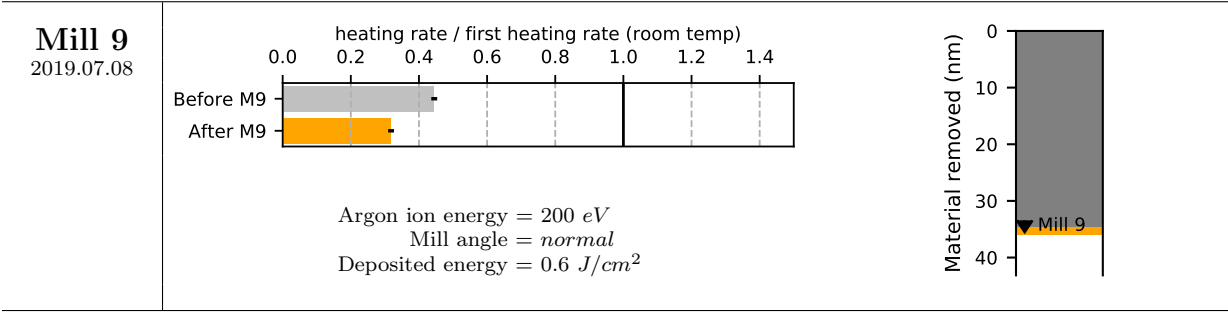
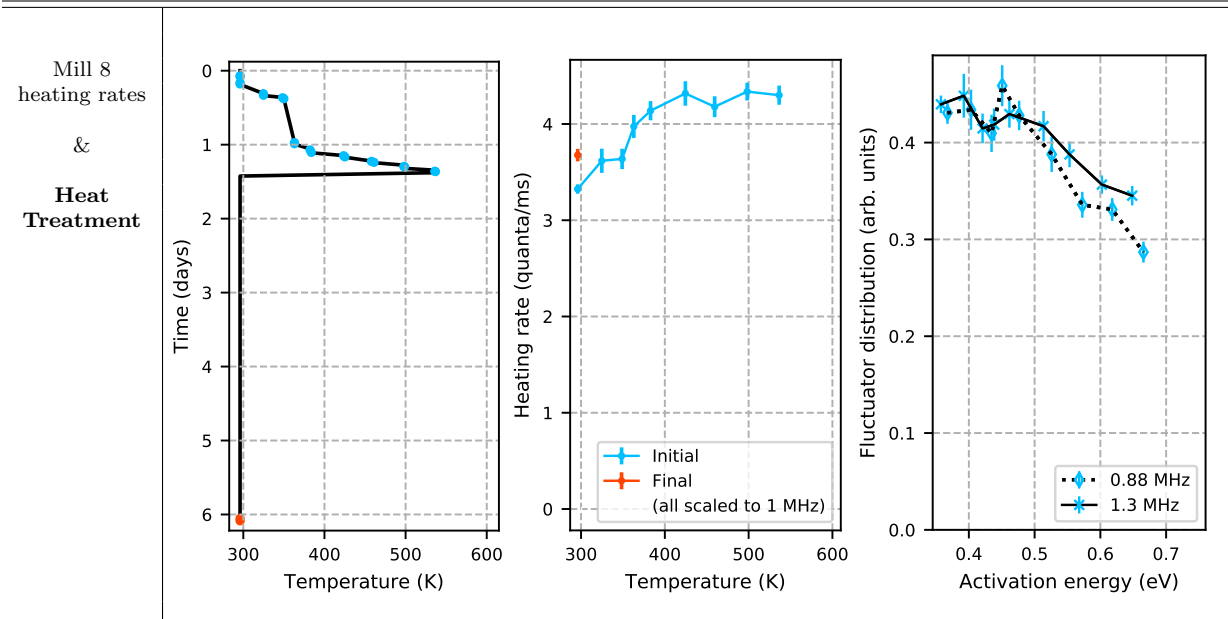




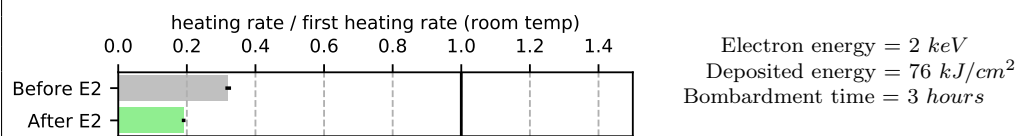




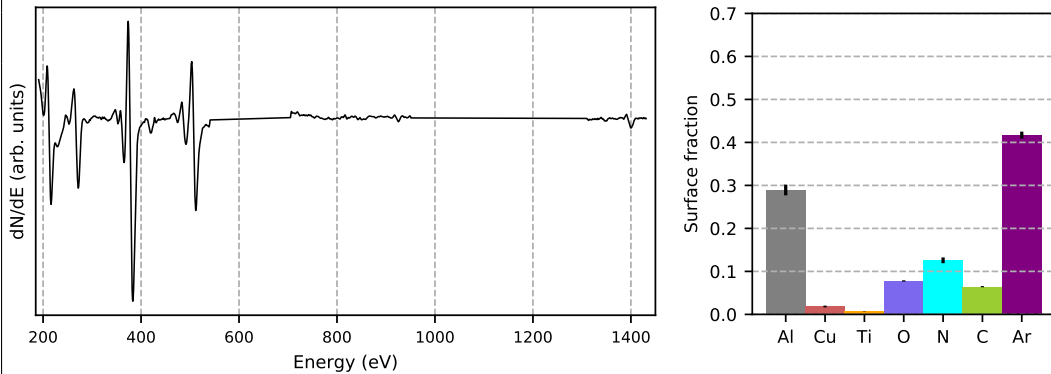




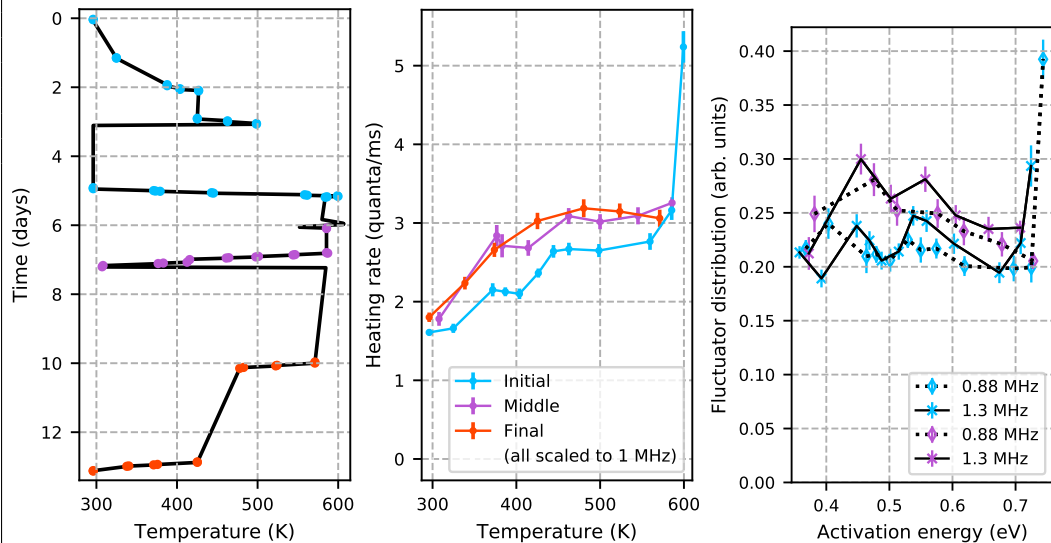
**Electron 2**  
2019.07.15



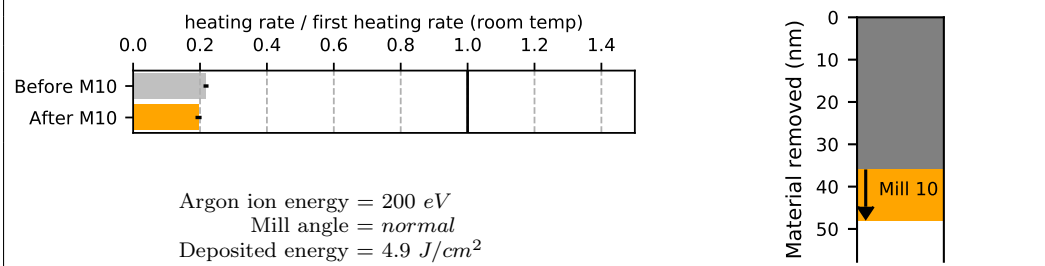
Electron 2  
Auger spectrum



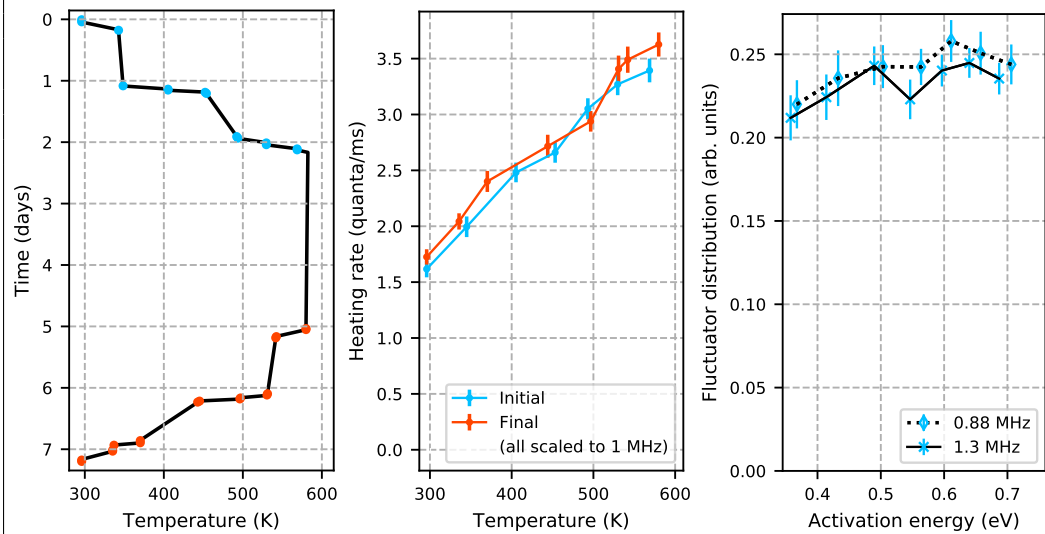
Electron 2  
heating rates  
&  
Heat  
Treatment



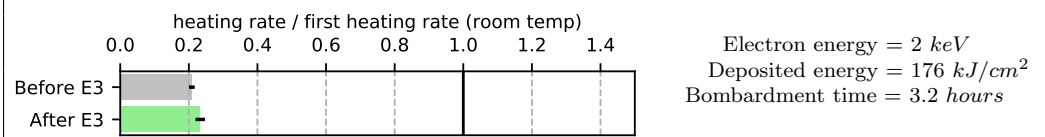
**Mill 10**  
2019.07.30



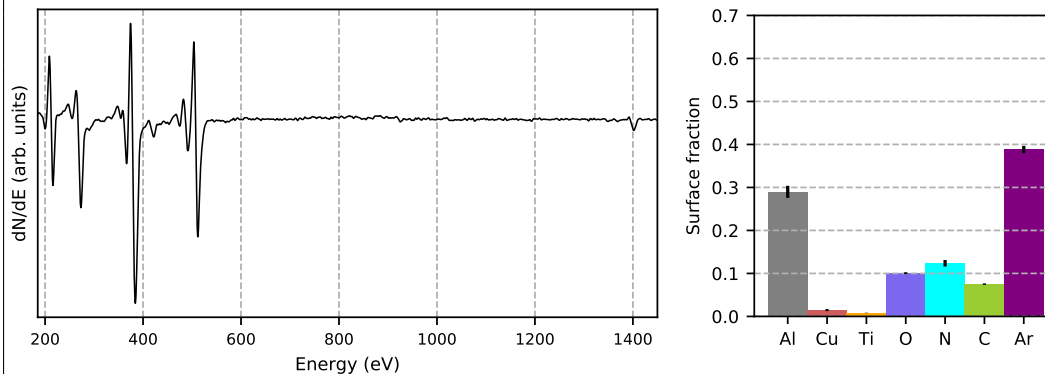
Mill 10  
heating rates  
&  
Heat Treatment

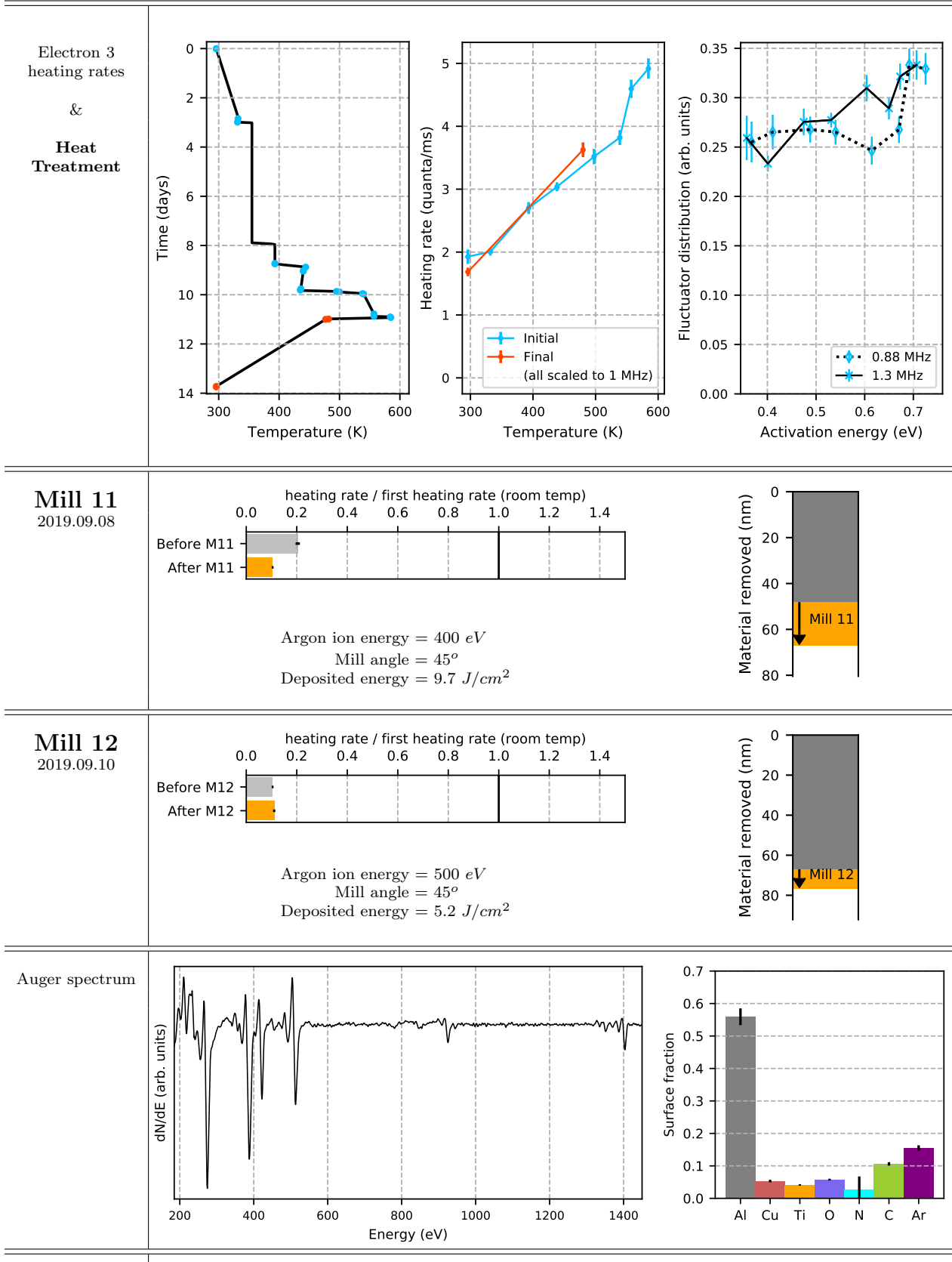


**Electron 3**  
2019.08.13

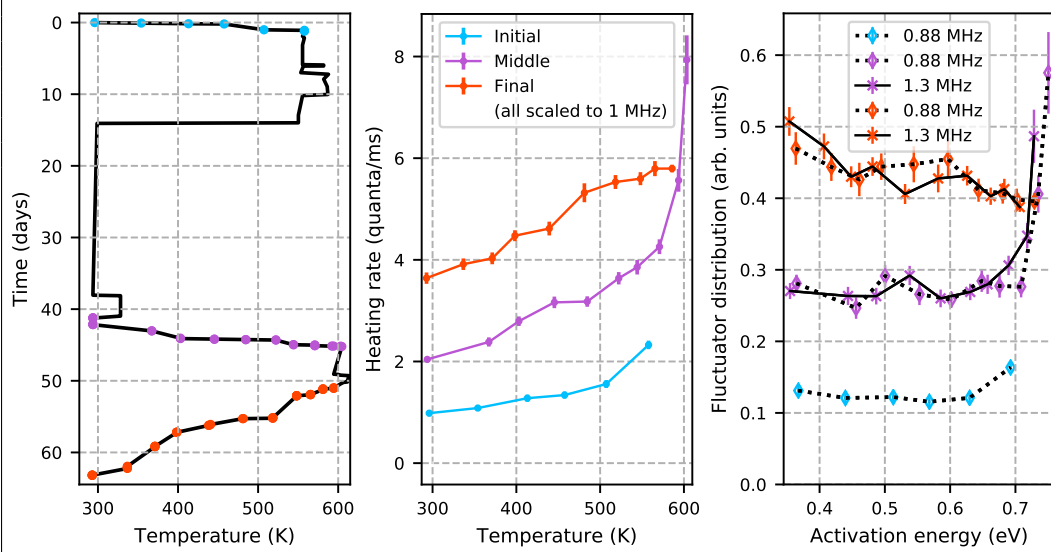


Electron 3  
Auger spectrum

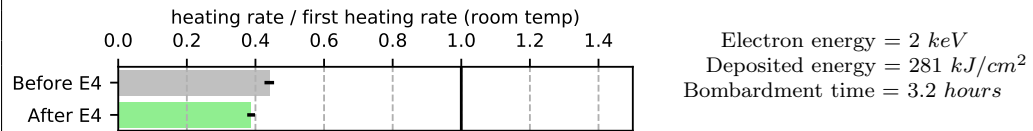




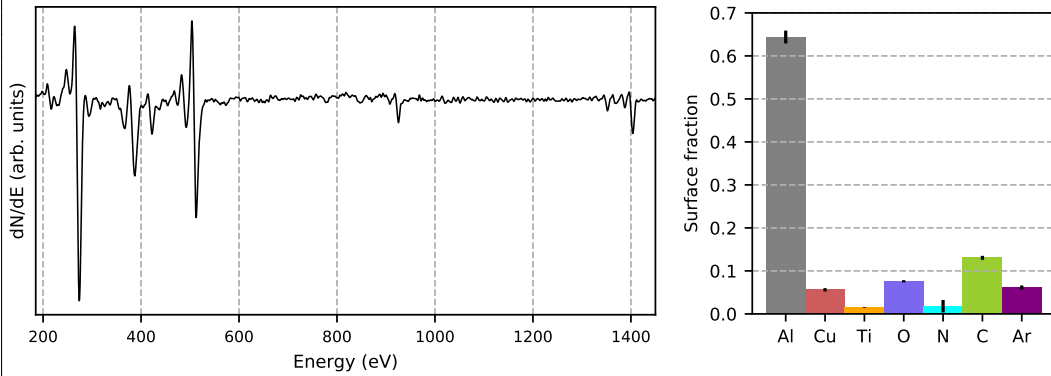
Mill 12  
heating rates  
&  
**Heat Treatment**

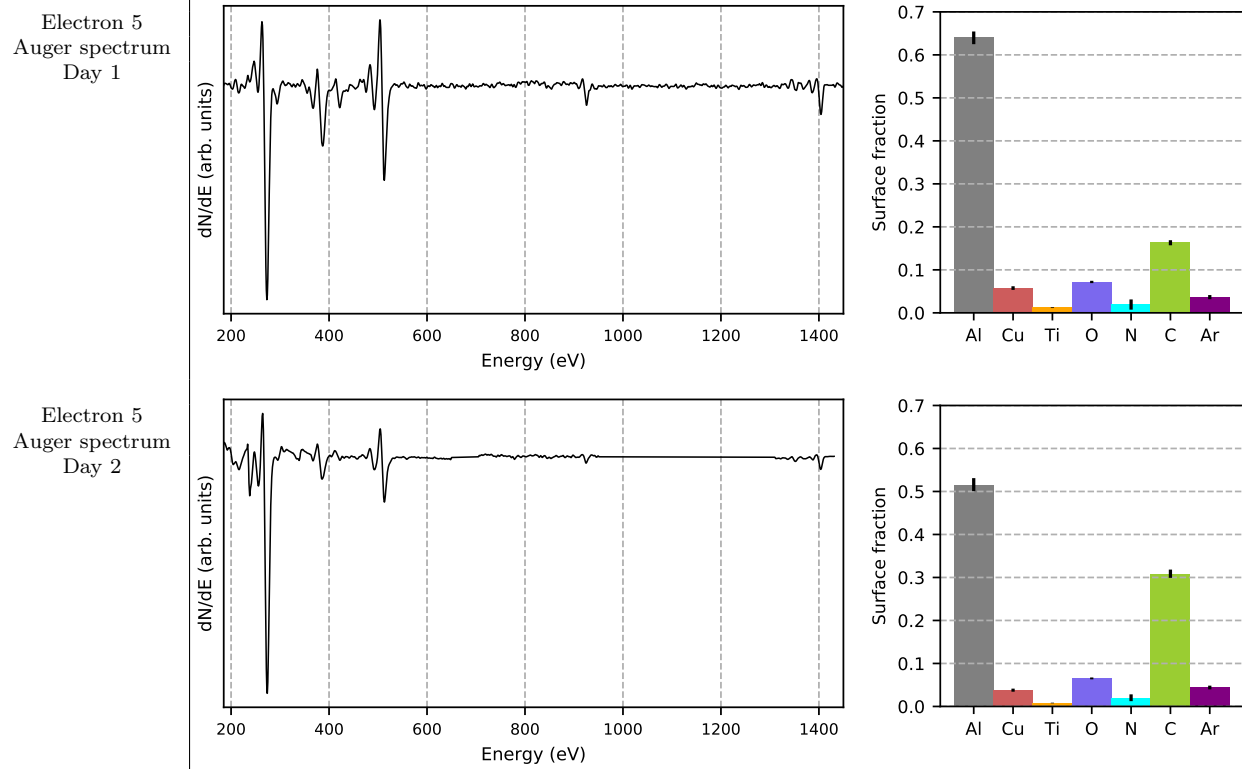
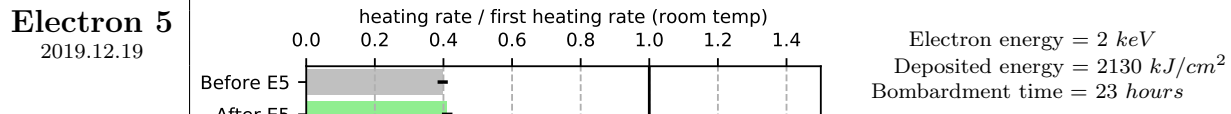
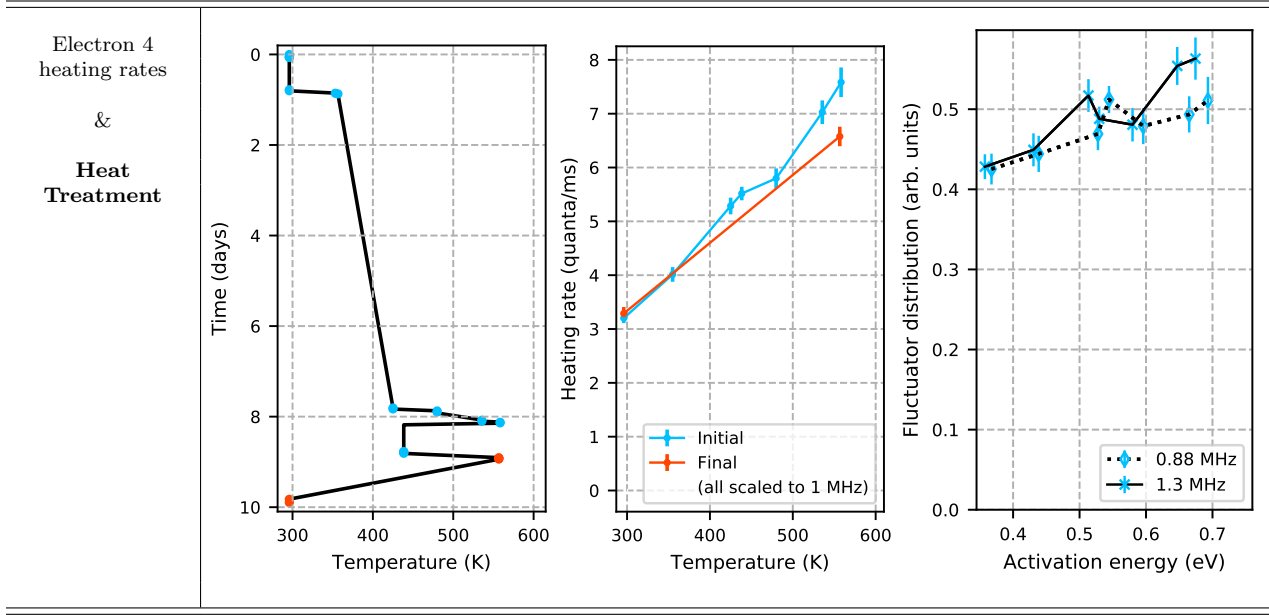


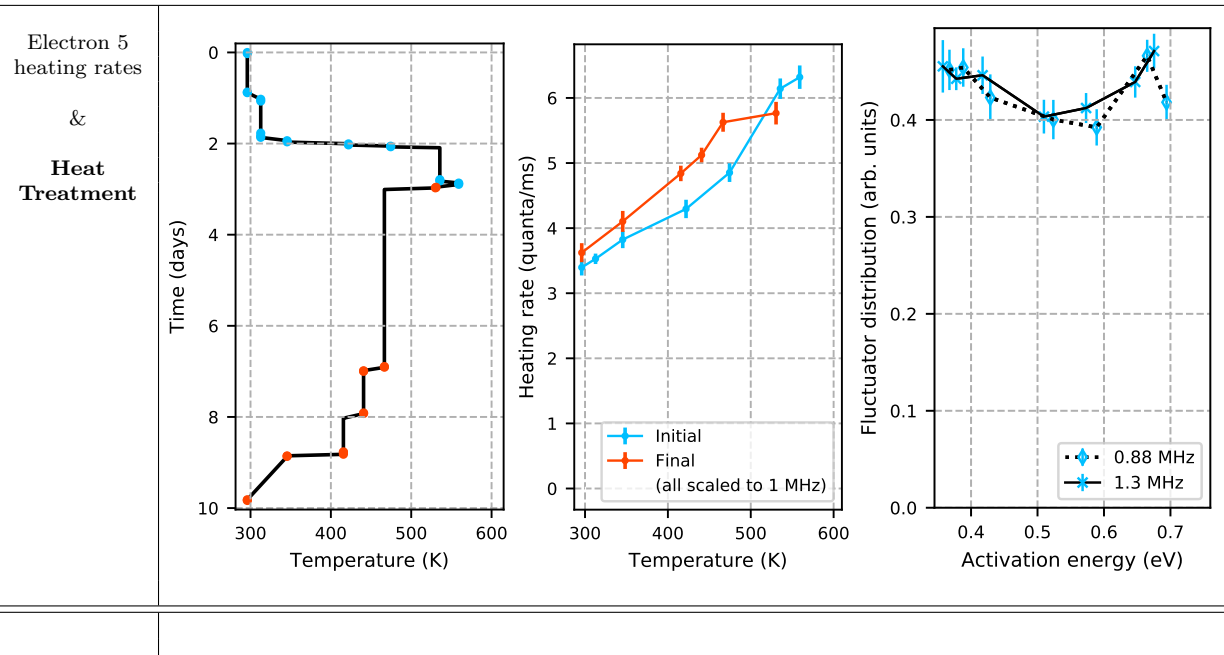
**Electron 4**  
2019.12.06



Electron 4  
Auger spectrum







# Chapter 8

## Heating rates in different aluminum-copper traps

Ion traps throughout the world have produced a widely varying and unpredictable range of heating-rate measurements [1]. Researchers have experimented with different trap materials and surface treatments, but little attention has paid to how variations in the ion-trap handling and fabrication process affect the electric-field noise in a trap.

We compare four Al/Cu ion traps that were fabricated and operated by members of the Häffner lab  collaboration with Translume. We find that the untreated Al/Cu traps have significantly different noise magnitudes, and that they also respond differently to surface treatments. We examine and compare these behaviors to determine their root causes in the fabrication and handling process. By doing so, we gain insight into where the noise is coming from, and how the noise quality of an ion trap can be controlled.

### 8.1 Background on four aluminum/copper ion traps

All of the measurements and surface treatments discussed in this dissertation, outside of the present chapter, took place on a single ion-trap chip. In this chapter, the ion trap from those experiments will be referred to as TRAP C. TRAP D was fabricated  together with TRAP C and operated in parallel in a second ion-trap experiment chamber . Experiments with TRAP A, TRAP B, and TRAP C took place at different times in the same ion-trap experiment chamber with the same ion-milling gun, Faraday cage, auger spectrometer, and trap manipulator.

All four of these traps were fabricated using identical materials, methods and facilities. Variations in trap geometries are summarized in Table 8.1, along with references where additional details of each trap can be found. This table also includes (scaled) heating rates measured in each trap. All heating rates reported in this chapter were taken at room temperature. Heating rates have been scaled to trap frequency of 1 MHz using the power law scaling:

$$\Gamma \propto f^{-2} \tag{8.1}$$

where  $\Gamma$  is the heating rate and  $f$  is the trap frequency. This frequency-scaling power law has been confirmed experimentally in all traps under discussion. Heating rates have been

scaled to a 72  $\mu\text{m}$  ion height using the power law scaling:

$$\Gamma \propto d^{-\beta} \quad (8.2)$$

where  $d$  is the ion height, and  $\beta$  is the distance-scaling exponent.  $\beta$  has been measured to be between 2.5 [7] and 4 [8]. Since  $\beta$  could not be measured in TRAP A or TRAP B where distance re-scaling is necessary, the error in the scaled heating rate accounts for both previously-measured values of  $\beta$ .

For example, if  $\beta=4$ , the TRAP A, pre-treatment, 1 MHz heating rate scales to  $0.54 \pm 0.03$  quanta/ms. If  $\beta=2.5$ , this heating rate scales to  $0.33 \pm 0.02$  quanta/ms. From this, we know the correctly scaled heating rate is likely between .31 and .57 quanta/ms. The  heating rates presented in Table 8.1 reflect this uncertainty.

Table 8.1: Ion trap comparison

Trap	Trench width x depth ( $\mu\text{m}$ )	Ion height ( $\mu\text{m}$ )	Ion trap chamber	Metal deposition date	Scaled heating rate (quanta / ms)
TRAP A [13]	10 x 100	100	Häffner_1	2012	$0.44 \pm 0.13$
TRAP B [48]	10 x 100	50	Häffner_1	2014	$0.33 \pm 0.13$
TRAP C	20 x 50	72	Häffner_1	2016.06.29	$5.7 \pm 0.20^*$
TRAP D [49]	20 x 100	70	Häffner_2	2016.06.29	$0.79 \pm .05$

\* Scaled initial heating rate

Heating rates measured in each of the four Al/Cu ion traps, and scaled to 1 MHz, are plotted in Figure 8.1. This plot also includes a survey of ion-heating-rate measurements compiled by Brownnutt et. al. in 2014 [1]. The black points mark measurements performed in untreated traps, and the grey points mark measurements performed after the trap surface had been treated.

The trap size on the  $x$ -axis corresponds to what we have referred to as the ion height. The dotted lines in Figure 8.1 indicate a distance scaling of  $\beta = 2$ , and the shaded and unshaded regions correspond to a distance scaling of  $\beta = 4$ . As shown in this plot, Häffner Lab Al/Cu traps perform well as compared with other ion traps.

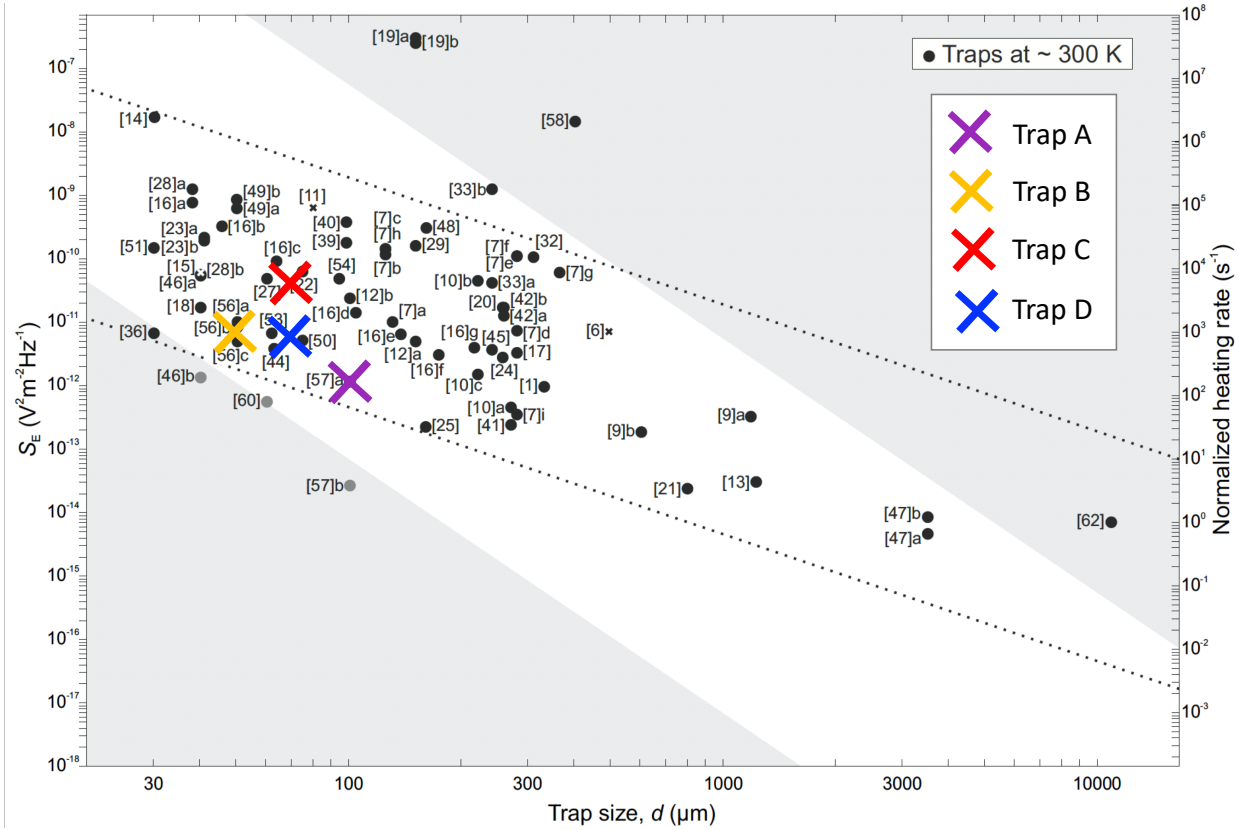


Figure 8.1: Heating rates in TRAP A, B, C, and D before surface treatments, scaled to 1 MHz. Data from these traps is shown in context with a 2014 survey of ion heating rates compiled by Brownnutt et. al. in 2014 [1].

## 8.2 Linking fabrication process variations & heating-rate magnitudes

Fabrication and measurement details specific to TRAP C can be found in Chapter ???. The basic procedure common to all traps is outlined here, followed by a discussion of which steps in the process may vary between traps, and how these variations may affect the electric-field noise.

**Step 1:** Pattern trenches into fused-silica chip  
(performed by Translume, Ann Arbor, MI [25])

- Laser weakening
- Hydrofluoric acid etch

**Step 2:** Deposit metal onto surface of the chip  
(performed at Berkeley Marvell Nanolab, Class100 clean room)

- Piranha bath removes organic contaminants
- Electron-beam evaporation, 45° to normal, pressure =  $10^{-8}$  to  $10^{-7}$  Torr
  - 15 nm Ti

- 500 nm Al
- 30 nm Cu
- Expose trap to atmosphere to manually rotate 180°
- Electron-beam evaporation, -45° to normal
  - 15 nm Ti
  - 500 nm Al
  - 30 nm Cu

**Step 3:** Package and store trap

(performed at Berkeley Marvell Nanolab, Class100 clean room)

- Mount trap & wirebond to chip carrier
- Store trap in atmosphere

**Step 4:** Install trap in vacuum

(performed at Häffner lab, UC Berkeley)

- Install chip carrier in vacuum chamber
- Bake vacuum chamber
  - Temperature = 160 to 180° C
  - Pressure during bake =  $10^{-8}$  to  $10^{-7}$  Torr

**Step 5:** Trap ions & take measurements

(performed at Häffner lab, UC Berkeley)

**Step 6:** If issues arrise with trapping or measurement: break vacuum, repair, & repeat Steps 3, 4 & 5

While there may be variations in **Step 1** that we are not aware of, all traps arrive at Berkeley with optically-smooth surfaces. In **Step 2**, the piranha bath cleaning process is repeated as needed until there is no dust or other contaminants visible on the surface of the trap. We do not think that these process variations affect electric-field noise properties.

Metal deposition in **Step 2** is always performed using the same CHA Solution e-beam evaporator, but a range of variations are inevitable during this process. The pressure in the evaporation chamber is anywhere between  $5 \times 10^{-7}$  and  $5 \times 10^{-6}$  Torr. The metal deposition rates vary within a factor of 3 (see more details in Chapter ??), and the atmosphere exposure between metal deposition steps can last from minutes to days. Intuitively, we would expect these variations to have a major effect on film quality and thus electric-field noise. However, we have found no evidence of this. The metal deposition process for TRAP A and C was identical, as they were mounted, coated, rotated, and recoated together. While variations in these processes may affect electric-field noise, the fact that TRAP B and TRAP C have such different noise magnitudes indicates that these effects are not dominant in our system.

Ion-trap measurement-system variations can have a significant impact on **Step 5** because electric-field noise measurements in ion traps can vary due to sources of noise that do not come from the trap surface. Technical noise is a particularly common limitation in ion trap systems. All of the electric-field noise measurements presented here were confirmed to be limited by surface noise, not technical noise. As shown in Table 8.1, measurements of TRAP A, B, and C were taken in the same ion trapping chamber. All four traps were measured with the same laser systems, though some upgrades and changes were made between when TRAP A and B were measured and when TRAP B and C were measured several years later.

The baking process, as described in **Step 4**, varies significantly between traps, yet does not appear to have a significant effect on pre-milling electric-field noise. TRAP A was baked at the lowest temperature, and TRAP B at the highest. The data in Figure 8.2a shows no correlation between the electric-field noise magnitude and the number of baking weeks. Both TRAP B and TRAP C were re-exposed to atmosphere and re-baked due to problems with vacuum systems and electronics (**Step 6**). The data in Figure 8.2b shows no correlation between the electric-field noise magnitude and the number of times the trap was exposed to atmosphere and baked.

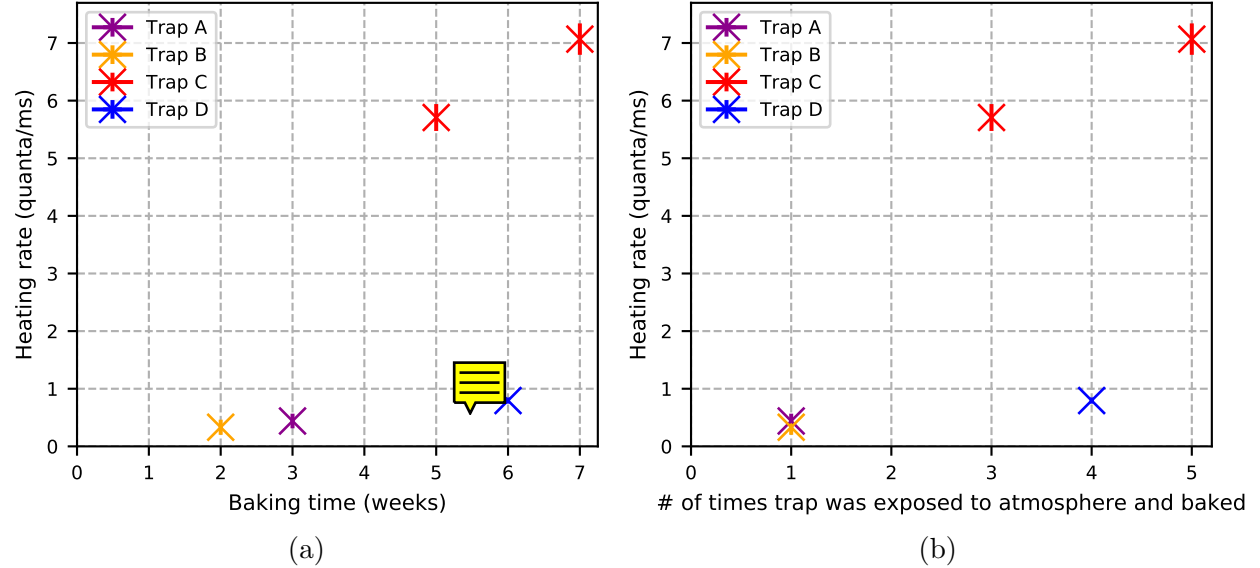


Figure 8.2: (a) Heating rates are not proportional to the number of weeks that the traps were baked in vacuum. (b) Heating rates are not proportional to the number of times the trap was exposed to atmosphere and baked.

Of all of the process variations that we tracked, only one was correlated with the electric-field-noise magnitude: the amount of time that the trap was stored in atmosphere during **Step 3** (after metal deposition). This is shown in Figure 8.3a. To confirm that the traps do not simply degrade over time, or as a result of the ion-trapping process, we also plot measurements from TRAP D taken in vacuum many months apart in Figure 8.3b.

We have demonstrated that the heating rate in TRAP C may have increased due to the trap's prolonged exposure to atmosphere. If the contaminant atoms are the primary source of electric-field noise, then the accumulation of contaminants from the air could explain why the heating rate of TRAP C was 1% greater than the heating rate of TRAP A.

We will explore this hypothesis further by comparing how the compositions of TRAP A and C change as the surface is milled away. This will give an indication of how the contaminant levels in the two traps compare.

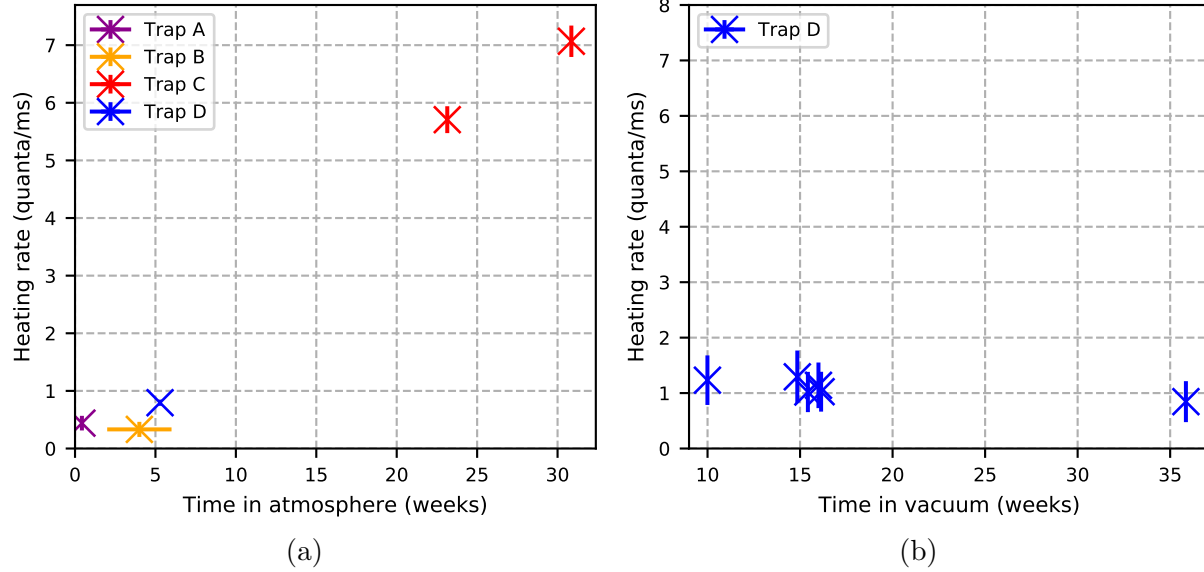


Figure 8.3: (a) Heating rates are correlated with atmosphere exposure time post metal deposition. (b) Heating rates do not increase over time as the trap is operated in vacuum.

### 8.3 Material removal & changes in surface composition

As shown in Figure 8.4, the surfaces of both TRAP A and C contained high levels of air-borne contaminants before in-situ argon milling was performed. The amount of contamination on TRAP A (after 3 days of atmosphere exposure) was lower than the amount of contamination on TRAP C (after 30 weeks of atmosphere exposure), as expected.

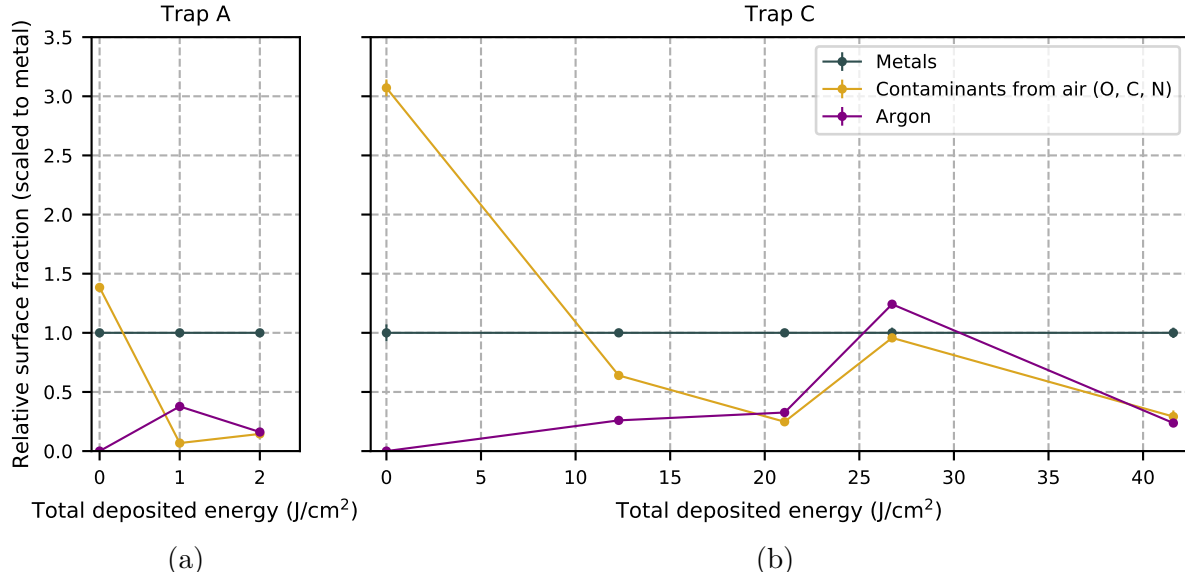


Figure 8.4: Depth profiles, measured through alternating Auger spectroscopy and argon ion milling, of (a) TRAP A [13], and (b) TRAP C.

After 1  $\text{J}/\text{cm}^2$  of argon ion milling, the amount of air-borne contamination on the surface

of TRAP A shrank considerably. This data is plotted in Figure 8.4a. The contaminant fraction reported here represents an upper bound on the amount of contamination present in the bulk of the trap, as the process of measuring an Auger spectrum deposits carbon onto the trap surface.

Relative contaminant fractions measured between milling steps in TRAP C are plotted in Figure 8.4b. The cumulative argon milling dose deposited into this trap was greater than the dose deposited into TRAP A by a factor of twenty, yet its contaminant levels never became as low as those observed in TRAP A.

This data supports the hypothesis that TRAP C was considerably more contaminated than TRAP A, but these differences in the post-milling contaminant levels may not be caused entirely by atmosphere exposure. Unlike TRAP A, TRAP C was heated to temperatures as high as 600 K before and between when these surface fraction measurements were taken. These heat treatments may have caused contaminants to diffuse deep into the bulk of the metal trap.

Evidence for the mixing of metals in TRAP C, likely drive by heat treatments, can be found in Figure 8.5. When the metals are fully mixed, the ratios of the Al:Cu:Ti surface fractions are 35:3:1. Copper is deposited last, and Auger spectroscopy is sensitive only to atoms within the top 5 nm of the surface. As a result, the copper fraction is disproportionately large when the metals are not fully mixed.

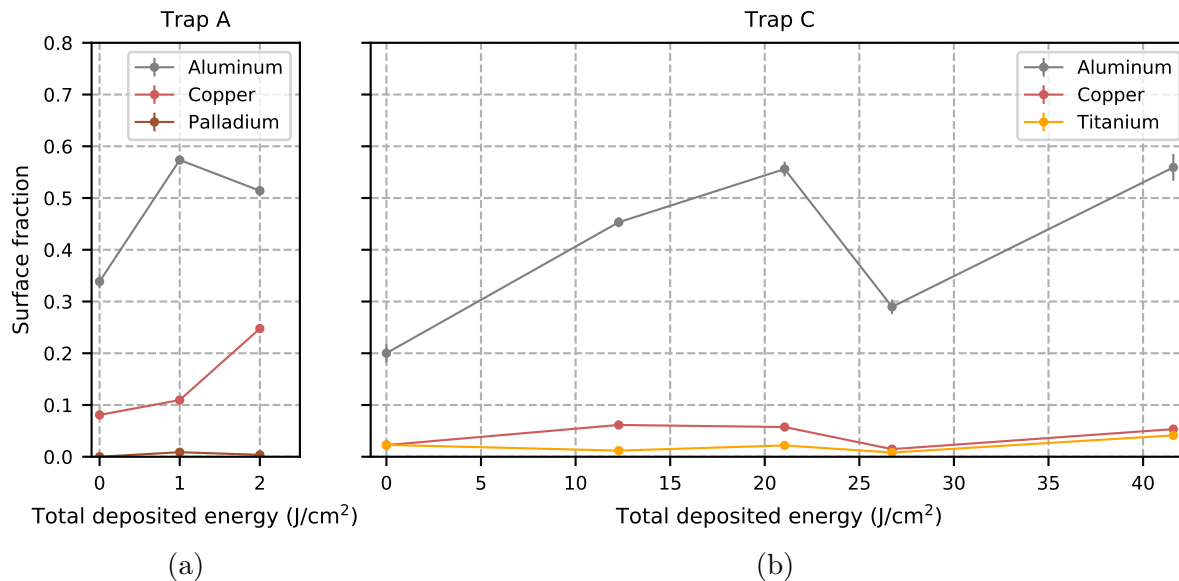


Figure 8.5: Surface fractions of all metals. (a) TRAP A, and (b) TRAP C.

As shown in Figure 8.5a, TRAP A had a large amount of copper at its surface. This indicates that the metals were not fully mixed. In TRAP C, the ratio of copper to aluminum was much smaller, indicating the metals were much more thoroughly mixed. The titanium present in TRAP C may originate from both the electron-beam-deposited titanium sticking layer and the titanium sublimation pump.

Figure 8.6 shows the fractions of surface contaminants carbon, oxygen and nitrogen as a function of milling dose in TRAP A and C. Although argon is present in the bulk after ion

milling, it is not considered to be in the category of surface contaminants. Argon is a noble gas. It can be embedded in the bulk, but it will not bind with the surface.

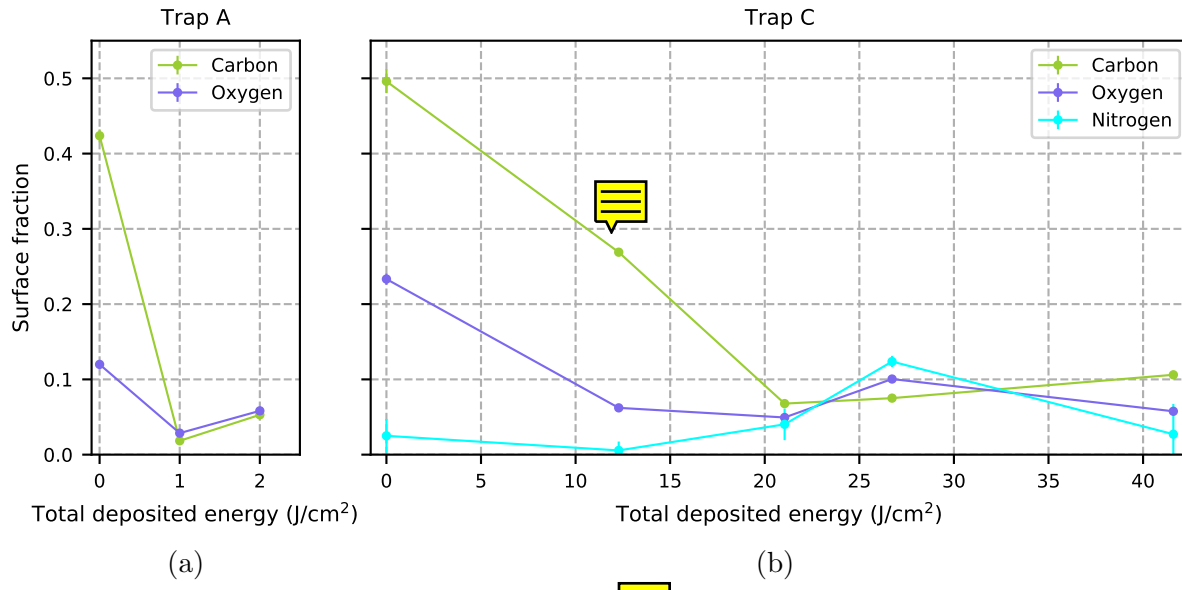


Figure 8.6: Surface fractions of all surface from the air. (a) TRAP A, (b) TRAP C.

The data presented in Figure 8.6 represents a convolution of contaminants incorporated into the metal film during metal deposition, atmosphere exposure, Auger spectroscopy, argon milling and UHV gas build up. The lowest surface fractions of all contaminants were achieved after 1.1 J/cm<sup>2</sup> of milling in TRAP A.

## 8.4 Material removal & ion heating rate reductions

We have demonstrated that TRAP A and TRAP C differed in their pre-treatment heating rates, and in their overall contamination levels. The data plotted in Figure 8.7 shows that TRAP A traps also differed in their responses to argon milling. After 20 nm of milling in TRAP A, the heating rate dropped by two orders of magnitude down to 0.007 quanta/ms. In contrast, after almost 35 nm of milling in TRAP C, the heating rate dropped by less than 1 order of magnitude down to 0.01 quanta/ms.

Compared to TRAP A, TRAP C was exposed to atmosphere for longer, which most likely added contaminants. TRAP C also was heated longer and to higher temperatures, which likely drove contaminants into the bulk of the metal. This can explain why there was always more contamination at the surface of TRAP C than at the surface of TRAP A, despite extensive milling.

The constant presence of contamination at the surface of TRAP C can explain why heating rates in TRAP C did not drop to the same level after milling as the heating rates in TRAP A. However, surface contamination alone cannot explain why the difference in the post-milling heating rates of the two traps was so large. Although TRAP C began with a higher contaminant fraction and a higher heating rate, after 12 J/cm<sup>2</sup> of milling it had significantly less surface contamination than TRAP A had before milling. Yet after 12 J/cm<sup>2</sup> of milling in

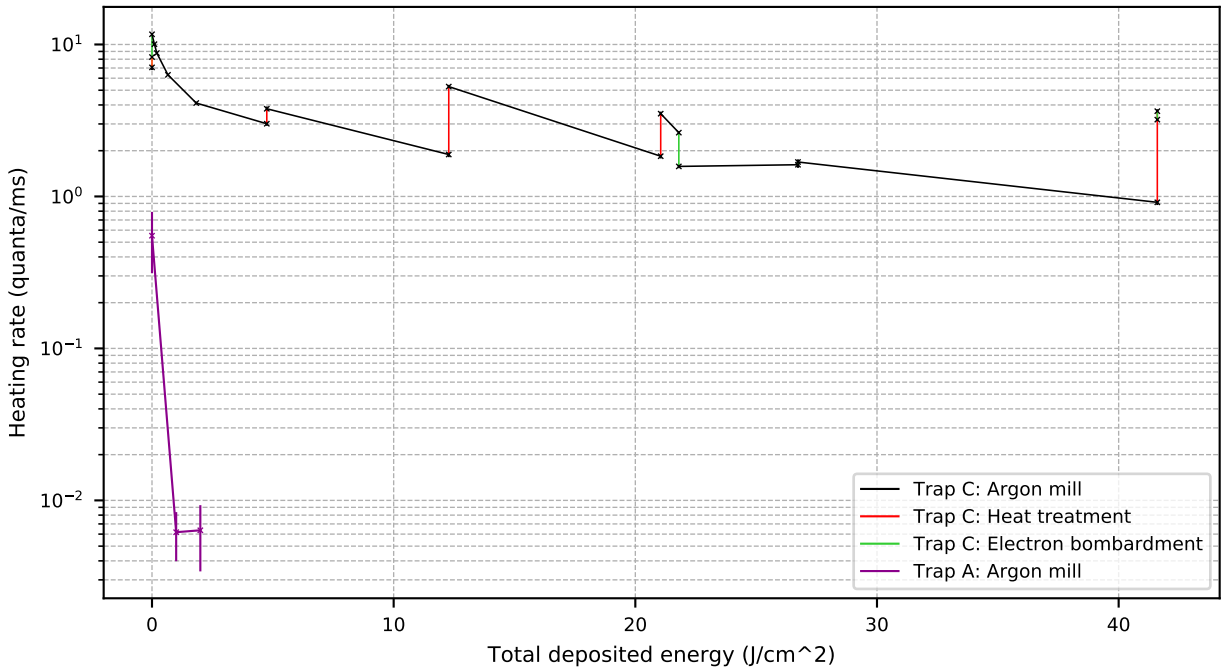


Figure 8.7: Heating rates in Traps A and C decreased as material was milled off of each surface.

TRAP C, its heating rates were almost 4 times greater than the pre-milling heating rates in TRAP A.

To explain these observations, we hypothesize that the noise in these ion traps is generated by contaminants in an extended contamination layer. After 12 J/cm<sup>2</sup> of milling in TRAP C, the surface was cleaner than the pre-mill TRAP A surface, but the bulk was far more contaminated. This is evidenced by the large contaminant fractions found on the surface of TRAP C after a large amount of additional milling.

## 8.5 Summary

In Section 8.1, we showed that the initial heating rates measured in TRAP C were higher than those measured in TRAP A. Then, in Section 8.2, we provided evidence that the heating rates in TRAP C rose due to extended atmosphere exposure. ~~The following section~~, Section 8.3, contained data on the fractional compositions of TRAP A and C, both before and after ion milling removed material from the surface. This data showed that TRAP A had less contamination than TRAP C, both before and after ion milling, indicating the presence of an extended contamination layer in TRAP C. In 8.4, we presented evidence that heating rates in TRAP A dropped in response to argon milling much more readily than in TRAP C. We hypothesized that this could be explained by noise generated from sub-surface contamination in TRAP C.

These experiments provide important considerations for those who fabricate, store and treat ion traps. Researchers should be thoughtful about whether they store their traps in atmosphere or in vacuum. Some materials build up contamination faster than others when

exposed to atmosphere, and this should be considered when choosing the material of a trap that will be shipped or stored in atmosphere.

For argon ion milling to be successful, the trap cannot be deeply contaminated, so fabrication processes should be designed to optimize for the purity of metal coatings. Aluminum is an interesting trap material in this regard, as its native oxide layer serves as a diffusion barrier to prevent extensive contamination. If this layer is milled off, the remaining surface and bulk could be very clean. Milling before baking may also be effective, as contaminants would be removed before they have had a chance to diffuse into the bulk.

# Chapter 9

## Thermal transformation of electric-field noise

This chapter will discuss the phenomenon in which a heat treatment transforms an ion trap substrate, causing ion heating rates to rise. The underlying physics of this transformation is explored through a series of heating, milling, and electron treatments performed in TRAP C.

With surface composition data from in-situ Auger spectroscopy, the behavior of the noise transformations can be correlated to the chemical state of the trap surface. These measurements allow us to rule out contaminant deposition as a possible underlying cause of noise transformations. They also allow us to more tentatively rule out heat-driven chemical reactions.

Of all hypotheses considered, only atomic restructuring is consistent with the results of all experiments. The data indicate that ion heating rates rise during thermal transformations as atoms on the trap surface restructure and reduce nanoscale surface roughness. Argon ion milling has the opposite effect on the ion heating rates by increasing nanoscale roughness. The deduction that a reduction in nanoscale roughness corresponds to an increase in ion heating rates can possibly be explained by rising noise-source correlation lengths or shifting TAF energy barriers.

All ion heating rates presented in this chapter have been scaled to a frequency of 1 MHz. This chapter will focus solely on the noise mechanisms that are dominant at  temperatures. We have excluded data from the *high-temperature shoot-off*, where a sharp rise in heating rates indicates that a different noise mechanism has begun to dominate.

### 9.1 Thermal transformation versus thermal activation

Two categories of thermal effects are relevant to electric-field noise in hot ion traps. These categories are thermal activations, and thermal transformations. When a noise source is being activated by heat, the heat is temporarily affecting its behavior. Thermally activated fluctuators, as discussed in Chapter 6, fit into this category. In contrast, when a noise source is transformed by heat, the physical properties of that noise source are changed. Transformations can include the addition and subtraction of material, chemical reactions, atomic restructuring, and more.

In TRAP C, temperature-scaling measurements of ion heating rates always had a positive slope near room temperature. This is evidence that the noise in this trap was thermally activated. When consecutive temperature-scaling measurements were significantly different from each other, this indicated that a noise transformation had taken place during the heat treatment, in addition to the always-present noise activation.

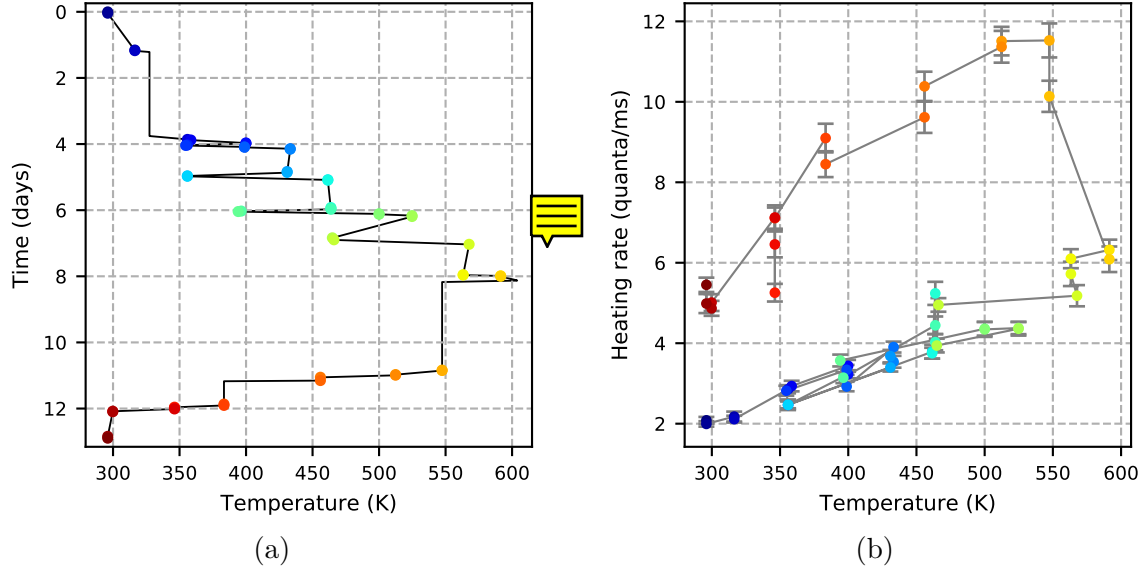


Figure 9.1: The data taken after surface treatment Mill 6 illustrate the difference between thermal activation and thermal transformation of noise. During the first seven days of the heat treatment, the noise sources were exclusively heat-activated. When the trap was held at high temperatures from Day 7 to Day 11, the activation persisted, but the noise sources were also transformed. (a) Temperature and timing of the heat treatment. (b) Ion heating-rates measured as a function of substrate temperature. To determine the time when each measurement was taken, match the color of each heating-rate data point plotted in (b) to the color of each point plotted in (a).

Examples of thermal activation and thermal transformation are shown in Figure 9.1, where data from the heat treatment following Mill 6 are plotted. During the first seven days of this heat treatment, we alternated between raising and lowering the temperature of the substrate between measurements. These measurements showed that the noise was exclusively heat-activated, as ion heating rates increased as the temperature was raised, and they decreased back to previously-measured values when the temperature was lowered. The noise transformation took place while the substrate was held at or above 550 K from day 7 to day 11. From day 11 onward, the heating rates throughout the full temperature range were elevated as compared to previously measured values.

## 9.2 Saturation of the thermal transformation effect

When the trap is held at a constant elevated temperature for an extended period of time, the noise transformation saturates. The saturation process was studied directly during the heat

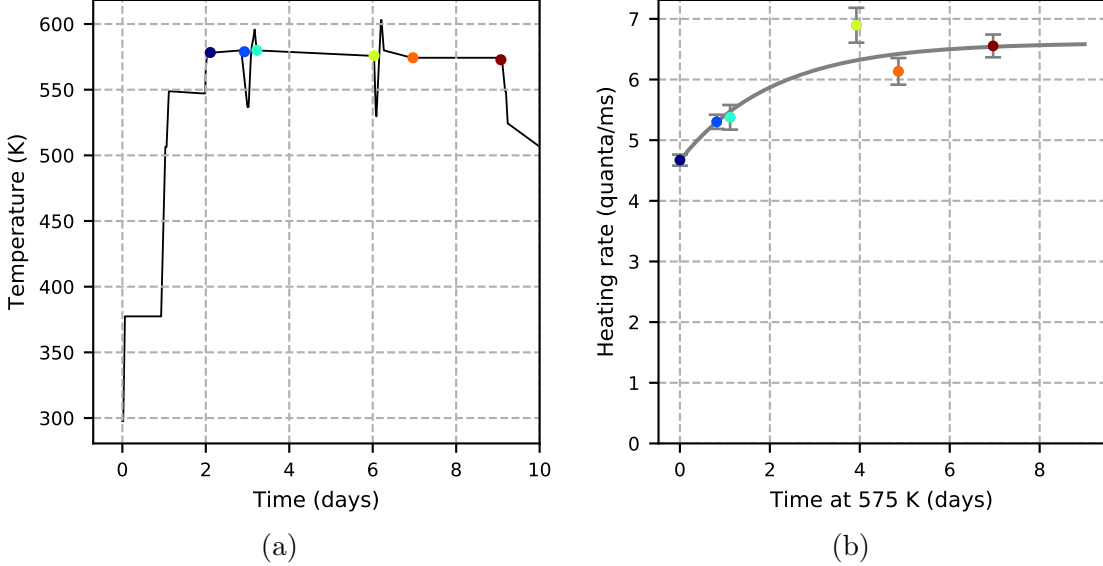


Figure 9.2: Ion heating-rates measured after treatment [Mill 7](#) while the substrate temperature was held at approximately 575 K show a saturating noise transformation with a half life of  $1.4 \pm 0.4$  days. (a) Timing and temperature of heat treatment. (b) Ion heating rates measured while the substrate temperature is held at 575 K, with a fit to [Equation 9.2](#). To determine the time when each measurement was taken, match the color of each heating-rate data point plotted in (b) to the color of each point plotted in (a).

treatment following [Mill 7](#). During this treatment, the substrate temperature was swiftly raised to 575 K, and then ion heating rates were repeatedly measured at 575 K for a full week. The parameters of this heat treatment, and the corresponding ion-heating-rate measurement results, are presented in Figure 9.2. The heating-rate measurements from Figure 9.2 were fit to [Equation 9.2](#):

$$\Gamma = \Gamma_0 + A(1 - e^{-kt}) \quad (9.1)$$

where  $\Gamma$  is the ion heating rate at 575 K,  $t$  is the amount of time spent at 575 K, and  $\Gamma_0$ , amplitude  $A$  and rate constant  $k$  are fit parameters. The half life  $\lambda$  of this transformation can be calculated directly from the rate constant  $k$ :  $\lambda = \ln(2)/k$ . At 575 K, the noise transformation process had a half life of  $1.4 \pm 0.4$  days.

During the heat treatment following [Mill 12](#), the trap temperature was raised to 555 K and held near that temperature for six days. During this time, the ion heating rate rose in a manner consistent with a saturation half life of one or two days. It appeared to be on track to saturate between 3 and 4 quanta/ms. When the trap temperature was subsequently raised above 600 K for a period of 3.5 days, however, the ion heating at 555 K rose all the way to  $5.6 \pm 0.1$  quanta/ms. This is evidence that a secondary thermal transformation was initiated at these higher temperatures.

In addition to providing direct insight into the underlying physics, understanding the temperature dependence and timescale of the transformation can help us identify which ion heating-rate measurements were taken during thermal transformations. This is important

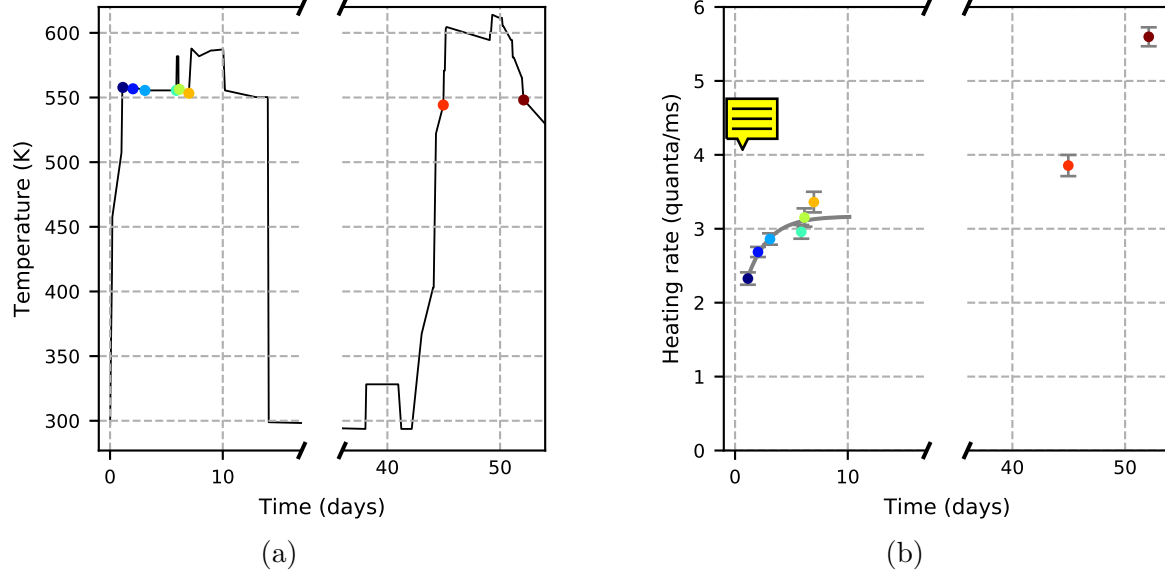


Figure 9.3: Initial ion heating-rates measured after treatment [Mill 12](#) while the substrate temperature was held at approximately 555 K are consistent with a saturating noise transformation with a half life of  $1.3 \pm 0.5$  days. (a) Timing and temperature of heat treatment. Between days 17 and 36 the trap was held at room temperature. (b) Ion heating rates measured while the substrate temperature is held at 555 K, with a fit to Equation 9.2. To determine the time when each measurement was taken, match the color of each heating-rate data point plotted in (b) to the color of each point plotted in (a).

because when a TAF distribution is calculated from a temperature-scaling, it must be assumed that the fluctuator distribution is stable. If fluctuators are transforming while a temperature scaling is being measured, the calculated TAF distribution is not a faithful representation of the true distribution.

For this reason, when we present TAF distributions and temperature scalings in this chapter, we include only data taken before or after (but not during) noise transformations. The temperature scalings labeled as *initial* were measured quickly, and the highest-temperature data has been excluded. The temperature scalings labeled as *final* were measured after the transformation had most likely saturated. For details on the parameters of the heat treatments corresponding to the thermal transformations presented in this chapter, refer to Chapter [7](#).

### 9.3 Insights from argon ion milling

After a thermal transformation process saturates, the surface can be reset by argon ion milling. To reset the surface means to reduce the heating rates back to (or below) pre-transformation levels, as shown in Figure 9.4a. When the surface is reset it is also primed for further thermal transformation to take place. The ability to reset and repeat the transformation process enables us to study this phenomenon under a variety of different conditions. In addition, the knowledge that heating and milling have counteracting effects on ion heat-

ing rates can directly inform our investigation of how these treatments drive changes in microscopic noise sources.

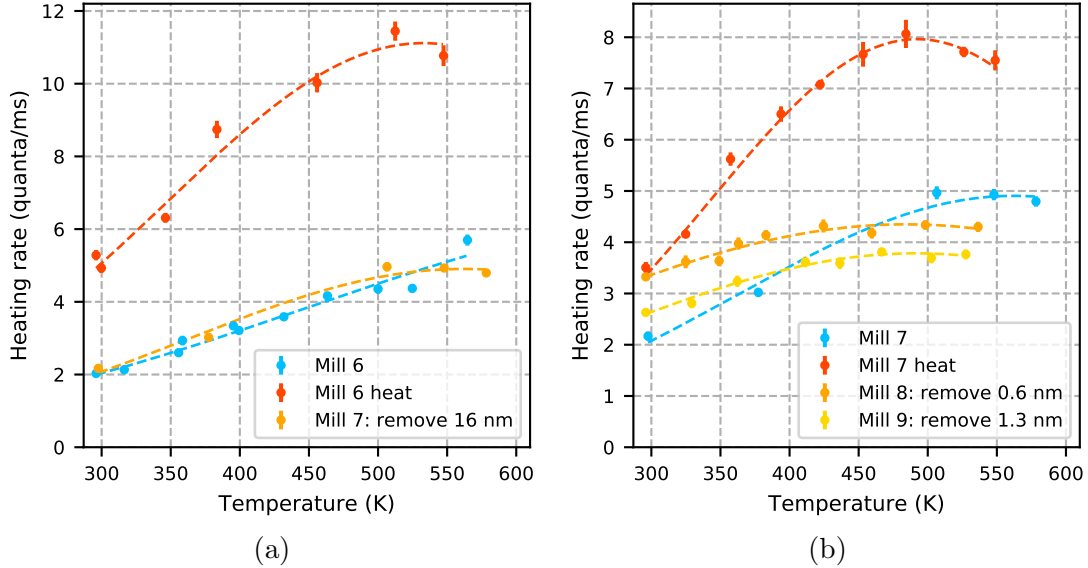


Figure 9.4: The effect of large and small milling doses on a thermally-transformed temperature scaling. (a) Temperature scaling after Mill 6, after the subsequent thermal transformation, and temperature scaling after Mill 7. (b) Temperature scaling after Mill 7, after the subsequent thermal transformation, and temperature scalings after Mill 8 and Mill 9 .

While annealing can alter both the bulk and the surface of a material, low-energy argon ion milling can only affect the surface. According to our simulations using the SRIM software [37], the 200 eV ions in surface treatments Mill 8 and Mill 9 only penetrated 2 nm into the metal surface of the trap substrate. These treatments removed 0.6 and 1.3 nm of material respectively. As shown in Figure 9.4b, these milling treatments were performed immediately after a noise transformation, and they had a major impact on the temperature scaling. The observation that a cumulative removal of 2 nm of material can almost entirely reverse the effects of the heat treatment is evidence that thermal transformations primarily affect noise originating from the surface of the ion trap.

## 9.4 Intermittent transformations

Over the course of its life, TRAP C was heated dozens of times to temperatures greater than 560 K. As shown in Figure 9.5, thermal transformations occurred intermittently. Figure 9.5 displays a representative set of heat treatments, including every thermal transformation observed throughout the surface treatment experiments described in Chapter 7.

Details of the precise timings and temperatures of all heat treatments are plotted in Chapter 7, and a summary of the heat treatment parameters can be found in Table 9.1. Although the parameters were different in each heat treatment, in all ten of the experiments

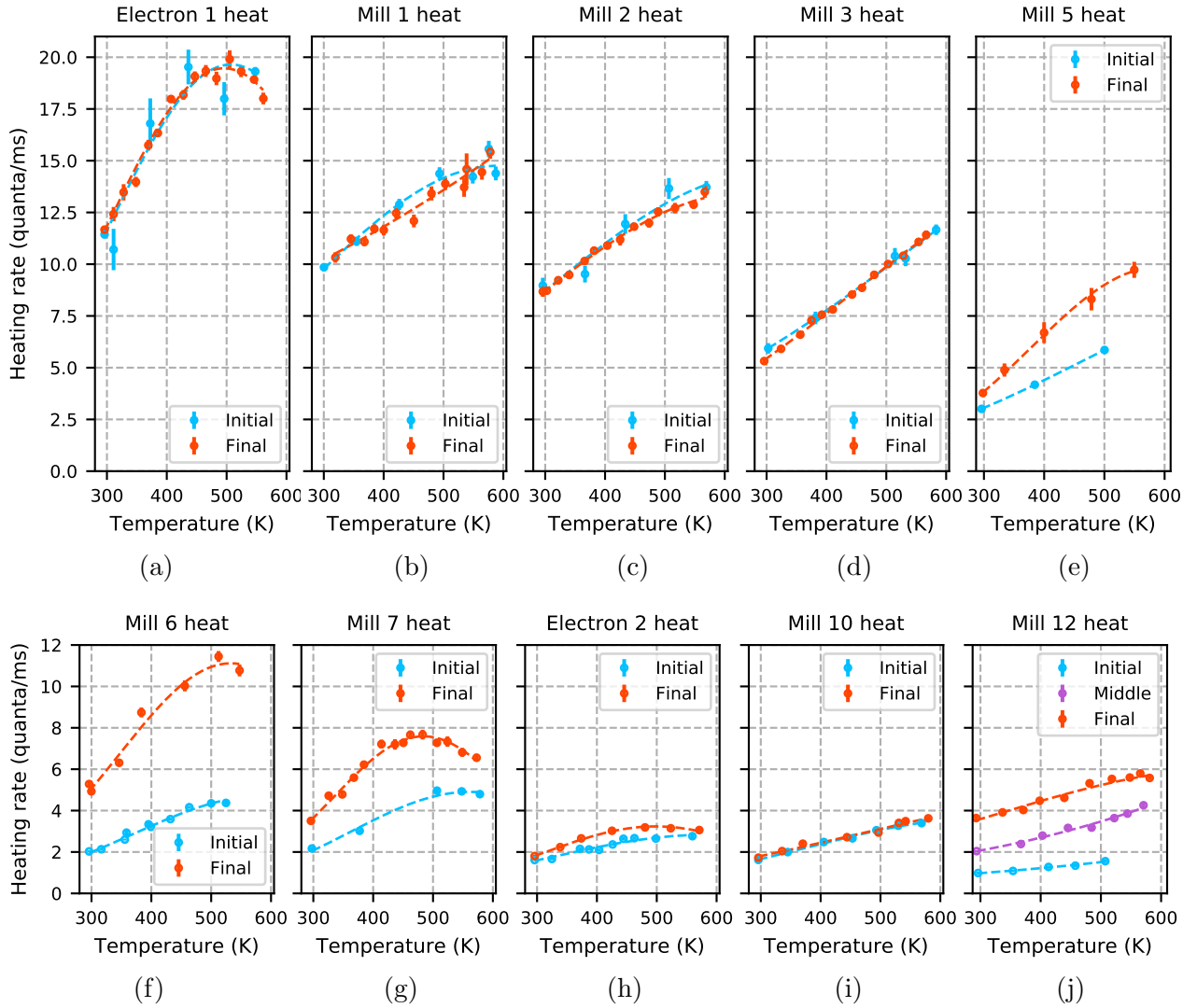


Figure 9.5: Temperature scalings measured after electron and milling treatments show intermittent thermal transformations of the noise sources. The first thermal transformation took place after a total of 6.3 nm of material was removed from the surface via argon ion milling. These temperature scalings were measured after: (a) Electron 1, (b) Mill 1 (0.13 nm material removed), (c) Mill 2 (0.26 nm total material removed), (d) Mill 3 (0.86 nm total material removed), (e) Mill 5 (6.3 nm total material removed), (f) Mill 6 (17.7 nm total material removed), (g) Mill 7 (34 nm total material removed), (h) Electron 2 (36 nm total material removed), (i) Mill 10 (48 nm total material removed), (j) Mill 12 (77 nm total material removed). Information on heat treatment parameters can be found in Chapter 7 and in Table 9.1.

shown in Figure 9.5, the trap was heated long enough and hot enough for a primed surface to thermally transform. As discussed in Section 9.2, the half-life of the thermal transformation was measured to be about a day and a half between 555 and 575 K. If the trap is heated to temperatures above 555 K for a full day and heating rates do not increase, it can be assumed that the trap surface is not primed for a thermal transformation.

Table 9.1: Summary of select heat treatments. For details, see Chapter 7.

Treatment	Time over 550 K (days)	Time over 575 K (days)
Electron 1 heat	2.5	2
Mill 1 heat	3	3
Mill 2 heat	2	0.3
Mill 3 heat	1.5	1
Mill 5 heat	5	3
Mill 6 heat	4	0.2
Mill 7 heat	7	4
Electron 2 heat	4.5	3.5
Mill 10 heat	3	3
Mill 12 heat	20	9

Plots of temperature scalings measured after Mill 5 (9.5e), Mill 7 (9.5g), and Electron 2 (9.5h) show thermal transformations that have been saturated by heat treatments at around 575 K. The Mill 6 heat treatment may not have fully saturated (9.5f), so this plot represents a lower bound on the magnitude of the transformation. The thermal transformation following Mill 12 doubled in magnitude when the trap was held above 600 K for 3.5 days, as shown in Figure 9.3, so the middle temperature scaling in Figure (9.5j) is most comparable to the other thermal transformations plotted.

After having identified which surface treatments primed the surface for the largest thermal transformations, we use data from measured Auger spectra to identify what was unique about the substrate during these experiments. From the spectra plotted in Chapter 7, it is evident that the composition of the trap surface was constantly changing throughout the surface treatment experiments. However, only one feature appears to be correlated with the presence of a thermal transformation: the chemical state of aluminum.

The chemical state of the aluminum on the trap surface can be deduced from the line-shape of the aluminum Auger peaks, combined with the fractional composition of the surface. A representative set of aluminum spectra are plotted in Figure 9.6a, and a representative set of relative atomic surface fractions (scaled to aluminum) are plotted in Figure 9.7.

The first spectrum plotted in Figure 9.6a was taken during treatment Electron 1, after the trap had been exposed to atmosphere for 30 weeks, and before its surface had been milled. When exposed to air, aluminum rapidly forms a native oxide layer. The large oxygen fraction plotted in Figure 9.7a is consistent with the presence of an oxide. In addition, the primary peak in the Electron 1 spectrum (the derivative of which is plotted in Figure 9.6a) is shifted to the left compared to all other measured spectra. As shown in Figure 9.6d, a -8 eV shift in the primary (high-energy) Auger peak of aluminum is indicative of aluminum oxide. From all of this evidence, we can infer that the aluminum at the trap surface was oxidized during Electron 1.

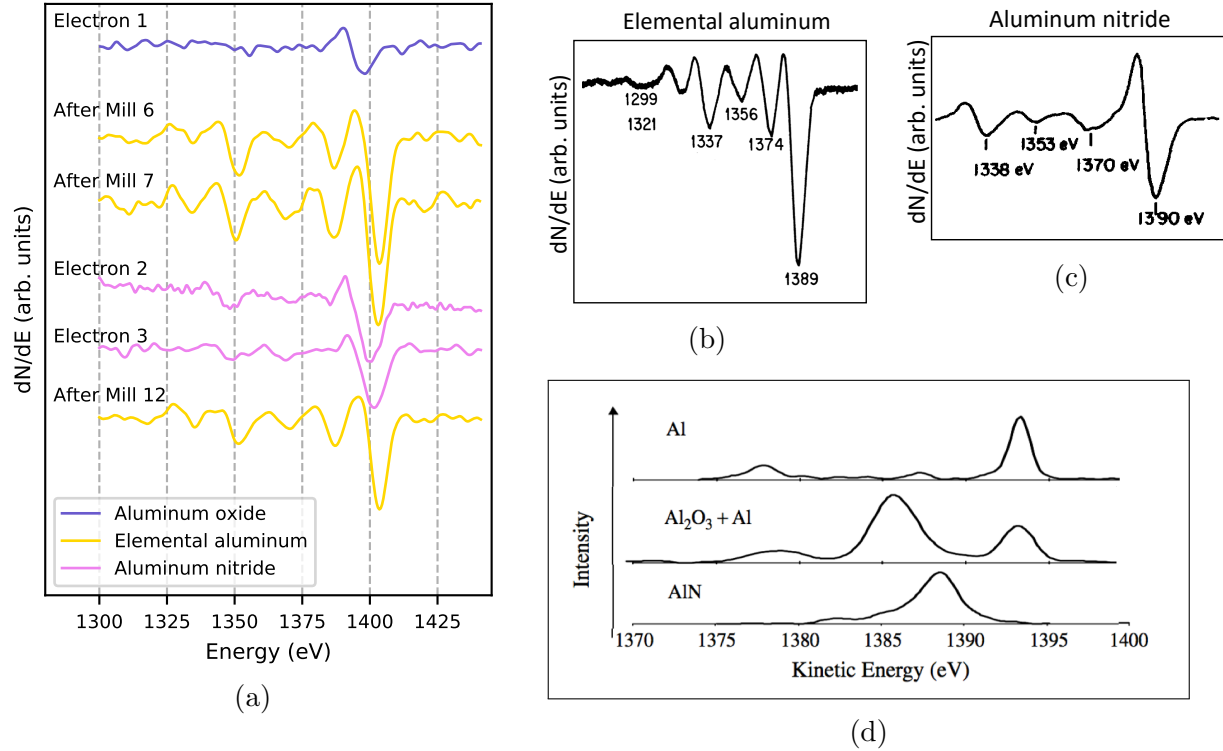


Figure 9.6: Aluminum Auger spectra. (a) Measurements in TRAP C. (b) Reference spectrum of elemental aluminum [34]. (c) Reference spectrum of aluminum nitride [51]. (d) Reference showing relative peak positions of aluminum, aluminum oxide, and aluminum nitride [51].

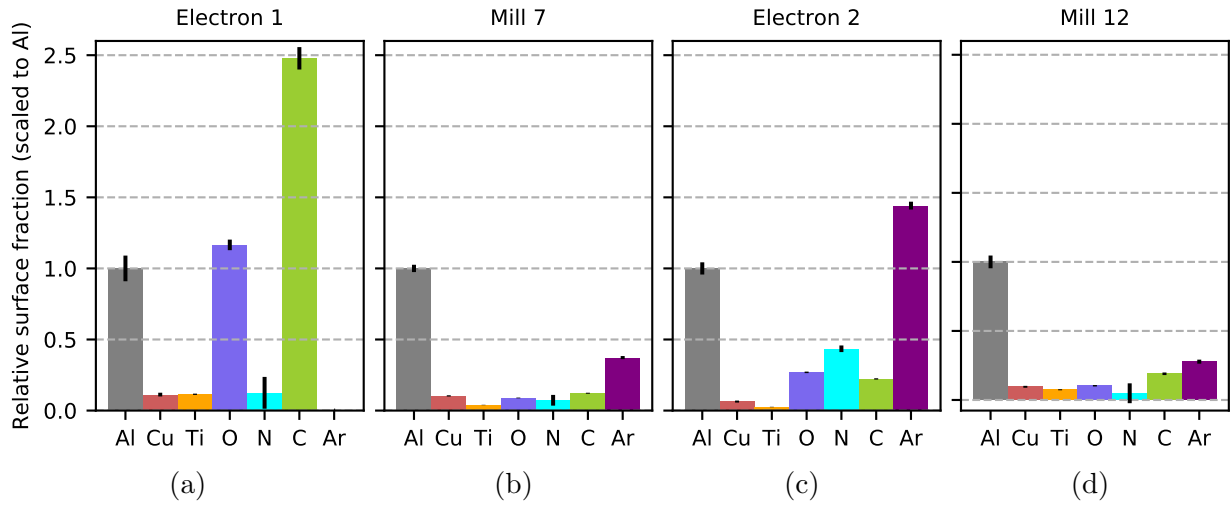


Figure 9.7: Relative fractional atomic composition of the trap surface, scaled to aluminum. These plots indicate that the surface was primarily (a) aluminum oxide and carbon during Electron 1, (b) elemental aluminum during Mill 7, (c) a combination of aluminum oxide and aluminum nitride during Electron 2, with a significant fraction of embedded argon, and (d) elemental aluminum after Mill 12.

The second and third spectra plotted in Figure 9.6a were taken immediately after treatments [Mill 6](#) and [Mill 7](#). There is a strong similarity between the line-shapes of these measured spectra and the line-shape of the elemental aluminum reference spectrum (Figure 9.6b). This similarity indicates that the aluminum on the trap surface was in its elemental state when this data was taken. This is supported by the full fractional composition of the surface, which is plotted in Figure 9.7b. Although there was a significant fraction of embedded argon present at this time, the small fractions of oxygen, nitrogen and carbon are consistent with a primarily elemental aluminum surface.

The fourth and fifth spectra plotted in Figure 9.6a were taken during [Electron 2](#) and [Electron 3](#). The significant fractions of oxygen and nitrogen present during these measurements (see Figure 9.7c) indicate that the aluminum on the trap surface was in the form of aluminum nitride and aluminum oxide when these measurements were taken. In addition, the observed diminishment of satellite Auger peaks (the small peaks to the left of the 1400 eV peak), and the downward energy shift of the primary peak, are characteristic of aluminum nitride, as shown in reference figures 9.6c and 9.6d respectively.

The surface contamination level measured during treatments Electron 2 and 3 was greater than the level measured after Mill 7, despite Mill 7 having been performed before these other treatments. It is possible that oxygen and nitrogen gases were introduced during or after [Mill 9](#), which is the treatment that immediately preceded Electron 2. It is also possible that these gases were incorporated into the metal film during the evaporation process.

Further milling of the trap surface after Electron 3 revealed an elemental aluminum surface once again, as shown in the final spectrum plotted in Figure 9.6a. The surface composition corresponding to this spectrum, which was taken immediately following [Mill 12](#), is plotted in Figure 9.7d.

Having demonstrated how the chemical state of aluminum can be extracted from an Auger spectrum measurement, we can now compare the evolving state of the aluminum surface to the presence and absence of thermal transformations. These features are plotted together in Figure 9.8. Orange bars indicate the measured fractional change of the room-temperature heating rate in response to various heat treatments. Yellow, purple and pink bars indicate the chemical state of aluminum as measured with the Auger spectrometer.

As shown in Figure 9.8, thermal transformations did not take place during early heat treatments when the aluminum on the surface of the trap was oxidized. The transformations first appeared after Mill 5, by which point milling had removed a total of 6.3 nm from the surface and had likely broken through parts of the oxide layer to reveal elemental aluminum (after 30 weeks of atmosphere exposure, the native aluminum oxide would have been 5 to 10 nm thick). Mill 6 revealed a surface that was primarily composed of elemental aluminum, and the subsequent thermal transformation was significant. Later, when elemental aluminum was replaced by aluminum nitride and aluminum oxide, the thermal transformations ceased. Finally, aggressive angled milling in treatments Mill 11 and Mill 12 removed the nitride/oxide layer and re-exposed elemental aluminum, at which point the thermal transformation returned.

In summary, the electric-field noise in an ion trap undergo a two-day thermal transformation at 575 K if the surface has been milled to reveal elemental aluminum. If the aluminum at the trap surface is in the form of aluminum oxide or aluminum nitride, this transformation will not take place. This information can be used to investigate which phys-

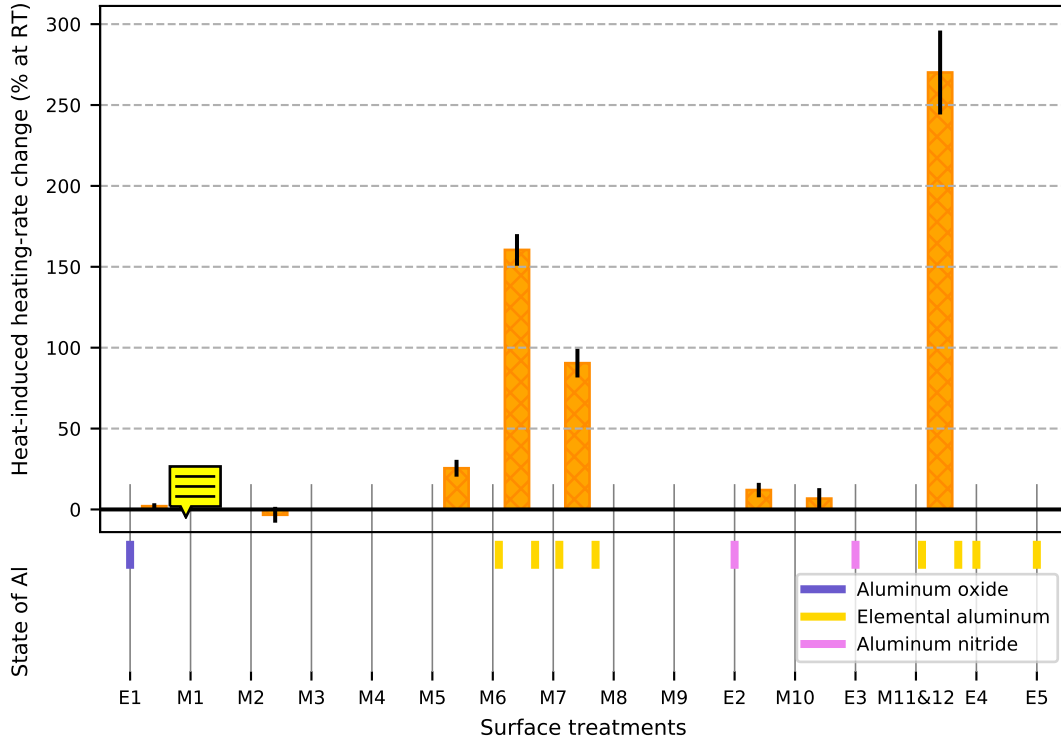


Figure 9.8: Data from heating rates measured at room temperature before and after heat treatments, shown in context with the chemical state of the aluminum on the trap surface as deduced from measurements of Auger spectra. ??.

ical processes may be responsible for thermal transformations.

## 9.5 Investigation of contaminant deposition

During a heat treatment, the ion trap is not the only hot element in the vacuum chamber. Other elements such as the heater itself, the copper heat sink, the heater wires, and the kapton-tape wire isolators also reach elevated temperatures. If these elements outgas contaminants when they are heated, then these contaminants can attach to the surface of the trap and become sources of electric-field noise. It is feasible that some of these gaseous contaminants would bind to elemental aluminum and not to aluminum oxide or nitride, so this hypothesis is consistent with the observed thermal-transformation intermittency.

To test for contaminant deposition, Auger spectra were measured before and after heat treatments following Mill 6, Mill 7, and Mill 12. In each case, a thermal transformation took place, and the measured spectra revealed no evidence of contaminant deposition.

Auger spectra measured before and after a thermal transformation are plotted in Figure 9.9. It is evident from the comparison of these two spectra that no new elements were introduced to the trap surface during the heat treatment. In addition, the relative peak heights of different elements are nearly identical before and after heating. This was the case for all spectra measured before and after heat treatments.

Figures 9.10 and 9.11 compare surface composition measurements taken before and after

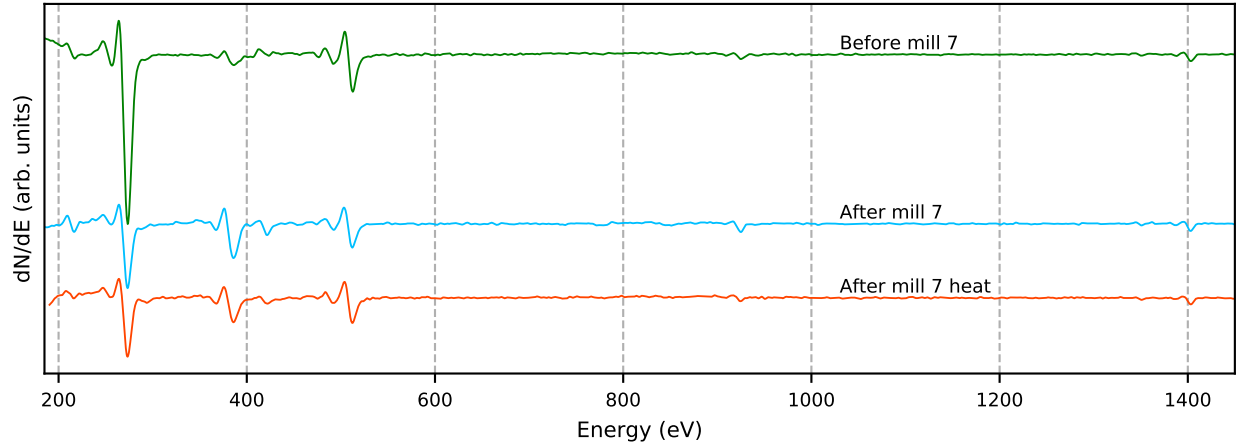


Figure 9.9: Auger spectra taken before and after the thermal transformation following Mill 7 show no new elements.

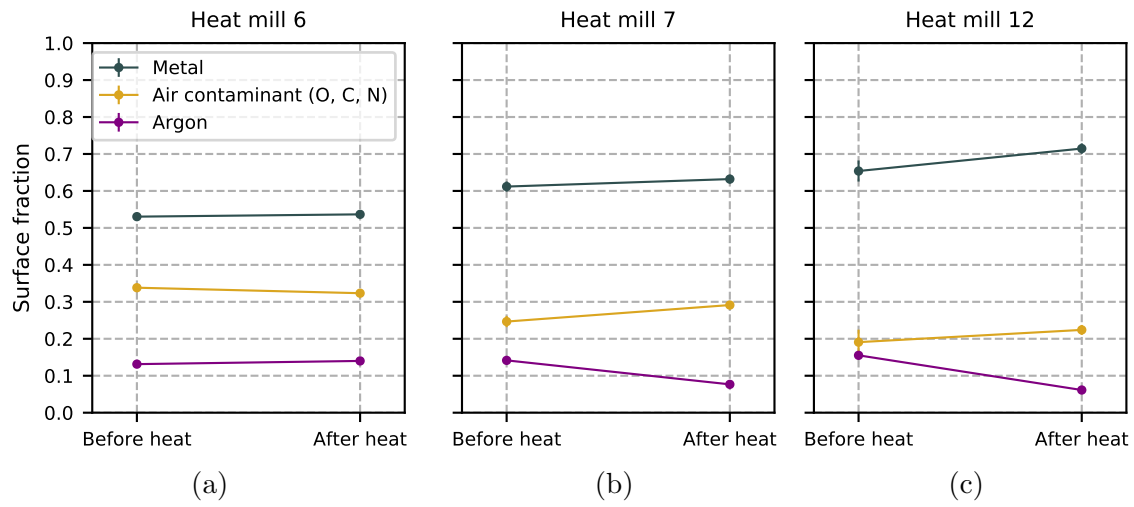


Figure 9.10: Surface fractions measured before and after thermal transformations following (a) Mill 6, (b) Mill 7, and (c) Mill 12.

three thermal transformations. Although compositional changes were observed, the plots do not show any consistent, statistically-significant trends. This indicates that contaminant deposition is not driving thermal transformations.

## 9.6 Investigation of chemical changes

A change in the chemical structure of noise-generating adsorbates could give rise to a change in the surface electric-field noise. Heat can drive chemical changes, so it is feasible that thermal transformations could be chemically driven. Since ion milling can break up chemical structures, this hypothesis is consistent with the observation that argon ion milling can reset a saturated noise transformation.

As discussed in the context of aluminum in Section 9.4, some chemical information can

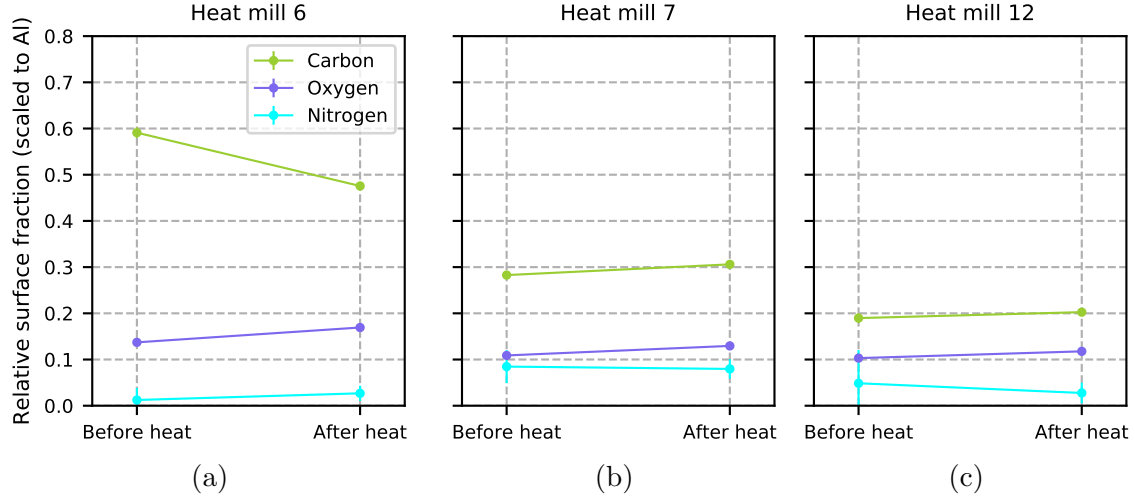


Figure 9.11: Surface fractions measured before and after thermal transformations, scaled to the surface fraction of aluminum, following (a) Mill 6, (b) Mill 7, and (c) Mill 12.

be deduced from the line-shapes of Auger spectra. In Figure 9.10, two full Auger spectra are plotted together. One spectrum was measured before a thermal transformation, and the other was measured after. These plots show no evidence of chemical changes taking place. Additional plots of aluminum, copper, oxygen and carbon spectra are shown in Figure 9.12. In these plots, the spectra have been scaled to enable a direct comparison of the line-shapes. These comparisons highlight that the plotted line-shapes were not altered by the heat treatments.

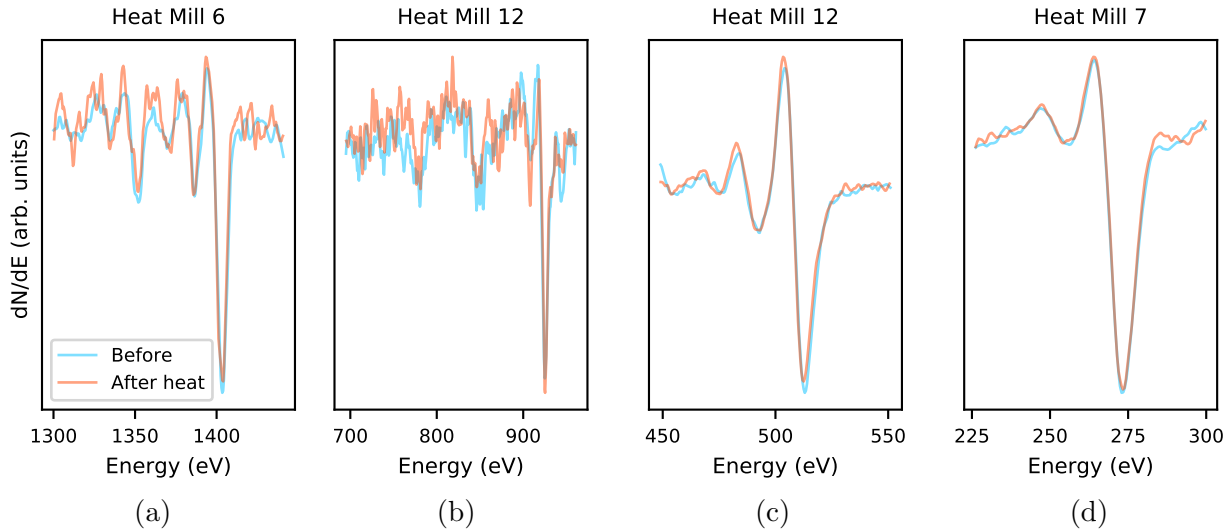


Figure 9.12: Scaled Auger spectra measured before and after thermal transformations: (a) aluminum in the heat treatment following Mill 6, (b) copper in the heat treatment following Mill 12, (c) oxygen in the heat treatment following Mill 12, (d) carbon in the heat treatment following Mill 7. No thermally-driven chemical changes are visible.

The Auger spectra show no evidence of thermally-driven chemical changes, but this is

not enough information to rule out chemistry as a driver of noise transformations. Some chemical changes are not visible with Auger spectroscopy. When the electron beam from the Auger spectrometer hits the metal surface of the trap, the electrons induce chemical bond-breaking, atomic desorption and carbon deposition. Hydrocarbon adsorbates are particularly sensitive to electron beam damage, so hydrocarbon growth cannot be studied with an Auger spectrometer.

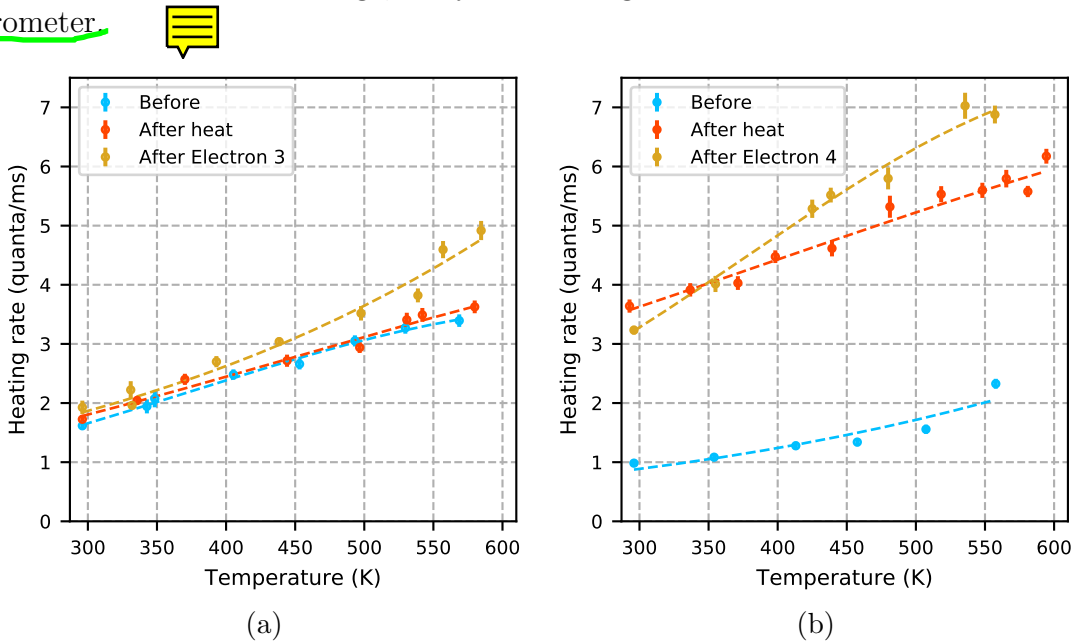


Figure 9.13: Temperature scalings of ion heating rates measured before and after the trap surface was bombarded by a 2 keV electron beam. (a) Electron treatment of  $180 \text{ kJ/cm}^2$  ([Electron 3](#)) performed on a trap surface that did not thermally transform after [Mill 10](#). (b) Electron treatment of  $280 \text{ kJ/cm}^2$  ([Electron 3](#)) performed immediately after the thermal transformation following [Mill 12](#).

Although electron damage inhibits the sensitivity of Auger spectroscopy, the electron beam itself can be used to test the hypothesis that thermal transformations are chemically driven. If heat treatments raise electric-field noise by growing hydrocarbon structures, then it should be possible to use an electron beam to reverse a thermal transformation. Electron treatments were performed on the trap immediately after it had undergone a thermal transformation (Figure 9.13b), and immediately after the trap had been heated and not transformed (Figure 9.13a). The change in the heating-rate temperature scaling due to electron treatments was nearly the same in both cases. The fact that electron bombardment did not reverse the thermal transformation is an indication that hydrocarbon growth does not drive the thermally-driven increase of electric-field noise.

We have found no direct evidence support the hypothesis that chemical changes are driving thermal transformations of surface-electric-field noise. It is still possible that a chemical processes is behind this effect, but given the results of our measurement results, it is not likely.

## 9.7 Investigation of atomic restructuring

Heat-induced atomic restructuring includes the smoothing out of sharp edges, the healing of defects, and the formation of hillocks. These changes take place when the atoms in a material have enough thermal energy to become mobile, and they are generally driven by strain reduction.

### 9.7.1 Recrystallization temperatures

As discussed in section 9.1, the thermal transformation of surface noise in TRAP C had a 1.4-day half life between 555 and 575 K, and did not occur at low temperatures. Studies of the recrystallization temperatures of similar metal films can provide insight into whether or not the observed noise transformations are consistent with atomic restructuring.

The *initial recrystallization temperature* of a material is the lowest temperature at which small crystal grains combine to form larger grains on a timescale of hours. The initial recrystallization temperature of a pure, bulk metal is typically about half of its melting temperature. Bulk aluminum, which melts at 930 K, has an initial recrystallization temperature of 470 K [52].

The addition of impurities to the metal slows down recrystallization through a process called *impurity drag* [53], where atomic impurities impede the motion of the bulk atoms due to atomic size mismatch. Drits et. al. did a series of experiments measuring recrystallization temperatures of bulk aluminum and aluminum foils with different types and concentrations of impurities [52]. They found that the addition of impurities raises the recrystallization temperature of both bulk aluminum and aluminum foils, with the effect saturating as the concentration of impurities is raised. Most relevant to our work is the addition of titanium, which raises the recrystallization temperature of aluminum by 110 K and saturates at an impurity concentration of 0.5%. Copper raises the recrystallization temperature by 30 K.

Grain growth in metal thin films has been found to be slower and more irregular than in bulk metals. In thin films, interactions between the metal and the substrate below suppress normal grain growth [53]. Given that TRAP C is an aluminum thin film with titanium and other impurities, it should have a bulk recrystallization temperature of over 580 K, and is likely to exhibit secondary grain growth at higher temperatures.

In Section 9.3 we presented evidence that thermal transformations affect noise originating from the top two nanometers of the trap surface. Having collected information on the recrystallization temperature of a contaminated aluminum thin film, we can confidently state that the atoms in the *bulk* of the ion trap are mobile enough at 555 K to recrystallize on a timescale of days or faster. However, we cannot make a definitive statement on the mobility of atoms at the trap surface. Atomic mobility can be considerably higher at surfaces than in the bulk of materials [54] but is also complicated by surface roughness. In addition, even at its cleanest, the surface of TRAP C always contained a small portion of oxygen, which impedes atomic motion.

Although it is impossible to predict the precise temperature dependence of atomic restructuring on the surface of TRAP C, atomic restructuring can directly explain the observed intermittency of thermal transformations. Aluminum oxide and aluminum nitride have melting temperatures of 2340 K and 2470 K respectively, putting their recrystallization tem-

peratures at around 1170 K and 1235 K. This is far higher than our highest measurement temperature of 615 K, and would explain why thermal transformations did not take place when the aluminum surface was oxidized or nitrogenized. In addition, thermal transformations were observed at multiple temperatures during the heat treatment following [Mill 12](#) (see the data plotted in [Figure 9.3](#)). This behavior is consistent with secondary recrystallization.

### 9.7.2 Morphological changes: annealing

Having demonstrated the relevance of atomic restructuring to thermal noise transformations, we will now explore how the properties of the surface may change as a consequence of this restructuring. When a thin film such as ours is annealed, three types of changes take place in the metal: the bulk recrystallizes, the surface roughness changes, and hillocks form.

Bulk recrystallization is driven by strain reduction. As the substrate is heated, atoms in the bulk gain enough energy to move and reduce strain at grain boundaries. Small crystals merge and form larger crystals. As large crystal grains form, the RMS roughness of the surface increases. At the same time, small crystals and individual atoms are incorporated into larger structures, thus decreasing the RMS roughness of features with small correlation lengths. This process is illustrated in [Figure 9.14](#).

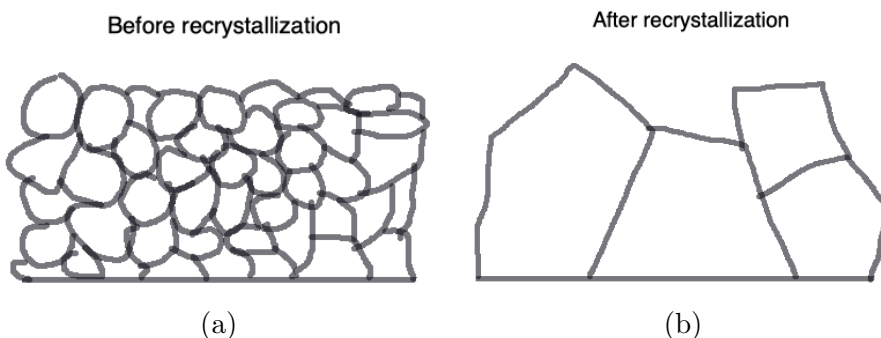


[Figure 9.14](#): This cartoon of recrystallization (inspired by [55]) illustrates how the growth of large features increases the high-correlation-length RMS roughness while decreasing the low-correlation-length RMS roughness. (a) Cross section before recrystallization. (b) Cross section after recrystallization.

Such topological changes have been observed experimentally in studies performed by H. Qin et al in reference [56]. In these experiments, an aluminum oxide thin film was annealed at a temperature of 770 K for varying lengths of time. Measurements presented in reference [56] (and reproduced in [Figure 9.15a](#)) show the RMS roughness increasing as the annealing process proceeds, while features with lateral correlation lengths on the order of 1 nm shrink ([Figure 9.15b](#)).

Hillocks are micron-scale mounds that form on metal surfaces during heat treatments. Their formation is driven by the strain mismatch between the surface and the bulk. Chang et. al. [found](#) that pure, unoxidized aluminum films do not form hillocks when heated, as the aluminum atoms on the surface are free to move and reduce strain as needed [57]. Aluminum films with native oxide layers form hillocks because the oxidation layers lock the

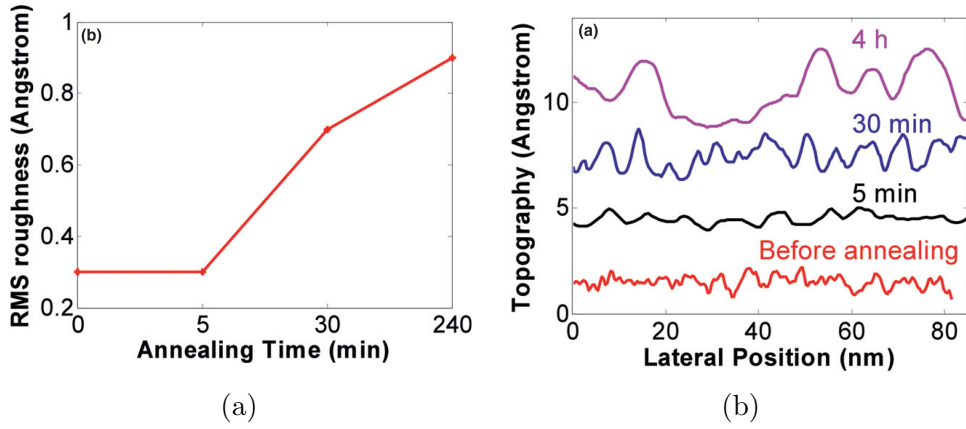


Figure 9.15: Results from experiments performed by Qin et. al. in which an aluminum oxide thin film was annealed at a temperature of 770 K for varying amounts of time [56]. (a) The overall RMS roughness increases as the thin film is annealed. (b) The heights of small-correlation-length features shrink as the film is annealed, while the heights of large-correlation-length features grow.

surface atoms in place. Strain builds up in the hot metal underneath the surface, and the pressure can only be reduced by the aluminum breaking through the oxide layer, piling up and forming a hillock.

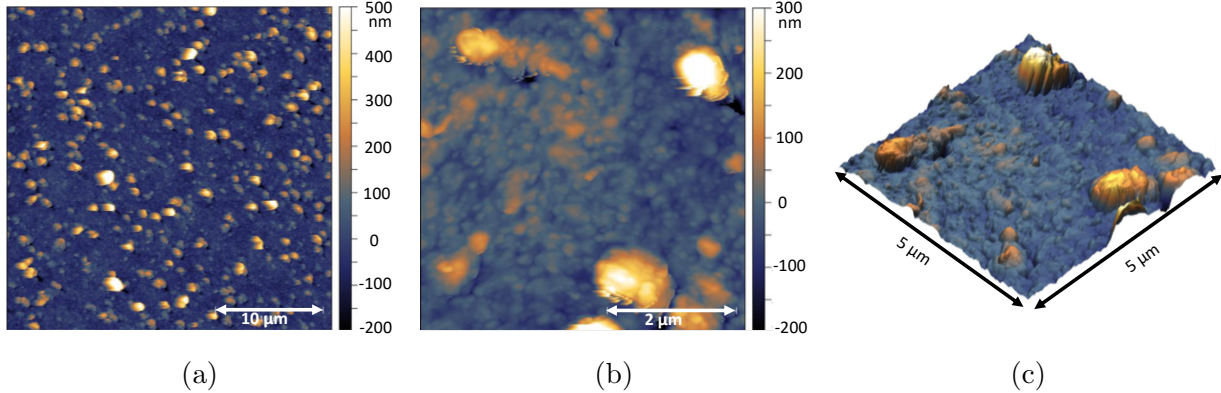


Figure 9.16: AFM measurements of Trap C, taken when the trap was removed from vacuum after surface treatment Electron 5. These bumps look like hillocks which have been studied and imaged in similar systems [58]. (a) Feature height color map, 30  $\mu\text{m}$  x 30  $\mu\text{m}$  measurement area. (b) Feature height color map, 5  $\mu\text{m}$  x 5  $\mu\text{m}$  measurement area. c) 3D visualization of (b). These measurements were taken by Chris Orme at Lawrence Livermore National Laboratory.

TRAP C was removed from vacuum following Electron 5, which was the final surface treatment presented Chapter ???. Subsequent AFM images revealed features on the surface of the trap that are about 1  $\mu\text{m}$  wide, 300 nm high, and look like hillocks imaged in similar systems [58]. Given the extensive heat treatments performed on this trap, both with and without a native oxide layer, it is no surprise that hillocks are present. However, this does

not mean that hillock growth drives noise growth during heat treatments. Hillock growth is enhanced by native oxide layers, not impeded by them. This  is in direct opposition to our observation the thermal noise transformations only take place when no oxide or nitride layer is present. In addition, we found that a treatment that milled 2 nm of material off of the trap surface almost entirely reversed the effect of the thermal noise transformation following [Mill 7](#). Since 2 nm of milling cannot remove a 300 nm-tall hillock, hillocks growth cannot explain the thermal transformation of noise observed in our system.

### 9.7.3 Morphological changes: milling

We have observed experimentally that argon ion milling can reset saturated thermal noise transformations. This means that whatever heat treatments are doing to increase the noise, milling must be doing the opposite. Milling can counteract the  effects of recrystallization by introducing defects into the bulk crystal structure via argon ion implantation. Milling can also remove hillocks and other large morphological features while increasing sub-nanometer-scale surface roughness .

To illustrate the  effects of ion milling on surface morphology, we performed a series of Monte-Carlo simulations. First, we construct a 2D array of atoms. In some scenarios all atoms are aluminum (shown in grey) and in others there is a mix of aluminum and carbon (shown in green). The substrates are extended to the left and right during the simulation, and then cut down to remove edge effects.

Next, each simulated column is ‘hit’ by an argon ion. Experimentally, when a 200 eV argon ion hits an aluminum surface at a 90° angle, there is a 40% chance that an aluminum atom will be removed from that surface. A carbon atom has a 3% chance of removal when hit by a 200 eV argon ion [\[59\]](#). To simulate this, when an aluminum atom is hit by an ion, we give it an equal probability of moving in one of eight directions: up, down, right, left, or the four diagonals. A direction is chosen randomly, and if the top atom in the column can move in the chosen direction without hitting anything, it is removed from the lattice. If it hits another atom, it joins the lattice at that new location (often this results in the atom remaining in place). When a simulated carbon atom is hit by an ion, 92% of the time it is left in place, and the remaining 8% of the time it follows the same procedure as the aluminum atoms. After each  column has been hit by an argon ion, the process is repeated with the now depleted lattice. The number of incident ions per column is specified in each simulation presented below. These simulations do not take into account all relevant physical processes, but they are a useful tool for illustrating the effects of milling.

The simulation shown in [Figure 9.17](#) begins with a flat aluminum surface, and each surface lattice site is hit with ten argon ions. The simulation shown in [Figure 9.18](#) begins again with a flat surface, but this time 20% of the atoms throughout the aluminum film are switched to carbon. Again each surface lattice site is hit with ten argon ions. In this simulation, needle-type structures form in places where carbon atoms have impeded the sputter rate.

The simulations in [Figure 9.19](#) explore the impact of milling on large, atomically smooth aluminum structures with heights and widths of 20 to 30 atoms. These features are milled away by milling (two rounds of 120 ions each), leaving a flat surface with atomic scale roughness. The simulation in [Figure 9.20](#) investigates the combined effects of large structures and a mixed-composition substrate. This material is 80% aluminum, and 20% carbon. After

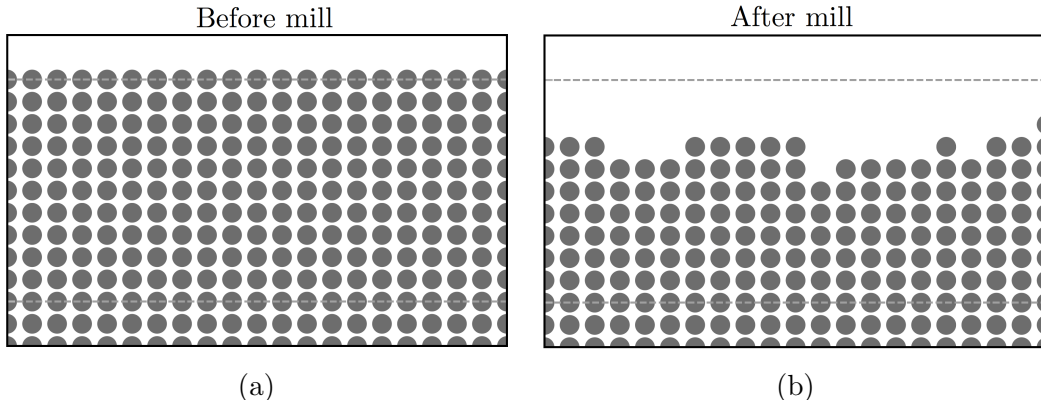


Figure 9.17: Monte-Carlo simulation with an all-aluminum substrate, and 10 ions bombarding each lattice column.

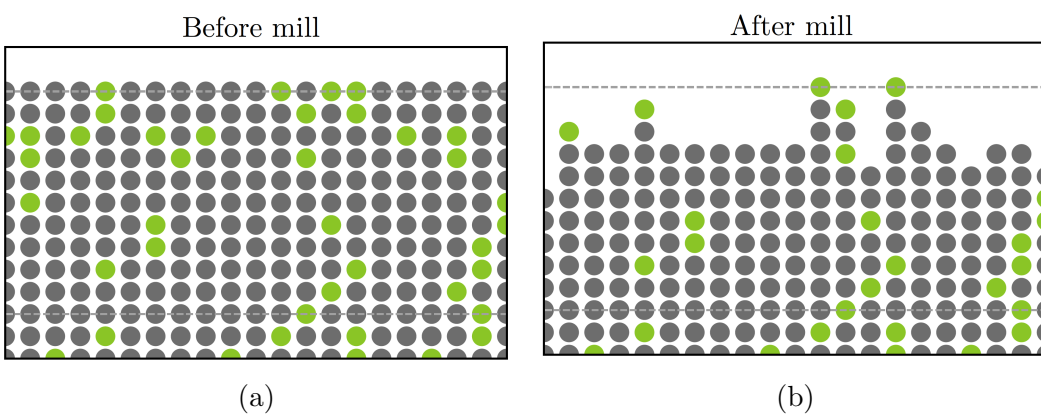


Figure 9.18: Monte-Carlo simulation with an aluminum and carbon substrate, and 10 ions bombarding each lattice column. Aluminum is preferentially removed, leaving a rough, unevenly-milled surface.

240 ions of milling, the initial features are mostly milled away, leaving a rough surface with 5-atom-wide features.

The lattice spacing in aluminum is about 0.4 nm. In Figure 9.4, we showed results from an experiment in which 0.6 nm of milling had a major impact on a thermally transformed temperature scaling, and 2 nm of milling reversed nearly the entire effect of the thermal transformation. This experiment indicates that the morphological features most relevant to thermal transformations have been between 1 and 5 monolayers of depth. With the right beam angle, energy, and substrate composition, it is possible to use ion milling to smooth out a surface. However, as illustrated in our simulations, when a mixed substrate is milled at a 90° angle, the milling proceeds unevenly. This type of surface treatment can remove large features such as hillocks, but will increase roughness on the length scale that is relevant to our experiments.

We have described data from thermal transformation experiments that is consistent with atomic restructuring, provided evidence that ion milling increases nanoscale roughness in

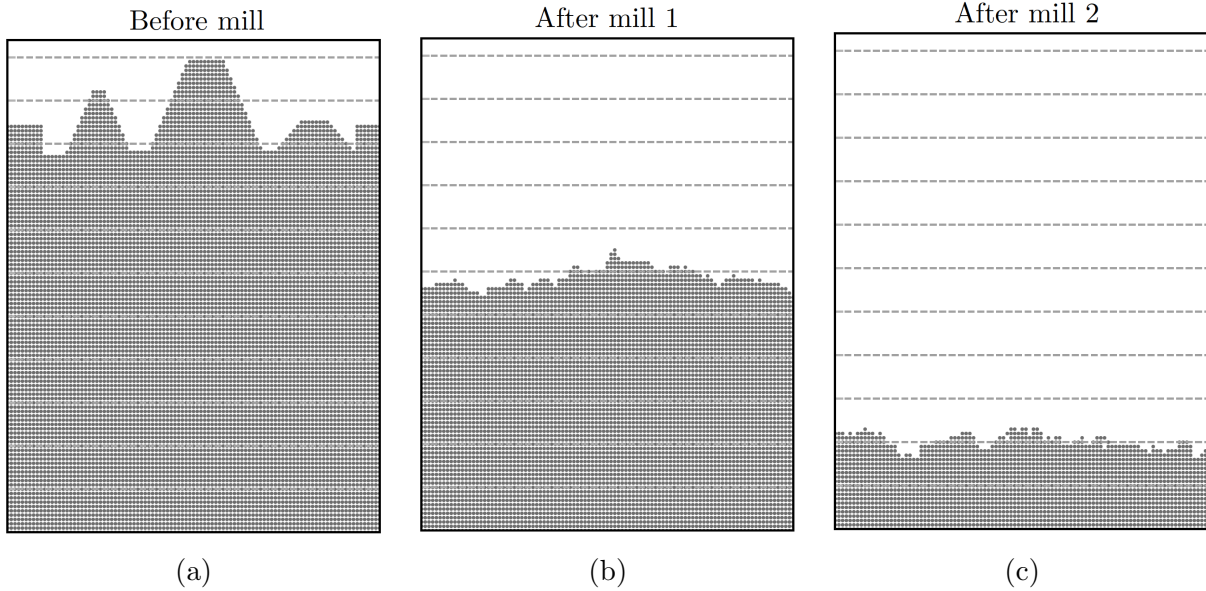


Figure 9.19: Monte-Carlo simulation with an all-aluminum substrate with large, atomically-smooth features. 120 ions bombard each lattice column during each milling step.

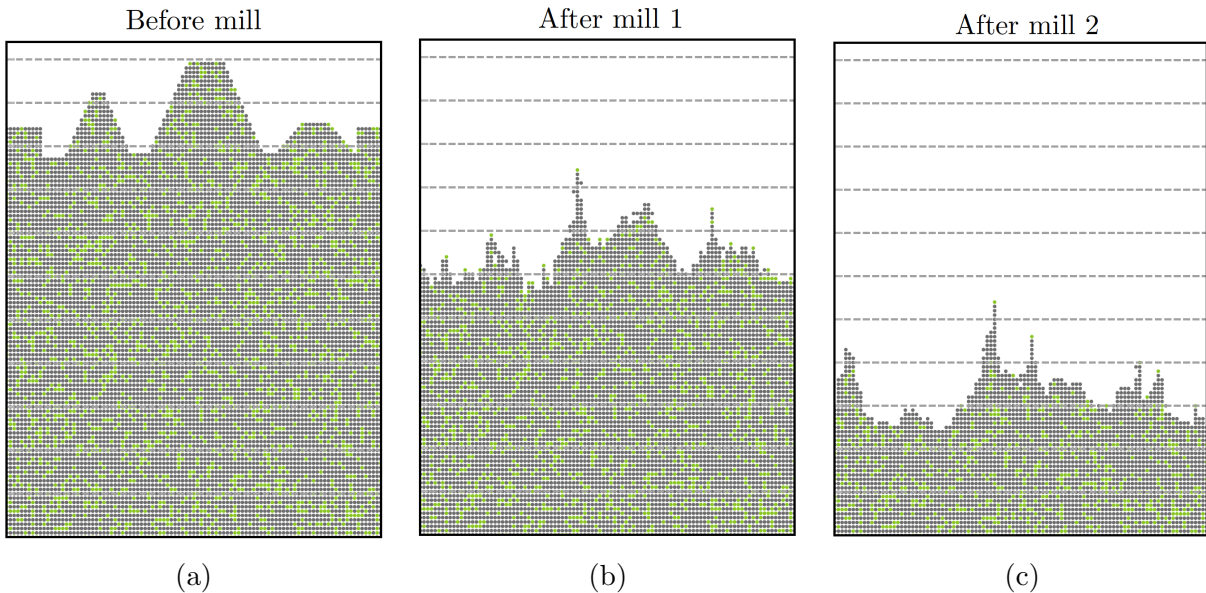


Figure 9.20: Monte-Carlo simulation with an aluminum and carbon substrate with large, atomically-smooth features. 120 ions bombard each lattice column during each milling step. The initial features with 20 to 30-atom widths are milled down, leaving features with 1 to 5-atom widths.

mixed substrates, and shown that annealing can reduce nanoscale roughness. This work supports the hypothesis that thermal transformations raise ion heating rates by smoothing out the surface, and that ion milling lowers ion heating rates, in part, but roughening the

surface. We will now consider physical noise processes that can explain this phenomenon.

#### 9.7.4 TAF distributions and surface binding energies

Consider the TAF distributions presented in Figure 9.21. In each of the first four thermal transformations (Mill 5, Mill 6, Mill 7, and Electron 2), the heat treatment caused the TAF distribution to narrow, increase in amplitude, and shift its peak to an energy between 0.5 and 0.6 eV. The thermally transformed TAF distributions are qualitatively similar to the pre-treatment distribution. This pattern did not continue after surface treatment Mill 

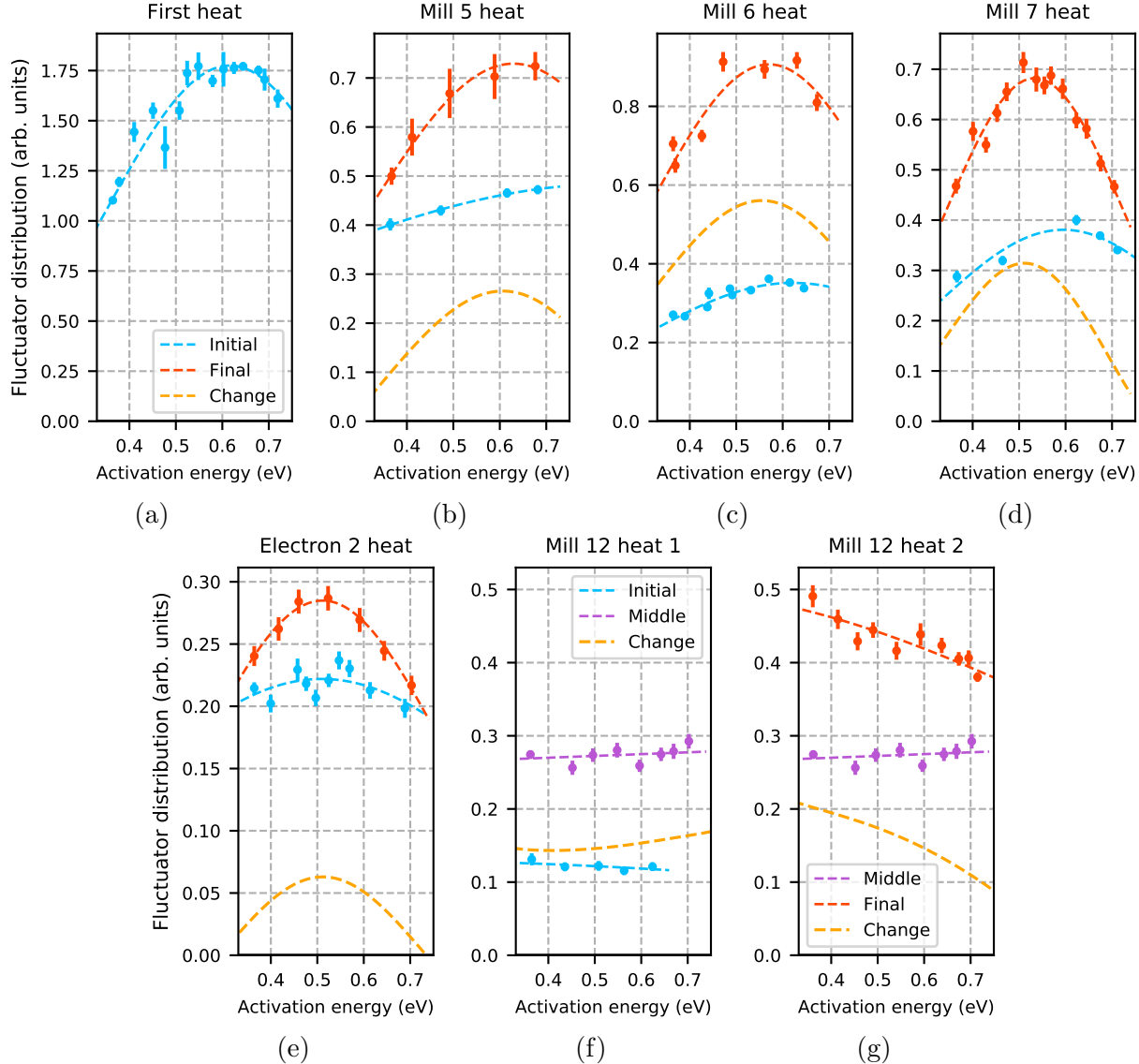


Figure 9.21: (a) Pre-bombardment TAF distribution. Thermal transformations after (b) Mill 5, (c) Mill 6, (d) Mill 7, (e) Electron 2, (f) Mill 12 heat 1, and (g) Mill 12 heat 2.

In exploring the significance of TAF distribution changes in the context of surface morphology, it is useful to consider a specific physical TAF manifestation. Suppose that each

adsorbate is a fluctuator. Suppose also that the energy barrier of each fluctuator is equal to the binding energy between the adsorbate and the metal surface. Adsorbates can fluctuate by moving between lattice sites, or by binding and unbinding at a single site. This process is illustrated in Figure 9.22. Electric-field noise is generated when the dipole moment of the adsorbate changes along with the adsorbate-surface binding configuration.

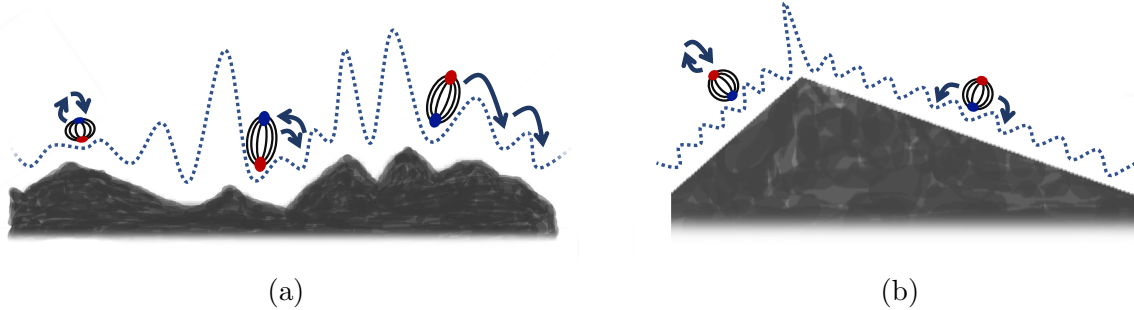


Figure 9.22: Illustration of TAF adsorbate dipoles. The potential landscapes are represented by dotted blue lines. (a) Adsorbate TAFs on a rough surface. (b) Adsorbate TAFs on a crystallized surface.

Adsorbate binding energies are stronger in areas with positive curvature (valleys), and weaker in areas with negative curvature (peaks) [47]. The van der Waals potential of an adsorbate on a surface with sub-nanoscale roughness can increase or decrease by about 50% depending on the local curvature of its binding site. As a consequence of this, the potential landscape of a rough surface is more varied than that of a smooth surface. Illustrations of the potentials of rough and smooth surfaces are shown in Figure 9.22.

If TAF energy barriers correspond directly to adsorbate-surface binding energies, then the TAF distribution of a contaminated, crystallized surface should peak at a discrete set of energies characteristic of the structure of the lattice. When this surface is roughened, these peaks will widen and lower in magnitude as a wider range of binding sites became available. This is consistent with the trend observed in our heat treatment experiments. In most cases when an ion-milled, presumably rough surface is annealed, the TAF distribution narrows and increases in magnitude. When a thermally transformed, presumably smooth surface is milled, the TAF distribution widens and decreases in amplitude. Plots of TAF distributions before and after milling are shown in Figure 9.23.

Figure 9.23a contains data from the first four ion milling treatments performed on TRAP C, and figure 9.23b contains data from the milling performed after the thermal transformation following Mill 7. After the Mill 7 thermal transformation, the TAF distribution was strongly peaked at 0.55 eV, and closely matched the pre-milling TAF distribution plotted in Figure 9.23a, but the amplitude is almost a factor of three lower.

This difference in amplitude between the pre-mill TAF distribution in Figure 9.23a and the post-heat TAF distribution in Figure 9.23b can be attributed to the removal of contaminants via argon ion milling. The similarity of the shapes and peak energies of the two distributions can be explained by similarities in the surface morphology. Having provided evidence that thermal transformation is linked to recrystallization, the similarity of these two TAF distributions indicates that the initial surface was crystallized.

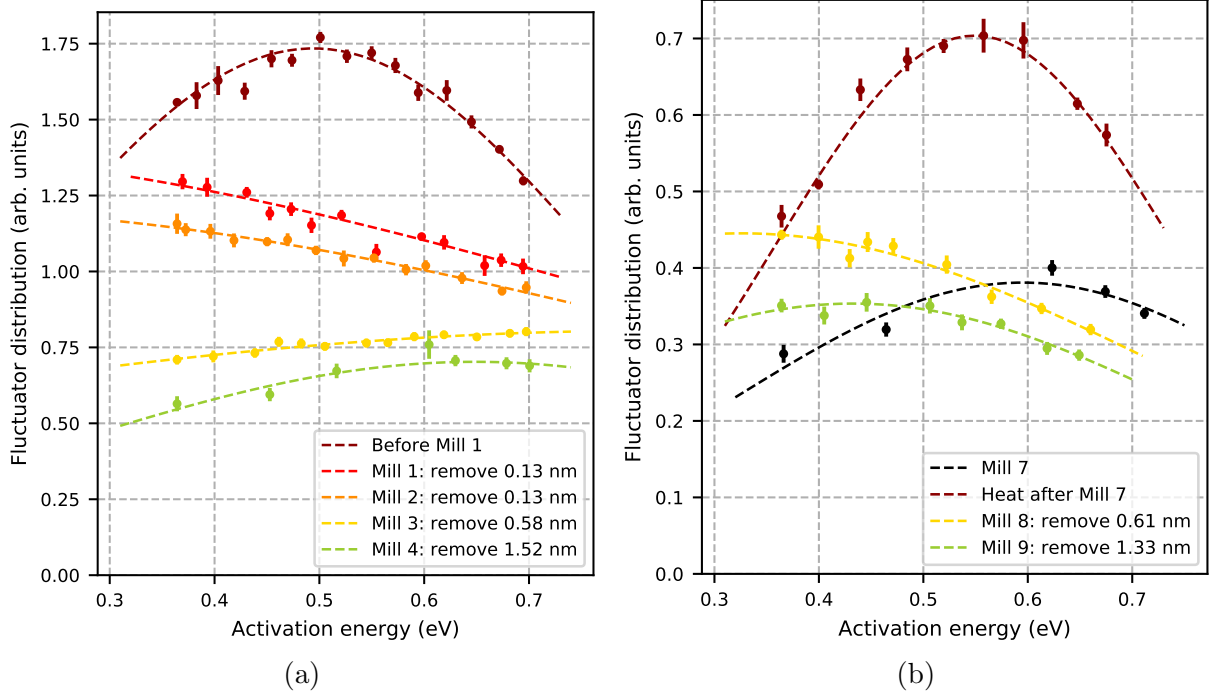


Figure 9.23: Low-dose milling widens the TAF distribution, lowers its magnitude, and shifts the peak to lower energies. Further milling shifts the peak to higher energies. (a) TAF distributions following Electron 1 and Mill 1, 2, 3, and 4. (b) Mill and heat 7, Mill 8, and 9.

When each of these TAF distributions was milled, the initial milling steps broadened the distribution and shifted its peak down in energy by preferentially removing high-energy TAFs. In both experiments, though it is more clear in Figure 9.23a, subsequent milling steps preferentially removed low energy TAFs.

It is possible to explain these behaviors by considering the evolution of the surface morphology. When a surface contaminated with carbon is milled a small amount, milling preferentially removes the aluminum. This produces a surface with aluminum valleys and carbon-topped peaks, as illustrated in Figure 9.18. In this scenario, a disproportionate number of carbon atoms occupy binding sites with negative curvature, and therefore have weakened binding energies. If carbon adsorbates produce electric field noise, and binding energies correspond to TAF energy barriers, then this could explain why the TAF peak goes down in energy after a small milling dose. As milling continues, the corners of larger features are milled down, and the surface is left with large areas with positive curvature, as shown in Figure 9.20. This might explain why large milling doses produce TAF distributions with peaks at high energies.

The transformations following Mill 12 did not fit the patterns observed in other heat treatments. Mill 11 and 12 were unique in that they were performed at a  $45^\circ$  angle rather than straight on, but this does not provide a physical explanation as to why this thermal transformation was qualitatively different than the others. It may be that the transformation never saturated, and that during the ion heating rate measurements the TAFs transformed quickly enough to invalidate the translation of temperature scalings into TAF distributions.

It also is possible that Mill 11 and 12 revealed material with unique physical properties, though we have not been able to identify what these properties might be.

We have discussed how changes in the variability of binding sites may affect the magnitude, width and energy of TAF distributions. These effects may be compounded by the relationship between binding energies and adsorbate dipole strengths [47]. We will not discuss this here, as to do so would require additional specificity about the physical composition and behavior of the TAFs. There is yet another way that changes in surface roughness could affect the electric-field noise magnitude: by changing the correlation length of the noise process. This we will discuss in the following section.

### 9.7.5 Correlation lengths of noise sources

A group of noise sources fluctuating in phase with each other produces more noise than the same group of noise sources fluctuating independently. This is because when noise sources fluctuate independently, they sometimes move in opposition and cancel each other out. This behavior may contribute to why noise from an ion trap increases after heat-induced atomic restructuring.

On a surface with nanoscale roughness, there are large variations in adsorbate-metal binding energies [47]. In contrast, smooth crystal facets contain arrays of well-defined, periodic binding sites. As illustrated in Figure 9.24, it may be that atoms bound in a periodic manner to a single crystal facet can start to fluctuate in sync. On a surface with nanoscale roughness, variations in binding energies (and therefore TAF energy barriers) could break up correlations between neighboring fluctuators.

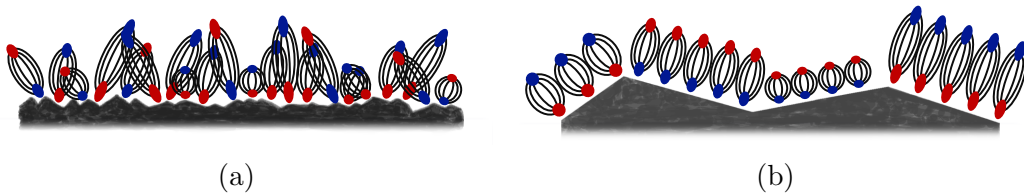


Figure 9.24: (a) Uncorrelated noise sources on a surface with nanoscale roughness. (b) Correlated noise sources on a crystal surface.

In the fluctuating-patch-potential noise model, as worked out in context of ion traps by Brownnutt et. al. [1], the noise magnitude is proportional to the average patch area multiplied by the surface coverage fraction. This applies to the limit where the patch size is much smaller than the ion-electrode separation. The patch size is proportional to the correlation length squared. Patches of correlated TAFs are analogous to fluctuating patch potentials. Therefore, the noise from a TAF-covered surface is proportional to the TAF correlation length squared. To raise the noise in an ion trap by a factor of three, as observed during the thermal transformation following treatment Mill 12, the TAF correlation length would need to rise by only a factor of  $\sqrt{3}$ .

Thermally-activated fluctuations of full nanocrystals have been observed experimentally in resistance noise measurements [60]. Further theoretical work will be critical to determining whether or not electric-field-noise-producing surface TAFs can become correlated in a similar way.



### 9.7.6 Ex-situ surface treatment and characterization experiments

The work described in this chapter would benefit from an additional series of experiments that directly correlate electric field noise with surface roughness and surface morphology.

Ideally, we would run parallel experiments in which we execute identical surface treatments in two separate vacuum chambers. The first setup would be our standard ion-trapping chamber, where we have our Auger spectrometer, ion-trapping tools, button heater and argon ion gun. The second setup would be an ex-situ characterization chamber, where we would have identical surface treatment tools, a second Auger spectrometer (for a direct comparison of the substrates and surface treatments), an AFM, an SEM, and an XPS.

At this time, we have access to all of these tools through the Berkeley Marvell Nanolab and through our collaboration with scientists at Lawrence Livermore National Laboratory. However, there is no single vacuum chamber containing everything required for ex-situ characterization. As a result, the trap must be exposed to atmosphere between treatments and measurements, which means that the ex-situ experiments cannot exactly mirror the ion-trapping experiments. As long as atmosphere exposure does not dramatically alter the nanoscale surface roughness, it should still be possible to gain valuable information from these types of experiments.

In our first attempt, a series of ex-situ experiments were done with an entirely different set of surface treatment and characterization tools than were used in the original ion trapping experiments. We have found that it is difficult to directly compare and sync up those ex-situ results with the in-situ results presented in this manuscript. At Berkeley we have built a vacuum chamber with a milling, heating and substrate-mounting setup almost identical to the one in the ion-trapping chamber. This could be a valuable system moving forward.

After Trap C underwent a long series of surface treatments and measurement experiments, as presented in Section 7, the trap was retired and brought to an AFM for further analysis. Evidence of hillocks found in these measurements was already presented in Figure 9.16. Additional measurements can be found in Figure 9.25, including an RMS roughness analysis and a topological map of the smoothest area of the trap surface.

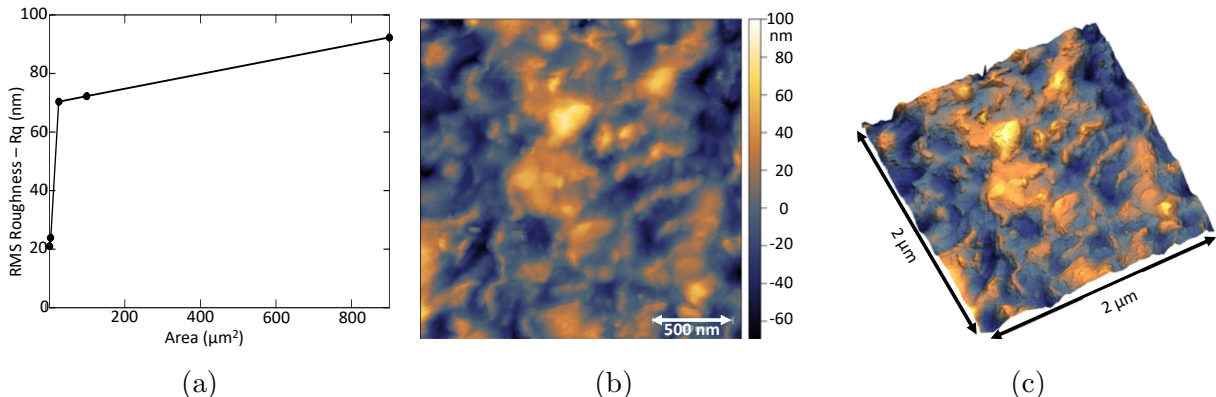


Figure 9.25: AFM measurements of Trap C, taken when the trap was removed from vacuum after [Electron 5](#). (a) RMS roughness versus correlation length. (b) Topology height color map with a  $2 \mu\text{m} \times 2 \mu\text{m}$  measurement area. (c) 3D visualization of (b).

Large topological features on the surface of the trap prevent us from measuring the

sub-nanoscale features that are most relevant to individual atomic TAFs. Some of the large features were likely brought on by heat treatments and ion milling, while others were introduced during the fabrication process. An SEM image of an ion trap, at the intersection of the metal surface and one of the trenches, is shown in Figure 9.26. Before this image was taken, this trap was baked in vacuum at 430 K for a total of 9 weeks, and underwent no further surface treatment. In this image,  $\mu$ m-scale features are visible.

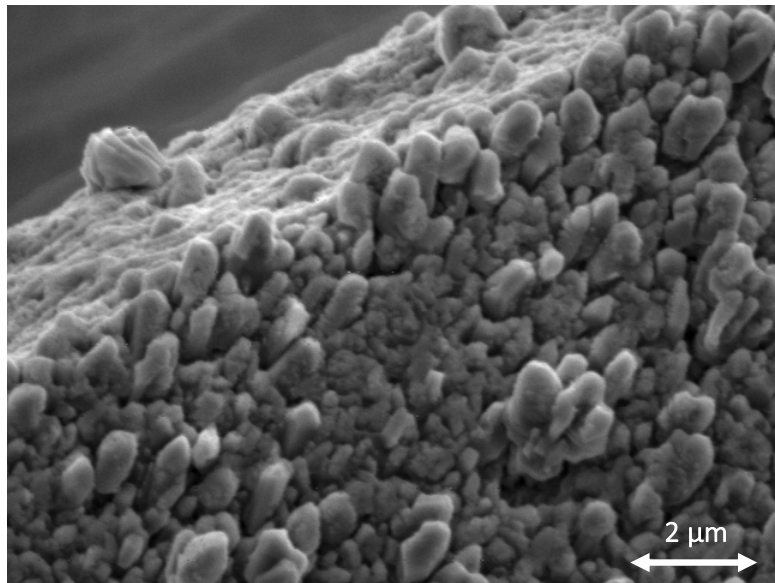


Figure 9.26: SEM of ion trap surface at edge of trench. This trap was baked for 9 weeks at 430 K under 5e-8 Torr vacuum before this image was taken.

Our ion-trap fabrication process, as it is currently implemented, is not conducive to the formation of a smooth metal film. We evaporate at a  $45^\circ$  angle, which has been known to enhance shadowing effects and grow bumpy surfaces [26]. The background pressure in the evaporation chamber during our deposition process is around 5e-7 Torr. Experiments by Chang et. al. showed that hillocks form during evaporation if the chamber pressure is higher than 1e-7 Torr [57]. Before taking measurements of sub-nanometer surface features, we would have to alter our metal deposition process to produce a much smoother film.

## 9.8 Summary

In a series of experiments performed on a single ion trap, we observed that ion heating rates can rise as a result of an in-situ heat treatment. In an effort to illuminate the underlying physics of this thermal transformation, we studied and characterized this process using ion milling, electron bombardment, heating treatments, Auger spectroscopy, and ion-heating-rate measurements.

To characterize the timescale and temperature dependence of the transformation, the trap was held at elevated temperatures while ion heating rates were repeatedly measured. The transformation was found to saturate on a timescale of 1.4 days at 575 K, and secondary transformations were observed at higher temperatures.

Argon ion milling treatments altered the composition of the trap surface, and these changes in composition were tracked with Auger spectroscopy. A correlation was found between the behavior of thermal transformations and the chemical state of the aluminum on the trap surface. If the aluminum was elemental, the noise would transform in response to a heat treatment. If the aluminum was oxidized or nitrogenized, no transformation would take place.

Auger spectra taken before and after thermal transformations allowed us to rule out contaminant deposition as the underlying driver of the rise in noise. Auger spectra combined with electron bombardment treatments allowed us to discount, though not entirely rule out, chemical changes.

All of the measured properties of the thermal noise transformations have been found to be consistent with atomic restructuring taking place on the surface of the trap. After studying how sub-nanoscale topology evolves with milling and heating, we conclude that heating raises ion heating rates by recrystallizing the surface, and that milling resets this transformation by roughing up the surface. The observed relationship between sub-nanoscale surface roughness and electric field noise may be linked to variations in adsorbate binding energies.

# Chapter 10

## Electron bombardment experiments

In this chapter, we present and discuss the five electron bombardment experiments performed in TRAP C. To our knowledge, this is the only project to-date in which electron bombardment has been used as a surface treatment to study electric-field noise in ion traps.

First, we present an overview of experimental results including Auger spectra and ion-heating-rate data taken before and after electron treatments. Next, we review literature that explores interactions between energetic electrons and materials such as metals, oxides, and organic molecules. We then discuss various dynamic processes that take place in solid-state systems and that can be modeled as thermally activated fluctuations (TAFs). Using the TAF model as a link between ion-heating-rate measurements, electron damage mechanisms, and atomic dynamics, we develop a set of hypotheses regarding the underlying physics taking place during each electron treatment.

The chemical and morphological properties of the trap surface were different in each of the electron bombardment experiments. As a result, each treatment affected ion heating rates in a different way. Sometimes heating rates rose, sometimes they fell, and sometimes they rose at some temperatures and fell at others. To explain this behavior, we hypothesize that many different surface properties affect surface electric-field noise, and that each electron treatment affected these properties in a different way. At the end of this chapter, we propose experiments to investigate some of these surface properties and electron effects more systematically.

### 10.1 Overview of experimental results

We performed five electron-bombardment experiments in Trap C. This section will include details of treatment parameters, ion-heating-rate data taken before and after electron bombardment, and a description of the physical state of the substrate at the beginning of each treatment. This will serve to focus the investigation of electron-material interactions in Section 10.2. The in-depth discussion and interpretation of these results will be reserved for Section 10.3.

### 10.1.1 Treatment parameters

The electron-bombardment experiment procedure went as follows, with a slight variation in treatment Electron 1:

1. Measure ion heating rates as a function of trap substrate temperature
2. Generate a 2 keV electron beam by passing a current though a filament
3. Align the beam to the ion-heating-rate measurement region of the trap
4. Bombard the substrate with electrons while recording the Auger spectrum
5. Measure ion heating rates as a function of trap substrate temperature

In treatment Electron 1, the electron beam bombarded the ion-heating-rate measurement region of the trap for approximately five minutes, and was then redirected to a new location on the substrate for the duration of the three-hour Auger measurement.

Table 10.1: Electron bombardment surface treatment parameters

Treatment	Energy deposited (kJ/cm <sup>2</sup> )	Duration (hr)	Current density (mA/cm <sup>2</sup> )	Beam energy (keV)
Electron 1	2	0.1	2.8	2
Electron 2	76	3.0	3.5	2
Electron 3	176	3.2	7.6	2
Electron 4	281	3.2	12.2	2
Electron 5	2130	23.0	12.9	2

When the electron beam in the Auger spectrometer is turned on, the pressure in the vacuum chamber rises from 1e-10 Torr to 1e-8 Torr. In Figure 10.1 we present typical RGA spectra showing a rise in peaks at 2, 12, 15, 16, and 28 amu as the electron filament is beginning to heat up. This rise in pressure is likely caused by outgassing of the tungsten filament, in combination with electron induced desorption.

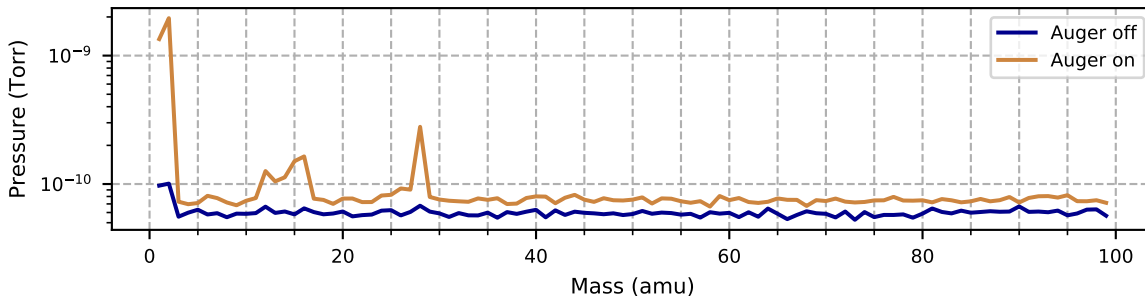


Figure 10.1: Turning on the electron beam in the Auger spectrometer releases compounds of mass 2, 12, 15, 16, and 28 amu. 

### 10.1.2 Substrate properties

The five electron-bombardment experiments executed on Trap C were interspersed with other surface treatments. As a result, at the beginning of each electron treatment, the substrate had a unique set of physical properties. This section will describe the methods we used to determine those properties, which are summarized in Table 10.2.

Table 10.2: Surface properties of the substrate during electron treatments

Treatment	Carbon at surface	Aluminum at surface	Primary surface material type	Morphology sub-nm scale (presumed)
Electron 1	Graphite	Oxide	Hydrocarbon adsorbates	Unknown
Electron 2	Carbide	Nitride & oxide	Insulator	Mixed
Electron 3	Carbide	Nitride & oxide	Insulator	Rough
Electron 4	Carbide	Elemental	Conductor	Smooth
Electron 5	Carbide	Elemental to Carbide	Conductor to insulator	Smooth

The chemical state of carbon at the surface is determined by comparing measured carbon Auger line-shapes to reference spectra, as shown in Figure 10.2. The Electron 1 Auger matches graphitic carbon, which is consistent with the presence of a thick layer of hydrocarbon contamination on the surface of the trap. Between treatments Electron 1 and Electron 2, the graphitic carbon was milled away from the surface, leaving behind a small amount of carbidic carbon. This is evidenced by the relative surface fractions in Figure 10.3, and by the Auger line-shapes in Figure 10.2.

The chemical state of aluminum is determined through consideration of the shape of the measured Auger spectrum (Figure 10.4a-c), the energy shift of the aluminum signal (Figure 10.4d), and the elemental composition of the trap surface (Figure 10.3).

During treatment Electron 1, the aluminum signal was lower in energy and there was a large concentration of oxygen on the surface, indicating that the aluminum was oxidized. During treatments Electron 2 and Electron 3, the aluminum line-shapes matched the reference spectrum of aluminum nitride (Figure 10.4a,c). There were significant fractions of both nitrogen and oxygen present on the trap, and no other metals for them to bind to (Figure 10.3b,c). It follows that during these treatments the aluminum was bound with both nitrogen and oxygen.

The aluminum spectra measured during treatments Electron 4 and Electron 5 match the elemental aluminum reference spectrum (Figure 10.4a,b). The presence of elemental aluminum is consistent with surface compositions presented in Figure 10.3d,e, as they indicate that the contaminant fractions were low at the start of both of these electron treatment experiments. However, during treatment Electron 5, a rise in the carbidic carbon signal indicates that the top monolayer of aluminum was transformed into aluminum carbide (Figure 10.5).

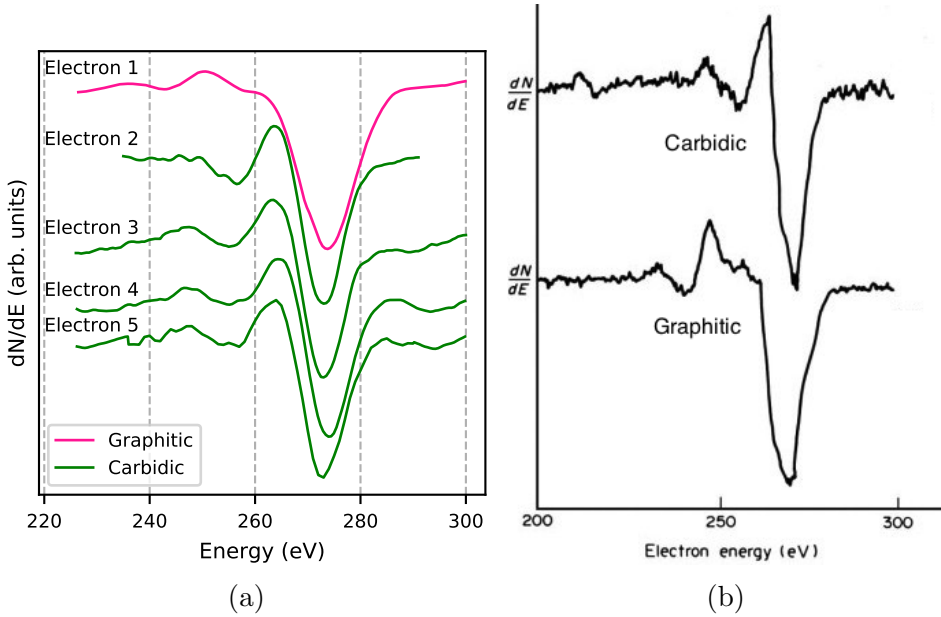


Figure 10.2: (a) Auger spectra of carbon measured during electron treatments (normalized)  
(b) Reference spectra of graphitic and carbidic carbon [61].

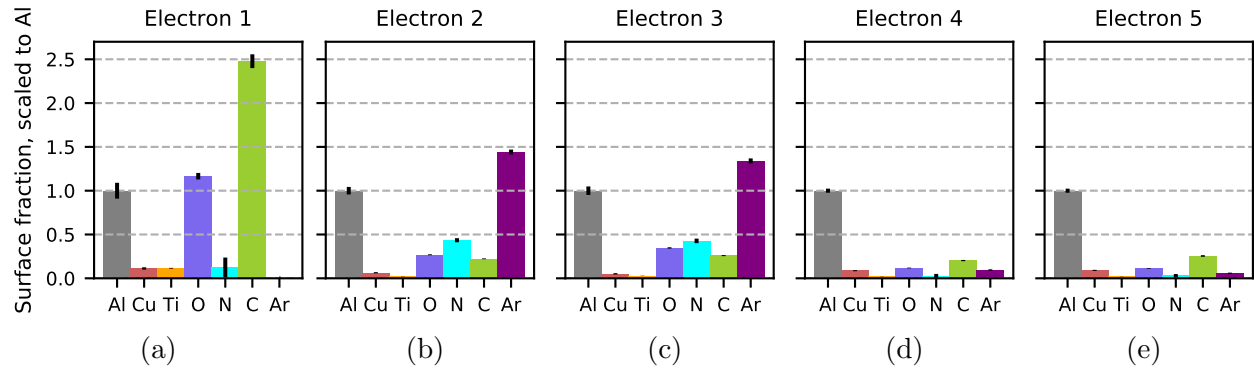


Figure 10.3: Elemental composition of the trap surface at the start of each electron treatment

In Figure 10.5, we present surface fractions of aluminum, argon, carbon and oxygen as they evolve due to heat treatments and electron bombardment experiments. This data begins with the Auger spectrum measured immediately after the final argon milling treatment (Mill 12), and ends with the final measurement of treatment Electron 5. The oxygen fraction remains constant throughout all of these experiments, the argon fraction decreases during heat treatments, and the carbon fraction rises steadily as a function of electron bombardment time.

Auger electrons from aluminum and carbon are able to escape from depths of five and ten monolayers respectively [33]. From the beginning of Electron 4 to the end of Electron 5, the aluminum fraction dropped by 25%, and the carbon fraction rose from 0.1 to 0.3. From these numbers, we estimate that between one and two monolayers of carbon were deposited. As the carbon detected by the Auger was carbidic, the top surface of the aluminum must have transformed into aluminum carbide.

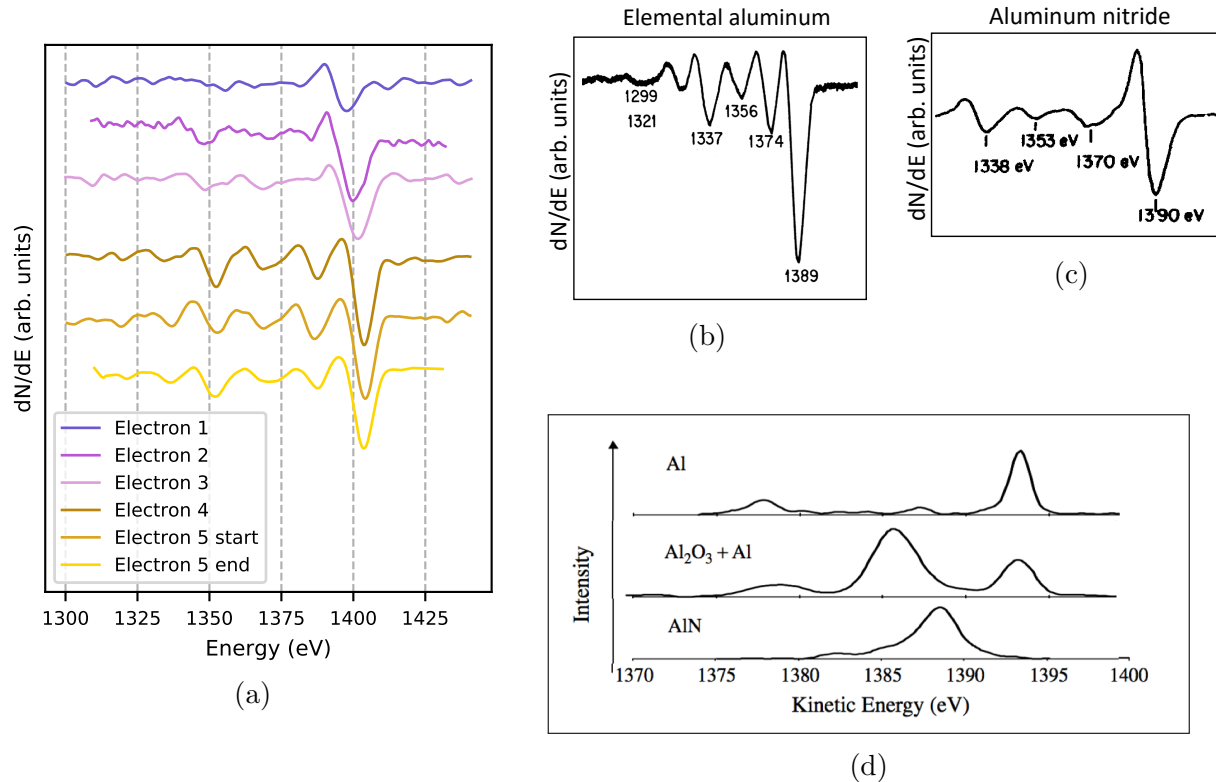


Figure 10.4: (a) Measured aluminum Auger spectra. (b) Reference spectrum of elemental aluminum [34]. (c) Reference spectrum of aluminum nitride [50]. (d) Reference showing relative peak positions of aluminum, aluminum oxide, and aluminum nitride [51].

It is not unusual for electron beams to deposit carbon onto metal surfaces. This phenomenon, commonly referred to as *electron beam induced deposition* (EBID), will be discussed in detail in Section 10.2.

In addition to determining the chemical state of the trap surface during each electron treatment, we also use information about the trap history to determine its probable morphological state. In Chapter 9, we presented evidence that argon milling reduced ion heating rates in part by increasing sub-nanoscale surface roughness, and that heat treatments raised ion heating rates by smoothing out the surface. To determine the topological state of the surface during each electron treatment, we consider the effects of the heating and milling experiments that preceded it. The context in which each electron treatment took place can be found in Chapter 7, and is simplified and summarized here in Figure 10.6.

We do not make a statement regarding the morphology during Electron 1 due to lack of information. Before Electron 2, the trap was thermally transformed and then milled. The milling dose was small and did not entirely return the heating rates to their pre-transformation state, so we designate the topology at the start of Electron 2 as a mix between rough and smooth (at the sub-nanometer scale). Electron 3 took place after extensive milling, and a transformation-free heat treatment, so the trap surface was most likely rough at that time. Electron 4 and 5 followed a thermal transformation in which the ion heating rates rose by a factor of three, indicating that the trap had smoothed out.

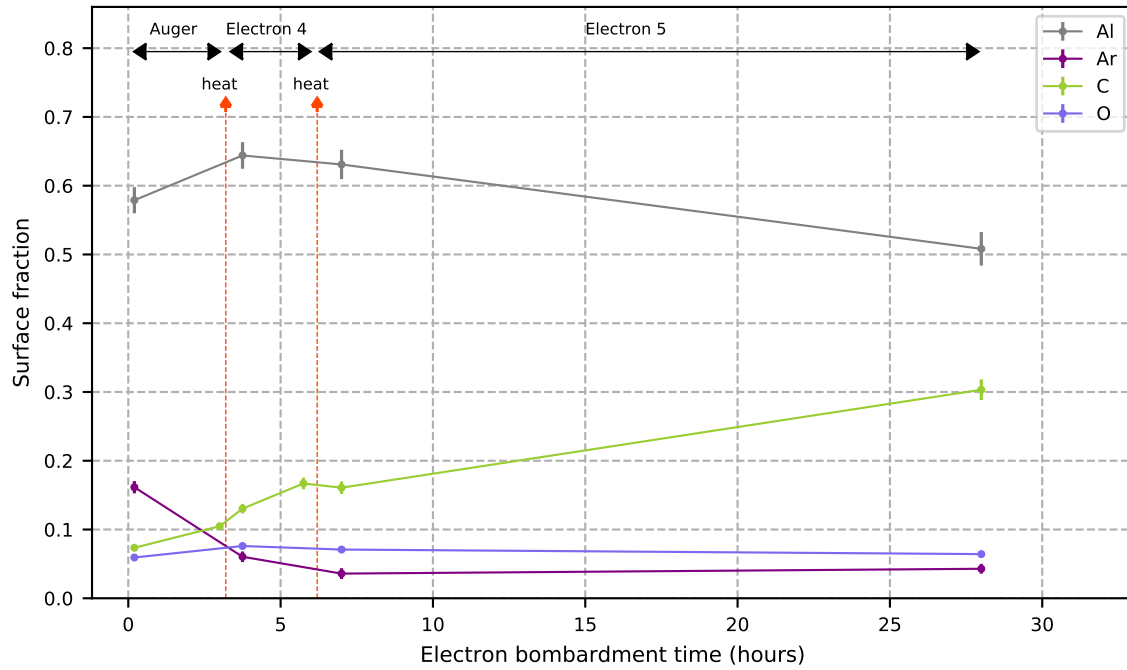


Figure 10.5: Surface fractions of the dominant materials on the trap surface plotted as a function of electron bombardment time.

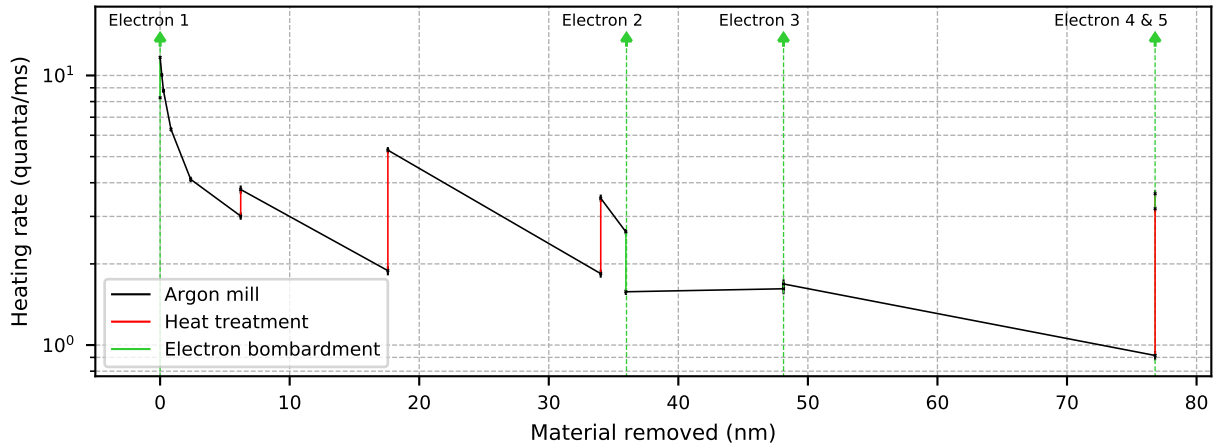


Figure 10.6: Heating rates measured at room temperature as the trap was treated.

### 10.1.3 Heating rate measurements

We have discussed the wide variety of conditions under which electron treatments took place. In Figure 10.7, we present heating rate measurements taken before and after these treatments.

In each case, the electron treatment had a different effect on the temperature scaling. In treatment Electron 1, room-temperature heating rates rose, and high-temperature heating rates fell. Treatment Electron 2 caused heating rates at all temperatures to fall by 40%. The effects of Electron 3 and Electron 4 were similar, raising heating rates only at high temperatures, but Electron 5 had the opposite effect, lowering heating rates slightly at high

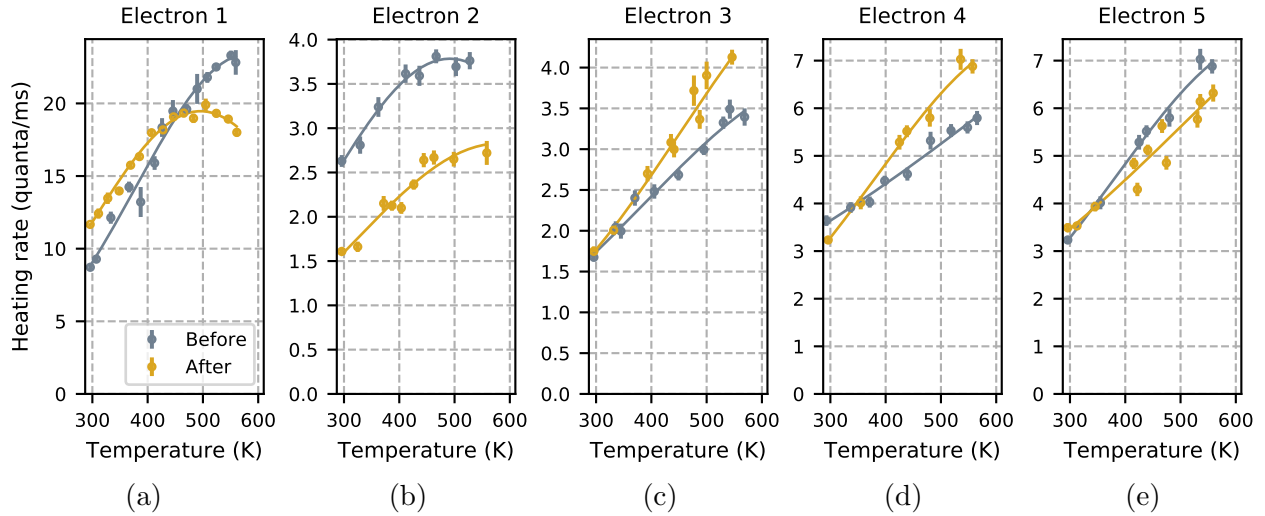


Figure 10.7: Temperature scalings measured before and after electron bombardment

temperatures.

Figure 10.8 combines data from Figures 10.7 and 10.5 to draw attention to the fact that as carbon built up on the surface of the substrate, the ion heating rate at room temperature did not change.

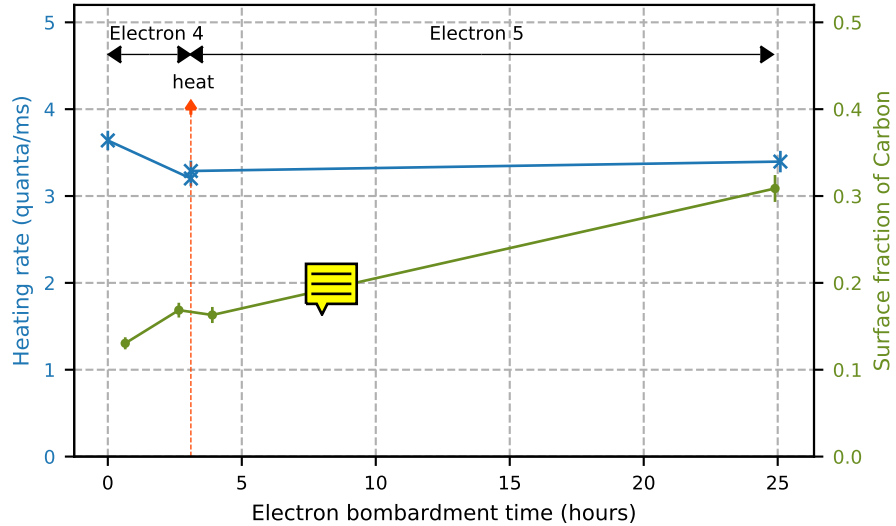


Figure 10.8: Heating rate and carbon fraction versus electron bombardment time.

In this section, we have presented a diverse set of experiments and data. In order to use these results to develop insight into the nature of electric-field noise in ion traps, we must determine what types of physical changes took place in the substrate as it was bombarded with electrons.

## 10.2 Materials interacting with energetic electrons

When a beam of energetic electrons bombards the surface of a material, three types of damage take place: knock-on damage, radiolysis damage, and damage by induced electric fields [62]. Knock-on damage is the direct transfer of momentum from an electron to an atom. This momentum knocks the atom out of its place in the lattice. In contrast, radiolysis damage is driven by electron-electron interactions. The incoming electrons excite and ionize atoms, breaking bonds and leaving behind reactive fragments that reform into new chemical structures. Unlike knock-on and radiolysis damage, which take place on the atomic scale, damage by induced electric fields (DIEF) can drive large-scale transformations. If the electron beam charges up the material at its point of impact, an electric-field gradient forms in the material. This gradient drives the collective motion of atoms towards or away from the electron beam.

Our ultimate goal is to determine how our electron beam drives changes in electric-field noise in our system. In order to do this, we must first narrow down which damage processes are taking place. We consider separately how an electron beam such as ours interacts with the three primary material types present in our substrate: conductors, insulators, and organic contaminants. We also discuss electron beam induced deposition, which is a consequence of energetic electrons interacting with gas molecules.

### 10.2.1 Conductors

Radiolysis damage takes place when electrons excite and ionize atoms, making them mobile and chemically reactive. In order for this to damage a material, the atoms must remain ionized for an extended period of time. Displacement takes place on a timescale of picoseconds. In a good conductor such as aluminum, ionization relaxation takes place on a femtosecond timescale. This does not leave enough time for displacement, so the material remains undamaged [62]. This also means that DIEF is not a problem in conductors. A damage-inducing electric-field gradient cannot form if ionized atoms relax on a picosecond timescale.

Knock-on damage does not require sustained ionization, but it only takes place if the electron energy exceeds a material-dependent threshold. This threshold can be calculated from the atomic displacement energy. Aluminum atoms have a displacement energy of 25 eV in the bulk [63], and about 5 eV at the surface [62]. From the surface displacement energy, and equations from reference [62], we calculate a knock-on threshold energy of 60 keV. As this is thirty times greater than the energy of our electron beam, no knock-on damage of metals can take place in our system.

### 10.2.2 Insulators

In insulators such as aluminum oxide and aluminum nitride, the dominant effect of a 2 keV, 10 mA/cm<sup>2</sup> electron beam is radiolysis damage. Insulators have long ionization relaxation times. For example, aluminum oxide relaxes on the timescale of minutes [62]. This is many of orders of magnitude longer than the picoseconds required for radiolysis damage.

Both DIEF and the thermal effects of radiolysis have been known to bring on collective atomic transformations such as phase changes, phase decomposition, and nanocrystal pre-

cipitation. However, since we use an electron beam with a current density of  $10 \text{ mA/cm}^2$ , we will not see any of these collective effects. In order to drive collective motion, the current density would need to be at least two orders of magnitude higher [62].

When radiolysis breaks bonds between atoms in the bulk of a material, new bonds quickly form, leaving little lasting damage. In contrast, bond-breaking at the surface of a material can lead to significant mass loss through electron stimulated desorption [64]. Electron stimulated desorption is distinctly different from electron sputtering. Electron sputtering refers to the removal of surface atoms through knock-on damage, and it can only be caused by high-energy electrons. In contrast, the typical threshold energies for electron stimulated mass loss are between 10 and 40 eV [65].

Electron-stimulated mass loss takes place after the bonds between an atom and the substrate are broken by radiolysis. Most neutral atoms will re-bond, but many ionized atoms will be repelled from the substrate by the charged-up surface. Low-mass atoms such as hydrogen, oxygen and nitrogen are preferentially removed by this process [64]. This can lead to an increase in atomic-scale surface roughness, as well as changes in the chemical composition of the surface. Electron decomposition of metal oxides takes place on the timescale of a few hours in experiments like ours [65].

### 10.2.3 Organic contaminants

Hydrocarbon contaminants are ubiquitous on unmilled ion trap surfaces. These molecules are deposited during atmosphere exposure, during imperfect handling, and during baking as oils outgas from vacuum-chamber components. Hydrocarbon molecules are strongly affected by radiolysis damage. This damage can manifest in a system such as ours through processes such as bond cleavage, cross linking, and mass loss.

Electrons cleave bonds and break down hydrocarbons through dissociative electron attachment, dipolar dissociation, and dissociation ionization. In other words, a hydrocarbon can fragment when it absorbs an electron, when it absorbs energy from an electron, and when one of its electrons is knocked out by another electron. From the discussion of damage thresholds in reference [65], we estimate that a 2 keV,  $10 \text{ mA/cm}^2$  electron beam will take about five minutes to do significant damage to a monolayer of adsorbates.

Hydrogen desorption is the primary hydrocarbon damage mechanism, as it leaves behind chemically reactive, unsaturated hydrocarbons. Electron bombardment can cause a set of distinctly independent structures on the surface of a substrate to form a single, tangled, cross-linked web [66]. Some unsaturated hydrocarbon fragments bond to the metal substrate directly and form carbidic surface layers. Others break off and desorb from the surface.

A hydrocarbon adsorbed to a metal surface has a hydrogen desorption resonance at 10 eV [67]. This is the energy at which electrons can most efficiently cleave carbon-hydrogen bonds. Electrons from our 2 keV beam are not in this energy regime. However, during an electron treatment, Auger electrons and inelastically scattered electrons with energies close to 10 eV can easily break apart carbon-hydrogen bonds throughout the substrate. In some cases, higher energy electrons may also affect hydrocarbon structures directly [68].

#### 10.2.4 Electron beam induced deposition

In the absence of energetic electrons, an aluminum substrate stored in UHV builds up a thin native oxide layer and a thin coating of saturated hydrocarbons. After about a monolayer of coverage, additional contamination slows dramatically as there are no unterminated bonding sites for new contaminants to attach to. In contrast, when energetic electrons are introduced to this system, a thick layer of carbon contamination can form through a process called electron beam induced deposition (EBID).

Hydrocarbons in the gas phase have a dissociative ionization cross-section peak at about 100 eV [69], and have significant interaction cross sections at higher energies as well. When a 2 keV electron beam passes through the background gas in a vacuum chamber, the gas molecules break apart into chemically reactive fragments. After passing through the gas and reaching the substrate, electrons activate bonding sites by breaking chemical bonds and removing hydrogen atoms. Ultimately, when the gas-state fragments hit the electron-activated substrate, they stick quickly and easily, and a thick contamination layer builds up. Layers of carbon formed through EBID are commonly found in electron microscopy experiments [68].

In our system, when the electron filament in the Auger spectrometer is turned on, the pressure in the chamber rises from 1E-10 to 1E-8 Torr. The electron beam deposits the newly-available gas molecules onto the surface of the ion trap. Evidence of deposition can be found in Auger spectra measured at different stages of treatments Electron 4 and Electron 5, as presented in Figure 10.5. During 28 hours of electron bombardment, EBID deposited between 1 and 2 monolayers of carbon onto the surface of the trap, as discussed in Section 10.1.2.

### 10.3 The underlying physics of five electron treatments

In the previous two sections, we presented the results of five electron bombardment experiments, determined the state of the substrate during each experiment, and discussed the different types of damage that take place when materials interact with energetic electrons. In this section each treatment is considered independently. We use all of the previously-gathered information to develop hypotheses about how the physical properties of the substrate changed during each treatment.

We also reframe all temperature scaling measurements taken before and after electron treatments in the context of the TAF model. We compare the physical changes in the substrate to the measured TAF distribution changes. With these comparisons, we gain new insight into what the TAFs are made out of, and how they generate electric-field noise in ion traps.

To calculate the TAF distribution from a temperature scaling measurement, we must choose an appropriate attempt time  $\tau_0$ . In Chapter 6, we demonstrated how the choice of  $\tau_0$  affects the energy range of an extracted TAF distribution, and we discussed how different physical systems may have different attempt times. Our measurements indicate that both surface adsorbates and sub-surface contaminants may affect the electric-field noise in TRAP C. In this section, we will be directly comparing extracted TAF energies to energy barriers

found in literature. Choosing a single value of  $\tau_0$  with which to analyze all of our data would introduce an unfounded restriction as to which physical processes could be relevant. For this reason, we plot all TAF distributions twice: once with an attempt time of  $10^{-13}$  s, and once with an attempt time of  $10^{-10}$  s.

### 10.3.1 Electron 1

Treatment Electron 1 was five minutes long. Before treatment, the aluminum surface was oxidized and coated with a thick layer of hydrocarbon adsorbates.

#### Physical changes in the substrate

When exposed to an electron beam from an Auger spectrometer, an oxide will become measurably damaged on a timescale of hours. Given that this treatment was five minutes long, oxide damage is unlikely to have been a significant damage mechanism in this case.

In contrast, radiolysis damage to hydrocarbons takes place on a timescale of minutes. Electron-stimulated desorption of hydrogen opens bonding sites on hydrocarbon molecules. This process causes molecules to fragment, cross-link, and form bonds with new elements if they are not quickly re-terminated by hydrogen. A portion of the molecular fragments desorb or, in a system such as ours, bond directly to the metal substrate. After five minutes of electron bombardment, we expect that the hydrocarbon layer in place during treatment Electron 1 would have exhibited measurable damage, but that it would not have been completely transformed.

#### Measured changes in the TAF distribution

As a result of this treatment, the peak of the TAF distribution shifted down in energy by 0.1 eV, while maintaining roughly the same magnitude (Figure 10.9).

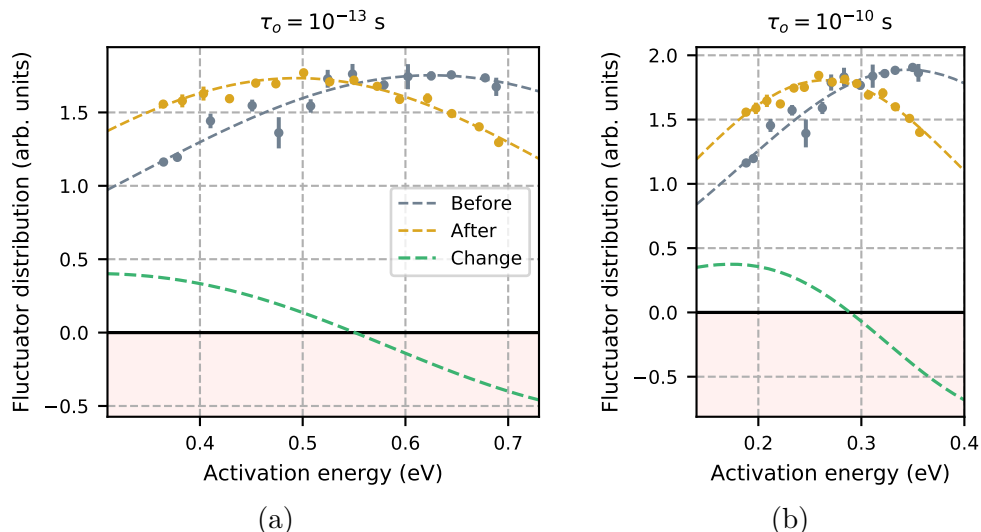


Figure 10.9: Changes in the TAF distribution as a result of treatment Electron 1, plotted using attempt times (a)  $\tau_0 = 10^{-13}$  s, and (b)  $\tau_0 = 10^{-10}$  s.

## Insights into fluctuator physics

In this experiment, we observed a shift in the TAF distribution after electron bombardment altered the chemical structure of hydrocarbon adsorbates. This indicates that hydrocarbon adsorbates contribute to the generation of electric-field noise, and that changing the chemical structure of the hydrocarbons has an effect on the noise.

In Section 6.3 we discussed how a molecular adsorbate hopping between binding sites on a surface could generate electric-field noise via dipole moment fluctuations. An attempt time of  $\tau_o = 10^{-10}$  s is realistic for hydrocarbon diffusion on metals [43], so we consider the fluctuator distribution in Figure 10.9b. If electric field noise is generated when adsorbates move between binding sites, then the TAF activation energies would correspond to the migration barriers of the adsorbates. After reviewing literature on migration barriers of carbon adsorbates on metal and aluminum oxide substrates [42, 44], we find that the energies of these migration barriers are similar to the TAF energy barriers shown in Figure 10.9b.

In some comparisons of similarly-sized hydrocarbon compounds, the slightly larger structures were found to have higher migration barriers [42]. This may be related to the fact that each C-H group adds about 0.1 eV of Van der Waals attraction between the adsorbate and the metal [70]. With this information, the shift in TAF energies observed during Electron 1 can reasonably be explained by the loss of C-H groups from hydrocarbon compounds due to radiolysis damage. In short, hydrocarbon compounds break up, and diffusion barriers go down.

### 10.3.2 Electron 2

Treatment Electron 2 was three hours long. Before treatment, we expect that the trap was partially smooth given its history. The surface was primarily composed of insulators aluminum nitride and aluminum oxide, and contained a small amount of carbide carbon contamination. A large number of argon atoms were embedded near the surface.

#### Physical changes in the substrate

Three hours of electron bombardment can do measurable damage to aluminum oxide and aluminum nitride through electron stimulated desorption. Preferential desorption of oxygen and nitrogen increases sub-nanoscale surface roughness and alters the chemical composition of the surface. Auger spectra taken 1.5 hours apart during treatment Electron 2 revealed a 20% decrease in the oxygen fraction, and no change in the nitrogen fraction (Figure 10.10). This indicates that preferential desorption of oxygen may have taken place.

Between treatments Electron 1 and Electron 2, the thick layer of hydrocarbon contamination on the surface of the trap was broken apart and removed by argon ion milling. However, some contaminants in the substrate were protected from argon damage. According to our simulations, a 200 eV argon ion beam only penetrates 2 nm into the substrate. Organic contaminants present in caverns or defects throughout the bulk of the film, or bound to the surface behind large morphological features, would not have been affected by the argon beam. In contrast, 2 keV electrons can penetrate 100 nm into an aluminum substrate [71]. Electron 2 was the first large electron treatment, and could have broken apart a large number of organic compounds that had been left intact by previous treatments.

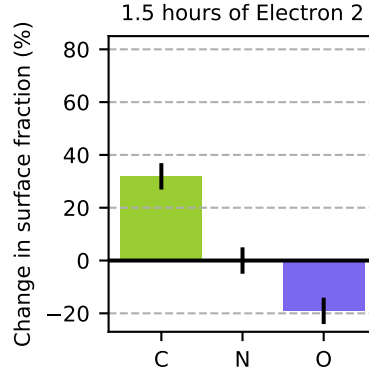


Figure 10.10: Change in the surface fractions of carbon, nitrogen and oxygen during 1.5 hours of treatment Electron 2.

Electron beam induced deposition also took place, as evidenced by the rise in carbon shown in Figure 10.10. Three hours of electron bombardment would have deposited about a quarter of a monolayer of carbon onto the trap surface.

### Measured changes in the TAF distribution

As a result of this treatment, the amplitude of TAFs decreased at all activation energies that we have access to (Figure 10.11). The decrease was most prominent at lower energies.

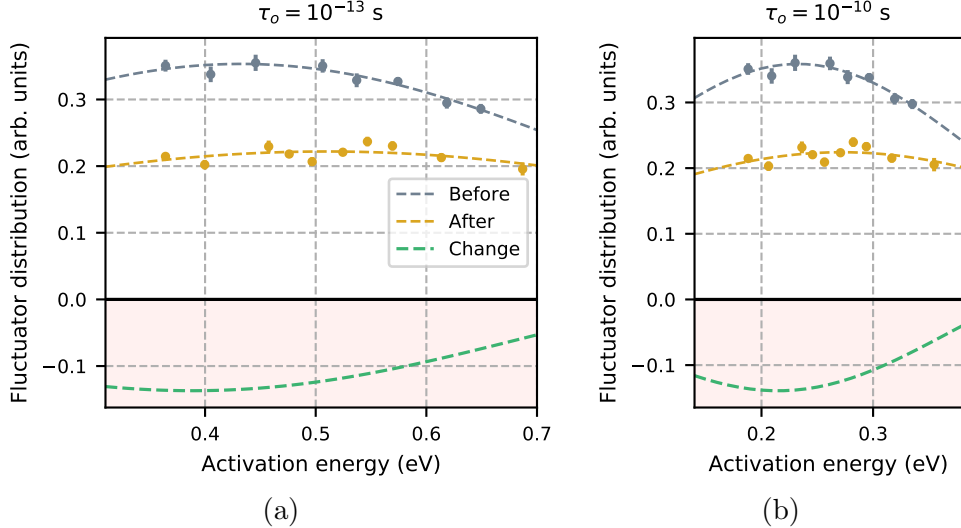


Figure 10.11: Changes in the TAF distribution as a result of treatment Electron 2, plotted using attempt times (a)  $\tau_o = 10^{-13}$  s, and (b)  $\tau_o = 10^{-10}$  s.

### Insights into fluctuator physics

As shown in Figure 10.12, treatment Electron 2 took place after the effects of a thermal transformation had been only partially reset by argon milling. However, after the ion heating

rate at room temperature was lowered by this electron treatment, subsequent argon milling had very little impact. We expect that if the argon milling and electron bombardment noise-reduction mechanisms were independent, the argon treatment following Electron 2 would have continued to lower the ion heating rate. We have established that electron bombardment can increase surface roughness in oxides, and in Chapter 9 we discussed evidence that argon milling likely reduces ion heating rates by increases nanoscale roughness. By extension, we hypothesize that treatment Electron 2 lowered heating rates, at least in part, by increasing sub-nanoscale surface roughness.

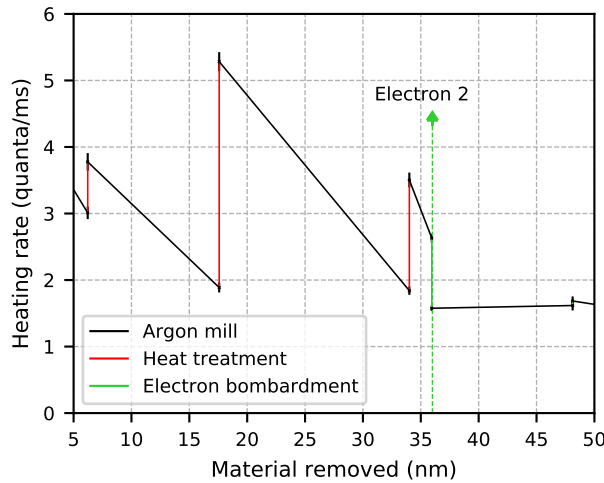


Figure 10.12: Room-temperature heating rates changing in response to surface treatments performed immediately before and after treatment Electron 2.

From the data plotted in Figure 10.12, it is evident that treatment Electron 2 not only counteracted the effects of the previous heat treatment, but also brought the ion heating rates lower than they ever had been before. This could potentially be explained by the electron-induced breakdown of organic contaminants that had been shielded from argon milling ~~damage~~ by large morphological features.

Unlike in treatment Electron 1, there were no complex hydrocarbon adsorbates present on the trap surface after treatment Electron 2. With this in mind, we consider whether defect motion in the substrate could feasibly explain the electric-field fluctuations that we observe. Solid-state defects have an attempt time of  $\tau_o = 10^{-13}$  s, so we consider the TAF distributions plotted in Figure 10.11a. Defects in polycrystalline aluminum and Al/Cu films have been observed to fluctuate with activation energies between 0.4 and 1 eV [40, 41, 39], which is reasonably consistent with the TAF distribution that we observe.

The effects of electron-induced carbon deposition will be explored in detail in the discussion of Electron 3, as there are fewer physical changes to consider in the context of that treatment. In short, we find evidence that EBID can raise the amplitude of high-energy TAFs by a small amount. This may partially explain why treatment Electron 2 reduced the amplitude of low-energy TAFs more than high-energy TAFs.

### 10.3.3 Electron 3

Treatment Electron 3 was three hours long. During this treatment, the surface was primarily composed of insulators aluminum nitride and aluminum oxide, and contained a small amount of carbide carbon contamination. A large number of argon atoms were embedded near the surface. Immediately before Electron 3, the surface was milled extensively and then did not undergo a thermal transformation upon subsequent heating. This means that at the start of Electron 3, the surface was presumably rough on the sub-nanometer scale.

#### Physical changes in the substrate

As described in the context of treatment Electron 2, aluminum nitride and aluminum oxide surfaces can be damaged by electron bombardment via electron induced desorption. Preferential desorption of oxygen and nitrogen can change the chemical composition of the surface, and increase atomic-scale surface roughness. The surface was presumably already rough, so changes to topology during this treatment would have been minimal.

About 12 nm of material was milled off of the substrate between treatments Electron 2 and Electron 3. As 2 keV electrons have a 100 nm penetration depth, and noise sources 100 nm deep in the substrate are well-shielded by the metal, we expect that Electron 3 would not have had much additional impact on noise from any embedded or shielded organic compounds. Three hours of electron bombardment would have deposited about a quarter of a monolayer of carbon onto the surface of the trap.

#### Measured changes in the TAF distribution

As a result of this treatment, the amplitudes of TAFs with activation energies on the high end of our measurement range increased (Figure 10.13).

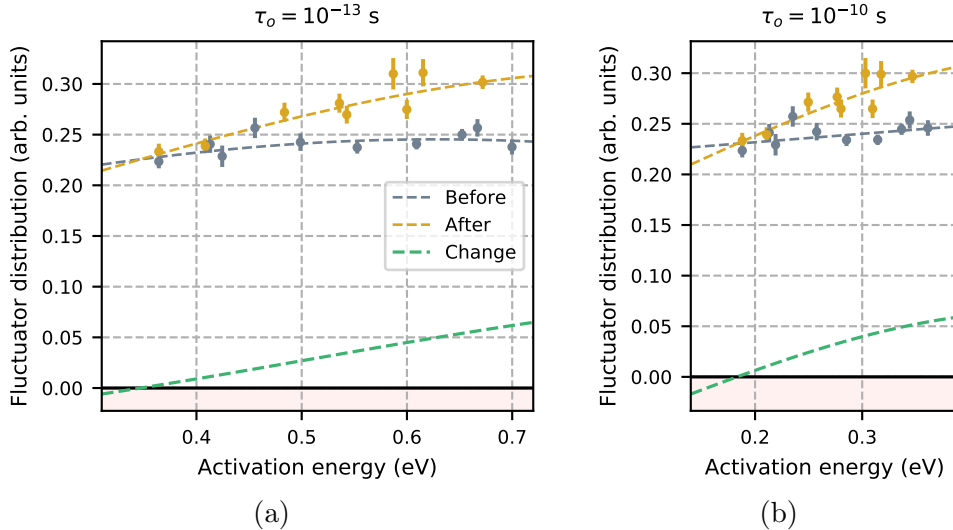


Figure 10.13: Changes in the TAF distribution as a result of treatment Electron 3, plotted using attempt times (a)  $\tau_o = 10^{-13}$  s, and (b)  $\tau_o = 10^{-10}$  s.

## Insights into fluctuator physics

At the start treatment Electron 3, we expect the effects of electron bombardment on shielded hydrocarbons and surface roughness to have already saturated. The processes most likely to be able to alter the TAF distribution at this time are the electron-induced desorption of nitrogen and oxygen, and the electron-induced de~~ep~~sorption of carbon. We will discuss carbon migration barriers in the context of treatment Electron 4, when EBID was the only process that could have affected the TAF distribution.

### 10.3.4 Electron 4

Treatment Electron 4 was three hours long. At the beginning of this treatment the surface was conductive, as it was primarily composed of elemental aluminum. Directly before this treatment, the trap underwent a thermal transformation, so presumably the surface was smooth.

#### Physical changes in the substrate

After three hours of electron bombardment, about a quarter of a monolayer of carbon was deposited on the surface, as evidenced by the rise in the carbon fraction shown in Figure 10.5. The conductive metal could not have been damaged by the electron beam, so the smooth surface morphology would have remained intact throughout this treatment.

#### Measured changes in the TAF distribution

As a result of this treatment, the amplitudes of TAFs with activation energies on the high end of our measurement range increased (Figure 10.13).

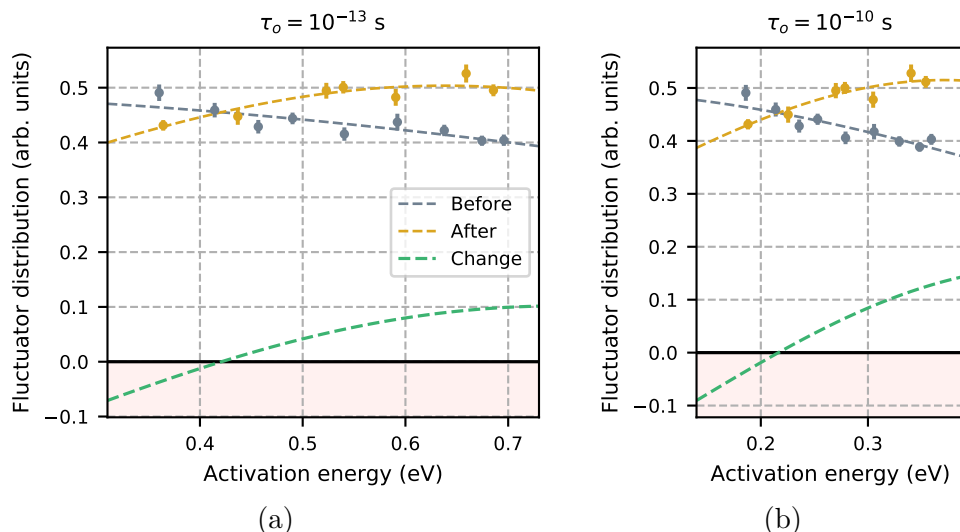


Figure 10.14: Changes in the TAF distribution as a result of treatment Electron 4, plotted using attempt times (a)  $\tau_o = 10^{-13} \text{ s}$ , and (b)  $\tau_o = 10^{-10} \text{ s}$ .

## Insights into fluctuator physics

In treatment Electron 4, the surface was conductive and composed almost entirely of elemental aluminum, so EBID is the only process that could have affected the TAF distribution. About a quarter of a monolayer of carbon was deposited, and the magnitude of high-energy TAFs increased.

Carbon adatoms bond more strongly to metal substrates than complex hydrocarbon molecules do [42]. Single, double and triple bonds between carbon atoms and aluminum substrates have binding energies of 3, 3.3 and 3.8 eV respectively [45]. Migration barriers of adatom adsorbates are typically about 20% of the binding energy [42], which means that the activation energy of a carbon adatom on aluminum is between 0.6 and 0.8 eV. This is consistent with the TAF changes observed in Figure 10.13a.

As shown in Figure 10.13, we observe a small rise in high-energy TAFs after the electron beam deposits about a quarter of a monolayer of carbon onto the trap surface. If carbon deposition is the cause of the increase, this indicates that carbon adatoms can generate electric-field noise at 1 MHz, but only when the temperature of the substrate is elevated. At room temperature, carbon adatoms do not appear to have a significant impact on ion heating rates.

The change in the TAF distribution caused by Electron 4 is similar to the change caused by Electron 3, indicating that EBID was also the dominant driver of TAF changes in treatment Electron 3.

### 10.3.5 Electron 5

Treatment Electron 5 was twenty-three hours long. Before treatment, the trap was atomically smooth. The surface was conductive, as it was composed primarily of elemental aluminum.

#### Physical changes in the substrate

The conductive metal could not have been damaged by the electron beam, so the smooth surface topology would have remained intact throughout this treatment. As shown in Figure 10.15, the surface fractions of nitrogen and oxygen did not change during this treatment, thus confirming that preferential electron-induced desorption did not take place.

After twenty-three hours of electron bombardment, at least one and possibly two full monolayers of carbidic carbon were deposited onto the surface, as evidenced by the rise in the carbon fraction shown in Figure 10.5.

#### Measured changes in the TAF distribution

The amplitudes of TAFs with activation energies on the high end of our measurement range decreased by a small amount (Figure 10.13). There may also have been a small increase in low-energy TAFs.

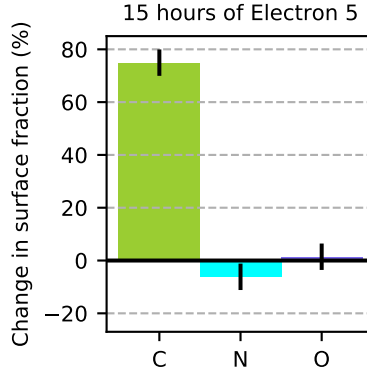


Figure 10.15: Change in the surface fractions of carbon, nitrogen and oxygen during 15 hours of treatment Electron 5.

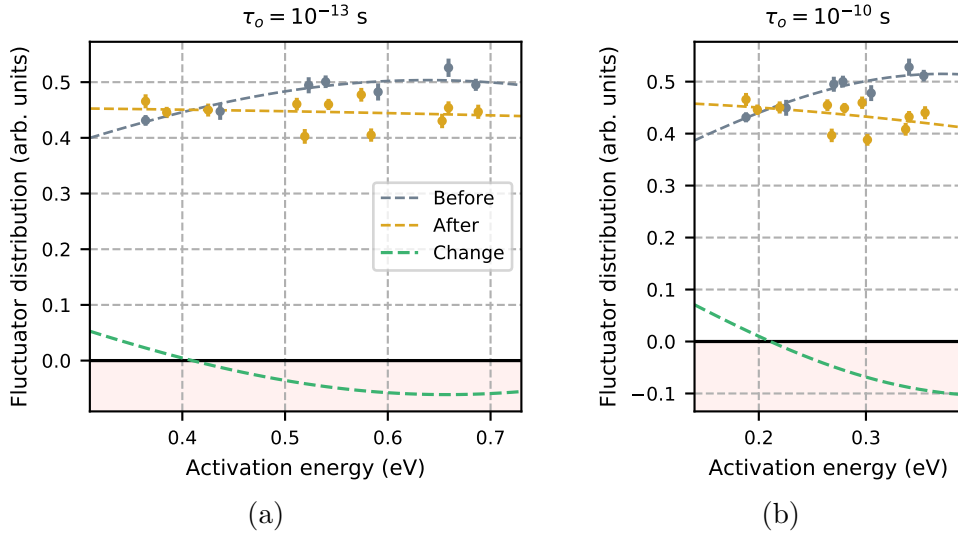


Figure 10.16: Changes in the TAF distribution as a result of treatment Electron 5, plotted using attempt times (a)  $\tau_o = 10^{-13}$  s, and (b)  $\tau_o = 10^{-10}$  s.

### Insights into fluctuator physics

In treatment Electron 5 the trap surface was conductive, so EBID is the only process that is likely to have affected the TAF distribution. Instead of raising the magnitude of TAFs at high energies, as presumably it had done in treatments Electron 4 and Electron 3, this treatment lowered the magnitude of TAFs at high energies.

The key difference between these treatments may be the amount of carbon that was present on the trap surface. Suppose that each carbon atom is a thermally-activated fluctuator. During the entirety of treatments Electron 3 and 4, less than a monolayer of carbon was present on the surface. As a result, each deposited carbon atom was able to move between aluminum bonding sites and generate electric-field noise.

In contrast, by the end of treatment Electron 5, well over a monolayer of carbon had been deposited. This means that the surface could no longer be described as an aluminum surface with carbon adatoms diffusing around. Instead, it had become an aluminum sub-

strate covered with a layer of aluminum carbide. It is not unreasonable that carbon atoms incorporated into a monolayer of aluminum carbide would follow different dynamics than individual carbon adatoms on an unsaturated aluminum surface.

## 10.4 Summary and plans for future work

Hydrocarbons were present during treatment Electron 1, as evidenced by the carbidic carbon signal, and the tendency of hydrocarbon adsorbates to build up on surfaces during extended atmosphere exposure. It has long been suspected that hydrocarbons may be responsible for much of the electric-field noise found in ion traps.<sup>18</sup> Physical models of electric-field noise are generally hydrocarbon-species dependent [1, 18]. While the change in ion heating rates caused by treatment Electron 1 cannot definitively prove that hydrocarbon adsorbates produce electric-field noise, it does establish electron treatments as a powerful tool in the study of noise from hydrocarbon adsorbates.

An experiment that investigates noise from hydrocarbon adsorbates could involve depositing hydrocarbons with a known chemical structure onto the surface of an ion trap, measuring ion heating rates, and then breaking up these structures via electron bombardment. These experiments should be performed on a conductive surface. When a surface has a nonconductive oxide or nitride layer, as it did during treatments Electron 1, Electron 2, and Electron 3, the interpretation of the results are complicated by electron-induced desorption. Electron-induced desorption can increase surface roughness at the sub-nanometer scale, and it can alter the chemical composition of the surface, both of which may affect electric-field noise.

Treatment Electron 2 caused a 40% decrease of heating rates at all measured temperatures. Although most of the hydrocarbon adsorbates would have been broken up and removed by argon milling by this point, the electron beam has a much greater penetration depth than the argon beam (100 nm versus 2 nm), so this electron treatment may have broken apart additional noise-generating contaminants. Given the noise reduction observed in this experiment, it would be interesting to determine whether the combination of electron bombardment and argon ion milling could produce a greater noise reduction than ion milling alone. This should be tested on a substrate in which heating rates have been reduced by argon milling to state-of-the-art levels.

Treatment Electron 2 was performed after a thermal transformation had been partially reversed by milling. As the surface was insulating at this time, electron-induced desorption of light elements could have affected the surface roughness. During this treatment, electrons reduced heating rates at all temperatures to pre-transformation levels, and subsequent milling had no additional impact on room-temperature heating rates. We use this behavior to inform the hypothesis that both argon ion milling and electron bombardment can reduce electric-field noise by increasing sub-nanometer-scale surface roughness.

A series of experiments combining argon milling, thermal transformations, electron bombardment, and strategic oxidation could be used to test this hypothesis. Electron bombardment would be performed on four distinct surfaces: thermally transformed and conductive, thermally transformed and insulating (oxidized), argon-roughened and conductive, and argon-roughened and insulating. Ex-situ surface roughness measurements of similarly-

treated substrates would provide concrete information about the topology of each surface. If electrons reduce heating rates only in the thermally transformed (smooth) and insulating surface, and ex-situ experiments confirm that this is the only case in which electron bombardment increases surface roughness, then this will support our surface roughness hypotheses. If both rough and smooth oxidized surfaces are similarly affected by electron bombardment, this will indicate that electron-induced oxygen removal affects the heating rates directly.

We have already performed the majority of these experiments in treatments Electron 2, 3 and 4. In treatment Electron 2, the surface was insulating and (partially) thermally transformed. In Electron 3 the surface was insulating and argon-roughened, and in Electron 4 the surface was conductive and thermally transformed. Only in Electron 2, the presumably (partially) smooth and insulating case, did the ion heating rates decrease. This indicates that changes in surface roughness, and not electron-induced contaminant removal, caused the heating-rate reduction. In a reproduction of this experiment, we would begin the experiment by saturating the effects of electron bombardment on shielded contaminants, and only then would the desired surfaces be produced.

Treatments Electron 4 and Electron 5 were performed on conductive surfaces composed almost entirely of elemental aluminum, with very little additional contamination. Since elemental aluminum is not affected by radiolysis damage, the electron bombardment should only have been able to affect these surfaces via carbon deposition. The carbon content on the surface is measured directly through Auger spectroscopy. From this data, we estimate that approximately 1/4 monolayer of carbon was deposited by treatment Electron 4, and between 1 and 2 monolayers were deposited by treatment Electron 5. In treatment Electron 4, the magnitude of high-energy TAFs rose by 25%, while in treatment Electron 5, the magnitude of high-energy TAFs fell by 10%. We attribute the rise of TAFs in Electron 4 to the addition of carbon-based fluctuating noise sources. We attribute the fall of TAFs in Electron 5 to a decrease in the fluctuator mobility as the full surface is converted to carbide.

Neither treatment Electron 4 nor Electron 5 had a significant impact on room-temperature heating rates. This is notable given that carbon is thought to play a major role in generating electric-field noise in ion traps.<sup>[1]</sup> To further study noise from carbidic carbon, carbon deposition experiments should be performed on traps with different metal compositions.

# Chapter 11

## High-temperature shoot off

Ion heating rates have been measured in TRAP C at temperatures between 295 and 615 K. When the substrate temperature nears 600 K, the temperature scaling rises sharply. We refer to this feature as the high-temperature shoot off.

### Measurements

The high-temperature shoot off was first observed after treatment Electron 1, and persisted throughout the full series of surface treatment experiments described in this dissertation. It is unclear whether surface treatment Electron 1 directly caused the shoot off to appear, or whether the shoot off became visible only when we were able to take measurements at previously-unreachable temperatures. Direct comparisons of the temperature scalings taken before and after Electron 1 are avoided as the temperature measurement method was altered during this time.

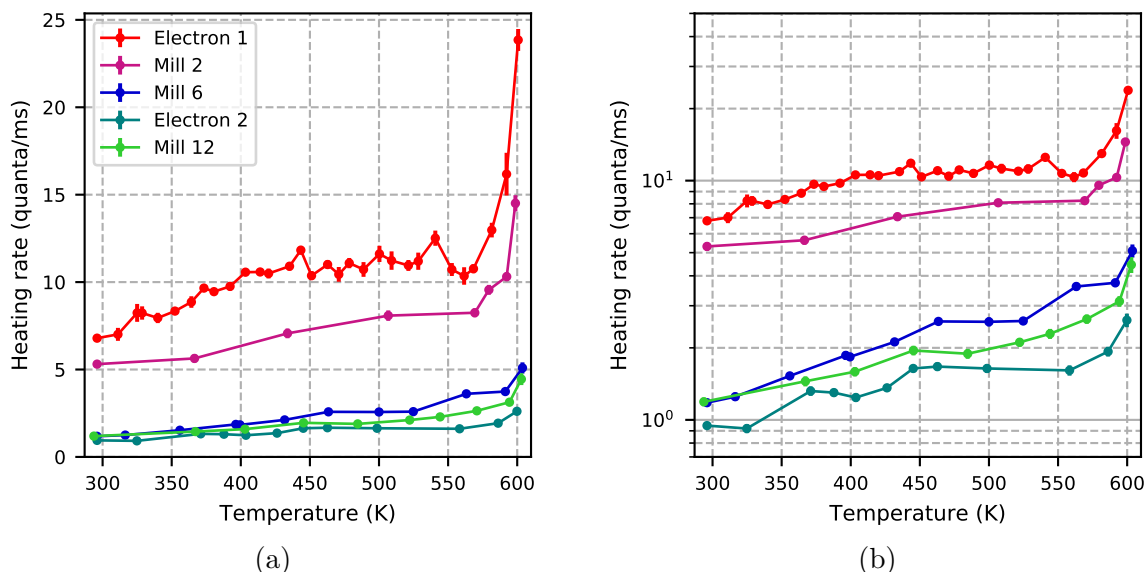


Figure 11.1: Temperature scaling measurements taken at trap frequency  $\omega=1.3$  MHz after surface treatments Electron 1, Mill 2, Mill 6, Electron 2, and Mill 12. (a) Linear/linear scale. (b) Log/linear scale.

A representative set of temperature scaling measurements are shown in Figure 11.1. This figure includes all datasets in which high-temperature measurements were taken at a trap frequency of 1.3 MHz. The high-temperature shoot-off emerges at temperatures between 560 and 590 K. In all cases, the ion heating rates approximately double in magnitude between 550 and 600 K.

The aluminum was oxidized after treatments Electron 1 and Mill 2, elemental after Mill 6 and Mill 12, and nitrogenized after Electron 2. Comparing temperature-scaling plots corresponding to each of these surface treatments (Figure 11.1), it is evident that the temperature and magnitude of the shoot off is not correlated with the chemical state of aluminum on the trap surface.

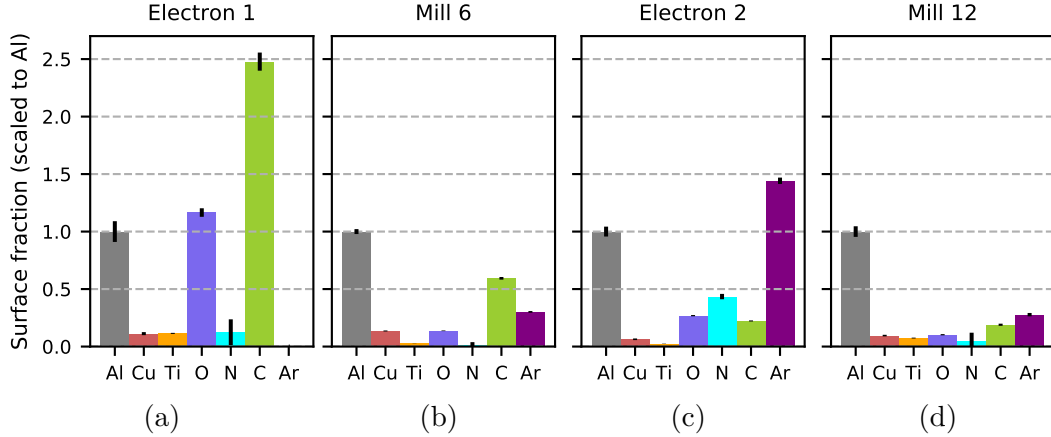


Figure 11.2: Surface composition measurements taken (a) during treatment Electron 1, (b) after treatment Mill 6, (c) during treatment Electron 2, and (d) after treatment Mill 12.

While the temperature of the shoot-off is roughly consistent throughout all measurements, its magnitude decreases as the baseline heating rate decreases. The baseline heating-rate magnitudes were lowered via argon milling, which also reduced the amount of carbon on the surface of the trap. Relevant surface compositions are plotted in Figure 11.2.

The frequency scaling exponent  $\alpha$  at the shoot off was not constant between data sets. Plots of  $\alpha$  as a function of temperature are shown in Figures 11.3b and 11.3d. After Electron 1,  $\alpha$  dropped in magnitude as the heating rates shot up. In contrast, after Mill 12,  $\alpha$  rose at the shoot off. As will be discussed later on, the shoot off measured after Mill 12 was found to be unstable on a timescale of hours, so the measured rise in  $\alpha$  may be an artifact of these dynamic changes.

Figure 11.3 also shows both the measured values of  $\alpha$ , and the  $\alpha$  predictions from the TAF model. The TAF model predicts that an increase in the slope of the temperature scaling will correspond to an increase in  $\alpha$ . The data in Figure 11.3b follows the opposite trend, indicating that the shoot off is not a TAF process. In addition, sharp changes in the temperature scaling slope, as seen at the onset of the shoot off, are not consistent with the TAF model.

The stability of the high-temperature shoot off was measured twice: once after treatment Electron 1, and once after treatment Mill 12. After Electron 1, repeated measurements of ion heating rates at the shoot off yielded consistent results, indicating that the shoot off

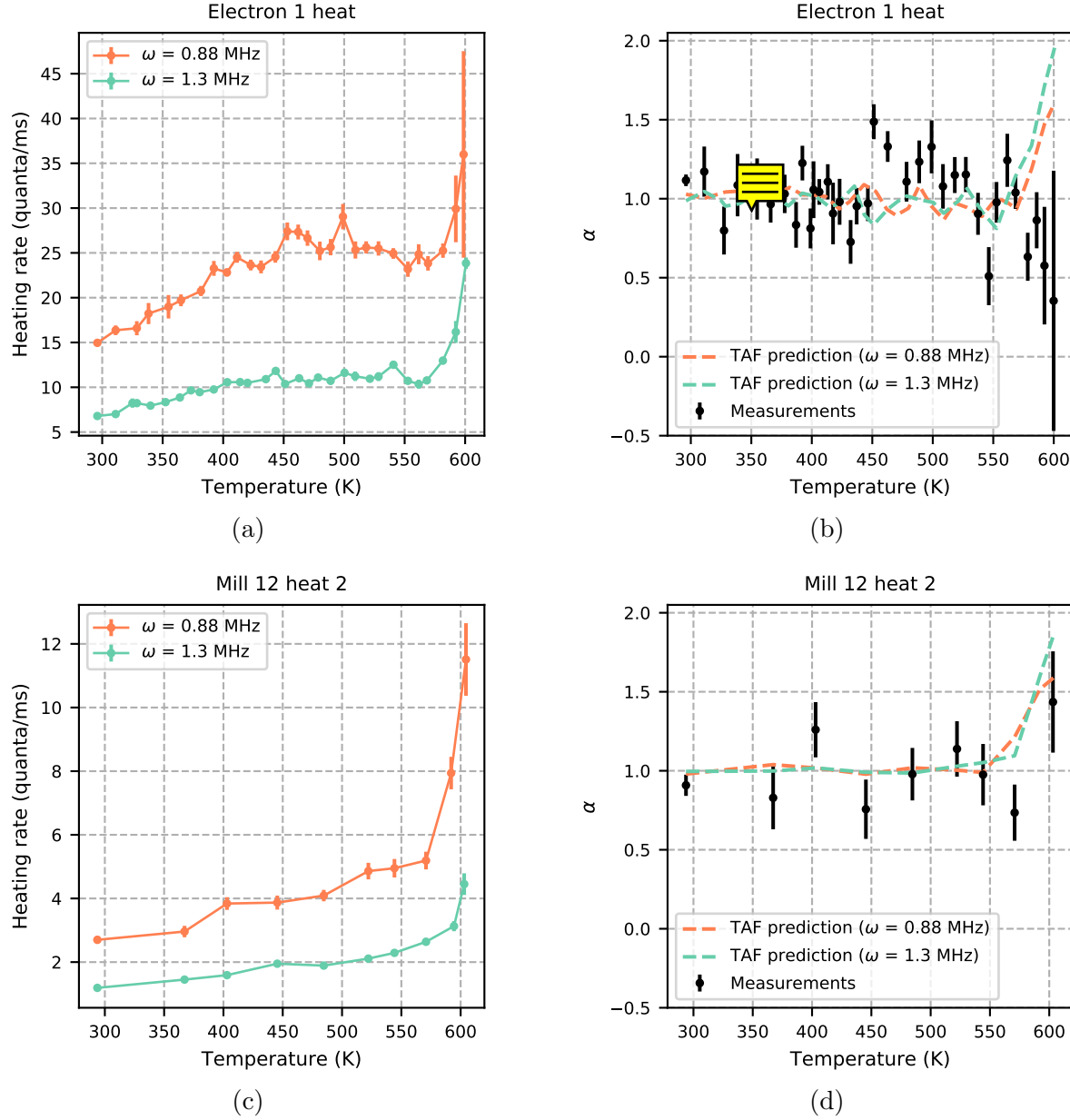


Figure 11.3: (a) Temperature scaling measured at two frequencies after treatment Electron 1. (b) Frequency scaling exponent  $\alpha$  measured as a function of temperature after treatment Electron 1, plotted with the TAF model predictions corresponding to the data plotted in (a). (c) Temperature scaling measured at two frequencies after treatment Mill 11. (d) Frequency scaling exponent  $\alpha$  measured as a function of temperature after treatment Mill 12, plotted with the TAF model predictions corresponding to the data plotted in (c).

was stable. This data is plotted in Figure 11.4b. During this heat treatment, no thermal transformation took place, so ion heating rates measured at temperatures below the shoot off were stable as well.

When the high-temperature shoot off was measured after treatment Mill 12, the magnitude of the shoot off decreased rapidly while the temperature of the trap was held at 605 K.

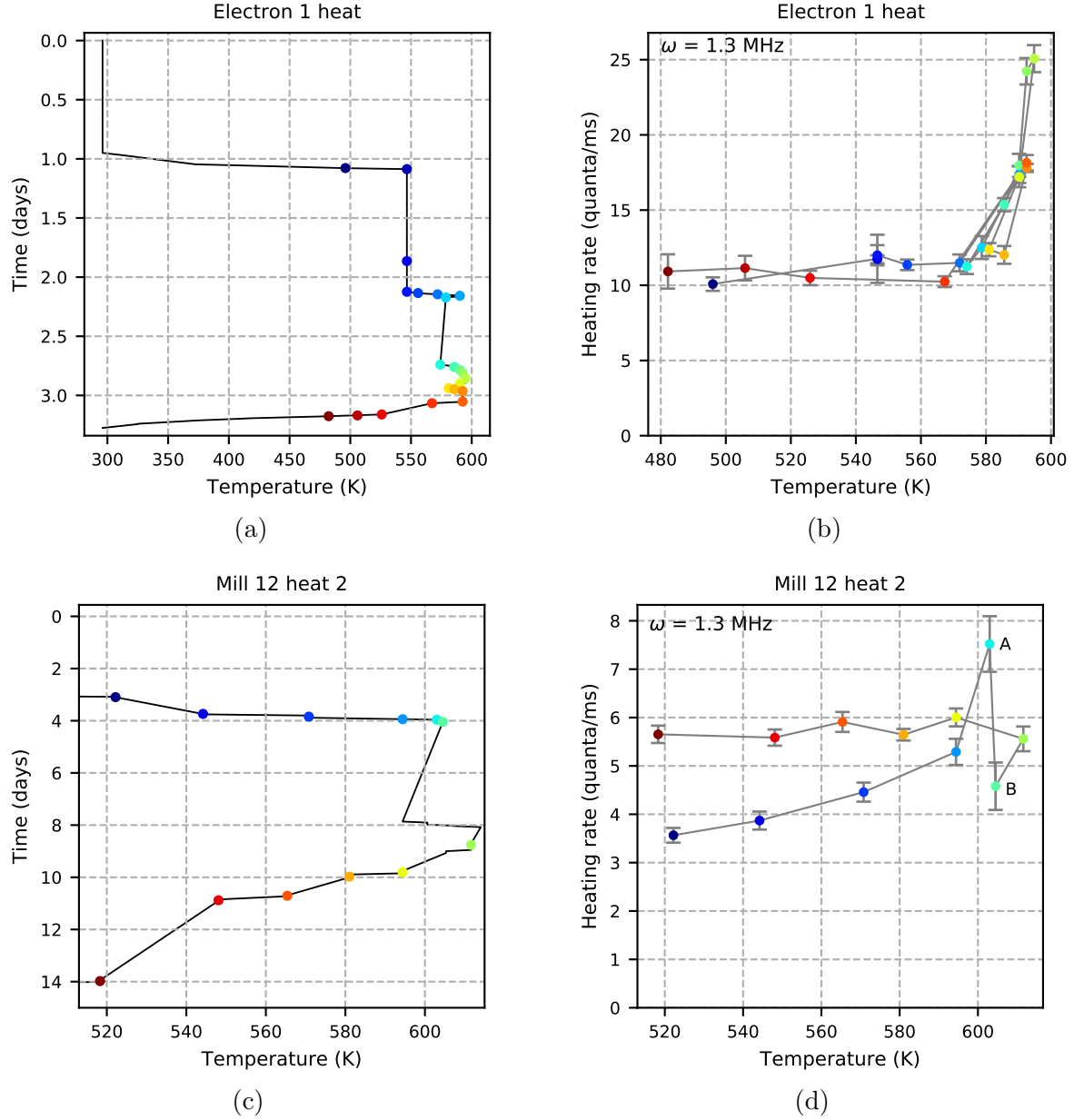


Figure 11.4: Measurements of the stability of the high-temperature shoot off. (a) Details of the heat treatment following Electron 1. (b) Heating rate measurements at the shoot off following Electron 1, when the magnitude of the shoot off was stable. (c) Details of the heat treatment following Mill 12. (d) Heating rate measurements at the shoot off following Mill 12, when the magnitude of the shoot off decreased on a timescale of two hours.

Data points A and B in Figure 11.4d were measured only two hours apart. The rise in heating rates after data point B was caused not by the re-emergence of the shoot off, but by a thermal transformation that affected ion heating rates at all temperatures.

## Discussion

Heating rates shoot up at the same temperatures at which collisions with desorbing gasses cause the ion lifetime to drop. Collisional heating of the ion could explain why heating rates rise as the local pressure at the ion rises. However, earlier temperature scaling measurements taken in the same trap were limited by ion loss at 530 K, and no shoot off was visible at that time ???. The same was true of the temperature scaling measured at the end of the thermal transformation following Mill 12. In addition, as the trap is milled the ion loss behavior remains consistent, while the magnitude of the high-temperature shoot off drops. From this we conclude that the high-temperature shoot off can be driven by the same collisions that drive ion loss.

The magnitude of the high-temperature shoot off is correlated with the magnitude of the low-temperature heating rates. This implies that the low-temperature noise process and the shoot-off noise process are connected. If an entirely new noise mechanism was taking place at high temperatures, then the magnitude of the noise in each temperature regime would be independent.

In our study of thermally driven noise transformations, the transformations began at temperatures between 550 and 580 K when the aluminum surface was elemental. The range of shoot-off emergence temperatures (560 - 590 K) is nearly identical to the observed thermal transformation temperatures. This is an indication that there may be a link between the physics of these processes. However, the temperature and magnitude of the shoot-off is not correlated with the presence or magnitude of the thermal transformation. In the heat treatments following Electron 2 and Mill 12, thermal transformations took place with small and large magnitudes respectively. In the treatments following Electron 1 and Mill 2, there was no thermal transformation. As shown in Figure 11.1, all four of these temperature scalings exhibited high-temperature shoot offs.

# Chapter 12

## Summary and outlook

This dissertation began with an overview of electric-field noise in ion traps. In Chapter 2 we introduced the concept of surface electric-field noise and the basic technology of ion trapping. The reduction of electric-field noise from metal surfaces can enable advances in trapped-ion quantum information processing. A summary of the body of literature that explores the underlying physics of these noise processes is provided.

Chapter 3 describes the micro-fabricated surface ion trap in which our experiments were performed. This description includes the operating principles of RF quadrupole traps, the design of our chip, and the details of our fabrication process. It also includes information on the topology and composition of the trap surface, as characterized by SEM and Auger spectroscopy.

In Chapter 4 we explain how to use a trapped calcium ion as an electric-field-noise detector. The vibrational energy of the ion can be read out via coherent optical manipulation of the ion's electronic energy state. Electric-field noise heats the ion, raising its vibrational energy. This heating rate can be measured and directly translated into the power spectral density of the noise. At the end of this chapter, we describe the specific tools that enable us to execute these optical control techniques, which are standard in the field of ion trapping.

Our experiments are unique in that we perform multiple types of in-situ surface treatments and characterization techniques on a single ion trap. Chapter 5 introduces the tools and methods we use to perform, characterize and interpret these treatments and measurements. The ion trap is heated between 295 and 615 K with a resistive button heater, and the substrate temperature is measured using an infrared camera. Electron treatments are performed using the electron beam in the Auger spectrometer. Fractional atomic surface compositions are calculated from Auger spectra using the ratios between Auger peaks from all visible elements. The ion current is measured continuously throughout each argon milling treatment, and the total dose deposited during the treatment is used to estimate the depth of material removed.

After measuring the temperature and frequency dependence of the surface noise, we find that the noise in our system is consistent with a Thermally Activated Fluctuator (TAF) model. This model provides a mathematical framework for the behavior of noise sources without specifying the physical embodiment of those sources. In Chapter 6 we introduce the TAF model and analyze our data in this context. We have found convincing evidence that the TAF model is relevant to noise in our trap, both before and after surface treatments.

Similar measurements will need to be performed in other ion traps to determine whether or not this model can be applied to metal surfaces more generally.

The experiments described in this dissertation include twelve ion milling treatments interspersed with five electron bombardment treatments. Between each treatment, ion heating rates were measured at multiple frequencies and temperatures, and sometimes the process of heating the trap had a permanent effect on the noise characteristics. In addition, Auger spectroscopy was performed at least twelve times throughout these experiments. Chapter 7 provides a timeline of all data taken and treatments performed. This timeline establishes a naming and numbering convention that is then used to refer to individual measurements and treatments throughout this dissertation.

Chapter 8 compares the noise characteristics of our trap to other surface ion traps. Although the heating rates in our trap are on par with heating rates measured in surface traps in general, our rates are significantly higher than those measured in traps fabricated with identical methods and materials. By studying the histories of four similar traps, we find evidence that heating rates in untreated aluminum/copper traps rise in response to extended atmosphere exposure. We also observe that in our trap, which is referred to as TRAP C, heating rates do not drop in response to argon milling as quickly or as far as they had in a similar trap. We attribute this behavioral difference to the combined effects of atmosphere exposure, which deposited contaminants onto the surface of TRAP C after extended heat treatments, which caused these contaminants to diffuse into the bulk. It is of great use to the ion trapping community to understand how trap storage and heating can affect noise characteristics of ion traps. Further experimentation with traps of different materials can further illuminate which materials and practices are best.

By combining argon ion milling, substrate heating, electron bombardment, and Auger spectroscopy, we are able to isolate, experiment on, and characterize a single type of noise. This noise source and the corresponding experiments are explored in Chapter 9. First we highlight two thermal noise processes: thermal activation, in which the behavior of a noise source is affected by heat, and thermal transformation, in which the properties of the noise source are fundamentally altered by heat. We observe that when an elemental aluminum surface is heated above 550 K for a period of days, a thermal transformation, corresponding to a rise in ion heating rates, will take place. When the aluminum surface is oxidized or nitrogenized, no transformation will occur at these temperatures. The transformation saturates in response to extensive heating, but can be reset by argon ion milling.

In Auger spectroscopy studies performed before and after transformations, we find no evidence that the thermal transformations are driven by deposition of material or chemical reactions. We explore in detail the hypothesis that thermal transformations are driven by atomic restructuring at the trap surface, and find the data to be consistent with this hypothesis. This work indicates that it may be possible to engineer ion trap surface morphology to minimize noise magnitudes. In particular, topological features with sub-nanometer correlation lengths appear to be favorable at room temperature as compared to a recrystallized surface.

In Chapter 10, we describe the results of five electron bombardment experiments. In each experiment, the properties of the trap surface were different, and the parameters of the electron bombardment were changed. As a result, each treatment had a unique affect on the measured ion heating rates. After presenting our measurement results, we review

the physics of how energetic electrons interact with conductors, insulators and organic contaminants. With this foundation, we develop a series of hypothesis to explain the observed behavior of the noise in response to each electron treatment. These hypothesis include electron beam damage to hydrocarbon adsorbates, changes in surface morphology due to electron induced desorption, and changes in surface composition due to electron induced deposition. The data indicates that the magnitude of ion heating rates is tied to the chemical structure of hydrocarbons on the trap surface. Future experimentation is necessary to clarify the role that hydrocarbon adsorbates play in the generation of surface electric-field noise. Promising experiments include controlled deposition of known contaminants and electron-induced destruction of surface adsorbates. Ultimately, understanding how hydrocarbon structure can impact surface electric-field noise may lead to the engineering of noise-stabilizing surface coatings.

At temperatures between 560 and 600 K, ion heating rates rise sharply. We refer to this phenomenon as the high-temperature shoot off, and it is discussed in Chapter 11. The temperature of the onset of the shoot off was consistent throughout all measurements, but the frequency scaling exponent and the stability of the shoot-off amplitude varied between measurements. The amplitude of the shoot off is proportional to the amplitude of heating rates at low temperatures, but unlike the low-temperature heating rates, the shoot-off is not consistent with the TAF model. The shoot off temperature is consistent with the temperature of thermal transformations, but unlike thermal transformations the presence of the shoot off was not intermittent. Measurements of high-temperature electric-field noise in different ion traps with different materials may further illuminate the underlying physics of the shoot off.

# Bibliography

- [1] M. Brownnutt et al. “Ion-trap measurements of electric-field noise near surfaces”. In: *Reviews of Modern Physics* 87.4 (Dec. 2015), pp. 1419–1482. ISSN: 0034-6861. DOI: [10.1103/RevModPhys.87.1419](https://doi.org/10.1103/RevModPhys.87.1419). arXiv: [1409.6572v1](https://arxiv.org/abs/1409.6572v1). URL: <http://link.aps.org/doi/10.1103/RevModPhys.87.1419>.
- [2] Colin D. Bruzewicz et al. “Trapped-ion quantum computing: Progress and challenges”. In: *Applied Physics Reviews* 6.2 (June 2019), p. 021314. ISSN: 19319401. DOI: [10.1063/1.5088164](https://doi.org/10.1063/1.5088164). arXiv: [1904.04178](https://arxiv.org/abs/1904.04178).
- [3] Ye Wang et al. “Single-qubit quantum memory exceeding ten-minute coherence time”. In: *Nature Photonics* 11.10 (Oct. 2017), pp. 646–650. DOI: [10.1038/s41566-017-0007-1](https://doi.org/10.1038/s41566-017-0007-1). URL: <http://www.nature.com/articles/s41566-017-0007-1>.
- [4] D. J. Wineland et al. “Quantum information processing with trapped ions”. In: *Phil. Trans. R. Soc. Lond. A* 361 (2003), pp. 1349–1361.
- [5] V. M. Schäfer et al. “Fast quantum logic gates with trapped-ion qubits”. In: *Nature* 555.7694 (Feb. 2018), pp. 75–78. ISSN: 14764687. DOI: [10.1038/nature25737](https://doi.org/10.1038/nature25737). arXiv: [1709.06952](https://arxiv.org/abs/1709.06952).
- [6] Crystal Noel et al. “Electric-field noise from thermally activated fluctuators in a surface ion trap”. In: *Physical Review A* 99.6 (June 2019), p. 063427. ISSN: 24699934. DOI: [10.1103/PhysRevA.99.063427](https://doi.org/10.1103/PhysRevA.99.063427). arXiv: [1809.05624](https://arxiv.org/abs/1809.05624). URL: <https://link.aps.org/doi/10.1103/PhysRevA.99.063427>.
- [7] D. An et al. “Distance scaling and polarization of electric-field noise in a surface ion trap”. In: *arxiv:1906:06489* (2019).
- [8] J. A. Sedlacek et al. “Distance scaling of electric-field noise in a surface-electrode ion trap”. In: *Physical Review A* 97 (2018), 020302(R). DOI: [10.1103/PhysRevA.97.020302](https://doi.org/10.1103/PhysRevA.97.020302). arXiv: [1712.00188](https://arxiv.org/abs/1712.00188).
- [9] C. D. Bruzewicz, J. M. Sage, and J. Chiaverini. “Measurement of ion motional heating rates over a range of trap frequencies and temperatures”. In: *Physical Review A - Atomic, Molecular, and Optical Physics* 91 (2015), p. 041402. ISSN: 10941622. DOI: [10.1103/PhysRevA.91.041402](https://doi.org/10.1103/PhysRevA.91.041402). arXiv: [1412.5119](https://arxiv.org/abs/1412.5119).
- [10] Jaroslaw Labaziewicz et al. “Temperature Dependence of Electric Field Noise Above Gold Surfaces”. In: *Physical Review Letters* 101 (2008), p. 180602. URL: <http://journals.aps.org/prl/abstract/10.1103/PhysRevLett.101.180602>.

- [11] J. Chiaverini and J. M. Sage. “Insensitivity of the rate of ion motional heating to trap-electrode material over a large temperature range”. In: *Physical Review A* 89.1 (Jan. 2014), p. 012318. ISSN: 1050-2947. DOI: [10.1103/PhysRevA.89.012318](https://doi.org/10.1103/PhysRevA.89.012318). arXiv: [1310.4385](https://arxiv.org/abs/1310.4385). URL: <http://link.aps.org/doi/10.1103/PhysRevA.89.012318>.
- [12] D. T.C. Allcock et al. “Reduction of heating rate in a microfabricated ion trap by pulsed-laser cleaning”. In: *New Journal of Physics* 13 (2011). ISSN: 13672630. DOI: [10.1088/1367-2630/13/12/123023](https://doi.org/10.1088/1367-2630/13/12/123023). arXiv: [1110.1486](https://arxiv.org/abs/1110.1486). URL: <http://www.njp.org/>.
- [13] N. Daniilidis et al. “Surface noise analysis using a single-ion sensor”. In: *Physical Review B* 89.24 (June 2014), p. 245435. ISSN: 1098-0121. DOI: [10.1103/PhysRevB.89.245435](https://doi.org/10.1103/PhysRevB.89.245435). URL: <http://link.aps.org/doi/10.1103/PhysRevB.89.245435>.
- [14] D. A. Hite et al. “100-Fold Reduction of Electric-Field Noise in an Ion Trap Cleaned with In Situ Argon-Ion-Beam Bombardment”. In: *Physical Review Letters* 109.10 (Sept. 2012), p. 103001. DOI: [10.1103/PhysRevLett.109.103001](https://doi.org/10.1103/PhysRevLett.109.103001). arXiv: [arXiv:1112.5419v1](https://arxiv.org/abs/1112.5419v1). URL: <http://link.aps.org/doi/10.1103/PhysRevLett.109.103001>.
- [15] K. S. McKay et al. “Ion-trap electrode preparation with Ne<sup>+</sup> bombardment”. In: *arXiv:1406.1778v1* (2014). arXiv: [1406.1778](https://arxiv.org/abs/1406.1778). URL: <https://arxiv.org/abs/1406.1778>.
- [16] J A Sedlacek et al. “Evidence for multiple mechanisms underlying surface electric-field noise in ion traps”. In: *Physical Review A* 98 (2018), p. 063430. ISSN: 24699934. DOI: [10.1103/PhysRevA.98.063430](https://doi.org/10.1103/PhysRevA.98.063430). arXiv: [1809.07761](https://arxiv.org/abs/1809.07761). URL: <https://journals.aps.org/prb/10.1103/PhysRevA.98.063430>.
- [17] Robert McConnell et al. “Reduction of trapped-ion anomalous heating by in situ surface plasma cleaning”. In: *Physical Review A - Atomic, Molecular, and Optical Physics* 92.2 (Aug. 2015), p. 020302. ISSN: 10941622. DOI: [10.1103/PhysRevA.92.020302](https://doi.org/10.1103/PhysRevA.92.020302). arXiv: [1505.03844](https://arxiv.org/abs/1505.03844).
- [18] Keith G Ray et al. “Van Der Waals-corrected density functional study of electric field noise heating in ion traps caused by electrode surface adsorbates”. In: *New Journal of Physics* 21.5 (May 2019), p. 053043. ISSN: 13672630. DOI: [10.1088/1367-2630/ab1875](https://doi.org/10.1088/1367-2630/ab1875). arXiv: [1810.10199](https://arxiv.org/abs/1810.10199). URL: <https://iopscience.iop.org/article/10.1088/1367-2630/ab1875>.
- [19] E. Kim et al. “Electric-field noise from carbon-adatom diffusion on a Au(110) surface: First-principles calculations and experiments”. In: *Physical Review A* 95 (2017), p. 033407. ISSN: 24699934. DOI: [10.1103/PhysRevA.95.033407](https://doi.org/10.1103/PhysRevA.95.033407). arXiv: [1610.01079](https://arxiv.org/abs/1610.01079).
- [20] Muir Kumph et al. “Electric-field noise above a thin dielectric layer on metal electrodes”. In: *New Journal of Physics* 18.2 (Feb. 2016). ISSN: 13672630. DOI: [10.1088/1367-2630/18/2/023020](https://doi.org/10.1088/1367-2630/18/2/023020). arXiv: [1511.00624](https://arxiv.org/abs/1511.00624).
- [21] Gebhard Littich. *Electrostatic Control and Transport of Ions on a Planar Trap for Quantum Information Processing*. Masters thesis. ETH Zürich and University of California, Berkeley, 2011.

- [22] Raymond E. March. “An Introduction to Quadrupole Ion Trap Mass Spectrometry”. In: *Journal of Mass Spectrometry* 32.4 (Apr. 1997), pp. 351–369. ISSN: 1096-9888. DOI: [10.1002/\(SICI\)1096-9888\(199704\)32:4<351::AID-JMS512>3.0.CO;2-Y](https://doi.org/10.1002/(SICI)1096-9888(199704)32:4<351::AID-JMS512>3.0.CO;2-Y).
- [23] Wolfgang Paul. “Electromagnetic traps for charged and neutral particles”. In: *Reviews of Modern Physics* 62.3 (July 1990), pp. 531–540. ISSN: 0034-6861. DOI: [10.1103/RevModPhys.62.531](https://doi.org/10.1103/RevModPhys.62.531). URL: <http://link.aps.org/doi/10.1103/RevModPhys.62.531>.
- [24] J. Chiaverini et al. “Surface-electrode architecture for ion-trap quantum information processing”. In: *Quantum Information and Computation* 5 (2005), pp. 419–439. URL: <http://dl.acm.org/citation.cfm?id=2011670.2011671>.
- [25] Yves Bellouard et al. “Fabrication of high-aspect ratio, micro-fluidic channels and tunnels using femtosecond laser pulses and chemical etching”. In: *Optics Express* 12.10 (May 2004), p. 2120. ISSN: 1094-4087. DOI: [10.1364/opex.12.002120](https://doi.org/10.1364/opex.12.002120).
- [26] Angel Barranco et al. *Perspectives on oblique angle deposition of thin films: From fundamentals to devices*. Mar. 2016. DOI: [10.1016/j.pmatsci.2015.06.003](https://doi.org/10.1016/j.pmatsci.2015.06.003).
- [27] Christian Felix Roos. “Controlling the quantum state of trapped ions”. Doctoral thesis. University of Innsbruck, 2000.
- [28] D. Leibfried et al. “Quantum dynamics of single trapped ions”. In: *Reviews of Modern Physics* 75.1 (Mar. 2003), pp. 281–324. ISSN: 0034-6861. DOI: [10.1103/RevModPhys.75.281](https://doi.org/10.1103/RevModPhys.75.281). URL: <http://dx.doi.org/10.1103/RevModPhys.75.281>.
- [29] Crystal Noel. “High temperature studies of electric-field noise in a surface ion trap”. PhD thesis. University of California, Berkeley, 2019. URL: [http://www.physics.berkeley.edu/research/haeffner/publications/Noel%7B%5C\\_%7Dthesis.pdf](http://www.physics.berkeley.edu/research/haeffner/publications/Noel%7B%5C_%7Dthesis.pdf).
- [30] D. Gorman. “Noise sensing and quantum simulation with trapped atomic ions”. PhD Thesis. University of California, Berkeley, 2018. URL: [http://research.physics.berkeley.edu/haeffner/publications/dylan%7B%5C\\_%7Dgorman%7B%5C\\_%7Dthesis.pdf](http://research.physics.berkeley.edu/haeffner/publications/dylan%7B%5C_%7Dgorman%7B%5C_%7Dthesis.pdf).
- [31] Thaned Pruttivarasin. “Spectroscopy , fundamental symmetry tests and quantum simulation with trapped ions”. PhD thesis. University of California, Berkeley, 2014, p. 141.
- [32] Michael Ramm. “Quantum Correlations and Energy Transport in Trapped Ions”. PhD thesis. University of California, Berkeley, 2014.
- [33] John C. Vickerman and Ian S. Gilmore. *Surface Analysis - The Principal Techniques: Second Edition*. John Wiley and Sons, Mar. 2009, pp. 1–666. ISBN: 9780470017630. DOI: [10.1002/9780470721582](https://doi.org/10.1002/9780470721582).
- [34] G. E. McGuire. *Auger Electron Spectroscopy Reference Manual*. Springer US, 1979. DOI: [10.1007/978-1-4757-1702-0](https://doi.org/10.1007/978-1-4757-1702-0).
- [35] P. T. Dawson and K. K. Tzatzov. “Quantitative auger electron analysis of titanium nitrides”. In: *Surface Science* 149.1 (Jan. 1985), pp. 105–118. ISSN: 00396028. DOI: [10.1016/S0039-6028\(85\)80016-9](https://doi.org/10.1016/S0039-6028(85)80016-9).

- [36] L. I. Vergara, M. C.G. Passeggi, and J. Ferrón. “Chemical changes induced on a TiO<sub>2</sub> surface by electron bombardment”. In: *Thin Solid Films* 515.23 (Sept. 2007), pp. 8365–8370. ISSN: 00406090. DOI: [10.1016/j.tsf.2007.04.031](https://doi.org/10.1016/j.tsf.2007.04.031).
- [37] James F. Ziegler, M. D. Ziegler, and J. P. Biersack. “SRIM - The stopping and range of ions in matter (2010)”. In: *Nuclear Instruments and Methods in Physics Research, Section B: Beam Interactions with Materials and Atoms* 268.11-12 (June 2010), pp. 1818–1823. ISSN: 0168583X. DOI: [10.1016/j.nimb.2010.02.091](https://doi.org/10.1016/j.nimb.2010.02.091).
- [38] P. Dutta, P. Dimon, and P. M. Horn. “Energy Scales for Noise Processes in Metals”. In: *Physical Review Letters* 43.9 (Aug. 1979), pp. 646–649. ISSN: 00319007. DOI: [10.1103/PhysRevLett.43.646](https://doi.org/10.1103/PhysRevLett.43.646). arXiv: [arXiv:1011.1669v3](https://arxiv.org/abs/1011.1669v3). URL: <https://link.aps.org/doi/10.1103/PhysRevLett.43.646>.
- [39] P. Dutta and P. M. Horn. “Low-frequency fluctuations in solids: 1/f noise”. In: *Reviews of Modern Physics* 53 (1981), pp. 497–516. DOI: [10.1103/RevModPhys.53.497](https://doi.org/10.1103/RevModPhys.53.497).
- [40] J. Briggmann et al. “Irradiation-induced defects in thin aluminium films studied by 1/f noise”. In: *physica status solidi (a)* 146 (1994), p. 325. ISSN: 1521396X. DOI: [10.1002/pssa.2211460128](https://doi.org/10.1002/pssa.2211460128).
- [41] R. H. Koch, J. R. Lloyd, and J. Cronin. “1/f noise and grain-boundary diffusion in aluminum and aluminum alloys”. In: *Physical Review Letters* 55 (1985), p. 2487. ISSN: 00319007. DOI: [10.1103/PhysRevLett.55.2487](https://doi.org/10.1103/PhysRevLett.55.2487).
- [42] J. V. Barth. *Transport of adsorbates at metal surfaces: From thermal migration to hot precursors*. Tech. rep. 3. 2000, pp. 75–149. DOI: [10.1016/S0167-5729\(00\)00002-9](https://doi.org/10.1016/S0167-5729(00)00002-9). URL: <http://ipent.ep>.
- [43] Jens Weckesser, Johannes V Barth, and Klaus Kern. “Direct observation of surface diffusion of large organic molecules at metal surfaces: PVBA on Pd(110)”. In: *Journal of Chemical Physics* 110.11 (1999), pp. 5351–5354. ISSN: 00219606. DOI: [10.1063/1.478430](https://doi.org/10.1063/1.478430). URL: <https://doi.org/10.1063/1.478430>.
- [44] J C Ornelas-Lizcano and R A Guirado-López. “Adsorption of carbon monoxide on small aluminum oxide clusters: Role of the local atomic environment and charge state on the oxidation of the CO molecule”. In: *Journal of Chemical Physics* 142.12 (2015), p. 124311. ISSN: 00219606. DOI: [10.1063/1.4916320](https://doi.org/10.1063/1.4916320). URL: <https://doi.org/10.1063/1.4916320>.
- [45] Douglas J. Fox et al. “The prototype aluminum-carbon single, double, and triple bonds: Al-CH<sub>3</sub>, Al=CH<sub>2</sub>, and Al—CH”. In: *The Journal of Chemical Physics* 73.7 (1980), pp. 3246–3254. ISSN: 00219606. DOI: [10.1063/1.440519](https://doi.org/10.1063/1.440519).
- [46] Alexandre G. Brolo, Donald E. Irish, and Brian D. Smith. “Applications of surface enhanced Raman scattering to the study of metal-adsorbate interactions”. In: *Journal of Molecular Structure* 405.1 (Mar. 1997), pp. 29–44. ISSN: 00222860. DOI: [10.1016/S0022-2860\(96\)09426-4](https://doi.org/10.1016/S0022-2860(96)09426-4).
- [47] Kuan Yu Lin, Guang Hao Low, and Isaac L. Chuang. “Effects of electrode surface roughness on motional heating of trapped ions”. In: *Physical Review A* 94.1 (July 2016), p. 013418. ISSN: 24699934. DOI: [10.1103/PhysRevA.94.013418](https://doi.org/10.1103/PhysRevA.94.013418). arXiv: [1605.02808](https://arxiv.org/abs/1605.02808).

- [48] I. Talukdar et al. “Implications of surface noise for the motional coherence of trapped ions”. In: *Physical Review A* 93.4 (Apr. 2016), p. 043415. ISSN: 2469-9926. DOI: [10.1103/PhysRevA.93.043415](https://doi.org/10.1103/PhysRevA.93.043415). URL: <http://link.aps.org/doi/10.1103/PhysRevA.93.043415>.
- [49] D. An et al. “Surface trap with dc-tunable ion-electrode distance”. In: *Review of Scientific Instruments* 89.9 (Sept. 2018), p. 093102. DOI: [10.1063/1.5046527](https://doi.org/10.1063/1.5046527). arXiv: [1807.06043](https://arxiv.org/abs/1807.06043). URL: <http://aip.scitation.org/doi/10.1063/1.5046527>.
- [50] J. A. Kovacich et al. “Auger electron and x-ray photoelectron spectroscopy of sputter deposited aluminum nitride”. In: *Journal of Applied Physics* 55.8 (Apr. 1984), pp. 2935–2939. ISSN: 00218979. DOI: [10.1063/1.333335](https://doi.org/10.1063/1.333335). URL: <http://aip.scitation.org/doi/10.1063/1.333335>.
- [51] B. Timmermans et al. “Chemical effects in Auger electron spectra of aluminium”. In: *Surface and Interface Analysis* 34.1 (Aug. 2002), pp. 356–359. ISSN: 0142-2421. DOI: [10.1002/sia.1316](https://doi.org/10.1002/sia.1316). URL: <http://doi.wiley.com/10.1002/sia.1316>.
- [52] M. E. Drits, E. S. Kadaner, and L. S. Toropova. “Recrystallization of aluminum and aluminum alloy foils”. In: *Metal Science and Heat Treatment* 13.5 (May 1971), pp. 399–401. ISSN: 15738973. DOI: [10.1007/BF00652447](https://doi.org/10.1007/BF00652447).
- [53] Carl V Thompson. *Grain growth in thin films*. Tech. rep. 1990, pp. 245–68. URL: [www.annualreviews.org](http://www.annualreviews.org).
- [54] G E Rhead. “Atomic mobility at solid surfaces”. In: *International Materials Reviews* 34.1 (1989), pp. 261–276. ISSN: 17432804. DOI: [10.1179/imr.1989.34.1.261](https://doi.org/10.1179/imr.1989.34.1.261). URL: <https://www.tandfonline.com/action/journalInformation?journalCode=yimr20>.
- [55] J Jurusik and L Zdanowicz. “Electron microscope investigations of the growth morphology of cadmium arsenide films vacuum deposited at various substrate temperatures”. In: *Thin Solid Films* 67.2 (1980), pp. 285–292. ISSN: 00406090. DOI: [10.1016/0040-6090\(80\)90461-7](https://doi.org/10.1016/0040-6090(80)90461-7).
- [56] Hailang Qin, Peter Sutter, and Guangwen Zhou. “The Crystallization of Amorphous Aluminum Oxide Thin Films Grown on NiAl(100)”. In: *Journal of the American Ceramic Society* 97.9 (Sept. 2014). Ed. by N. Jacobson, pp. 2762–2769. ISSN: 00027820. DOI: [10.1111/jace.13036](https://doi.org/10.1111/jace.13036). URL: <http://doi.wiley.com/10.1111/jace.13036>.
- [57] C. Y. Chang and R. W. Vook. “The effect of surface aluminum oxide films on thermally induced hillock formation”. In: *Thin Solid Films* 228.1-2 (May 1993), pp. 205–209. ISSN: 00406090. DOI: [10.1016/0040-6090\(93\)90599-K](https://doi.org/10.1016/0040-6090(93)90599-K).
- [58] Shien Ri and Masumi Saka. “Diffusion-fatigue interaction effect on hillock formation in aluminum thin films under thermal cycle testing”. In: *Materials Letters* 79 (July 2012), pp. 139–141. ISSN: 0167577X. DOI: [10.1016/j.matlet.2012.03.109](https://doi.org/10.1016/j.matlet.2012.03.109).
- [59] Yasunori Yamamura and Hiro Tawara. “Energy dependence of ion-induced sputtering yields from monatomic solids at normal incidence”. In: *Atomic Data and Nuclear Data Tables* 62.2 (Mar. 1996), pp. 149–253. ISSN: 0092640X. DOI: [10.1006/adnd.1996.0005](https://doi.org/10.1006/adnd.1996.0005).

- [60] Sheng Shiuan Yeh, Wen Yao Chang, and Juhn Jong Lin. “Probing nanocrystalline grain dynamics in nanodevices”. In: *Science Advances* 3.6 (June 2017), e1700135. ISSN: 23752548. DOI: [10.1126/sciadv.1700135](https://doi.org/10.1126/sciadv.1700135). URL: <https://advances.sciencemag.org/content/3/6/e1700135>.
- [61] H L Marcus. *Auger Electron Spectroscopy*. Jan. 2001. DOI: [10.1016/B0-08-043152-6/00078-4](https://doi.org/10.1016/B0-08-043152-6/00078-4).
- [62] Nan Jiang. *Electron beam damage in oxides: A review*. Dec. 2015. DOI: [10.1088/0034-4885/79/1/016501](https://doi.org/10.1088/0034-4885/79/1/016501).
- [63] Gary S. Was. *Fundamentals of radiation materials science: Metals and alloys, second edition*. Berlin, Heidelberg, 2016. Chap. 2, pp. 1–1002. ISBN: 9781493934386. DOI: [10.1007/978-1-4939-3438-6](https://doi.org/10.1007/978-1-4939-3438-6).
- [64] R. F. Egerton, P. Li, and M. Malac. “Radiation damage in the TEM and SEM”. In: *Micron*. Vol. 35. 6. Aug. 2004, pp. 399–409. DOI: [10.1016/j.micron.2004.02.003](https://doi.org/10.1016/j.micron.2004.02.003).
- [65] C. G. Pantano and Theodore E. Madey. “Electron beam damage in Auger electron spectroscopy”. In: *Applications of Surface Science* 7.1-2 (Jan. 1981), pp. 115–141. ISSN: 03785963. DOI: [10.1016/0378-5963\(81\)90065-9](https://doi.org/10.1016/0378-5963(81)90065-9).
- [66] M Zharnikov et al. “Modification of alkanethiolate monolayers on Au-substrate by low energy electron irradiation: Alkyl chains and the S/Au interface”. In: *Physical Chemistry Chemical Physics* 1.13 (1999), pp. 3163–3171. ISSN: 14639076. DOI: [10.1039/a902013f](https://doi.org/10.1039/a902013f).
- [67] P Rowntree, L Parenteau, and L Sanche. *Anion Yields Produced by Low-Energy Electron Impact on Condensed Hydrocarbon Films*. Tech. rep. 1991, pp. 4902–4909. URL: <https://pubs.acs.org/sharingguidelines>.
- [68] W. F. Van Dorp and C. W. Hagen. “A critical literature review of focused electron beam induced deposition”. In: *Journal of Applied Physics* 104.8 (2008), pp. 081301–081301–42. ISSN: 00218979. DOI: [10.1063/1.2977587](https://doi.org/10.1063/1.2977587).
- [69] Cechan Tian and C R Vidal. “Cross sections of the electron impact dissociative ionization of CO, and”. In: *Journal of Physics B: Atomic, Molecular and Optical Physics* 31.4 (1998), p. 895. ISSN: 0953-4075. DOI: [10.1088/0953-4075/31/4/031](https://doi.org/10.1088/0953-4075/31/4/031).
- [70] B A Sexton and A E Hughes. *A comparison of weak molecular adsorption of organic molecules on clean copper and platinum surfaces*. Tech. rep. 1984, p. 227.
- [71] Gregory Wilson and J R Dennison. “Approximation of range in materials as a function of incident electron energy”. In: *IEEE Transactions on Plasma Science*. Vol. 40. 2 PART 1. 2012, pp. 291–297. DOI: [10.1109/TPS.2011.2176515](https://doi.org/10.1109/TPS.2011.2176515). URL: <http://ieeexplore.ieee.org..>